



University
of Glasgow

Tavares, Adriana A.S. (2011) *Development of novel radiotracers as tools for imaging the human brain.*
PhD thesis.

<http://theses.gla.ac.uk/2919/>

Copyright and moral rights for this thesis are retained by the author

A copy can be downloaded for personal non-commercial research or study, without prior permission or charge

This thesis cannot be reproduced or quoted extensively from without first obtaining permission in writing from the Author

The content must not be changed in any way or sold commercially in any format or medium without the formal permission of the Author

When referring to this work, full bibliographic details including the author, title, awarding institution and date of the thesis must be given

Development of Novel Radiotracers as Tools for Imaging the Human Brain

Adriana Alexandre dos Santos Tavares

B.Sc, M.Sc

A thesis submitted to the University of Glasgow, Institute of
Neuroscience and Psychology, College of Medical, Veterinary and Life
Sciences, for the degree of Doctor of Philosophy



University
of Glasgow

© Adriana Alexandre S. Tavares

October 2011

Abstract

Introduction

Brain imaging using single photon emission computed tomography (SPECT) or positron emission tomography (PET) can be used to study the processes underlying neurological and psychiatric disorders. In addition, *in vivo* brain imaging using SPECT or PET may provide new approaches for drug target identification, pre-clinical testing and occupancy studies, and therefore improve drug discovery (1). The utility of *in vivo* brain imaging using SPECT or PET relies on the ability of different radiotracers (typically organic compounds labelled with radionuclides) to bind to a wide variety of targets, including receptors, transporters and enzymes (2-3). Therefore the development of novel radiotracers for *in vivo* brain imaging using SPECT or PET is of vital importance. This thesis is focused on the process of developing novel radiotracers as tools for imaging the human brain, where the radiotracer discovery and development pipeline is discussed and each step prior to clinical trials investigated.

Radiotracer discovery

Previously, discovery of novel brain radiotracers has largely relied on simplistic screening tools. Improved selection methods at the early stages of radiotracer discovery and an increased understanding of the relationships between *in vitro* physicochemical and *in vivo* radiotracer properties are needed. This thesis investigated if high performance liquid chromatography (HPLC) methodologies could provide criteria for lead candidate selection by comparing HPLC measurements with radiotracer properties in humans. In this study, ten molecules, previously used as radiotracers in humans, were analysed to obtain the following measures: partition coefficient (Log P); permeability (P_m); percentage of plasma protein binding (%PPB); and membrane partition coefficient (K_m). Relationships between brain entry measurements (Log P, P_m and %PPB) and *in vivo* brain percentage injected dose (%ID); and K_m and specific binding *in vivo* (BP_{ND}) were investigated. Results showed that HPLC measurements of P_m , %PPB and K_m were potentially useful in predicting *in vivo* performance and hence allow evaluation and ranking of compound libraries for the selection of lead radiotracer candidates at early stages of radiotracer discovery. The HPLC tool developed provides information on *in vivo* non-specific binding and binding potential that is not possible using conventional screening methods. Another important finding reported in this thesis is that Log P should not be relied on as a predictor of brain entry.

The HPLC tool developed, together with competition binding assays, was used to characterise a newly synthesised library of compounds for imaging of the translocator protein (TSPO) in brain using SPECT. Results showed that compound LS 1 was the most likely to succeed within the library investigated, but the high %PPB observed for LS 1 suggested novel compounds with improved %PPB were needed. Thus, a novel library of compounds for imaging of TSPO in brain using SPECT is currently being developed for future testing using the HPLC tool developed here and competition binding assays.

Pre-clinical research: radiotracers for imaging the noradrenaline transporter (NAT) in brain using SPECT

In this thesis, NKJ64, a novel iodinated analogue of reboxetine, was successfully radiolabelled *via* electrophilic iododestannylation and evaluated as a potential SPECT radiotracer for imaging the NAT in brain using rodents and non-human primates. Biological evaluation of the novel radiotracer, $^{123/125}\text{I-NKJ64}$, in rodents included: *in vitro* ligand binding assays; *in vitro* and *ex vivo* autoradiography; *in vivo* biodistribution studies and *ex vivo* pharmacological blocking studies. In rats, $^{123/125}\text{I-NKJ64}$ displayed saturable binding with nanomolar affinity for the NAT in cortical homogenates, regional distribution consistent with the known density of NAT in the rodent brain and high maximum brain uptake of around 2.93 % of the injected dose. The specific: non-specific ratio (locus coeruleus:caudate putamen) of $^{123}\text{I-NKJ64}$ uptake was 2.8 at 30 minutes post intravenous injection and prior administration of reboxetine significantly reduced the accumulation of $^{123}\text{I-NKJ64}$ in the locus coeruleus (> 50% reduction). Data obtained using rodents indicated that further evaluation of $^{123}\text{I-NKJ64}$ in non-human primates was needed to determine its utility as a SPECT radiotracer for imaging of NAT in brain. Consequently, *in vivo* kinetic modelling studies using SPECT imaging with $^{123}\text{I-NKJ64}$ and two baboons were carried out to determine $^{123}\text{I-NKJ64}$ brain binding kinetics, brain distribution and plasma metabolism in non-human primates. Even though a high brain uptake of around 3.0% of the injected dose was determined, the high non-specific binding observed throughout the brain, a low binding potential ($\text{BP}_{\text{ND}} < 2$) in NAT rich regions and a brain distribution that was inconsistent with the known NAT distribution in non-human primate brain precludes the translation of $^{123}\text{I-NKJ64}$ into humans.

Another NAT radiotracer, $^{123}\text{I-INER}$, developed by Tamagnan and colleagues at Yale University and Institute for Degenerative Disorders, New Haven, USA, was also investigated as part of this thesis. Kinetic modelling analysis of $^{123}\text{I-INER}$ in baboon brain was investigated for different models, namely invasive and reference tissue models. Bolus plus constant infusion experiments with displacement at equilibrium using six different doses of atomoxetine and four different doses of reboxetine were carried out

in several baboons to obtain occupancy measurements as a function of injected dose (mg/kg) for the two NAT selective drugs. Results showed that reference tissue models were able to determine BP_{ND} values of ^{123}I -INER in different brain regions. In addition the volume of distribution could be determined by dividing concentration in tissue by the concentration in venous blood at 3 hours post-injection. After administration of atomoxetine or reboxetine, dose-dependent occupancy was observed in brain regions known to contain high densities of NATs. Results supported the translation of ^{123}I -INER into humans studies, despite the slow kinetics determined over the imaging period. Pharmacokinetic properties of ^{123}I -INER described in this thesis may be used to simplify future data acquisition and image processing.

Conclusion

In conclusion, this thesis reported: (1) the development of novel radiotracers for brain imaging, namely NAT and TSPO; and (2) the development of a new methodology for aiding lead molecule identification at early stages of radiotracer discovery (i.e. prior to radiolabelling). In addition, an overview of radiotracer discovery and development process is provided in a single document, with a focus on brain radiotracers.

Table of contents

Abstract.....	2
List of tables.....	9
List of figures.....	11
Acknowledgements.....	15
Author's declaration.....	17
Abbreviations.....	19
1 Introduction.....	23
1.1 Radionuclide imaging.....	23
1.2 The process of radiotracer discovery and development.....	25
1.2.1 Target identification and lead molecule discovery.....	25
1.2.2 Pre-clinical research.....	26
1.2.3 Clinical trials.....	28
1.3 Novel radiotracers for imaging the human brain.....	29
1.4 Thesis aims and objectives.....	31
1.5 Thesis outline.....	33
2 Development of a novel tool for brain radiotracer discovery.....	34
2.1 Introduction.....	34
2.1.1 Crossing the BBB and reaching the brain.....	34
2.1.2 Methods for predicting BBB penetration.....	37
2.1.3 Lipophilicity and phospholipophilicity.....	38
2.1.4 Partition systems.....	39
2.1.5 IAM chromatography.....	40
2.1.6 Plasma protein binding.....	43
2.1.7 HPLC: advantages and limitations.....	44
2.1.8 Hypothesis and aims.....	44
2.2 Material and Methods.....	45
2.2.1 HPLC system and general preparation.....	45
2.2.2 C ₁₈ chromatography.....	46
2.2.3 IAM chromatography for P _m and K _m determination.....	47
2.2.4 HSA chromatography.....	49
2.2.5 Flask methods for Log P determination.....	50
2.2.6 In silico algorithms for Log P determination.....	51
2.2.7 HPLC analyses of existing radiotracer compounds.....	51
2.2.8 Data analysis and curve fitting.....	54
2.2.9 HPLC analyses of radiotracer candidates for SPECT imaging of the TSPO in the brain.....	54

2.3	Results	55
2.3.1	Investigation of HPLC analyses as a novel tool for brain radiotracer discovery	55
2.3.2	HPLC analyses of radiotracer candidates for SPECT imaging of the TSPO in the brain	63
2.4	Discussion	66
2.4.1	Investigation of HPLC analyses as a novel tool for brain radiotracer discovery	66
2.4.2	HPLC analyses of radiotracer candidates for SPECT imaging of the TSPO in the brain	70
2.5	Conclusion	74
3	Radiosynthesis of ^{123/125} I-NKJ64: a novel SPECT radiotracer for imaging of NAT in brain	75
3.1	Introduction	75
3.1.1	The role of the NAT in noradrenergic neurotransmission and consequences of its dysregulation on brain function	75
3.1.2	Radiotracers for imaging of NAT	77
3.1.3	Design and synthesis of novel iodoreboxetine analogues for imaging of NAT in brain	79
3.1.4	Introduction to radiosynthesis of novel radiotracers	83
3.1.5	Nucleophilic and electrophilic radiolabelling techniques	84
3.1.6	Separation and purification of radiotracers	87
3.1.7	Hypothesis and aims	88
3.2	Material and Methods	88
3.2.1	General	88
3.2.2	Analytical HPLC system	89
3.2.3	Radiolabelling	89
3.2.4	Purification and specific activity determination	90
3.2.5	Labelling using Na ¹²⁷ I and mass spectrometry analysis	92
3.2.6	Stability testing	93
3.3	Results	93
3.4	Discussion	98
3.5	Conclusion	101
4	Biological evaluation of ^{123/125} I-NKJ64 in rodents	103
4.1	Introduction	103
4.1.1	Central noradrenergic system in rodent brain	103
4.1.2	Hypothesis and aims	105
4.2	Material and Methods	105

4.2.1	General	105
4.2.2	Rats.....	106
4.2.3	General preparation and monitoring of rats.....	106
4.2.4	Saturation binding assays using ¹²⁵ I-NKJ64.....	106
4.2.5	In vitro rat brain autoradiography using ¹²³ I-NKJ64.....	107
4.2.6	Whole body dynamic planar imaging of rats following intravenous administration of ¹²³ I-NKJ64	108
4.2.7	In vivo/ex vivo pharmacological blocking experiments using ¹²³ I-NKJ64	109
4.3	Results	110
4.4	Discussion.....	122
4.5	Conclusion	127
5	Biodistribution and pharmacokinetics of ¹²³ I-NKJ64 in non-human primate brain....	129
5.1	Introduction	129
5.1.1	Noradrenergic system in non-human primate brain	129
5.1.2	Brain imaging and kinetic modelling - main concepts and considerations ..	131
5.1.3	Hypothesis and aims	134
5.2	Material and Methods	135
5.2.1	Non-human primates.....	135
5.2.2	Animal general preparation and monitoring.....	135
5.2.3	General SPECT acquisition protocol	136
5.2.4	Administration of ¹²³ I-NKJ64 and displacer	136
5.2.5	Analysis of plasma pharmacokinetics.....	137
5.2.6	Image processing and co-registration with magnetic resonance images	138
5.2.7	Data analysis	139
5.3	Results	140
5.4	Discussion.....	153
5.5	Conclusion	155
6	Kinetic modelling and occupancy measures of NAT in baboons using SPECT with ¹²³ I-INER	157
6.1	Introduction	157
6.1.1	Hypothesis and aims	157
6.2	Material and Methods	158
6.2.1	Non-human primates.....	158
6.2.2	Animal general preparation and monitoring.....	158
6.2.3	General SPECT acquisition protocol	158
6.2.4	¹²³ I-INER baseline and pre-blocking experiments in non-human primates...	159
6.2.5	¹²³ I-INER displacement studies in non-human primates	160
6.2.6	Analysis of plasma pharmacokinetics.....	161

6.2.7 Image processing and co-registration with magnetic resonance imaging (MRI)	161
6.2.8 Data analysis	161
6.3 Results	163
6.3.1 ^{123}I -INER baseline and pre-blocking experiments	163
6.3.2 ^{123}I -INER displacement studies	175
6.4 Discussion	176
6.5 Conclusions	180
7 Final conclusions and future work	182
Appendix 1	185
Appendix 2	186
List of references	191

List of tables

Table 2.1 Main advantages and disadvantages of ultrafiltration versus HPLC-HSA.	43
Table 2.2 <i>In vivo</i> measures of whole brain peak %ID and BP _{ND} obtained from previously published studies in healthy human volunteers.....	53
Table 2.3 HPLC analyses for all radiotracer compounds evaluated.....	56
Table 2.4 Summary of Log P values obtained by different methodologies.	60
Table 2.5 The %COV of the Log P determined for β -CIT and I-PK11195 using either traditional flask or HPLC C ₁₈ methodology.....	63
Table 2.6 Affinity and physicochemical properties of PK11195 and the novel library of analogues.....	63
Table 2.7 Proposed guidelines for aiding lead molecule identification using developed HPLC tool.....	69
Table 3.1 Binding affinity (K _i) of four antidepressant drugs for NAT reuptake sites in rat frontal cortical membranes.....	80
Table 3.2 Affinity (K _i) of reboxetine for other brain receptors and transporters in rat whole brain homogenates.....	81
Table 3.3 Affinity (K _i) of iodoreboxetine analogues for NAT, SERT and DAT in rat whole brain homogenates.....	82
Table 3.4 Summary of the main radioiodination methods.	87
Table 3.5 Summary of analytical HPLC results showing the yield of ¹²³ I-NKJ64 from the small scale reactions investigated.	94
Table 3.6 Summary of radiolabelling reactions for the preparation of ^{123/125} I-NKJ64. ...	95
Table 4.1 Distribution of specific binding of ³ H-nisoxetine to NATs in rat brain.....	104
Table 4.2 Elimination half-life and peak %injected dose of total radioactivity in rats.	113
Table 4.3 Biodistribution of radioactivity in saline and reboxetine pre-treated rats at 30 minutes post-injection.	122
Table 5.1 Distribution of specific ³ H-nisoxetine binding to NATs in rhesus monkey brain.....	130
Table 5.2 Percentage of ¹²³ I-NKJ64 present in arterial blood over 4 hours.....	142
Table 5.3 Percentage washout of ¹²³ I-NKJ64 from the whole brain and selected brain regions following radiotracer bolus intravenous injection.	146
Table 5.4 Summary of the kinetic parameters obtained from data following bolus injection of ¹²³ I-NKJ64 in baboon 1.	148
Table 5.5 Summary of the kinetic parameters obtained from data following bolus injection of ¹²³ I-NKJ64 in baboon 2.	149
Table 6.1 Summary of atomoxetine and reboxetine doses investigated using six baboons.....	160

Table 6.2 Kinetic analysis of the results obtained from the baseline and pre-blocking experiments following bolus injection of ^{123}I -INER.	168
Table 6.3 BP_{ND} values for ^{123}I -INER in baboon brain determined using analysis with SRTM and MRTM2 models.	170
Table 6.4 The percentage NAT occupancy by atomoxetine in baboon brain determined by SPECT imaging with ^{123}I -INER and different calculation methods.....	174

List of figures

Figure 1.1 Typical radiotracer discovery and development pipeline.	25
Figure 2.1 The brain vascular system and the blood brain barrier (BBB).	35
Figure 2.2 Main screening methods used for prediction of biological relevant molecule properties.	38
Figure 2.3 Schematic representation of cell membrane, liposome and IAM structures. .	41
Figure 2.4 Schematic representations of the three major IAM.PC surfaces used for prediction of molecule properties.	41
Figure 2.5 Molecule interaction and transport in fluid membranes and IAM surfaces....	42
Figure 2.6 Schematic representation of C ₁₈ chromatographic principle for determination of Log P.	46
Figure 2.7 Schematic representation of IAM chromatography used for the determination of P _m and K _m	49
Figure 2.8 Schematic representation of the measurement of compound binding to plasma proteins by HSA chromatography.	50
Figure 2.9 Chemical structures of the radiotracer compounds evaluated.	52
Figure 2.10 The chemical structures of novel PK11195 analogues.	55
Figure 2.11 Relationship between Log P measured using HPLC C ₁₈ methodology and %ID.	57
Figure 2.12 Relationship between %PPB measured using HPLC HSA methodology and %ID.	57
Figure 2.13 Relationship between permeability measured using HPLC IAM methodology and %ID.....	58
Figure 2.14 Relationship between K _m measured using HPLC IAM methodology and BP _{ND} . 58	
Figure 2.15 Comparison of relationship between Log P determined by HPLC or flask method and %ID.	61
Figure 2.16 Comparison of the relationship between Log P calculated using different computational methods and %ID.	62
Figure 2.17 Novel PK11195 analogues and the process of lead molecule selection.	72
Figure 3.1 Schematic representation of the noradrenergic neurotransmission process. 76	
Figure 3.2 Chemical structures of reboxetine and iodinated analogues for <i>in vivo</i> imaging of NAT.	82
Figure 3.3 Schematic of electrophilic and nucleophilic radioiodination methods.	86
Figure 3.4 Schematic representations of HPLC and SPE purification methods.	88
Figure 3.5 Analytical HPLC system used for radiosynthesis of NKJ64.....	89
Figure 3.6 Radiolabelling of ^{123/125} I-NKJ64 from the corresponding organotin precursor <i>via</i> a two step reaction.	90

Figure 3.7 Semi-preparative HPLC systems used for radiosynthesis of $^{123/125}\text{I}$ -NKJ64.....	91
Figure 3.8 Representative amount /response curve for I-NKJ64 (method B).....	92
Figure 3.9 A typical analytical HPLC trace following co-injection of NKJ64 precursor, BOC-intermediate standard and I-NKJ64 standard.	94
Figure 3.10 Representative semi-preparative HPLC UV trace and radiotracer from a radiosynthesis of ^{123}I -NKJ64.	97
Figure 3.11 Deprotected protodestannylated precursor.....	98
Figure 3.12 Representative analytical HPLC trace of ^{125}I -NKJ64 stability tests.	98
Figure 4.1 Anatomical distribution of the main noradrenergic projections in the rat brain.....	104
Figure 4.2 Schematic representation of <i>in vitro</i> rat brain autoradiography using ^{123}I -NKJ64.	107
Figure 4.3 Schematic representation of whole body dynamic planar imaging acquisition using ^{123}I -NKJ64.	109
Figure 4.4 Schematic of <i>in vivo/ex vivo</i> pharmacological studies using ^{123}I -NKJ64.	110
Figure 4.5 <i>In vitro</i> binding of ^{125}I -NKJ64 to rat cortex.	111
Figure 4.6 Representative autoradiogram of <i>in vitro</i> binding of ^{123}I -NKJ64 to rat coronal brain sections.	112
Figure 4.7 ^{123}I -NKJ64 whole rat body sum images.	113
Figure 4.8 Whole rat body <i>in vivo</i> ^{123}I -NKJ64 images obtained by dynamic planar imaging.	114
Figure 4.9 Whole rat body <i>in vivo</i> ^{123}I -NKJ64 sequential images, each summed over a 3 minute period, from 0-60 minutes.....	115
Figure 4.10 Time activity curves of ^{123}I -NKJ64 uptake in different organs.....	116
Figure 4.11 Time activity curves of ^{123}I -NKJ64 uptake in anterior brain, posterior brain and whole brain.	117
Figure 4.12 Percentage of peak uptake of ^{123}I -NKJ64 in anterior, posterior and whole brain and blood over time.	118
Figure 4.13 <i>In vivo/ex vivo</i> pharmacological studies results of ^{123}I -NKJ64 in rat brain.	120
Figure 4.14 Comparative analysis of ^{123}I -NKJ64 rat brain autoradiograms.	121
Figure 5.1 One tissue and two tissue compartmental model schematics.	134
Figure 5.2 A reference tissue model schematic.....	134
Figure 5.3 Schematic outline of the experimental procedure in baboons using ^{123}I -NKJ64.	137
Figure 5.4 Summary of the main steps of SPECT image analysis and processing.....	138
Figure 5.5 Parent radiotracer fraction present in arterial plasma following bolus injection of ^{123}I -NKJ64 in baboon 1.	141

Figure 5.6 Parent radiotracer fraction present in arterial plasma following bolus injection of ^{123}I -NKJ64 in baboon 2.	141
Figure 5.7 Examples of HPLC chromatograms obtained from analysis of arterial blood taken following bolus injection of ^{123}I -NKJ64.	142
Figure 5.8 Brain SPECT images showing the distribution of ^{123}I -NKJ64 in baboon 1.	143
Figure 5.9 Brain SPECT images showing the distribution of ^{123}I -NKJ64 in baboon 2.	144
Figure 5.10 Time-activity curves for ^{123}I -NKJ64 in multiple brain regions.	145
Figure 5.11 Binding ratios in brain regions over time following bolus injection of ^{123}I -NKJ64.	146
Figure 5.12 V_T values obtained using 2T compartmental model and arterial input function.....	150
Figure 5.13 Brain ^{123}I -NKJ64 SPECT images pre- and post-administration of reboxetine in baboon 1.....	151
Figure 5.14 Uptake of ^{123}I -NKJ64 in baboon 1 brain pre- and post-administration of reboxetine.....	152
Figure 5.15 Target:non-target ratio of ^{123}I -NKJ64 pre- and post-administration of reboxetine in baboon 1 brain.....	152
Figure 6.1 Experimental procedure for the baseline and pre-blocking experiments performed in a single baboon using ^{123}I -INER and atomoxetine.	159
Figure 6.2 Experimental procedure for <i>in vivo</i> ^{123}I -INER displacement studies in baboons using atomoxetine and reboxetine.	160
Figure 6.3 MRI co-registered SPECT images of ^{123}I -INER distribution in baboon brain at baseline.....	164
Figure 6.4 Time activity curves of ^{123}I -INER uptake in multiple baboon brain regions. .	165
Figure 6.5 Time-activity curves of the parent fraction present in both venous and arterial plasma after intravenous injection of ^{123}I -INER in the baseline study.	165
Figure 6.6 V_T values in baboon brain determined during the baseline study using the 2T compartmental model.	167
Figure 6.7 ^{123}I -INER brain SPECT images co-registered with MRI (transverse, sagittal and coronal planes from left to right), showing the distribution at baseline (a) and following pre-blocking with atomoxetine (b).	169
Figure 6.8 Comparison of the BP_{ND} values for ^{123}I -INER in baboon brain calculated using different methods.....	171
Figure 6.9 C_t/C_p values calculated for ^{123}I -INER in baboon brain over time.....	172
Figure 6.10 The relationship between $V_{T \text{ app}}$ and V_T values calculated for ^{123}I -INER in baboon brain.	173
Figure 6.11 NAT occupancy by atomoxetine in baboon brain measured by SPECT with ^{123}I -INER.....	175

Figure 6.12 NAT occupancy by reboxetine in baboon brain measured by SPECT with ^{123}I -
INER.176

Acknowledgements

I would like to start by thanking my supervisors, Dr. Sally Pimlott and Dr. Deborah Dewar, for their continual advice and valuable support over the last 3 years. I thank them for trusting in my abilities and ideas, for providing me with invaluable scientific opportunities and for many hours of exciting scientific discussion. I would also like to give a special thank you to my adviser, Professor Mhairi Macrae, not only for the continuous interest in my research but also for her invaluable support through some of the toughest times.

The non-human primate work reported in this thesis would have not been possible without the support from Molecular Neuroimaging LLC (MNI) and Yale University - USA, in particular, Dr. Gilles Tamagnan, Dr. John Seibyl, Dr. Olivier Barret, Dr. Jeff Batis, Dr. Ronald Baldwin and Dr. Sharon Lee; so to all of them my very special thanks. Acknowledgements must also go to Dr. Jonathan Owens for his interest in my research and for providing funding for my visit to MNI and Yale University.

I would also like to thank Dr. Hank Kung from Pennsylvania University, Dr. Franklin Aigbirhio from Cambridge University, Dr. Frederic Bois from Yale University and Dr. Andrew Sutherland from University of Glasgow for kindly providing ADAM, PIB, Iomazenil and I-PK11195 reference compounds, respectively. Without these gifts it would have not been possible to develop the novel tool for aiding brain radiotracer discovery presented in this thesis.

Collaborative approaches are of extreme importance in research and thus, I'm very thankful to Dr. Andrew Sutherland and his chemistry group, in particular Nicola Jobson and Louise Stevenson, for developing the libraries of compounds and for synthesising the precursors for radiolabelling.

Thanks to Dr. Sue Champion for the valuable support, from HPLC/chemistry discussions and hands on in the lab to more personal help when needed.

Many thanks also go to all WSI staff and my fellow colleagues for all the help over the last 3 years. A particular thank you must go to Mrs. Linda Carberry. Linda gave me a fantastic technical help in the lab, truly my right arm. I will always remember our time in the lab with care.

I would also like to thank Mrs. Aileen Miller and Mrs. Margaret Phillips for technical assistance with samples counting; also Bio-Images Research Ltd. for kindly providing access to the gamma camera facilities for the rodent *in vivo* studies; and Dr. Jim Patterson for his comments and advice on multiple studies performed as part of this thesis.

I'm also grateful to Scottish Imaging Network: A Platform for Scientific Excellence Collaboration (SINAPSE), a Pooling Initiative funded by the Scottish Funding Council and the Chief Scientist Office of the Scottish Executive, for the full studentship and for supporting my research. A special thanks to Professor David Wyper for his enthusiastic interest in my research and for believing in me from the very first day.

Thanks to all my “tuga” friends for sharing my complaints about the Glasgow rainy weather and for providing me with some of the most amazing moments in Glasgow. Without those long Portuguese dinners/lunches what would I have done? They helped me to keep mentally sane and made me feel so much closer to home. Very special thanks to all: Ana, André, Arcélio, Cíntia, Francisca, Frederico, Joana, Luís, Manuel, Mariana, Miguel & Joana, Patrícia, Ricardo, Sérgio.

At last but not least, my warmest thanks go to my family that have helped me to get through this last 3 years and always believed in my ability to succeed (you will always be in my heart). My most sincere thanks go to my mother Edite and father Joaquim for always encouraging me to pursuit my dreams. Thanks to my “baby” brother Pedro for believing in me (you will always be my little boy!). And a very special thanks to my grandparents, Maria Lina and José, for many life-time experiences, from fishing in the river to supporting my move to another country.

Author's declaration

This thesis represents the original work of Adriana Alexandre dos Santos Tavares unless explicitly stated otherwise in the text. This thesis has not been submitted in any form to any other University. Portions of the work described herein have been published elsewhere as listed below.

Signature: _____

Adriana Alexandre dos Santos Tavares

September 2011

List of papers:

1. Stevenson L, Tavares AAS, Brunet A, McGonagle FI, Dewar D, Pimlott SL, Sutherland A (2010). New iodinated quinoline-2-carboxamides for SPECT imaging of the translocator protein. *Bioorganic Med Chem Lett*, 20:954-957.
2. Tavares AAS, Jobson N, Dewar D, Sutherland A, Pimlott S (2011). Development of the radiosynthesis of high-specific-activity ^{123}I -NKJ64. *Nuc Med and Biol*, 38:493-500.
3. Tavares AAS, Jobson N, Dewar D, Sutherland A, Pimlott S (2011). ^{123}I -NKJ64: A Novel SPECT Radiotracer for Imaging the Noradrenaline Transporter in Brain. *Synapse*, 65:658-667.
4. Tavares AAS, Lewsey J, Dewar D, Pimlott S (2011). Radiotracer properties determined by high performance liquid chromatography: a potential tool for brain radiotracer discovery. *Nuc Med Biol* [in press]
5. Tavares AAS, Barret O, Batis J, Seibyl J, Tamagnan G. Kinetic modelling and occupancy measurements of the norepinephrine transporters in baboons using SPECT with ^{123}I -INER. *Eur J Nuc Med Mol Imag* [in preparation]
6. Tavares AAS, Jobson N, Dewar D, Sutherland A, Barret O, Batis J, Seibyl J, Tamagnan G, Pimlott S. Iodine-123 labelled reboxetine analogues for imaging of

noradrenaline transporter in brain using single photon emission computed tomography. Synapse [in preparation]

List of abstracts:

1. **Tavares A**, Dewar D, Sutherland A, Pimlott S (2010). (R,S)-2-Iodo-Reboxetine: Development as a Novel SPECT Radiotracer for Imaging the Noradrenaline Transporter in Brain. *Neuroimage*, 52(S1):99
2. Stevenson L, **Tavares A**, Dewar D, Pimlott S, Sutherland A (2010). New SPECT Imaging Agents For The Translocator Protein. *Neuroimage*, 52(S1):111
3. **Tavares A**, Dewar D, Pimlott S (2011). A New Approach to Central Nervous System Radiotracer Discovery using High Performance Liquid Chromatography. *Journal of Cerebral Blood Flow and Metabolism*. BrainPET2011 (Barcelona, Spain)

Abbreviations

A	Abraham H-bond acidity parameter
Aβ	β -amyloid
ADAM	2-((2-((dimethylamino)methyl)phenyl)thio)-5-iodophenylamine
ADHD	Attention-deficit/hyperactivity disorder
ADME	Absorption, distribution, metabolism stability and excretion
AGP	Alpha-acid glycoprotein
AIC	Akaike information criterion
Aq.	Aqueous
Atomoxetine	(-)- <i>N</i> -Methyl-3-phenyl-3-(ortho-tolyloxy)-propylamine
B_{avail}	Number of available receptors <i>in vivo</i>
BBB	Blood brain barrier
β-CIT	2 β -carbomethoxy-3 β -(4-iodophenyl)tropane
BCSFB	Blood cerebrospinal fluid barrier
B/I	Bolus/infusion
B_{max}	Maximum binding capacity / receptor density
BOC	<i>tert</i> -butyloxycarbonyl
BP	Binding potential
BP_{ND}	Binding potential, defined at equilibrium as the ratio of specifically bound to non-displaceable radiotracer in tissue
ΔBP_{ND}	Change in BP _{ND}
¹¹C-DMI	¹¹ C-Desipramine
CHI	Chromatographic hydrophobicity index
CI	Chemical ionisation
CNS	Central nervous system
%COV	Coefficient of variation
Cpm	Counts per minute
CT	Computed tomography
C₁₈	Octadecyl silica
D	Drug dose
DASB	3-amino-4-(2-dimethylaminomethylphenylsulfanyl)benzotrile
DAT	Dopamine transporter
D_m	Membrane diffusion coefficient
DMS	Dimethyl sulphide
EDTA	Ethylenediaminetetraacetic acid
ED₅₀	Drug dose for 50% occupancy
¹⁸F-FDG	¹⁸ F-fluodeoxyglucose

f_r	Flow rate
HCl	Hydrochloric acid
HPLC	High performance liquid chromatography
HSA	Human serum albumin
5-IA85380	3-[2(S)-2-azetidylmethoxy]pyridine
IAM	Immobilized artificial membrane
IBZM	3-iodo-6-methoxybenzamide
%ID	Percentage injected dose
INER	(S,S)-2-[α -(2-ethoxyphenoxy)phenylmethyl]-morpholine
^{125}I -INXT	(R)-N-methyl-(2-[^{125}I]iodo-phenoxy)-3-phenylpropylamine
lomazenil	Ethyl-7-iodo-5,6-dihydro-5-methyl-6-oxo-4H-imidazo[1,5- α][1,4]-benzodiazepine-3-carboxylate
I-PK11195	1-(2-iodophenyl)-N-methyl-N-(1-methylpropyl)-3-isoquinolinecarboxamide
^{125}I -PYINXT	(R)-N-methyl-3-(3-[^{125}I]pyridin-2-yloxy)-3-phenylpropan-1-amine (^{125}I -PYINXT)
KCl	Potassium chloride
K_D	Dissociation constant
K_i	Inhibition constant
k_{IAM}	Solute capacity factor on the IAM column
K_m	Membrane partition coefficient
k_{off}	<i>In vitro</i> dissociation rate constant
k_{on}	<i>In vitro</i> association rate constant
K_1	Rate constant for transport from plasma to tissue
k_2, k_3, k_4	Rate constants used for kinetic modelling
L	Membrane length
Log D	Distribution coefficient
Log P	Partition coefficient
MAO	Monoamine oxidase
MDCK	Madin-Darby Canine Kidney
MR	Magnetic resonance
MRTM2	Multilinear reference tissue model 2
MS	Mass spectrometry
MSC	Model selection criterion
MW	Molecular weight
NaCl	Sodium chloride
NaOH	Sodium hydroxide
NAT	Noradrenaline transporter

NCA	Non-carrier added
NKJ64	(<i>R,S</i>)-2-[α -(2-ethoxyphenoxy)phenylmethyl]-morpholine
Oct.	Octanol
O_{max}	Maximum occupancy
PA	Phosphatidic acid
PAA	Peracetic acid
PAMPA	Parallel artificial membrane permeability assay
PBS	Phosphate buffered saline
PC	Phosphocholine
PE	Phosphatidylethanolamine
PET	Positron emission tomography
PG	Phosphatidylglycerol
P-gp	P-glycoprotein
PIB	[<i>N</i> -methyl]-2-(4'-methylaminophenyl)-6-hydroxybenzothiazole
PK11195	1-(2-chlorophenyl)- <i>N</i> -methyl- <i>N</i> -(1-methylpropyl)-3-isoquinolinecarboxamide
P_m	Permeability
PPB	Plasma protein binding
PS	Phosphatidylserine
Reboxetine	2-[α -(2-ethoxyphenoxy)benzyl]morpholine
OHDMI	1-(10,11-Dihydro-dibenzo[<i>b,f</i>]azepin-5-yl)-3-methylamino-propan-2-ol
ROI	Region of interest
Rpm	Rotations per minute
(<i>R,R</i>)-I-QNB	3-quinuclidinyl-4-iodobenzilate
RSA	Rat serum albumin
SB	Specific binding
SC	Schwartz criterion
SD	Standard deviation
SEM	Standard error of mean
SERT	Serotonin transporter
SNRI	Selective noradrenaline reuptake inhibitor
SPA	Scintillation proximity assay
SPE	Solid phase extraction
SPECT	Single photon computed tomography
SPR	Surface plasma resonance
SRTM	Simplified reference tissue model
SS	Absolute sum of squares

(S,S)-¹⁸F-FMeNER-D₂	(S,S)-2-(α-(2-[¹⁸ F]Fluoro[² H ₂]methoxyphenoxy)phenoxy)benzyl)morpholine
(S,S)-¹⁸F-FRB-D₄	(S,S)-2-[α-(2-(2-[¹⁸ F]Fluoro[² H ₄]ethoxyl)phenoxy)benzyl]morpholine
(S,S)-MeNER	(S,S)-2-(α-(2-Methoxyphenoxy)benzyl)morpholine
SUV	Standard uptake value
SUVr	SUV target region relative to SUV in occipital cortex
Sy.x	Standard deviation of the vertical distances of the points from the line
TFA	Trifluoroacetic acid
TSPO	Translocator protein
t_r	Retention time
t₀	Retention time of the un-retained compound
T_{1/2}	Half-life
T_{1/2 eff}	Effective half-life
T_{1/2 bio}	Biological half-life
UV	Ultra-violet
V	Molar volume
V_m	Total volume of solvent within the IAM HPLC column
V_{ND}	Non-displaceable volume of distribution
VOI	Volume of interest
V_s	Specific volume of distribution
V_s'	Volume of the IAM interface created by the immobilized phospholipids
V_T	Volume of distribution
V_{T app}	Apparent volume of distribution
φ₀	Volume percent of organic phase concentration in the mobile phase when the retention time is twice the dead time
1T	One tissue compartmental model
2T	Two tissue compartmental model

1 Introduction

In vivo imaging can be used to evaluate structure and function non-invasively in a living subject. Multiple imaging techniques are available, including computerised tomography (CT), magnetic resonance (MR) imaging and radionuclide imaging (planar imaging, single photon emission computed tomography (SPECT) and positron emission tomography (PET)). Generally, imaging modalities can be divided in two main groups: those that primarily provide structural information (for example, CT and MR) and those that primarily provide functional and molecular information (for example, SPECT and PET) (4). This thesis will focus on the radionuclide imaging modalities, namely PET and SPECT.

Radionuclide imaging involves the quantitative measurement of the distribution of a radiotracer (typically an organic compound labelled with a radionuclide), to provide information on a specific biological or biochemical process in the living body. Imaging with radiotracers is based on the principle that the radiotracer does not alter or perturb the biological system under investigation. For this to be possible, the injected mass of a radiotracer should be as low as possible so that it occupies only a small percentage of the target. For example, in brain receptor imaging, radiotracers should not occupy more than 1% of the available receptors (5). Radiotracers are therefore essential tools in radionuclide imaging and this thesis is focused on the process of novel radiotracer development for imaging the human brain. This introductory chapter outlines the process of radiotracer development and the characteristics required for an ideal radiotracer for brain imaging. The aims and objectives of the experimental work conducted for the thesis are provided at the end of the chapter.

1.1 Radionuclide imaging

Molecular imaging has been defined as the *in vivo* characterisation and measurement of biological processes at the cellular and molecular level (6). Radionuclide imaging is at the leading edge of molecular imaging as it enables the *in vivo* measurement of a biological process and changes in physiology (7). The use of a radiotracer allows exceptional target specificity at the molecular level that cannot be accomplished with other imaging techniques (8). Another advantage of radionuclide imaging is the ability to perform real time imaging studies, in order to increase understanding of physiological mechanisms underlying pathological processes or the effects of drug administration (9). A disadvantage of radionuclide imaging is the limited spatial resolution and poor anatomic context compared to other imaging techniques, such as CT and MR, which are

less sensitive and convey less specific molecular information, but have higher spatial resolution (8, 10-11).

There are three main radionuclide imaging techniques: planar imaging, SPECT and PET. Tomographic techniques have a higher resolution than planar imaging. Nonetheless, planar imaging and particularly dynamic planar imaging can still provide some important biodistribution and kinetic information, either in clinical practice or research (12-13). Many have argued the superiority of PET over SPECT based on the ability of PET to measure, directly, the attenuation effect of the object being viewed; the greater number of PET radiotracers that have been synthesised and tested around the world over the past years, in comparison to SPECT radiotracers; and the higher resolution and higher accuracy involved in the quantitative assessment of the regional concentration of a radiotracer (5, 12). However, some limitations and challenges of PET have also been identified. The short lived PET radionuclides, such as ^{15}O and ^{11}C , require a cyclotron located in close proximity to the scanning site, presenting a challenge in terms of market distribution. PET is also associated with high scanning costs in comparison to SPECT scanning. It has been estimated that the total fixed costs associated per scanning minute is 3.82 € and 2.21 € for PET and SPECT, respectively (14). Currently there is also limited access to PET scanners in comparison to SPECT scanners. SPECT can be performed using conventional gamma cameras that are present in the majority of nuclear medicine departments. In addition, the cost of a PET clinical scanner is 1,200,000 € compared with 500,000 € for a SPECT clinical scanner (1, 14).

Regardless of the radionuclide imaging technique used, the real challenge is to keep radionuclide imaging competitive and/or complementary with CT and MR. For this to be a reality, nuclear medicine needs to discover new “work horses”, in addition to currently commercially available $^{99\text{m}}\text{Tc}$ -radiotracers and ^{18}F -Fluorodeoxyglucose (^{18}F -FDG), and to provide services at a lower cost in order to continue to have a crucial position in diagnostic and research imaging (13). As the physical limits of PET and SPECT detection are approached, the development of novel radiotracers becomes more important. Increasing the number of selective radiotracers available will increase the number of biological sites and processes that can be imaged *in vivo* (5, 13). Consequently, the development of novel radiotracers is necessary to study and understand multiple pathophysiological processes and also to accelerate and aid drug discovery (5, 7, 9, 13). It is clear, therefore, that discovery and development of novel radiotracers is essential in order to expand the utility of PET and SPECT.

1.2 The process of radiotracer discovery and development

In order to develop novel radiotracers for SPECT or PET, three major steps need to be undertaken prior to product licensing, commercialisation and marketing: radiotracer discovery, preclinical research and clinical trials (Figure 1.1).

The development of novel radiotracers is a lengthy and costly process, where the highest cost is associated with clinical trials. The cost of developing an *in vivo* imaging agent within a company was estimated to be 100-200 million dollars over 8-10 years. However, the small number of radiotracers successfully developed as a result is striking. For example, Schering and Amersham spent around 150 million dollars for the period of 1999-2004 on imaging agents research, and as a result they did not obtain one new radiotracer, new drug or new indication approval in any modality in the USA (up to mid-2007) (15). This high rate of failure is a concern whether developing novel radiotracers in industry or academia. In the following sections, the radiotracer discovery and development steps are outlined, including a discussion of the strategies that have attempted to reduce costs and failure rates.

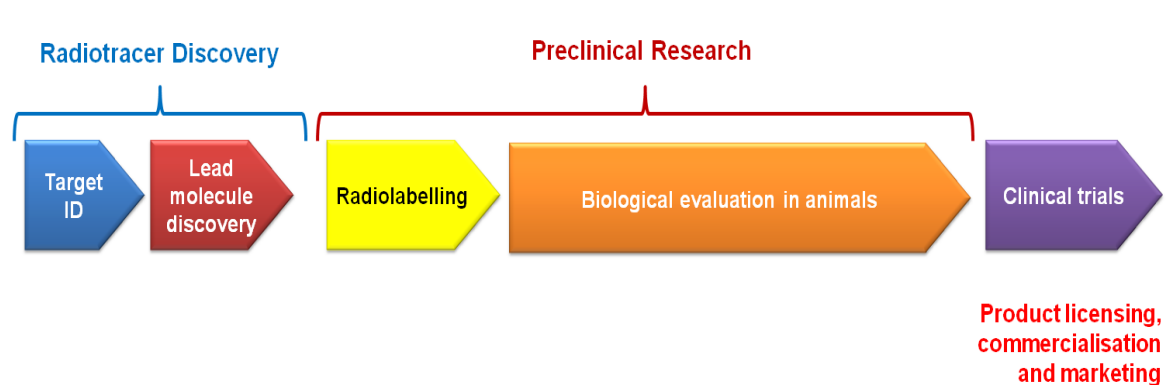


Figure 1.1 Typical radiotracer discovery and development pipeline.

1.2.1 Target identification and lead molecule discovery

The first step in the radiotracer discovery process is target identification. In this phase, evidence that the target plays an important mechanistic role in a disease (i.e. does the target have a functional impact?) is evaluated. This first phase forms the basis for the development of a specific radiotracer and outlines the clinical question that needs to be addressed. Following target identification, it is necessary to develop a library of compounds, or use an existing library of compounds, which can be tested for target

affinity in order to select the lead molecule to be radiolabelled i.e lead candidate selection. Ligand/target interactions can be investigated using various techniques, such as ligand-binding competition assays. Ligand-binding competition assays can be performed using tissue homogenates or cell lines and require a radiolabelled ligand for the target which is usually either tritiated or radioiodinated. By performing binding assays, the specificity and selectivity of candidate radiotracer compounds can be evaluated. The K_i value, which is the dissociation constant, of the candidate molecule is calculated to provide a measure of affinity to the site under investigation (9, 16). The determination of a compound's specificity and selectivity for the target is an essential but simplistic measure that does not predict the other *in vivo* characteristics that are critical for a radiotracer to be successful (2). Thus, in order to improve molecule selection and reduce attrition during radiotracer discovery, other important characteristics of radiotracer candidates need to be investigated. One of the important characteristics for a brain radiotracer is its ability to penetrate the blood brain barrier (BBB). Previously this has been predicted using lipophilicity measurements, but it can also be investigated using other *in vitro* and *in silico* methods for the prediction of *in vivo* behaviour (2, 17-20). Over the years, these other *in vivo* properties have gained increasing importance for lead candidate selection, in order to reduce the risk and costs associated with radiotracer discovery and development. An overview of the *in vitro* methodologies that can be used for the prediction of the *in vivo* behaviour of a molecule will be presented in chapter 2, section 2.1.

1.2.2 Pre-clinical research

Once the lead candidate molecule has been selected, it needs to be radiolabelled and its biological properties evaluated *in vitro* and *in vivo*. At this stage, animal research is conducted in order to evaluate affinity, saturability, reversibility, pharmacokinetics, metabolism and biodistribution of the radiotracer candidate.

Saturability and affinity are typically determined using saturation binding assays. These assays provide a B_{max} value (maximum binding capacity), which is a measure of receptor density, and a K_D value (the dissociation constant), which is the concentration of the radiotracer at which half of the total number of receptors is occupied (9, 21-23). In saturation binding assays, separation of bound and free radiotracer is usually accomplished by filtration, however this method has some disadvantages: (1) it relies upon ligand dissociation being much slower than the filtration step, an assumption that is not always true; (2) the protocol is time consuming; (3) the receptors may be present in membrane fragments that are too small to be retained by conventional filters; and

(4) the assay requires liquid handling and is thus not easy to automate (24-25). Alternative methods have been developed to improve and accelerate the determination of target affinity (compared to saturation binding assays and competition binding assays outlined in section 1.2.1) that are amenable to automation. Examples include the scintillation proximity assay (SPA) and surface plasmon resonance (SPR). SPA is a technique for performing binding assays without separation of bound and unbound radioligand, allowing quantification of binding reactions without washing or filtration procedures. On the other hand, SPR quantifies, in real time, reversible interactions of biological macromolecules through optical techniques (26-28). However, traditional saturation and competition binding assays using filtration are still the mainstay for the determination of target affinity. This is mainly due to the low cost of these traditional binding assays compared to SPA and SPR techniques. Furthermore, SPA and SPR are less flexible and therefore less readily available, since they require specific beads for scintillation or highly specialised optical equipment, respectively.

In addition to *in vitro* assays, *in vivo* studies using rodents or non-human primates are required to evaluate a wide variety of parameters. The aims of the *in vivo* studies are to determine the uptake in the target organ, the signal to noise ratio, the kinetics and the metabolism of the radiotracer (16). Previously these *in vivo* properties were determined using static methods of imaging, such as autoradiography and *ex vivo* dissections at different time points following administration of the radiotracer. More recently, the development of dedicated SPECT and PET cameras for imaging of small animals and non-human primates has allowed longitudinal dynamic studies to be performed *in vivo*. Compared to autoradiography or dissection techniques, *in vivo* imaging reduces the number of animals used (up to 80% to 90% depending on the study) and provides real time imaging of the biodistribution and kinetics of a radiotracer (9, 29). Furthermore, imaging techniques in living animals provide the unprecedented ability to link detailed molecular information with the complexity of whole organism physiological responses over time (29). Nonetheless, multiple considerations need to be assessed when performing *in vivo* imaging of animals. Careful animal preparation is key to obtaining high quality images and producing reliable results. For example, gender can have significant effects on the pharmacokinetics and metabolism of a radiotracer and other physiological parameters. This can be due to the influence of hormones, glucose levels, sex hormones and hepatic enzymes. In addition, fasting and dietary conditions may influence the image obtained, depending on the target of the radiotracer under investigation. An example includes ^{18}F -FDG imaging of glucose metabolism. Circadian cycles are another important consideration when imaging live animals. For example, when evaluating drug efficacy using imaging in rodents it is necessary to take into account the fact that rodents are nocturnal animals and most of their activity takes

place during the dark cycle. The injection volume and any effects of the radiotracer itself on the animal physiology also need to be considered, especially when performing sequential imaging in the same animal. The general recommendation for the maximum volume of an intravenous injection is around 4% to 5% of the animal's blood volume. Therefore the volume injected should be no more than approximately 200 μL for a mouse and 1000 μL for a rat (8, 30). In addition, the administration of large amounts of radiotracer in terms of mass can result in pharmacological mass effects, contradicting the principle of tracer imaging (31-32). Anaesthesia is also a very important consideration when performing radionuclide imaging studies in experimental animals. Multiple studies have shown that the physiological effects of anaesthetic agents may confound the results of imaging studies, depending on the radiotracer and imaging target under examination. Under anaesthesia, changes in respiration and cardiac function can influence radiotracer uptake, distribution and kinetics. Rigorous control of anaesthesia is therefore crucial in *in vivo* imaging experiments to obtain highly reproducible results (8, 30, 33) and careful selection of the anaesthetic agent or, when possible, conscious imaging is essential when designing an *in vivo* imaging experiment. Further to *in vivo* studies that evaluate the target organ uptake, the signal to noise ratio, the kinetics and the metabolism of a radiotracer, toxicology studies in animals to assure radiotracer safety prior to translation into humans can also be performed.

1.2.3 Clinical trials

Once target identification, lead molecule discovery and pre-clinical research steps have identified a radiotracer candidate with suitable characteristics for imaging the target, studies establishing safety and dosimetry properties are performed to enable approval for human use (16). This stage represents the translation between pre-clinical research and clinical use, and involves clinical trials. Clinical trials, particularly at early stages (i.e. Phase I), have a high failure rate. This has been associated with species differences that result in problems translating the radiotracer from animals to humans. Parameters such as metabolism, affinity to efflux pumps, receptor density, receptor distribution in brain and ability to cross the BBB can vary significantly between animals and humans (18). As a consequence, undesirable properties of radiotracers are frequently observed in early human studies (7, 18, 20). Therefore radiotracers that have ideal characteristics in animal studies may fail later in human studies.

Until recently, rodent dosimetry was considered to be sufficient for predicting human dosimetry. However, it has been identified that human dosimetry predictions based on rodent data can be inaccurate for certain organs such as the liver and gallbladder. A low

human radiation dosimetry is essential for a radiotracer to pass regulatory approval, and therefore human dosimetry is one of the final determinants of the success of a radiotracer. Another important requirement of a radiotracer is that administration to humans will not elicit any toxicological effect. Despite the underlying tracer principle, a few radiotracers have failed due to toxicological issues. Examples include the epibatidine derivatives developed as radiotracers for imaging of the nicotinic cholinergic receptors. The epibatidine derivatives showed initial success in both rodent and non-human primates, however in humans this class of compounds, even at tracer levels, had a very small safety margin that prevented their use (20).

Generally, the design of phase I clinical trials includes safety studies in healthy human volunteers, such as dosimetry and toxicology studies. Phase II and III are designed to define the clinical setting where the radiotracer will be valuable. Each clinical indication must be supported by clinical trial data. Since clinical trials are a very expensive process and there is a compelling need for more radiotracers, previous studies have suggested that collaborative approaches may be of value. Partnering may: (1) reduce the risk associated with these later stages of radiotracer development by spreading the costs between different companies and/or universities, and (2) obtain more rapidly the necessary number of subjects (15).

1.3 Novel radiotracers for imaging the human brain

Radiotracer discovery and development is a multi-step process that requires fine-tuning depending on the imaging target (i.e. brain, heart, tumour, etc). Specific adjustments may need to be made at the molecule design step in order to obtain the desired characteristics for the imaging target. In this section the characteristics that have been proposed for an ideal radiotracer for brain imaging are outlined.

The suggested criteria for the passive diffusion of a molecule across the BBB include (19-20, 34):

- A molecular weight lower than 450 g/mol;
- A polar surface area below 60-90 Å²;
- The number of hydrogen bond donors in a molecule lower than five or the sum of nitrogen and oxygen atoms less than ten;

- A Log P (partition coefficient) lower than 4, with an ideal range of 1 to 3.5. Typically, the ideal range for Log P is reported to be between 1 and 3.5, however, a calculated Log P value of ≥ 3 has also been suggested when *in silico* methods are used for lipophilicity determination.
- Minimal affinity for efflux pumps (such as P-glycoprotein or P-gp);
- No affinity for enzymes at the BBB.

Other parameters that are thought to be required in order to obtain an ideal radiotracer for brain imaging include (19-20, 34):

- Absence of functional groups that will strongly ionize at physiological pH;
- No appreciable affinity for specific binding sites on high capacity peripheral sites, such as albumin and other plasma proteins;
- Suitable kinetics quantifiable *in vivo*, preferably reversible or not completely irreversible binding;
- Dissociation or inhibition constants for the target *in vitro/in vivo* in the nanomolar range;
- Selectivity for the target site in comparison with other non-target sites;
- Brain uptake in rodent and non-human primate of $\geq 0.5\%$;
- Low or modifiable dosimetry for critical organs;
- Radiolabelled metabolites inactive at the target organ and not rapidly generated in the imaging time frame.

In addition to the parameters outlined above, the feasibility of radiolabelling the candidate molecule and the radiosynthesis route needs to be considered prior to *in vitro* testing (18, 20). Another important consideration when developing a radiotracer for imaging the brain is the potential differences in the target between species, such as density or protein structure. Determination of these differences at an early stage would help interpretation of results and potentially reduce problems when translating the radiotracer to human studies. The target site density and distribution pattern also needs

to be considered in terms of “imageability”. Imaging targets with a low density (low B_{\max}) and a widespread distribution can be problematic, compared to a target with a high density and localised distribution.

1.4 Thesis aims and objectives

To date the successful development of novel radiotracers for brain imaging has been limited. The long list of the ideal characteristics a brain radiotracer should possess reveals the complexity associated with developing novel radiotracers for imaging the brain. These characteristics are not definitive and they cause significant attrition during the process of radiotracer discovery and development. To date the development of novel radiotracers has essentially been conducted through a process of trial and error (2-3, 20). Consequently, two common errors in radiotracer development may occur: type I error, going too far through the development process with a radiotracer that ultimately fails; and type II error, not going far enough through the development process with a radiotracer that would have ultimately succeeded (20). Both errors are difficult to eliminate, since radiotracer development is a multi-step process, where biological evaluation is performed in different species prior to translation into humans.

The careful characterisation of a radiotracer candidate prior to pre-clinical research has the potential to enable the more informed selection of lead candidate compounds, prior to expensive radiolabelling and subsequent evaluation studies. This may reduce the instance of radiotracers failing to meet the criteria set out in section 1.3 later on in the development process. However to date there has been a lack of methodology developed that enables the simple and fast characterisation of large libraries of compounds. In order to fill this gap in the field of radiotracer development, new approaches are required to aid lead candidate selection. The first part of this thesis aimed to develop a new tool for use in lead candidate selection during the early stages of radiotracer discovery in an attempt to fill this gap. There are a number of radiotracers that have been successfully used in SPECT or PET studies of the human brain. Despite this, the relationships between the physicochemical properties of compounds and the *in vivo* performance of the radiotracer are still not sufficiently understood (3). In this thesis a high performance liquid chromatography (HPLC) tool was investigated to gain information on the physicochemical properties of existing radiotracers and the relationship between these properties and *in vivo* performance was determined. The aim was to outline whether HPLC analysis could be used to predict the *in vivo* characteristics of a radiotracer.

As discussed above, section 1.1, the development of novel radiotracers for *in vivo* brain imaging using SPECT or PET is of vital importance. The increased demand for novel radiotracers for imaging the human brain is a consequence of the increased number of imaging targets that are continuously being identified. Two brain targets that are lacking suitable SPECT radiotracers are the translocator protein (TSPO) and noradrenaline transporter (NAT). Attempts to develop radiotracers for these targets have been made in the past, but with limited success. This thesis aimed to develop novel radiotracers for imaging the TSPO and NAT in human brain using SPECT.

In brain, the TSPO is expressed by reactive glial cells and can therefore be used as a marker of neuroinflammation. Neuroinflammation is implicated in a number of brain disorders such as cerebral ischaemia, epilepsy, nerve injury, neurodegenerative diseases and immune system diseases. Therefore, the TSPO is an attractive target for molecular imaging of neuroinflammation in human brain diseases. In addition, a TSPO selective radiotracer would be valuable in imaging studies evaluating drugs targeting the TSPO (35). A novel library of compounds for imaging of the TSPO was developed at the School of Chemistry at the University of Glasgow. It was necessary to identify the lead candidate from this library of compounds and therefore the novel library of TSPO ligands was screened using the HPLC tool developed in the first part of this thesis and also using competition binding assays. The aim was to select the compound most likely to succeed as a radiotracer for imaging of the TSPO.

Dysregulation of noradrenergic function has been implicated in a variety of psychiatric and neurodegenerative disorders, including depression, post-traumatic stress, anxiety, attention-deficit/hyperactivity disorder (ADHD) and Alzheimer's disease (36-42). A NAT selective radiotracer would enable imaging studies investigating disease progression and treatment response in different psychiatric and neurodegenerative disorders. In addition a NAT selective radiotracer would also be extremely valuable in imaging studies evaluating drugs targeting NAT, such as drug occupancy studies, thereby aiding the drug discovery process. Therefore a radiotracer specific for *in vivo* assessment of changes in NAT density, either in disease states or as a consequence of drug treatment, is desirable. A library of compounds for imaging of NAT in brain was synthesised and tested at the University of Glasgow. Biological testing of these compounds indicated that one compound in particular, NKJ64, was the lead candidate (43-45). Following identification of the lead candidate, it was necessary to radiolabel NKJ64 and to perform the biological evaluation of the radiotracer in animals to determine the utility of NKJ64 as a radiotracer for imaging the NAT in brain. This thesis aimed to radiolabel NKJ64 and to test it in rodents and non-human primates. In addition another NAT SPECT

radiotracer, ^{123}I -INER, was assessed in non-human primates as a radiotracer for imaging the NAT.

1.5 Thesis outline

This thesis is organised according to the typical radiotracer discovery and development pipeline, where each main step prior to human studies is addressed and discussed. This document is divided in five results chapters and a brief outline of each chapter is below:

- Chapter 2. The development of a novel tool for selection of lead candidates to be taken forward as brain radiotracers and its application to a library of compounds developed for imaging the TSPO.
- Chapter 3. The radiosynthesis of high specific activity $^{123/125}\text{I}$ -NKJ64, a novel radiotracer for imaging the NAT in brain.
- Chapter 4. Biological evaluation of $^{123/125}\text{I}$ -NKJ64 in rodents including *in vitro*, *in vivo* and *ex vivo* studies for evaluation of affinity, biodistribution, kinetics and target-non target ratios.
- Chapter 5. *In vivo* kinetic modelling studies using ^{123}I -NKJ64 in non-human primate brain to determine brain binding kinetics, brain distribution and plasma metabolism.
- Chapter 6. *In vivo* kinetic modelling studies and occupancy measures of the NAT in non-human primate brain using SPECT with ^{123}I -INER.

The chronological order of the experiments performed as part of this thesis was as follows: 1) radiosynthesis of NKJ64; 2) biological evaluation of $^{123/125}\text{I}$ -NKJ64 in rodents; 3) development of novel HPLC tool for selection of lead candidates during radiotracer discovery process; 4) biological evaluation of ^{123}I -NKJ64 in non-human primates; and 5) kinetic modelling and NAT occupancy studies in non-human primate brain using SPECT with ^{123}I -INER. All experiments were performed at University of Glasgow except for the non-human primate work that was performed at Molecular NeuroImaging, LLC and Yale University, CT-USA.

2 Development of a novel tool for brain radiotracer discovery

2.1 Introduction

Radiotracer development is a multi-step process and a variety of obstacles need to be overcome in order to obtain a successful radiotracer (see Chapter 1 for a review). One of the most important challenges in brain radiotracer discovery is delivery of the radiotracer to the brain parenchyma. To reach the brain, molecules that are to be developed as brain radiotracers must firstly be able to cross the BBB. A brief introduction to BBB characteristics and functions will be outlined in this chapter. Other *in vivo* processes, including metabolism and non-specific binding, also play an important role in determining the behaviour of a radiotracer *in vivo* and will also be briefly outlined in this chapter.

The important role that the BBB plays in allowing radiotracer entry into the brain has gained increasing awareness over the years and different methods for predicting BBB penetration and the *in vivo* behaviour of molecules have been developed. In this introductory section, the different methods available for the prediction of BBB penetration and *in vivo* behaviour of molecules will be discussed. A particular emphasis will be on methodology investigated as part of the current chapter, including: octadecyl silica (C₁₈) chromatography, immobilized artificial membrane (IAM) chromatography and plasma protein binding (PPB) chromatography. An overview of the principles underlying these techniques will be included in this introductory section along with the main concepts of lipophilicity and phospholipophilicity in order to facilitate the interpretation of results presented later in the chapter.

2.1.1 Crossing the BBB and reaching the brain

Despite its high blood flow, the brain is one of the least accessible organs for delivery of molecules. This is mainly due to the presence of two physiological barriers separating the brain from the blood supply and controlling the entry and exit of endogenous and exogenous compounds. One barrier is the BBB and the other is the blood cerebrospinal fluid barrier (BCSFB). Since the surface area of the human BBB is estimated to be 5000 greater than the BCSFB, the BBB is considered the main obstacle to radiotracer brain uptake (Figure 2.1a) (46-49).

Transport across the BBB involves movement across two membranes in series: the luminal and the abluminal membranes of the capillary endothelium, which are separated by 200 nm of endothelial cytoplasm. Due to the existence of tight junctions (Figure 2.1b), through which adjacent endothelial cells adhere together and hence prevent paracellular transport, circulating molecules gain access to the brain interstitium *via* transcellular routes (50-51). Further to the transcellular route, several specific transport (carrier) proteins in endothelial membranes can shuttle necessary nutrients into the brain by means of uptake carriers. Such carriers can also remove molecules from the brain by way of efflux carriers, such as P-gp. Molecules that are too large for carrier-mediated transport, such as proteins and peptides, may cross the endothelium *via* a vesicular route, either by specific receptor-mediated transcytosis or following non-specific adsorption of cationic molecules to the membrane surfaces. The BBB also expresses several surface and intracellular enzymes (Figure 2.1c), such as, peptidases, monoamine oxidase and cytochrome P450 enzymes (51). The surface area available for passive diffusion in the individual BBB endothelial cell membrane is composed of only 15% lipid while typical cells contain 50% lipids. The relatively low lipid content in BBB endothelial cells can explain why passive diffusion is lower in these cells compared to others (47, 52). The BBB is a particularly difficult barrier for radiotracers to penetrate for two main reasons: first, radiotracer entry is minimised because of the BBB characteristics previously discussed; and second, once a compound enters the intracellular compartment of the BBB, it may be pumped out of the cell by efflux transporters. The complex nature of the BBB can explain why occasionally particular compounds cannot penetrate the barrier even though existing screens suggest they will (52).

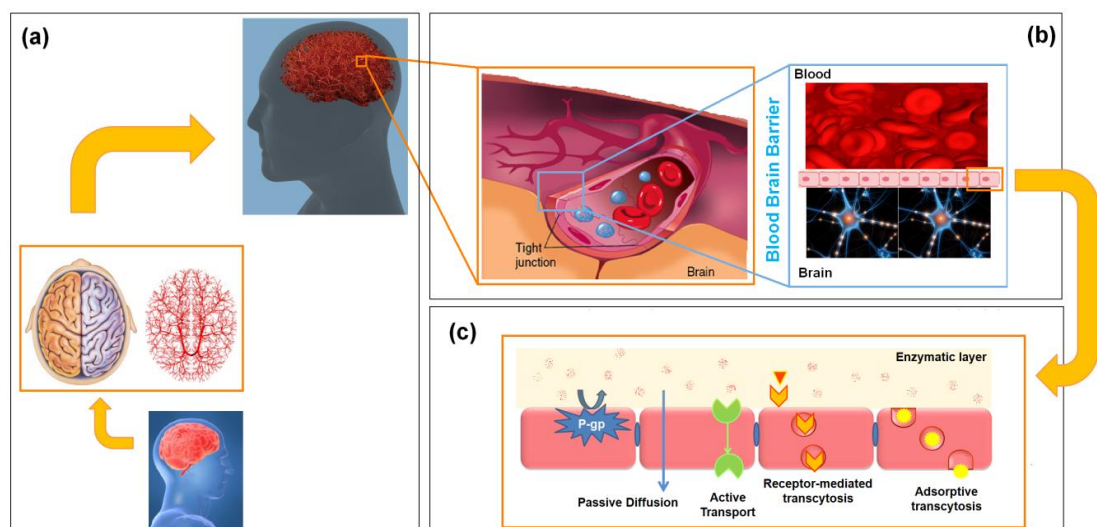


Figure 2.1 The brain vascular system and the blood brain barrier (BBB).

(a) Representation of the brain vascular system, (b) the BBB (note the tight junctions) and (c) different mechanisms of transport, efflux pumps and metabolically active layer of the BBB.

Another important *in vivo* phenomenon that contributes to the challenge of getting a radiotracer into the brain is radiotracer metabolism. The nature and degree of metabolism can vary considerably across animal species, with less extensive metabolism expected in higher species such as primates. Metabolism of a radiotracer should ideally occur outside the brain, since less lipophilic radiometabolites in the periphery will have poor brain entry and minimal or no interaction with the target receptor. If radiotracer metabolism occurs outside the brain to produce non-BBB-penetrating radiometabolites, a faster elimination of the parent radiotracer from the plasma can be achieved, which can be beneficial for radiotracer washout from non-target tissues, as well as, from the brain. This means that not all metabolism is disadvantageous and may not limit a radiotracer's performance *in vivo*. However, radioactive metabolites that are able to cross the BBB or those that are generated in the brain tissue are considered troublesome, as they will interfere with receptor brain imaging *in vivo* (18). Many successful radiotracers have between 50% to 90% metabolism towards the end of the imaging time. Problematic radiotracers are those that are fully metabolised within the first 10 minutes after injection, making quantification difficult. Although radiometabolites are typically unwanted, previous studies have shown that every so often, a radiolabelled metabolite may be more suitable for imaging of a certain target than the parent radiotracer itself. This could be because the radiosynthetic route for labelling the parent compound is inaccessible or the parent compound metabolises rapidly *in vivo* during the imaging time. Hence, pursuit of a radiolabeled metabolite that might be more stable or where the radiosynthesis may be more facile has been a successful strategy, provided that a substantial loss in affinity and/or selectivity did not occur (20). Furthermore, the careful design of chemical structure could minimise the probability of radiotracer metabolism. For example, the choice of position for radiolabelling may be key to avoiding troublesome radiometabolites (18).

High non-specific binding is another common challenge to overcome when developing novel radiotracers for imaging the human brain. High non-specific binding to peripheral organs can significantly reduce brain uptake. For example, high non-specific binding to plasma proteins can increase deposition of radiotracers in peripheral organs including liver, lungs and spleen, reducing the amount of radiotracer available for brain penetration (19). In addition, high non-specific binding can also be caused by high levels of binding to non-target sites in the brain. This can be due to low selectivity of a radiotracer for the target site and results in a reduced target:non-target ratio. Defining an ideal *in vivo* specific to non-specific binding ratio for a PET and SPECT radiotracer is complex and dependent upon multiple factors, including target size, resolution of the detection instrument and radioactive concentration at the target site. Nonetheless, a minimum specific binding ratio of between 2 and 3 has been suggested to be desirable

in order to reliably analyse *in vivo* images (53-54). This means that the specific binding of a radiotracer in brain should be two to three fold higher than non-specific binding in order to obtain high quality images of the target using PET or SPECT.

2.1.2 Methods for predicting BBB penetration

There is a wide variety of methods available for prediction or measurement of BBB penetration. Examples include *in vivo* and *in situ* methods for measurement of brain penetration, rate of brain penetration, free molecule concentration in brain and P-gp efflux. These measurements can be collected using imaging techniques, such as SPECT and PET; *ex vivo* animal experiments, namely, *in situ* brain perfusion and brain/plasma ratio; ventricular sampling of cerebral-spinal fluid; tissue microdialysis; and knockout or gene deficient animals. *In vitro* techniques have also been used for assessment of brain penetration and include evaluation using specialised cell cultures (such as Madin-Darby canine kidney (MDCK) cell lines and Caco-2 cells), IAM chromatography, parallel artificial membrane permeability assay (PAMPA) (51, 55) and the traditional partition systems, like octanol-water partition and octanol-buffer distribution. Finally, *in silico* methods have been used to generate predictive rules or equations for BBB penetration, as a “first screen” in the radiotracer discovery process (48, 51).

Screens used to predict biologically relevant properties can be listed in order of experimental convenience as shown in Figure 2.2. Despite being the “gold standard”, *in vivo* methods are frequently expensive, labour intensive and are not suitable for high throughput screening (48, 51, 55). Also cell-based *in vitro* techniques are resource intensive, can potentially lose the *in vivo* BBB phenotype over the timeframe of the cell culture and are also unsuitable for high throughput screening. Physicochemical methods (such as, octanol-water partition, liposome partitioning, hydrophobicity measurements and membrane binding constants) are simpler to perform and can be used to predict passive transport across cell membranes in the early stages of molecule discovery. While molecule penetration also includes active and facilitated transport, passive transport is the most common screen because it is experimentally simpler and it is either completely or partially responsible for molecule uptake into cells (52). *In silico* methods are the simplest and fastest of all methods; however, frequently, the trade-off is that they are less accurate predictors (48, 51).

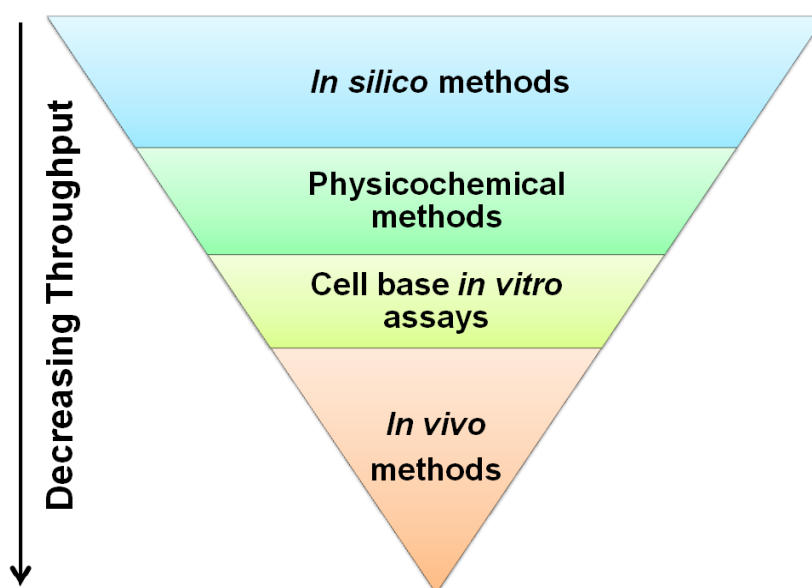


Figure 2.2 Main screening methods used for prediction of biological relevant molecule properties.

Methods are ordered from the most experimentally convenient and highest throughput (*in silico* methods) to the least convenient and more labour intensive (*in vivo* methods).

2.1.3 Lipophilicity and phospholipophilicity

Cell membrane transport properties are frequently considered to be decisive during lead molecule discovery (52). Molecule lipophilicity measurements have been associated with molecule transport across the cell membrane and, consequently, across the BBB cells. However, lipophilicity can only model polar and non-polar interactions. Non-polar interactions are associated with hydrophobicity (expressed by molecular volume, molar refractivity and polarisability), while polar interactions include ion-dipole, dipole-dipole and hydrogen bond interactions (expressed in electronic constants, dipole moments or hydrogen bond parameters). This dual nature of lipophilicity can be expressed according to equation 2.1. However, when the aim is to study the lipophilicity in biological membranes another additional electrostatic interaction must be considered. Since phospholipids present a dipole field that is determined by the polar headgroups, the surface water molecules and the lipid carbonyls, a process denoted phospholipophilicity needs to be addressed. Thus, the traditional lipophilicity equation must be adjusted to phospholipophilicity, according to equation 2.2 (56).

$$\text{Lipophilicity} = \text{hydrophobicity} - \text{polarity} \quad (\text{Eq. 2.1})$$

$$\text{Phospholipophilicity} = \text{hydrophobicity} - \text{polarity} + \text{ionic bonds} \quad (\text{Eq. 2.2})$$

2.1.4 Partition systems

Within the physicochemical methods that are available for prediction of radiotracer BBB penetration, partitioning systems are the most well known and established *in vitro* methodology (2). There are three main *in vitro* models of organic-solvent-aqueous partitioning systems: octanol-water partitioning systems, chromatographic partitioning systems using HPLC and liposome partitioning systems (57).

At first, the octanol-water partition system was considered an advantageous system, due to its hydrophobic chain with polar head, as well as, to its moderate water saturation, which allowed relatively easy and reliable experimental determination. However, more recently, it was found that the water present in the octanol layer, seems to play a more complex role in the interaction with solute structures than anticipated for an isotropic system (56, 58). Nonetheless, since brain uptake and brain/blood concentration ratio of radiotracers have been reported to show a parabolic dependence on octanol-water partitioning (17, 19), it has been widely accepted that the octanol-water partition coefficient is the main design parameter for brain entry (with an ideal Log P value of 1–3.5 for optimised BBB penetration).

More recently, HPLC methodology was proposed to model the octanol-water partitioning of a compound. Two lipophilicity indexes can be obtained from reverse-phase HPLC using C_{18} columns: the volume percent of organic phase concentration in the mobile phase when the retention time is twice the dead time (φ_0) and the chromatographic hydrophobicity index (CHI). The main difference between these two measurements is that φ_0 is derived from a series of isocratic measurements, while CHI is derived from the retention time in a calibrated generic HPLC gradient. Due to its greater versatility and short measurement time, the gradient method used for measurement of CHI was introduced as a high-throughput method for lipophilicity determination (59). Briefly, the CHI method is based on the relationship between the retention time and the percentage of acetonitrile required to achieve equal distribution of the compound between the mobile and stationary phase. The calibration curve, generated by using a set of reference compounds and by plotting their CHI values versus retention time, is then used to determine the CHI values of unknown compounds from their retention times (60-62). The CHI value can then be converted to the logarithmic scale, as Log P or Log D, which are parameters typically used by chemists. In comparison to the traditional flask method, determination of the CHI by means of HPLC is faster, easier to automate, suitable for a wider range of compounds and independent of impurities present in the test sample (60).

Octanol-water and C_{18} chromatographic partitioning systems can only model the hydrophobic contribution of molecule-membrane interactions. However, since the partition of a molecule into a cell's membrane results from all possible interactions, including electrostatic interactions, some limitations have been identified when these methods are used for prediction of BBB penetration (57). Liposome suspensions prepared from phospholipids, exhibit structural similarities to the phospholipid bilayer and can be used to investigate all molecule-membrane interactions (52). Overall, liposome suspensions are a good model of the lipid environment in a cell and frequently predict the molecule passive transport through cell membranes. Nevertheless, the use of liposomes is labour intensive and it is difficult to establish routine methods for molecule screening, especially on a large scale. Additionally, liposome methodology is time consuming and requires correction for the amount of molecule that has partitioned into the aqueous space of the liposomes (52, 57). Thus, an alternative method using artificial membranes as column packing material and HPLC was developed, i.e. IAM chromatography.

2.1.5 IAM chromatography

The IAM surface imitates the lipid surface in fluid artificial liposome membranes and biological cell membranes (Figure 2.3). IAMs are prepared by covalently immobilising phospholipid analogs on chromatographic materials. Currently more than twenty different IAM surfaces are available; however, only three IAM surfaces have been extensively used to evaluate molecule-membrane interactions: $^{\text{ester}}\text{IAM.PC}^{C10/C3}$, $^{\text{ether}}\text{IAM.PC}^{C10/C3}$ and $^{\delta G}\text{IAM.PC}^{C10/C3}$ (IAM.PC.DD) (Figure 2.4) (52, 57). All three IAM surfaces are prepared from a phosphocholine (PC) ligand, which explains the acronym IAM.PC. In addition to PC, it may be possible to incorporate other phospholipids (minor components in natural membranes), such as phosphatidylethanolamine (PE), phosphatidylglycerol (PG), phosphatidic acid (PA) and phosphatidylserine (PS), in order to mimic membrane physiology more closely. For example, it could be useful to incorporate PS phospholipids in the HPLC column, because they are present in natural BBB cells in concentrations of approximately 15%. These mixed ligand IAM surfaces can minimise the differences between natural membrane and the IAM surface. The IAM surfaces containing zwitterionic PC headgroups, i.e. IAM.PC.DD (or $^{\delta G}\text{IAM.PC}^{C10/C3}$, Figure 2.4c), are considered to be the best model of molecular interactions found in BBB cell membranes during molecule partitioning (52, 57).

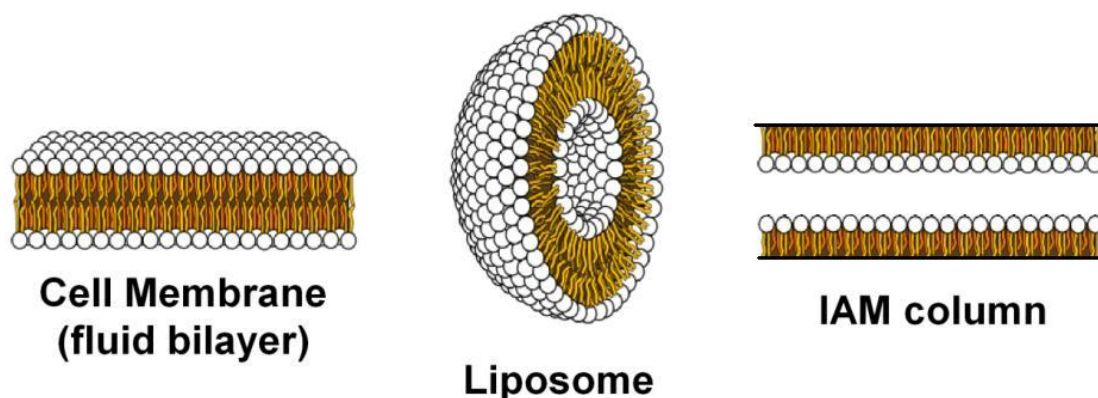


Figure 2.3 Schematic representation of cell membrane, liposome and IAM structures.

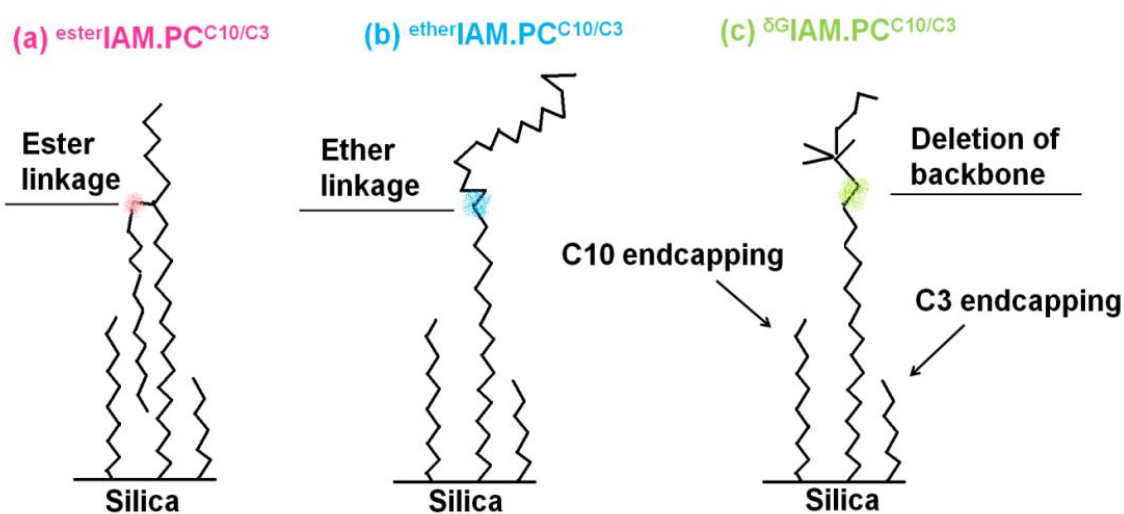


Figure 2.4 Schematic representations of the three major IAM.PC surfaces used for prediction of molecule properties.

The left superscripts describe structural differences of the PC ligands. The superscript “ester” denotes an ester linkage between two acyl chains and glycerol backbone of the PC ligand; the superscript “ether” denotes an ether linkage between the alkyl groups tethered to the PC ligand; finally, the superscript “ δG ” denotes the deletion of the glycerol backbone from the PC ligand (the PC polar headgroup is linked directly to an alkyl group through a phosphoester bond). The right superscript “C10” indicates endcapping residual amino groups using decanoyl groups and “C3” means endcapping with propionic acyl group.

For each compound-membrane lipid mixture it is possible to derive an equilibrium constant, K_m , which is characteristic for a certain molecule interacting with a fluid membrane (Figure 2.5a). Since IAM chromatography can model both hydrophobic and electrostatic interactions between molecules and membranes, this technique can be used to estimate K_m (Figure 2.5b)(52).

In terms of molecule transport, the membrane partition coefficient, K_m , does not directly predict membrane transport. This is because in intact cells, molecules must enter and exit the membrane to permeate into the cytosol and for molecules travelling

across cells, such as endothelial cells, a second membrane entry and exit event occurs. Thus, in order to consider this dynamic mechanism, besides the K_m value, another measure needs to be considered: molecule permeability (P_m) (Figure 2.5a). P_m is linearly related to K_m according to equation 2.3 (52, 57, 63):

$$P_m = \frac{D_m \times K_m}{L} \quad (\text{Eq. 2.3})$$

where D_m is the membrane diffusion coefficient of the solute and L is the membrane thickness.

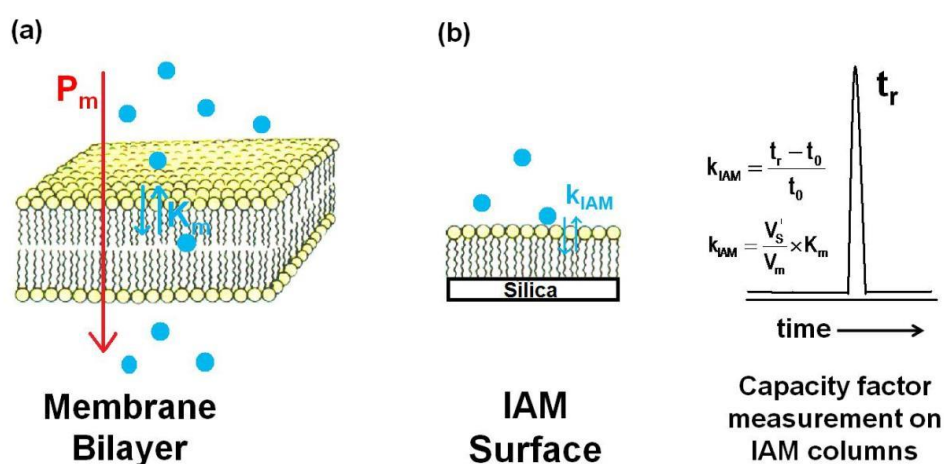


Figure 2.5 Molecule interaction and transport in fluid membranes and IAM surfaces.

(a) representation of membrane partition coefficient (K_m) and permeability (P_m) in fluid membranes and (b) compound-IAM surface equilibrium constant (k_{IAM}) and its correlation with measure parameter (retention time – t_r , unretained compound retention time – t_0 , total volume of solvent within the HPLC column – V_m and volume of the IAM interphase created by the immobilized phospholipids – V_s'). Further detail on these calculations will be presented in the section 2.2.3).

The affinity of solutes to IAM surfaces can be due to the solute partitioning into IAM hydrocarbon region, solute adsorption on the surface of IAM or both. The most important lipid structure features needed for IAMs to model biological partitioning are phospholipid head groups, hydrocarbon chains and ordered membrane layers. All characteristics are present in IAMs surfaces and may explain why IAM chromatography is considered to be a superior method for prediction of BBB penetration compared to octanol-water and C_{18} partitioning systems (52). Compared to liposomes, IAM chromatography is experimentally much simpler, faster, easier to automate and reproducible (47, 52, 63). Thus, IAM chromatography can be a valuable tool for prediction of membrane permeability (47). However, this is not always the most appropriate method to model the biological membrane partition for a compound. For example, it has been shown that the BBB can be modelled well with IAM columns, but skin permeation seems to be better evaluated by C_{18} columns (64).

2.1.6 Plasma protein binding

Various critical pharmacokinetic parameters, such as the rate of hepatic metabolism, renal excretion and biomembrane partition as well as the steady-state distribution volume, are a function of plasma protein binding (PPB). Thus, it is crucial to determine the percentage of protein binding (%PPB) during the radiotracer development process (65).

Three main methodologies can be used to study molecule-plasma protein binding: equilibrium dialysis, ultrafiltration and HPLC. Equilibrium dialysis separates molecules across a semi-permeable membrane, according to molecular size, by using the driving force of concentration differences between two solutions on either side of a membrane. Ultrafiltration is a method that allows rapid, mechanical separation of free molecules from protein-bound ones using a membrane. These methods have some limitations: equilibrium dialysis requires a long analysis time and both methods require additional analytical steps. Thus, an alternative is to use HPLC and protein coated columns (65-67). Typical examples of coating material include: human and rat serum albumin (HSA and RSA, respectively) and α -acid glycoprotein (AGP). HSA is the most extensively studied plasma protein, not only because it is the most common in plasma, but also due to its main functions in the human body that include binding and transport of various compounds, such as hormones, fatty acids and a wide variety of small molecules (65). In comparison to ultrafiltration and equilibrium dialysis, HPLC is a much simpler and faster method in terms of sample preparation, protocol and analysis (65-67). In Table 2.1 HPLC-HSA and ultrafiltration methods are compared.

Ultrafiltration	HPLC – HSA
Can work successfully with high PPB values (around 92-96%).	High organic concentrations to elute strongly bound compounds may damage the column.
Results comparable to <i>in vivo</i> process such as ultrafiltration of molecule in kidney.	----
Time consuming and requires additional analytical steps.	Suitable for routine PPB estimation in molecule discovery programs.
Estimates protein binding to all plasma proteins.	Estimates binding only to albumin.
Measures all specific and non-specific binding to all plasma components.	Measures only specific and non-specific binding to one particular protein.

Table 2.1 Main advantages and disadvantages of ultrafiltration versus HPLC-HSA.

2.1.7 HPLC: advantages and limitations

HPLC provides an automated platform for determination of multiple measurements (lipophilicity, phospholipophilicity and other biometric measures), based on the retention time of a molecule on different stationary phases. The acid-base character of a compound can also be determined by performing measurements at different pH. Some of the main advantages of HPLC over other *in vitro* techniques include: (1) high throughput characterisation of compound libraries at early stages of the molecule discovery; (2) facile automation, producing reliable and accurate measurements; and (3) the measurements are independent of compound concentration and impurities, therefore different properties of closely related analogues can be more easily distinguished (61, 68). Despite these advantages, there are some disadvantages of using HPLC retention times: (1) it may be difficult to build up a large database, due to different inter-laboratory methodologies; and (2) column aging requires the use of reference compounds for system corrections and calibrations (68). In addition, IAM and C₁₈ chromatography only model passive diffusion across the BBB. It is well known that other transport mechanisms are involved in BBB penetration, such as active transport and endocytosis. Despite these disadvantages, IAM and C₁₈ chromatography may have a potential role in the early stages of the radiotracer discovery process, when these techniques may be used to provide rapid and efficient methodology for the prediction of whether a compound has favourable BBB transport properties or not (52, 63).

2.1.8 Hypothesis and aims

The work presented in this chapter is divided in two parts. The first part investigated a novel *in vitro* HPLC tool for aiding brain radiotracer discovery. The second part used the *in vitro* HPLC tool for the selection of a lead radiotracer candidate from a library of new compounds designed for SPECT imaging of neuroinflammation.

1. Investigation of HPLC analyses as a novel tool for brain radiotracer discovery

Radiotracers that have been used successfully in human imaging studies were investigated and *in vitro* HPLC measures of Log P, K_m, P_m and %PPB were compared to selected *in vivo* characteristics of the radiotracers reported from previous imaging studies in humans. It was hypothesised that: (1) HPLC measures of Log P, P_m and %PPB have the potential to provide information on the ability of the compound to enter the brain and therefore, on the amount of radiotracer uptake *in vivo* in the human brain; and that (2) a HPLC measure of compound-membrane interactions defined by K_m may

have the potential to provide information on the non-specific binding of a radiotracer *in vivo* in the human brain. The aim was to determine whether *in vitro* HPLC techniques can be used early in the radiotracer development process to aid in the selection of the most promising molecule for further validation. Since there is a considerable lack of standardisation in the method used for Log P determination (2, 19-20, 34), a further aim was to establish how the methodology used influences the Log P value determined. Log P values obtained from the flask method, the HPLC method and computational algorithms were compared.

2. HPLC analyses as a tool for the selection of a lead radiotracer candidate for SPECT imaging of TSPO in brain

The HPLC methodology investigated as a tool for molecule selection early in the radiotracer discovery process was applied to a new library of compounds synthesised at the School of Chemistry at the University of Glasgow. The compound library consisted of iodinated PK11195 analogues that were synthesised with the aim of developing a novel SPECT radiotracer for imaging of TSPO. It was hypothesised that the *in vitro* HPLC techniques would provide selection criteria that could be applied to the newly synthesised library of compounds. The aim was to screen the novel library of compounds using *in vitro* HPLC analysis in order to select a lead radiotracer candidate for SPECT imaging of the TSPO in the brain.

2.2 Material and Methods

2.2.1 HPLC system and general preparation

A Dionex Ultimate 3000 series HPLC (Dionex, UK) was used and data acquisition and processing were carried out using Chromeleon 6.8 Chromatography Software (Dionex, UK). All compounds were dissolved in mobile phase (50% aqueous and 50% organic), with a final concentration of 0.5 mg/mL. A 5 μ L HPLC sample injection volume was used for all methodologies. The column temperature was 25 °C and ultraviolet (UV) detection was performed using a diode array detector (190 nm-800 nm). The Abraham H-bond acidity parameter (A) used to calculate Log P was determined with ADME Suite 5.0 software (Advanced Chemistry Development Inc., Canada). All chemicals, unless otherwise stated, were obtained from Sigma Aldrich, UK. Organic HPLC solvents were obtained from Rathburn Chemicals, UK and ethanol from Fisher Scientific, UK. Sodium hydroxide (NaOH) was purchase from VWR, UK.

2.2.2 C₁₈ chromatography

All HPLC measurements for determination of Log P were performed using a Phenomenex Luna 5 micron C₁₈ 100A (50 × 3mm) column. The C₁₈ method used was based on previously developed methodology (Figure 2.6) (60, 62). Each compound was tested using an acetonitrile and 0.01 mM phosphate buffered saline (PBS) mobile phase at pH=7.4 and also adjusted pH for acidic/basic conditions (pH=4.0 and pH=10.0 respectively) by adding hydrochloric acid (HCl) or 0.05 M sodium hydroxide (NaOH) solutions, respectively. CHI values were determined by measuring the compound retention time (t_r) using the following conditions: 0-10.5 minutes, 0-100% acetonitrile; 10.5-11.5 minutes, 100% acetonitrile; 11.5-12.0 minutes, 100-0% acetonitrile; 12.0-15.0 minutes, 0% acetonitrile. The mobile phase flow rate was 1.0 mL/min.

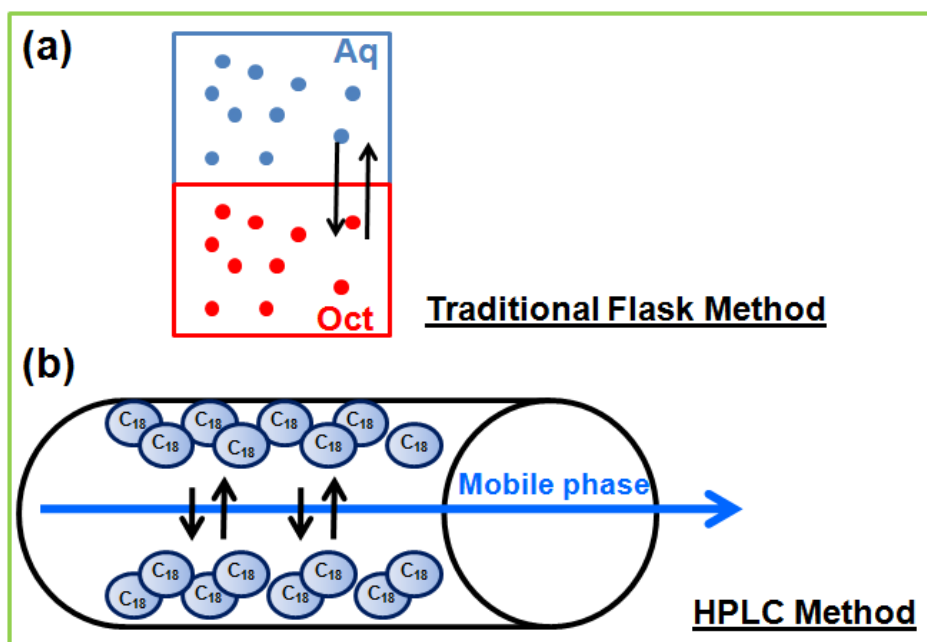


Figure 2.6 Schematic representation of C₁₈ chromatographic principle for determination of Log P.

(a) Determination of Log P by traditional flask methods is based on the partitioning of the molecule between the lipid (octanol - Oct) and aqueous (aqueous - Aq) phases. (b) Log P measured by HPLC is based on t_r of compound, which is determined by the compound interaction between C₁₈ chains and the mobile phase.

The system was calibrated by injecting the following compounds and plotting their CHI values against the obtained t_r: theophylline (CHI = 15.76), phenyltetrazole (CHI = 20.18), benzimidazole (CHI = 30.71), colchicine (CHI = 41.37), acetophenone (CHI = 64.90), indole (CHI = 69.15), propiophenone (CHI = 78.41), butyrophenone (CHI = 88.49) and valerophenone (CHI = 97.67) (62). Log P of the compounds tested was calculated according to equation 2.4 and 2.5, previously validated (60), and by using Excel 2003 software (Microsoft Office, Microsoft Corporation, USA).

$$\text{CHI Log D} = 0.054 \text{ CHI} - 1.467 \quad (\text{Eq.2.4})$$

where CHI Log D represents the CHI values projected to the logarithmic scale.

$$\text{Log P} = 0.054 \text{ CHIN} + 1.32 \text{ A} - 1.88 \quad (\text{Eq.2.5})$$

where CHIN = CHI values of unionised forms of the molecules and A = Abraham H-bond acidity parameter.

2.2.3 IAM chromatography for P_m and K_m determination

IAM chromatography was carried out using a Registech IAM.PC.DD2 (15 cm × 4.6 mm) column and was used to determine P_m and K_m , according to previously developed methodology (Figure 2.7) (52, 56-58, 63). Briefly, 0.01 mM PBS with pH=7.4 and acetonitrile were used as the mobile phase. For determination of both P_m and K_m , the t_r of compounds were obtained using an isocratic method and a mobile phase of 100% PBS over 30 minutes. For compounds that did not elute over 30 minutes using 100% PBS, isocratic mobile phases containing acetonitrile (between 40% and 70%) were used, where the t_r was plotted against the concentration of acetonitrile and regression analysis was used to estimate the t_r using 100% PBS. The flow rate was 1.0 mL/min and citric acid was used as an unretained compound for system corrections. K_m and P_m were calculated using equations 2.6 to 2.12 and Excel 2003 software (Microsoft Office, Microsoft Corporation, USA) (52, 69).

$$k_{\text{IAM}} = \frac{(t_r - t_0)}{t_0} \quad (\text{Eq. 2.6})$$

where k_{IAM} = solute capacity factor on the IAM column, t_r = retention time of the compound, t_0 = t_r of unretained compound.

$$k_{\text{IAM}} = \left(\frac{V_s'}{V_m} \right) \times K_m \quad (\text{Eq. 2.7})$$

where V_s' =volume of the IAM interphase created by the immobilized phospholipids, V_m =total volume of solvent within the IAM HPLC column and K_m =membrane partition coefficient.

$$V_m = f_r \times t_0 \quad (\text{Eq. 2.8})$$

where f_r = flow rate.

$$V'_s = \frac{W_{\text{PhC}}}{\delta_{\text{PhC}}} + \frac{W_{\text{C}_{10}}}{\delta_{\text{C}_{10}}} + \frac{W_{\text{C}_3}}{\delta_{\text{C}_3}} \quad (\text{Eq. 2.9})$$

where specific weight of PhC (δ_{PhC}) = 1.01779 g/mL and C_{10}/C_3 ($\delta_{\text{C}_{10}/\text{C}_3}$) = 0.86g/mL; W_{PhC} = 133 mg, $W_{\text{C}_{10}}$ = 12.73 mg and W_{C_3} = 2.28 mg.

The equation for the calculation of P_m (Eq. 2.3, section 2.1.5) can be simplified based on the assumption that membrane thickness (L) for a given cell is constant and does not contribute to the variability of P_m values for different compounds. In addition, it has been shown that the membrane diffusion coefficient (D_m) depends on molecular size (V) according to equation 2.10.

$$D_m \propto \frac{1}{V} \quad (\text{Eq. 2.10})$$

Assuming that molecular weight (MW) is proportional to molecular size, D_m will be:

$$D_m \propto \frac{1}{MW} \quad (\text{Eq. 2.11})$$

Consequently, equation 2.3 (P_m equation, section 2.1.5) is simplified to:

$$P_m = \frac{K_m}{MW} \quad (\text{Eq. 2.12})$$

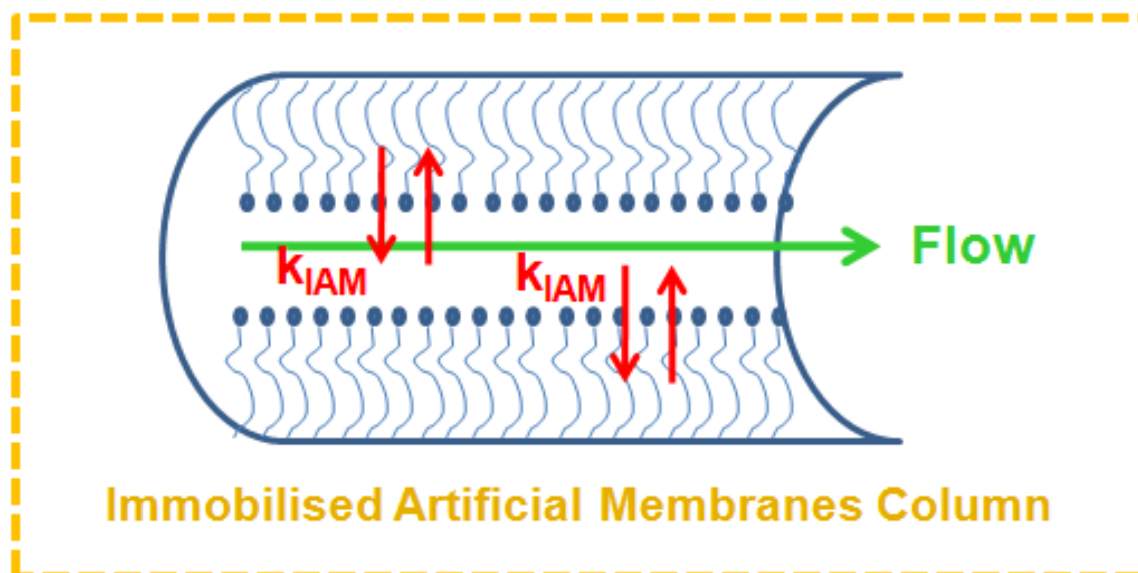


Figure 2.7 Schematic representation of IAM chromatography used for the determination of P_m and K_m .

IAM chromatography can model the solute capacity factor, k_{IAM} , which is proportional to K_m and P_m according to equations 2.7 and 2.12.

2.2.4 HSA chromatography

A ChromTech HSA 5 μm (3.0 \times 50 mm) column was used for determination of %PPB (Figure 2.8) based on previously developed methodology (60-61, 66). Briefly, 0.01 mM PBS with pH=7.4 and isopropanol were used as the mobile phase and the t_r was measured using the following conditions: 0-3 minutes, 0-30% isopropanol; 3-10 minutes, 30% isopropanol; 10.5-11.0 minutes, 30-0% isopropanol; 11.0-15.0 minutes, 0% isopropanol. The mobile phase flow rate was 1.8 mL/min. The system was calibrated by injecting the following reference compounds: warfarin (%PPB=98.0), nizatidine (%PPB=35.0), bromazepan (%PPB=60.0), carbamazepine (%PPB=75.0), budesonide (%PPB=88.0), nocardipine (%PPB=95.0), ketoprofen (%PPB=98.7), indomethacin (%PPB=99.0) and diclofenac (%PPB=99.8). The %PPB for the reference compounds (taken from literature (66)) were converted to the linear free energy related log K values, according to equation 2.13; then the t_r values obtained from the HSA column were plotted against the log K values. The line equation obtained by plotting log K values from reference compounds and their t_r on a HSA column was used to obtain the log K values of the test compounds. Finally, the %PPB values were determined according to equation 2.14 (66). All calculations were performed using Excel 2003 software (Microsoft Office, Microsoft Corporation, USA).

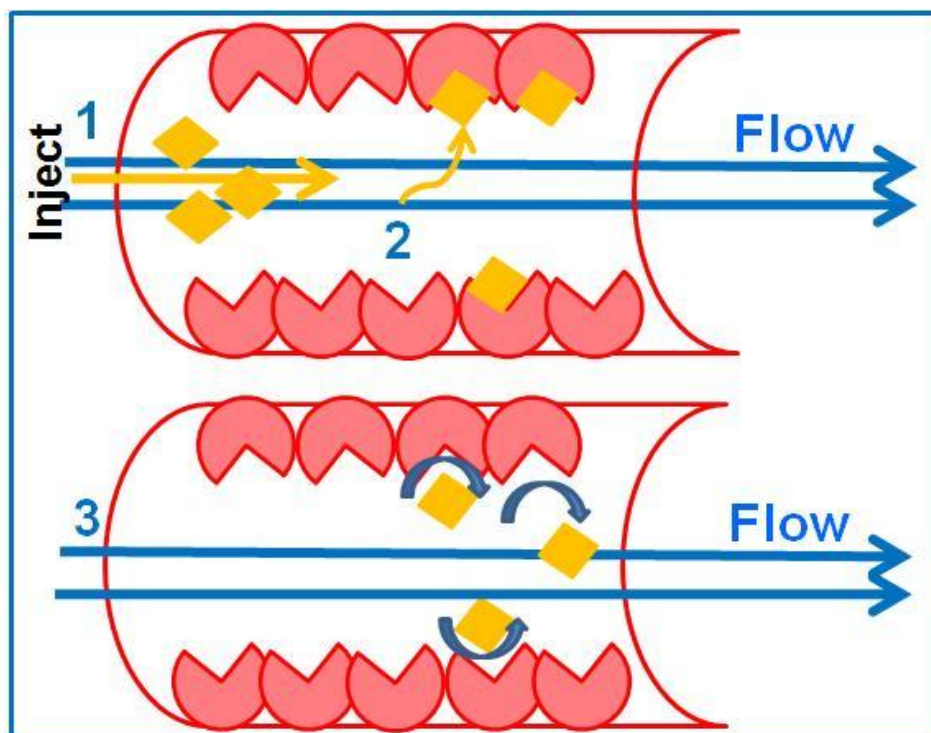


Figure 2.8 Schematic representation of the measurement of compound binding to plasma proteins by HSA chromatography.

1) the compound is injected onto a HSA column, 2) compound is retained on the HSA column and 3) mobile phase elutes compound. The compound t_r is proportional to %PPB.

$$\text{Log } k = \text{Log} \left[\frac{\% \text{PPB}}{(101 - \% \text{PPB})} \right] \quad (\text{Eq. 2.13})$$

$$\% \text{PPB} = \left[\frac{(101 \times 10^{\log k})}{(1 + 10^{\log k})} \right] \quad (\text{Eq. 2.14})$$

2.2.5 Flask methods for Log P determination

Partition coefficient values obtained using flask methodology were either taken from the literature or measured in the laboratory (70-79). Log P values measured in the laboratory were determined in triplicate by mixing in a test tube 10-20 μL of [^{123}I] labelled radiotracer (>99% radiochemical purity) with 1.0 mL of octanol as the organic phase and 1.0 mL of water as the aqueous phase (Figure 2.6a). The test tube was vortexed for 1 minute at room temperature, then centrifuged for 60 minutes at 4000 rpm. After centrifugation, the radioactivity in 200 μL samples of each phase was measured using Packard Cobra gamma counter. The partition coefficient was determined using equation 2.15.

$$\text{Partition coefficient} = \frac{\text{cpm octanol}}{\text{cpm water}} \quad (\text{Eq. 2.15})$$

where cpm=counts per minute.

2.2.6 *In silico* algorithms for Log P determination

Two *in silico* packages were used for determination of Log P: ChemDraw 8.0 (CambridgeSoft Corporation, USA) and ADME Suite 5.0 (Advanced Chemistry Development Inc., Canada). From the latter package, two different Log P values were obtained depending on the algorithm used for its calculation (ADC algorithm or Pharma algorithm). ChemDraw 8.0 also provided two different values: Log P and cLog P.

2.2.7 HPLC analyses of existing radiotracer compounds

Ten compounds, which have already been used as radiotracers in human studies (7 SPECT and 3 PET) were examined (Figure 2.9): 2-((2-((dimethylamino)methyl)phenyl)thio)-5-iodophenylamine (**ADAM**), a gift from Dr. Hank Kung (Pennsylvania University, USA); 2 β -carbomethoxy-3 β -(4-iodophenyl)tropane (**β -CIT**), from ABX (Advanced Biochemical Compounds, Germany); 3-amino-4-(2-dimethylaminomethylphenylsulfanyl)benzotrile (**DASB**), from ABX (Advanced Biochemical Compounds, Germany); 3-iodo-6-methoxybenzamide (**IBZM**), from ABX (Advanced Biochemical Compounds, Germany); ethyl 7-iodo-5,6-dihydro-5-methyl-6-oxo-4*H*-imidazo[1,5- α][1,4]-benzodiazepine-3-carboxylate (**lomazenil**), a gift from Dr. Frederic Bois (Yale University, USA); 1-(2-chlorophenyl)-*N*-methyl-*N*-(1-methylpropyl)-3-isoquinolinecarboxamide (**PK11195**), from Tocris Bioscience (Tocris Bioscience, USA); 1-(2-iodophenyl)-*N*-methyl-*N*-(1-methylpropyl)-3-isoquinolinecarboxamide (**I-PK11195**), a gift from Dr. Andrew Sutherland (University of Glasgow, UK); [*N*-methyl]-2-(4'-methylaminophenyl)-6-hydroxybenzothiazole (**PIB**), a gift from Dr. Franklin Aigbirhio (Cambridge University, UK); (*R*)-3-quinuclidinyl-(*R*)-4-iodobenzilate [**(*R,R*)I-QNB**], from Target Molecules, UK; and 3-[2(*S*)-2-azetidylmethoxy]pyridine (**5-IA85380**), from ABX (Advanced Biochemical Compounds, Germany).

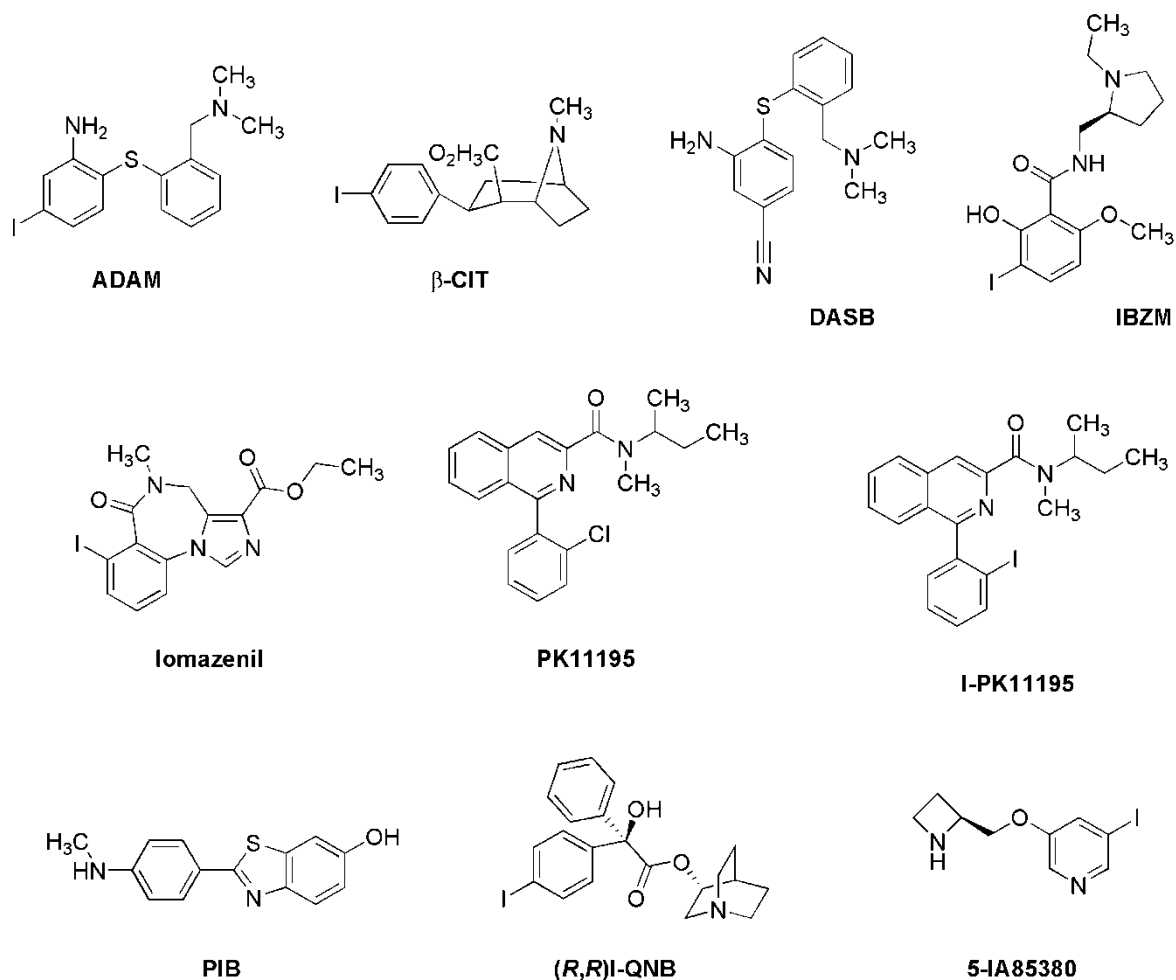


Figure 2.9 Chemical structures of the radiotracer compounds evaluated.

Whole brain peak percentage injected dose (%ID) and binding potential, BP_{ND} (defined at equilibrium as the ratio of specifically bound to non-displaceable radiotracer in tissue) [9], were used as *in vivo* measures of radiotracer performance. Both *in vivo* measurements were derived from studies using healthy human volunteers and were obtained from the published literature (Table 2.2) [10-29]. The literature review was performed by searching for radiotracer biodistribution, dosimetry and kinetic modelling studies in healthy human subjects using ISI Web of Knowledge and Ovid databases. Only radiotracers with reported data for whole brain peak uptake as %ID and binding potential as BP_{ND} were selected for HPLC analyses. BP_{ND} was either obtained directly from the publication or calculated using the published k_3 and k_4 values ($BP_{ND}=k_3/k_4$). The selection of the ten radiotracers included in the study was also determined by availability of the cold compounds.

Compound	%ID	Reference	BP_{ND}	Reference
lomazenil	13.70±2.40 (n=8)	(80)	12.50±0.05 (n=10)	(81)
β-CIT	7.00±2.00 (n=6)	(82)	6.66±1.54 (n=5)	(83)
5-IA85380	5.00 (n=10)	(84)	4.43±0.06 (n=6)	(85)
(R,R)-I-QNB	5.00*	(86)	4.85 (n=11)	(87)
DASB	4.00 (n=7)	(88)	2.68±0.68 (n=5)	(89)
IBZM	3.72±1.16 (n=9)	(90)	0.86±0.11 (n=10)	(91)
ADAM	3.70 (n=11)	(92)	1.62±0.57 (n=7)	(93)
PK11195	2.75 (n=5)	(94)	1.60±0.40 (n=13)	(95)
I-PK1195	2.00±0.50 (n=5)	(96)	---	---
PIB	---	---	0.11±0.15 (n=13)	(97)

Table 2.2 *In vivo* measures of whole brain peak %ID and BP_{ND} obtained from previously published studies in healthy human volunteers.

Values are mean ± standard deviation (if reported); n is number of healthy volunteers; *sample size not reported.

2.2.8 Data analysis and curve fitting

The relationships between Log P, P_m and %PPB and *in vivo* peak %ID were investigated. The relationship between K_m and specific binding *in vivo* (BP_{ND}) was also investigated. The reported mean peak %ID and BP_{ND} values were used. Relationships between the different parameters were assessed using nonlinear regression models in GraphPad Prism version 4.0 (GraphPad Software, USA). Nonlinear regression was used to adjust the values of the variables in the model to find the curve that best predicts Y (%ID or BP_{ND}) from X (Log P, P_m , %PPB and K_m). A variety of mathematical formulations were tested to determine the best fitting model that described the investigated relationships and included, Gaussian, polynomial, exponential and logarithmic functions. The best fitting model was determined by the following goodness of fit measures: r^2 value, absolute sum of squares (SS), standard deviation of the vertical distances of the points from the line ($Sy.x$) and F-test.

The variability of Log P measured using the internal flask and HPLC C_{18} methodology was determined by calculating the coefficient of variation (%COV), according to equation 2.16.

$$\% \text{ COV} = \left[\frac{\text{SD}}{\text{Mean}} \right] \times 100 \quad (\text{Eq. 2.16})$$

where SD = standard deviation.

2.2.9 HPLC analyses of radiotracer candidates for SPECT imaging of the TSPO in the brain

A novel library of PK11195 analogues (Figure 2.10) was synthesised by two collaborators, Louise Stevenson and Aurélie Brunet, under the supervision of Dr Andrew Sutherland in the School of Chemistry at the University of Glasgow. The PK11195 analogues were tested for binding affinity to TSPO using traditional competition binding assays by Louise Stevenson. Further screening of the library was conducted using the HPLC methodology described in sections 2.2.1-2.2.4 for the determination of Log P, K_m , P_m and %PPB.

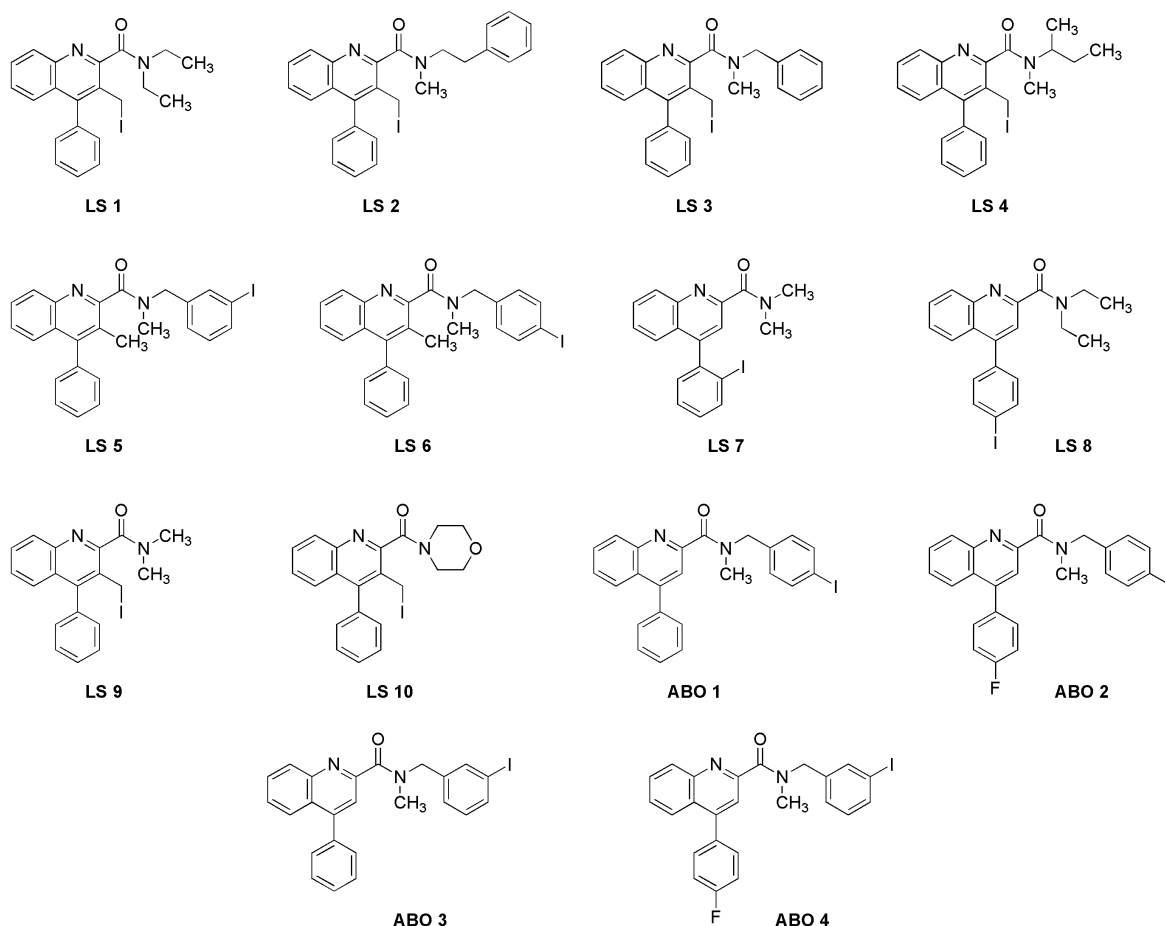


Figure 2.10 The chemical structures of novel PK11195 analogues.

2.3 Results

2.3.1 Investigation of HPLC analyses as a novel tool for brain radiotracer discovery

The results from the HPLC analyses of evaluated radiotracer compounds are summarised in Table 2.3. ADAM had the highest Log P (5.13), while β -CIT had the lowest value (1.02). ADAM and lomazenzil had the highest and lowest P_m values, respectively (1.47 for ADAM and 0.04 for lomazenzil). The %PPB results demonstrate that ADAM had the highest binding to HSA (97%), while the lowest binding to plasma proteins was obtained with 5-IA85380 (45%). ADAM had the highest K_m ($K_m = 563.68$), conversely, lomazenzil presented the lowest K_m value of all evaluated compounds ($K_m = 11.34$).

Compound	HPLC measure			
	Log P (mean±SD, n=3)	Permeability *	%PPB_{HSA} (mean±SD, n=3)	K_m*
Iomazenil	1.58±0.00	0.04	55.51±1.25	11.34
β-CIT	1.02±0.02	0.22	67.34±0.00	84.26
5-IA85380	1.54±0.03	0.29	44.96±0.08	83.55
(R,R)-I-QNB	3.67±0.00	0.60	86.44±0.42	279.65
DASB	4.10±0.00	1.20	83.35±0.00	341.06
IBZM	4.39±0.00	1.04	90.15±0.14	421.71
ADAM	5.13±0.00	1.47	97.79±0.22	563.68
PK11195	3.85±0.03	0.64	92.28±0.01	225.78
I-PK1195	4.03±0.04	0.50	93.94±0.02	223.60
PIB	3.00±0.00	1.00	97.45±0.02	256.14

Table 2.3 HPLC analyses for all radiotracer compounds evaluated.

*regression analysis was used to estimate the result using 100% PBS.

The best fitting model describing the association between Log P determined *via* HPLC C₁₈ methodology and *in vivo* brain uptake is shown in Figure 2.11. The r^2 of 0.47 indicates that approximately half of the variance of *in vivo* brain uptake is explained by the equation which involves Log P determined *via* HPLC C₁₈ methodology. A Gaussian curve described the relationship between %PPB and peak %ID (Figure 2.12). The best fitting model for the association between *in vivo* brain uptake and %PPB showed that approximately two-thirds of the variance of *in vivo* brain uptake is explained by the equation. Brain uptake had an inverse relationship with P_m, where the peak %ID in brain tended to decrease as P_m increased (Figure 2.13). The best fitting model for the association between brain uptake and P_m showed approximately three-quarters of the variance of *in vivo* brain uptake is explained by the equation. An inverse relationship was observed between K_m and BP_{ND} (Figure 2.14), where almost 90% of the variance of BP_{ND} was explained by its modelled relationship with K_m.

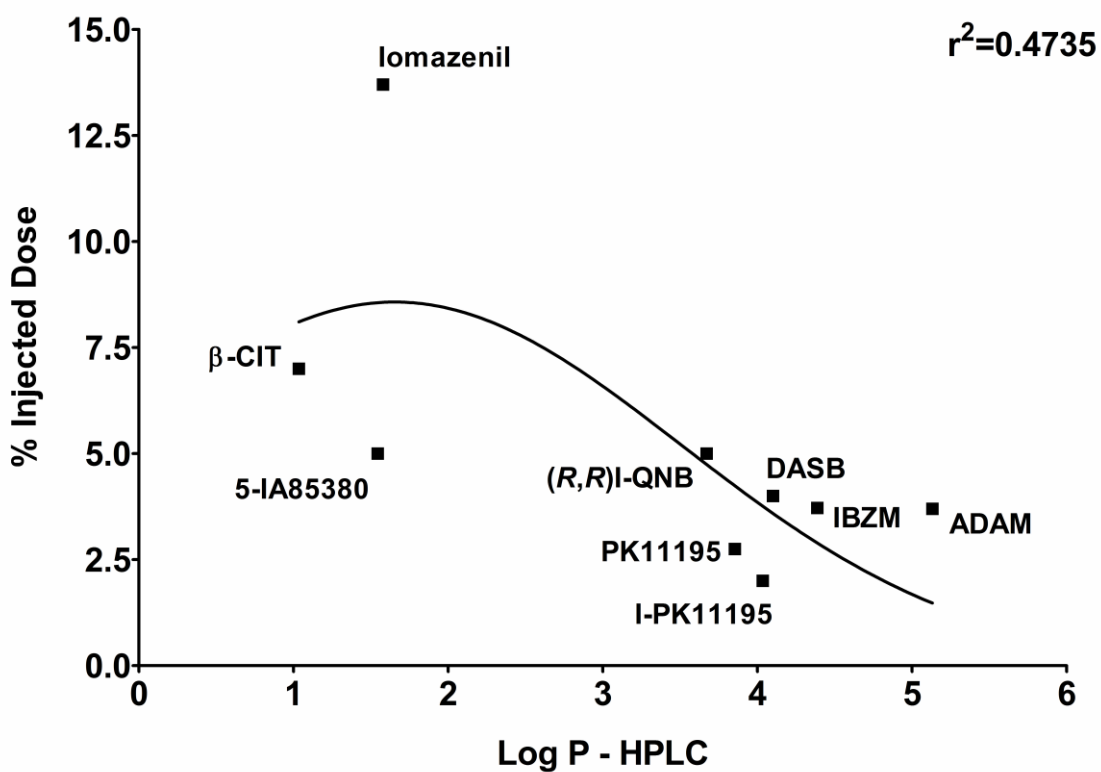


Figure 2.11 Relationship between Log P measured using HPLC C_{18} methodology and %ID.

Best fitting curve was Gaussian. $y = 3.42 \times \exp\left[-0.5 \times \left(\frac{x - 1.656}{1.853}\right)^2\right]$

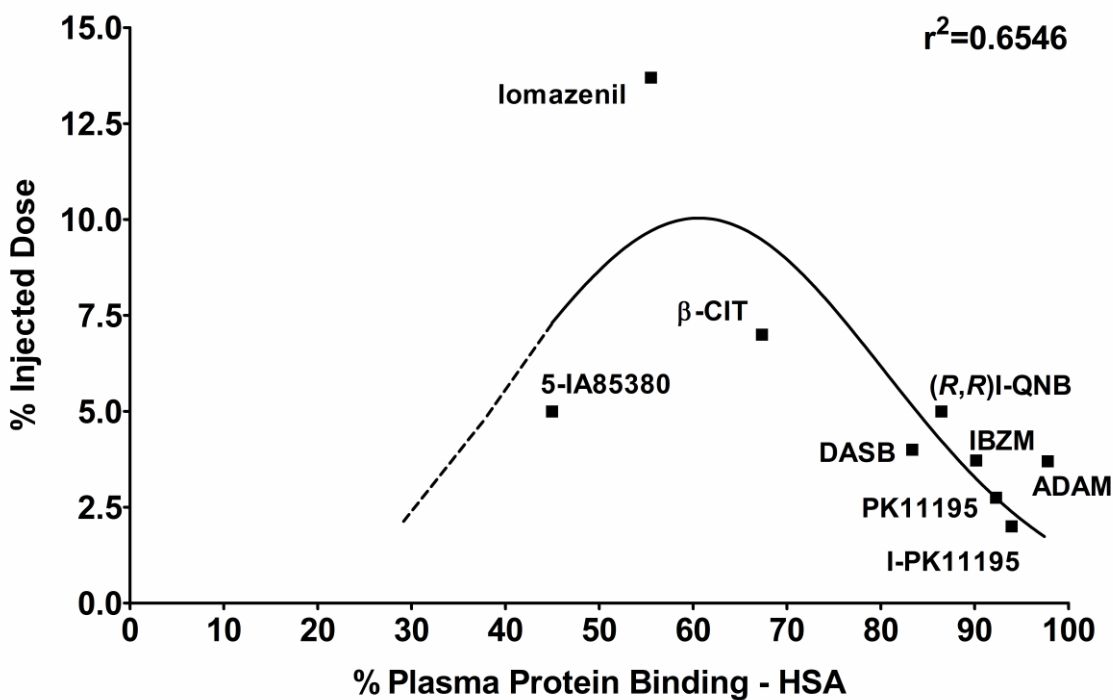


Figure 2.12 Relationship between %PPB measured using HPLC HSA methodology and %ID.

Best curve fitting was Gaussian. $y = 7.10 \times \exp\left[-0.5 \times \left(\frac{x - 60.63}{19.65}\right)^2\right]$

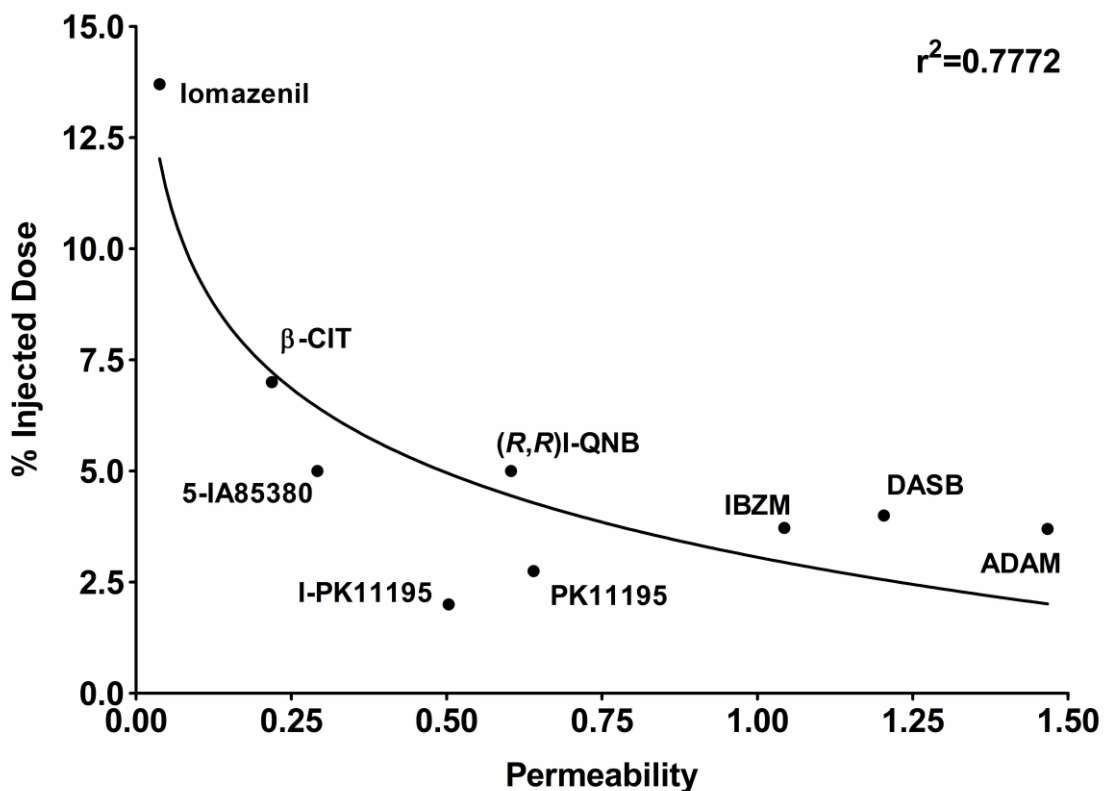


Figure 2.13 Relationship between permeability measured using HPLC IAM methodology and %ID.

Best curve fitting was logarithmic. $y = -2.74 \ln(x) + 3.06$

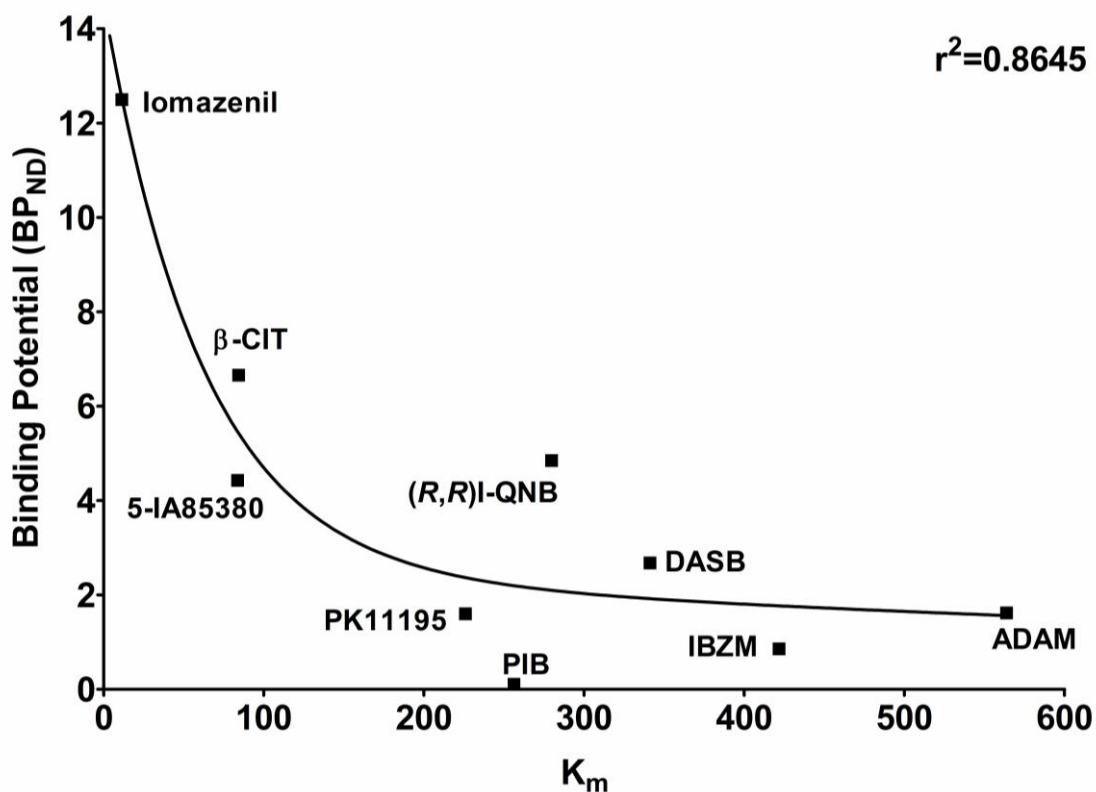


Figure 2.14 Relationship between K_m measured using HPLC IAM methodology and BP_{ND} . Best fitting curve was exponential. $y = 4.66 \exp(-3.15 \times 10^{-4}x) + 12.27 \exp(-1.66 \times 10^{-2}x) - 2.383$

Log P values were highly variable, depending on the methodology used to determine them (Table 2.4). The values obtained using the traditional flask method tended to be lower than those obtained by the HPLC C₁₈ method. Log P values determined using *in silico* methodology were highly variable, dependent on the algorithm used. Overall *in silico* methods tended to produce Log P values higher than those obtained by the HPLC C₁₈ method. None of the methods investigated for Log P determination showed a good correlation with %ID (Figures 2.15 and 2.16), where the flask methods presented the weakest correlation with %ID. I-PK11195 and β -CIT, available in house, were used to compare the %COV for the flask and HPLC C₁₈ method. The %COV was greater for the flask method than for the HPLC C₁₈ method (Table 2.5).

Compound	Log P HPLC (mean±SD, n=3)	Log P Flask methods (mean±SD)	Reference	Log P ADC algorithms	Log P Pharma algorithms	cLog P ChemDraw	Log P ChemDraw
lomazenil	1.58±0.00	1.48* [†]	(75)	1.70	1.32	2.07	2.30
β-CIT	1.02±0.02	1.22±0.07 (n=3)	Determined internally	3.40	3.65	4.50	4.11
5-IA85380	1.54±0.03	0.44±0.01 [†]	(79)	1.24	1.24	1.89	1.39
(R,R)I-QNB	3.67±0.00	1.60* [†]	(78)	4.29	4.13	4.07	4.47
DASB	4.10±0.00	2.38±0.03 (n=8)	(72)	3.20	3.10	3.21	3.31
IBZM	4.39±0.00	2.85* [†]	(74)	3.57	3.23	3.93	2.65
ADAM	5.13±0.00	2.53* [†]	(70)	4.75	3.96	4.51	4.63
PK11195	3.85±0.03	1.41±0.08 (n=4)	(77)	4.58	5.18	4.62	5.30
I-PK1195	4.03±0.04	2.37±0.46 (n=3)	Determined internally	5.10	5.14	4.77	6.09
PIB	3.00±0.00	1.30* [†]	(76)	3.33	3.72	3.99	3.41

Table 2.4 Summary of Log P values obtained by different methodologies.

*SD values not reported; [†]n value not reported.

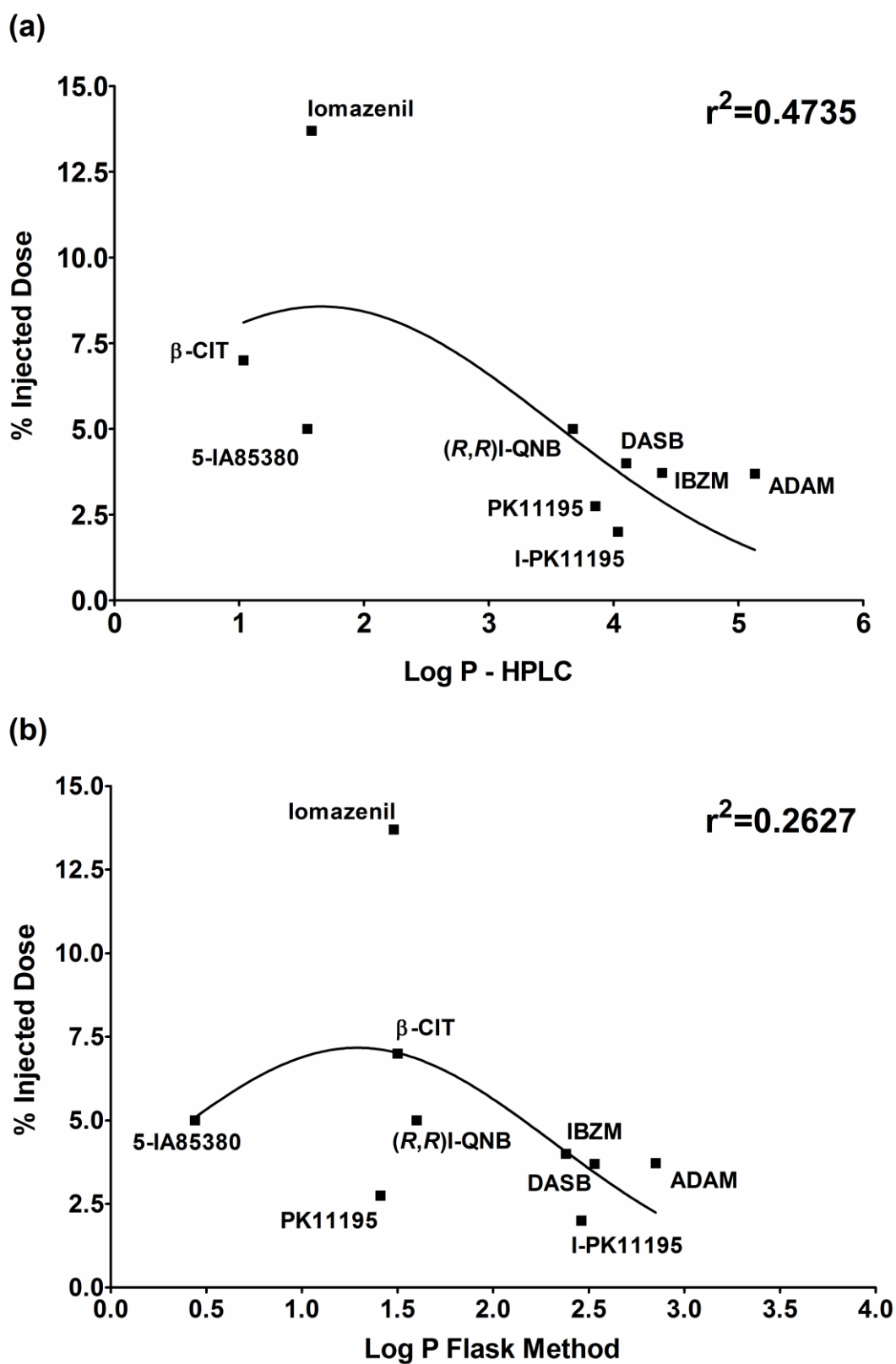


Figure 2.15 Comparison of relationship between Log P determined by HPLC or flask method and %ID.

(a) Relationship between Log P determined by HPLC and %ID; and (b) relationship between Log P determined by flask method and %ID. Best fitting curve was Gaussian.

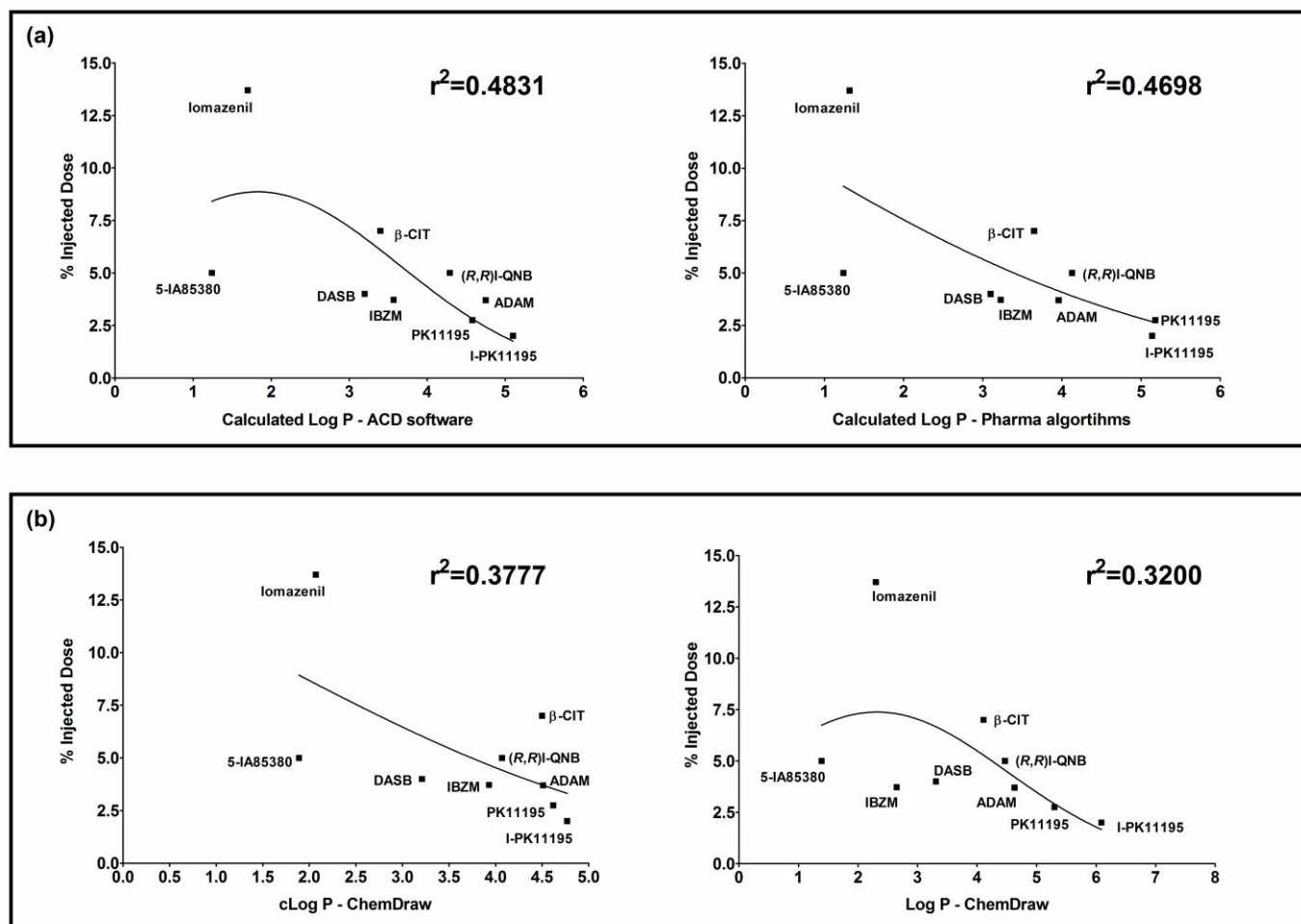


Figure 2.16 Comparison of the relationship between Log P calculated using different computational methods and %ID.
 (a) Log P determined by ADC/Pharma algorithms and (b) Log P determined by ChemDraw software.

Compound	Log P flask method	%COV	Log P HPLC	%COV
β -CIT	1.22 \pm 0.07 (n=3)	5.90%	1.02 \pm 0.02 (n=3)	1.84%
I-PK11195	2.37 \pm 0.46 (n=3)	19.27%	4.03 \pm 0.04 (n=3)	0.88%

Table 2.5 The %COV of the Log P determined for β -CIT and I-PK11195 using either traditional flask or HPLC C₁₈ methodology. Values are mean \pm standard deviation.

2.3.2 HPLC analyses of radiotracer candidates for SPECT imaging of the TSPO in the brain

The *in vitro* binding affinities (K_i) of PK11195 and the novel library of analogues to the TSPO in whole rat brain are shown in Table 2.6. Physicochemical properties determined using the HPLC techniques described are also shown in Table 2.6.

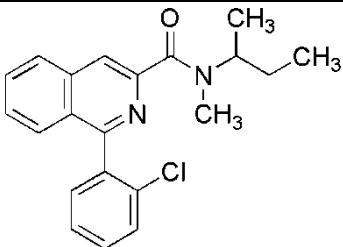
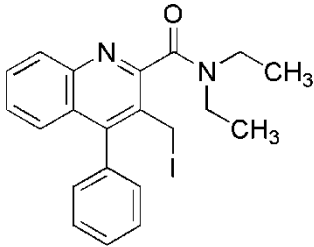
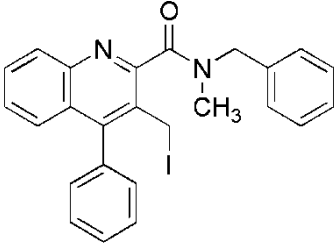
Compound	K_i (nM)	Log P	%PPB	P_m	K_m
 PK11195	9.8 \pm 1.6*	3.85*	92.28	0.64	225.78
 LS 1	12.0 \pm 1.3*	4.76*	96.64	0.31	136.51
 LS 3	26.1 \pm 4.7*	5.39*	98.36	0.59	289.65

Table 2.6 Affinity and physicochemical properties of PK11195 and the novel library of analogues.

Affinity data shown as mean \pm SEM n=3, except where ^a is assigned n=2. Compounds are listed in order of ascending K_i values. * K_i and Log P values published at (35).

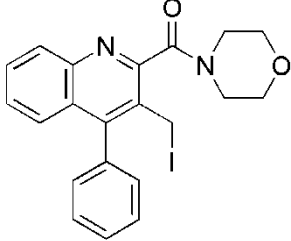
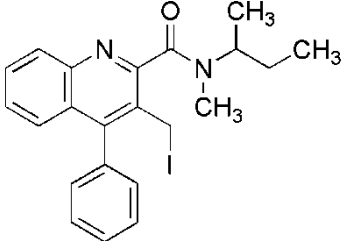
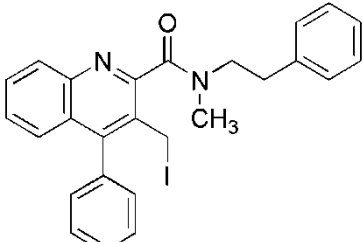
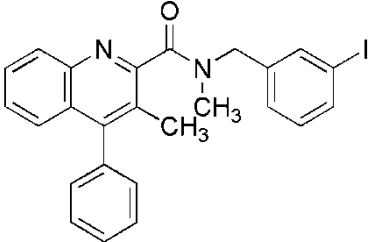
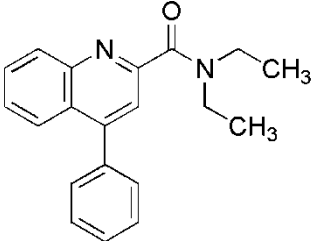
Compound	K_i (nM)	Log P	%PPB	P_m	K_m
 <p>LS 10</p>	27.8±2.9 ^a	3.62	95.30	0.54	246.85
 <p>LS 4</p>	173±35*	5.17*	97.35	0.41	189.83
 <p>LS 2</p>	411±62*	5.41*	98.21	0.83	418.14
 <p>LS 5</p>	455±51*	5.02*	98.30	0.62	303.84
 <p>LS 8</p>	491±154	4.50	96.63	0.50	214.49

Table 2.6 (cont).

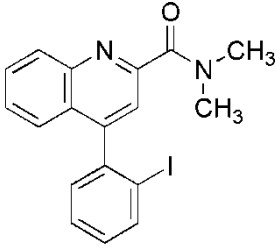
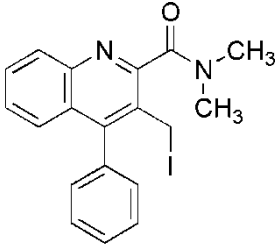
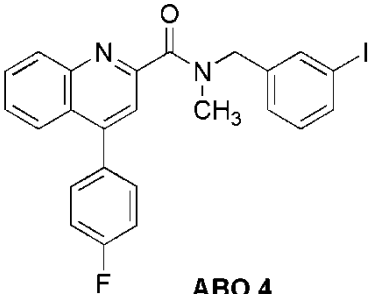
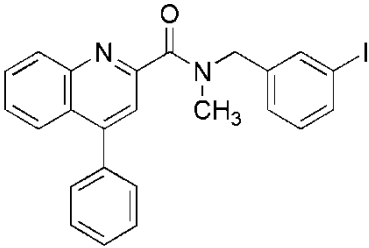
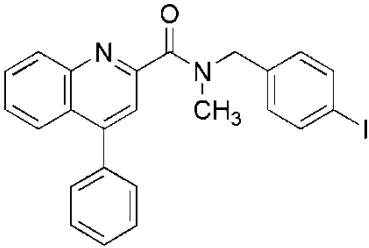
Compound	K_i (nM)	Log P	%PPB	P_m	K_m
 LS 7	1255±218	2.91	92.32	0.30	120.18
 LS 9	1339±168 ^a	4.50	95.02	0.55	238.61
 ABO 4	1432±80*	5.16*	99.18	0.62	306.52
 ABO 3	3812±383 ^{a*}	5.12*	99.15	0.63	302.22
 ABO 1	4026±256 ^{a*}	5.11*	98.88	0.69	331.77

Table 2.6 (cont).

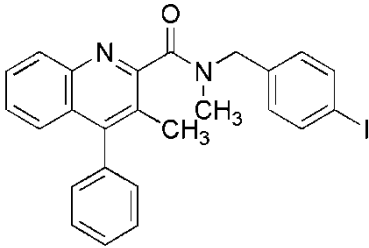
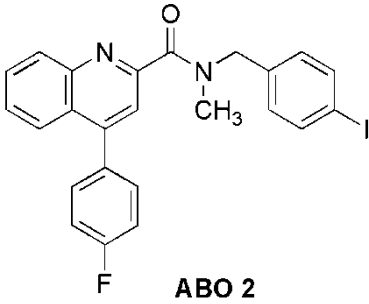
Compound	K_i (nM)	Log P	%PPB	P_m	K_m
 LS 6	4083±88 ^{a*}	5.12*	98.27	0.68	333.59
 ABO 2	12675±647 ^{a*}	5.21*	98.87	0.68	336.11

Table 2.6 (cont).

2.4 Discussion

2.4.1 Investigation of HPLC analyses as a novel tool for brain radiotracer discovery

In this chapter, HPLC methods were used to determine the physicochemical properties of radiotracers that have been characterised *in vivo* in humans and the predictive relationships between HPLC measures and *in vivo* brain measures were described. The HPLC methodology used has the potential to provide a high-throughput and cost-effective approach that may improve lead candidate identification and reduce the current high level of attrition in radiotracer discovery.

As previously outlined, Log P values between 1 and 3.5 have been considered optimal for brain penetration of a compound (section 1.3) and the Log P value is frequently used as a selection criterion to take compounds forward in the radiotracer development process (19, 34). Of the three HPLC-derived measurements examined as useful predictors of BBB penetration, Log P was the weakest; where the described association between it and peak %ID in brain had an r^2 value of 0.47. The basis for this comparatively weak association may be that while Log P provides a measure of hydrophobicity and polarity interactions (i.e. lipophilicity), it does not reflect the ionic bonding that is also involved in compound-membrane interactions (52, 56-58). Log P is

therefore a relatively simplistic measure since it does not predict all aspects of BBB penetration. A number of different methods that can be used to determine Log P were investigated and the values varied considerably depending on the method used to measure or calculate it. Taken together the findings suggest that using Log P as a basis for lead candidate identification may contribute to the high attrition rate in radiotracer discovery. It was interesting to note that the reproducibility of the HPLC method was greater than that of the commonly used flask method. Log P values that are determined by the traditional flask method may be affected by very small amounts of impurities present in the sample. One advantage of HPLC is that impurities present in a test sample will not affect the retention time and therefore will not affect the Log P determined.

In order for a molecule to penetrate the BBB, it has to cross brain capillary endothelial cells and thus permeability across the plasma membrane is a crucial factor in BBB penetration (98). It has been shown that artificial membranes, such as IAMs, are able to mimic compound-membrane interactions more reliably than octanol-water or C_{18} chromatography (further detail in sections 2.1.3 to 2.1.5) (52, 56-58). Consequently, in this study, permeability (measured using IAM chromatography) was evaluated as a predictor of brain uptake. The results obtained show that there is a stronger association between permeability and peak %ID in the brain ($r^2 = 0.78$) than between Log P and peak %ID in the brain ($r^2 = 0.47$). Radiotracers with high permeability had the lowest brain uptake, which is in line with previous observations that highly diffusible molecules exit brain tissue rapidly by transport across local capillaries, thus resulting in low %ID measured in the brain (99).

The best fitting curve describing the relationship between %PPB and brain uptake was Gaussian; the higher levels of brain uptake being observed when radiotracer binding to plasma proteins was approximately between 45 and 85%. This suggests that both lower and higher limits of PPB define a range within which brain uptake will be optimal. A consensus view is that to optimise brain uptake, radiotracer binding to plasma proteins should be lower than 95% based on findings that avid binding of compounds to plasma proteins (above 95%) results in low blood clearance and low brain penetration (66). High binding to plasma proteins is associated with high lipophilicity and this can increase deposition of radiotracer in peripheral organs including liver, lungs and spleen (19). Thus, when PPB is high, brain uptake may be reduced as a consequence of both low blood clearance and increased peripheral organ deposition. The results from this study show that low PPB is also associated with low brain uptake, which is consistent with drug pharmacokinetic studies demonstrating that molecule-protein complexes are less available to enzymes involved in first-pass metabolism (67). However, this

interpretation would be strengthened by future analysis including additional radiotracers with PPB lower than 45%.

Two of the major factors in the phenomenon of BBB penetration, and hence brain uptake, are PPB and BBB permeability (50). The approach investigated in this study suggests that the determination of both %PPB and permeability for compounds would facilitate lead molecule selection during radiotracer discovery process. A guideline for selection of compounds may be proposed based on the results obtained, where a low permeability value (< 0.5) and %PPB between 45-85% is suggested to most likely yield the highest brain uptake (Table 2.7). These proposed thresholds aim to provide further confidence in the selection of molecules to be taken forward as radiotracers.

Another important consideration when developing a novel radiotracer is its specific/non-specific interactions, frequently expressed *in vivo* as binding potential. The competition binding assays that are typically used for screening compound affinity provide little insight into its non-specific binding *in vivo*. Non-specific binding has been found to be a frequent limitation of novel radiotracers (100-101). A high throughput approach providing information on specific/non-specific binding interactions is therefore desirable to reduce attrition during radiotracer development. In this investigation IAM chromatography was used to model non-specific interactions with cell membranes and the relationship of the measured K_m value with the selected *in vivo* measurement, BP_{ND} , was examined. There was a negative association between K_m and BP_{ND} , such that for K_m values higher than 250, the BP_{ND} was below 2 and for K_m values higher than 150 the BP_{ND} was below 3. A minimum specific binding ratio between 2 and 3 has been suggested to be desirable in order to reliably analyse *in vivo* images (53-54). Our findings suggest that a K_m value of between 150-250, as determined by IAM chromatography, may be useful as lower cut-off threshold for selection of compounds for future development (Table 2.7). Defining an ideal specific to non-specific binding ratio *in vivo* by means of PET or SPECT is complex and dependent upon multiple factors, including target size, resolution of the instrument, radioactive concentration on the target site and signal to noise ratio. Measurement of K_m using IAM chromatography can provide a simpler approach for estimation of specific to non-specific binding during early compound screening.

<i>HPLC measurements</i>	<i>Predicted in vivo measurements</i>
$P_m < 1.5$	%ID > 2.0%
$P_m < 0.5$	%ID > 4.0%
PPB < 95%	%ID > 2.0%*
45% < PPB < 85%	%ID > 4.0%
$K_m < 250$	BP _{ND} > 2.0
$K_m < 150$	BP _{ND} > 3.0

Table 2.7 Proposed guidelines for aiding lead molecule identification using developed HPLC tool.

*except highly hydrophilic compounds, where PPB < 30% = %ID < 2.0%

The HPLC methodologies described in this chapter for determination of P_m , K_m and %PPB may provide a high throughput approach that could be easily automated and used to build a large database of radiotracer characteristics. Nevertheless, given the complexity of radiotracer design and *in vivo* biological systems, there are several limitations to this approach. One of the weaknesses is that it assumes passive diffusion across the BBB, although it is well known that the BBB contains several active transport mechanisms, efflux pumps and metabolically active enzymes (46, 55). Currently a high-throughput method for prediction of active transport, such as P-gp mediated transport, remains to be developed (18, 51, 100, 102). Another limitation of the HPLC approach outlined is its inability to account for radiotracer metabolism. Increased probability for enzymatic metabolism in blood has been associated with very low binding to plasma proteins, while increased probability for metabolism in tissue has been linked with very high binding to plasma protein (19, 50, 66-67). However evaluation of plasma protein binding by means of HPLC provides only limited insight into the likelihood of radiotracer metabolism and additional *in vitro* methods, such as assays using liver microsomes, may also reduce attrition in radiotracer development. The HPLC methodology investigated here is also unable to mimic the effects of certain pathologies on the BBB function. For example, one of the radiotracers examined (¹¹C-PIB) has been used for imaging of A β plaques in patients with dementia. Previous studies have shown that A β plaques are frequently present in the vicinity of the cerebral microvasculature and as consequence, the BBB function can be severely compromised (101). This may result in increased brain uptake of this tracer. Ideally, an *in vitro* model able to mimic effects of pathologies on BBB function would also further improve the HPLC approach proposed here.

The evaluation of predictive relationships between the data derived from HPLC analyses and the *in vivo* characteristics of radiotracers only used %ID and BP_{ND} data obtained from normal human brain. Due to the availability of published values and compounds, this meant that only 10 radiotracers were included in the present analysis. This is due to two main reasons: (1) studies investigating radiotracers in human brain that fail to

produce the expected outcome are frequently not published; and (2) there is a lack of either human biodistribution and/or time-activity curves published in the literature. A multicentre approach making unpublished data available would add to this initial analysis. Future developments of the current approach using HPLC could include a computational model that incorporates the *in vitro* HPLC measurements reported along with other *in vitro* measurements (e.g. P-gp transport assays) so that the probability of a molecule being a successful radiotracer could be more accurately predicted.

In summary, the results demonstrate that Log P should not be relied upon as a predictor of BBB penetration during brain radiotracer discovery. However the HPLC measurements of permeability, PPB and membrane interactions that are described here may have potential to predict *in vivo* performance and hence allow evaluation and ranking of compound libraries, improving selection of lead radiotracer candidates. No method is without its drawbacks; however, there is a compelling need for better selection of candidate molecules in the early stages of radiotracer development and therefore simple and cost-effective methodologies able to predict *in vivo* radiotracer characteristics are desirable. An approach employing the proposed HPLC measurements would enable screening of large libraries of compounds and identification of those most likely to succeed.

2.4.2 HPLC analyses of radiotracer candidates for SPECT imaging of the TSPO in the brain

The novel HPLC methodology investigated in this study as a tool for brain radiotracer discovery was applied to a new library of PK11195 analogues developed at the School of Chemistry at the University of Glasgow. The compound library was also tested for affinity to the target, TSPO, using the traditional competition binding assays (35). Over the past decades, a significant number of new radiotracers for imaging the TSPO in the brain were synthesised and evaluated, including the most well known TSPO radiotracer, PK11195. In spite of these efforts, the currently available radiotracers for imaging of the TSPO have considerable disadvantages, including low sensitivity, high non-specific binding and limited capacity to quantify subtle differences in TSPO expression *in vivo* (103). Therefore novel radiotracers for imaging of the TSPO with improved characteristics are required. The present study set out to aid the development of a novel SPECT radiotracer for imaging of the TSPO in the brain.

The two compounds from the library of novel PK11195 analogues with the highest affinity for TSPO were LS 1 and LS 3 (Figure 2.17). The benzyl analogue LS 3 was found

to have a K_i value of 26.1 nM, while diethyl analogue LS 1 had a higher binding affinity that was comparable to that of PK11195 (K_i of LS 1 and PK11195 was 12.0 and 9.8 nM, respectively). The morpholine analogue, LS10 also had a sub-100 nM affinity (K_i value of 27.8 nM). In general, the results showed that substantially increasing or decreasing the size of the side-chain of the amide results in a poor affinity for the TSPO. The higher affinity of 3-methyl analogue LS 5 (K_i 455 nM) compared to the desmethyl analogue ABO 3 (K_i >1000 nM) confirmed previous observations that semi-rigid compounds (restricted rotation of the amide carbonyl) bind with higher affinity to the TSPO (35). The use of competition binding assays to determine the affinity of a compound has a number of limitations, including a high dependency on the assay conditions used. This limits the comparison of affinity data from novel compounds with affinity data from radiotracers in the literature. In this study, the binding affinity of PK11195 was determined in the same assay as the new library of analogues so that a direct comparison could be made.

HPLC analyses showed that LS 1 and LS 7 had the most promising physicochemical characteristics of all evaluated compounds (Figure 2.17). LS1 and LS7 are the only compounds to have both P_m values of less than 0.5 and K_m values of less than 150. When taken together with affinity data, LS 1 is identified as the most promising PK11195 analogue within the library of compounds developed for imaging the TSPO in the brain. LS 7 is suggested to be unsuitable for imaging of TSPO due to its low affinity for this target (K_i > 1000 nM), even though good physicochemical properties were determined by HPLC. LS 3 had the second highest affinity for TSPO; however the poor physicochemical properties determined by HPLC (P_m value of greater than 0.5, K_m value of greater than 150 and %PPB of > 98%) suggests this compound should not be taken forward as a candidate for further development.

As mentioned above, LS1 had the highest affinity for the TSPO and also promising P_m and K_m values. In comparison with PK11195, LS 1 had a lower P_m and K_m but the %PPB was higher than PK11195. The HPLC selection guidelines outlined in section 2.4.1 suggest that the lower K_m and P_m values of LS1 compared with PK11195 will result in a higher *in vivo* binding potential and brain uptake for LS1 compared with PK11195. However, the higher %PPB determined for LS1 in comparison to PK11195 is predictive of problems in radiotracer delivery to the brain.

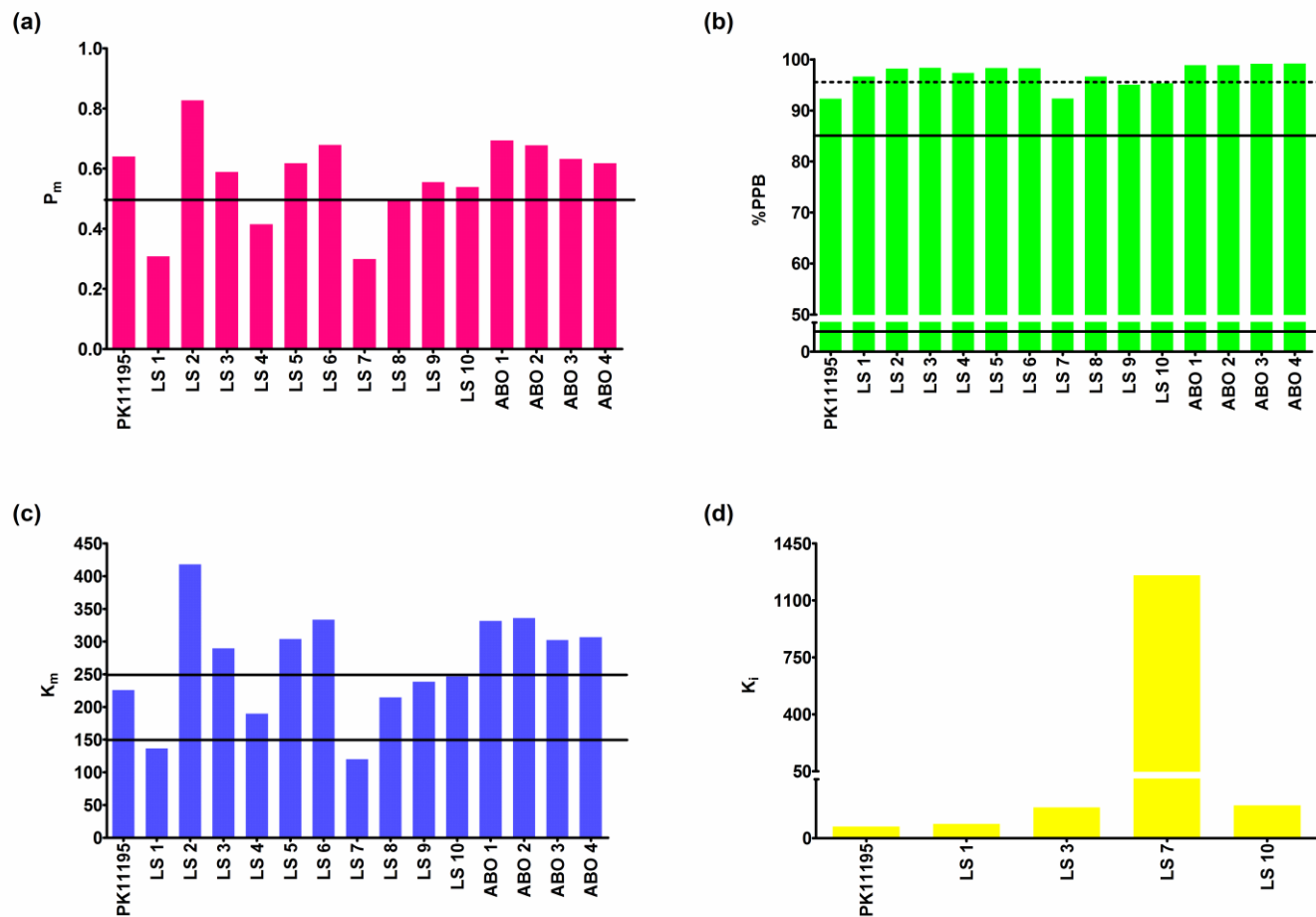


Figure 2.17 Novel PK11195 analogues and the process of lead molecule selection.

(a) P_m value determined by HPLC, (b) %PPB values determined by HPLC, (c) K_m values measured by HPLC and (d) affinity values determined by competition binding assays. HPLC data show that LS 1 and LS 7 are the most likely to succeed candidates, while affinity data show LS 1 and LS 3 are the compounds with highest affinity for TSPO. Combined analysis of the data shows that LS 1 is the lead candidate. Solid black lines represent the guidelines proposed for lead molecule selection based on developed HPLC tool (further detail in section 2.4.1) and dashed black line represents the proposed limits used previously in the literature.

Binding to plasma proteins is saturable and therefore, drugs administered at high enough mass may still enter the brain, even when highly bound to plasma proteins. However, at radiotracer levels (<10 µg per dose) specific binding to albumin or other plasma protein binding sites can severely inhibit radiotracer entry into the brain. Nonetheless, some radiotracers with high %PPB (>95%), such as ADAM and PIB, are still able to cross the BBB and reach the brain. An explanation for this may be that non-specifically bound radiotracer to plasma proteins may still enter the brain by free diffusion if the plasma proteins come into close contact with the endothelial membrane (19). The nature of the binding of LS 1 to plasma proteins, as determined by HPLC is unknown. Therefore without conducting *in vivo* studies it is not possible to definitively predict that the high %PPB measured *in vitro* will result in problems with radiotracer delivery to the brain.

It is interesting to note that if the lead candidate selection was based on the current dogma of a desired Log P value between 1 and 3.5, interpretation of the results would have been considerably different. For example, using the Log P value determined by HPLC as measured in this study, PK11195 would have been excluded as a potentially useful compound. PK11195 has well known limitations as a brain imaging radiotracer, including high non-specific binding (103), however it is still currently the most useful radiotracer for imaging of the TSPO. LS 1 would rank below LS 8, LS 9 and LS 10 when a Log P value between 1 and 3.5 is used as a selection criterion (Table 2.6). Nonetheless, LS 8, LS 9 and LS 10 showed higher P_m and K_m values than LS 1, more similar to that of PK11195, suggesting these compounds would have poor uptake and high non-specific binding.

The application of HPLC analyses to a library of PK11195 analogues has demonstrated the ability of HPLC to provide a simple method for the ranking of compound libraries. By examining compounds in a series, with minor changes in chemical structure, it is possible to gain insight into how structural changes affect physicochemical properties such as lipophilicity and permeability [7]. This insight can be used to influence and aid the future design of novel libraries targeting the TSPO. In summary, from the library of compounds investigated LS 1 was identified as the lead candidate for imaging the TSPO in the brain using a combination of affinity data and the HPLC selection guidelines outlined in section 2.4.1. However, the high plasma protein binding measured for LS 1 suggests that this compound may have problems with radiotracer delivery. Based on this finding, the further development of LS1 is not recommended. At the time of writing this thesis, a new library of compounds was being synthesised by the Glasgow radiotracer development group with the aim of obtaining a candidate with improved physicochemical characteristics, while maintaining affinity for the TSPO.

2.5 Conclusion

In this chapter a novel tool for use in brain radiotracer discovery based on HPLC analysis was outlined. The results from this study showed that HPLC measurements of P_m and %PPB may have the potential to predict radiotracer brain uptake in humans, while K_m may have the potential to predict binding potential and non-specific binding in the human brain. The results also showed that Log P should not be relied upon as selection criteria during brain radiotracer discovery. These results were used to propose guidelines from HPLC derived criteria for lead candidate selection. The proposed guidelines were applied to the HPLC measurements obtained from a new library of PK11195 analogues. Taken together with affinity data the results showed that LS 1 was the lead candidate from the library, however high %PPB precluded this candidate from further development.

The developed HPLC tool can be applied to select the lead radiotracer candidate during brain radiotracer discovery by following four main steps:

- 1) Synthesise or use an already existent library of compounds targeting a brain receptor, transporter or enzyme and determine the compound's affinity to the target by means of competition binding assays.
- 2) Test each compound using the HPLC methodology investigated in this chapter, in order to obtain %PPB (from the HSA column), P_m and K_m (from the IAM column) values.
- 3) The obtained values of %PPB, P_m and K_m can then be used to predict the %ID in brain, BP_{ND} and non-specific binding by using the proposed selection criteria (Table 2.7). An example of application of the proposed thresholds was given in Figure 2.17, where the novel TSPO ligands were tested using the proposed tool.
- 4) The lead candidate will be the compound with the highest affinity for the target combined with the more favourable physicochemical properties, i.e. lowest P_m and K_m and %PPB between 45-85%.

In summary, *in vitro* HPLC analysis can be used to provide useful information on the properties of compound libraries in the early stages of radiotracer discovery, offering increased confidence in the selection of a lead candidate for further *in vivo* evaluation.

3 Radiosynthesis of $^{123/125}\text{I}$ -NKJ64: a novel SPECT radiotracer for imaging of NAT in brain

In this thesis, the compound NKJ64 was investigated as a novel NAT radiotracer. This chapter introduces the rationale for developing a novel SPECT radiotracer for imaging of the NAT in brain by outlining the importance of the NAT in noradrenergic neurotransmission and the implications of its dysregulation on normal brain function. The current need for the development of a suitable radiotracer for imaging of NAT in brain is also outlined.

NKJ64 is an iodinated analogue of reboxetine, a selective noradrenaline reuptake inhibitor (SNRI). Initial work to develop a novel NAT radiotracer based on reboxetine involved the synthesis of a small library of compounds. This work was performed by Nicola Jobson, a PhD student in the School of Chemistry at the University of Glasgow, as part of a collaboration with the Glasgow radiotracer development group. These initial studies are outlined in the introduction section of the current chapter. A brief overview of different iodination techniques is also provided in the introduction section to facilitate interpretation of radiolabelling results and discussion of the radioiodination methodology used.

3.1 Introduction

3.1.1 The role of the NAT in noradrenergic neurotransmission and consequences of its dysregulation on brain function

Noradrenaline and adrenaline are catecholamines formed along an enzymatic cascade that begins with tyrosine. Noradrenaline is the main sympathetic neurotransmitter in the periphery and is prevalent throughout the brain. Adrenaline, which is formed by the *N*-methylation of noradrenaline, is primarily released from the adrenal medulla and its role as a neurotransmitter in the CNS is relatively unknown.

Tyrosine hydroxylase is the rate-limiting enzyme in the production of noradrenaline, transforming L-tyrosine into L-DOPA in the neuronal cell body and its nerve terminals. DOPA-decarboxylase rapidly converts L-DOPA into dopamine, which is the precursor of noradrenaline. Dopamine is then transported inside storage vesicles to noradrenaline-producing neurons *via* amine-specific transporters. Once inside noradrenaline-producing neurons, dopamine- β -hydroxylase within the vesicles transforms dopamine into

noradrenaline *via* hydroxylation of the β -carbon. On arrival of an action potential at a noradrenergic synapse, neurotransmission occurs by release of intravesicular noradrenaline into the synaptic cleft *via* exocytosis. After release into the synaptic cleft, noradrenaline is rapidly returned to the synaptic terminals *via* the NAT. The NAT is a specific transporter (69 kDa transmembrane protein with 617 amino acids, belonging to the Na^+/Cl^- dependent class of co-transporters) located in the outer membrane of the synaptic terminal. If noradrenaline is not rapidly removed from the synaptic cleft by the NAT, then it is biochemically degraded by monoamine oxidase (MAO) (104-105). Figure 3.1 is a schematic representation of the noradrenergic transmission process.

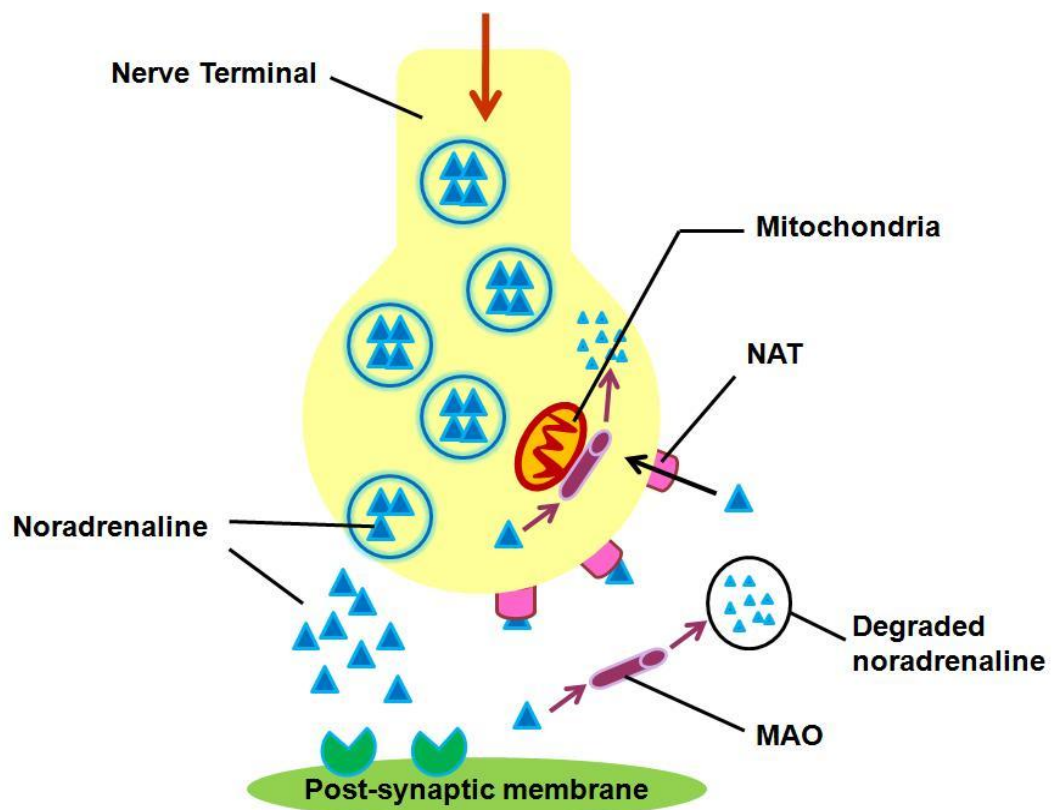


Figure 3.1 Schematic representation of the noradrenergic neurotransmission process.
Note NAT reuptake function.

The locus coeruleus, a dense cluster of noradrenergic neurons, is located in the brainstem and presents the highest density of NATs in the mammalian brain (41, 106). The locus coeruleus has been implicated in multiple brain functions, including: vigilance, attention, sensory processing, synaptic plasticity, network resetting, memory formation, memory retrieval, decision making and performance facilitation (107). Dysregulation of the noradrenergic system has been implicated in multiple psychiatric and neurodegenerative disorders, including: depression, post-traumatic stress, anxiety, ADHD, Alzheimer's disease and Parkinson's disease (36-41).

3.1.2 Radiotracers for imaging of NAT

Non-invasive imaging using a selective NAT radiotracer and PET or SPECT could be used for *in vivo* investigations of disease progression and treatment response in different psychiatric and neurodegenerative disorders. In addition a NAT radiotracer would also be extremely valuable in imaging studies designed to evaluate drugs targeting NAT, such as drug occupancy studies, thereby aiding the drug discovery process. Therefore, a radiotracer specific for *in vivo* assessment of changes in NAT density, either in disease states or as a consequence of drug treatment, is desirable. It has been postulated that an ideal radiotracer for imaging of the NAT in brain should have (38, 40-41):

1. high binding affinity for the NAT and high selectivity versus other brain receptors;
2. moderate lipophilicity, usually lying in the log $P_{7.4}$ range of 1-3.5 for good initial brain entry and low non-specific binding;
3. high target to non-target ratio (≥ 1.5 in non-human primates) to provide a clear image of the NAT;
4. specific binding to the NAT reaching peak equilibrium during SPECT/PET measurement to allow quantification of NAT occupancy;
5. lack of radiolabelled metabolites in the brain (<5%);
6. small molecular weight (lower than 450);
7. high stability in plasma;
8. easy radiolabelling for imaging;
9. good initial brain uptake (>0.5% dose/organ) at 2 minutes after intravenous injection;
10. a binding profile that reflects the NAT biodistribution, illustrated by *ex vivo* autoradiography or *in vivo* imaging.

Multiple NAT-selective radiotracers have been developed over the years for *in vivo* and *in vitro* brain imaging, including: ^{11}C -desipramine (^{11}C -DMI) and its hydroxylated

derivate (*R*)- ^{11}C -OHDMI; ^{11}C -nisoxetine and its derivatives (^{125}I -INXT and ^{125}I -PYINXT); ^{11}C -thionisoxetine; ^{11}C -oxaprotiline; ^{11}C -lortalamine; ^{11}C -talopran; ^{11}C -talsupran; two ^{11}C -labelled analogues of mazindol; and ^{11}C -labelled, ^{18}F -labelled and ^{123}I -labelled analogues of reboxetine (38-41). However, all radiotracers developed to date are considered to be far from ideal as NAT brain imaging agents. The most common limitations of previously developed NAT radiotracers include high non-specific binding, slow kinetics, low brain uptake and poor *in vivo* selectivity.

The most promising PET radiotracers developed for *in vivo* imaging of the NAT are analogues of reboxetine (further details on the properties of reboxetine can be found in section 3.1.3) and include: (*S,S*)- ^{11}C -MeNER, (*S,S*)- ^{18}F -FMeNER-D₂ and (*S,S*)- ^{18}F -FRB-D₄ (108-109). Studies investigating (*S,S*)- ^{11}C -MeNER, an *O*-methyl derivate of reboxetine, showed a high hypothalamus-to-striatum uptake ratio of 2.5 at 60 minutes post-injection in rats (110). PET imaging with (*S,S*)- ^{11}C -MeNER in cynomolgus monkeys and baboons demonstrated a regional distribution consistent with known distribution of NATs and a thalamus-to-striatum uptake ratio of 1.4-1.6. However, the specific binding of (*S,S*)- ^{11}C -MeNER to the NAT did not reach peak equilibrium during a 90 minutes PET measurement, hampering successful quantification of the biodistribution of this radiotracer *in vivo*. In addition, the relatively noisy signal at later time points further restricted the utility of (*S,S*)- ^{11}C -MeNER for the quantitative assessment of NAT binding occupancy in the brain (41, 111). *O*-Fluoromethyl and *O*-Fluoroethyl analogues, (*S,S*)- ^{18}F -FMeNER-D₂ and (*S,S*)- ^{18}F -FRB-D₄, were subsequently synthesised to take advantage of the longer half-life of ^{18}F (the half life of ^{11}C and ^{18}F is 20 and 110 minutes, respectively). (*S,S*)- ^{18}F -FMeNER-D₂ was found to have a thalamus-to-striatum binding ratio of approximately 1.5 in PET imaging studies in cynomolgus monkeys and humans, which is comparable to the specific binding ratio of (*S,S*)- ^{11}C -MeNER (41, 111). Moreover, (*S,S*)- ^{18}F -FMeNER-D₂ had a lower signal noise level compared to (*S,S*)- ^{11}C -MeNER and the specific binding peak equilibrium was achieved at 15 minutes post-injection, within the duration of PET study imaging time frame. Nevertheless, *in vivo* defluorination was detected and high skull uptake, especially in the late phases of image acquisition, was observed even though there was a deuterium substitution on the fluoroalkyl side chain (41, 112). Drug displacement studies with (*S,S*)- ^{18}F -FMeNER-D₂ in non-human primates were performed to evaluate the dose-dependent occupancy of the NAT by atomoxetine, an SNRI used to treat mood disorder and ADHD. These studies showed that: (1) clinical doses of atomoxetine could occupy the NAT almost completely (113); and (2) (*S,S*)- ^{18}F -FMeNER-D₂ was able to measure a dose-dependent change in NAT occupancy in the brain. These results encouraged the use of (*S,S*)- ^{18}F -FMeNER-D₂ for human PET imaging, despite the high skull uptake observed (112).

Three NAT radiotracers for SPECT imaging have previously been developed: (*R*)-*N*-methyl-(2-[¹²⁵I]iodo-phenoxy)-3-phenylpropylamine (¹²⁵I-INXT); (*R*)-*N*-methyl-3-(3-[¹²⁵I]-pyridin-2-yloxy)-3-phenylpropan-1-amine (¹²⁵I-PYINXT); and (*S,S*)-2-[α -(2-ethoxyphenoxy)phenylmethyl]-morpholine (¹²³I-INER) (37-38, 40, 114-116). ¹²⁵I-INXT has a K_i value of 0.03 nM in rat frontal cortex membrane preparations, a K_D value of 0.06 ± 0.01 nM in membrane preparations of LLC-PK₁ cells overexpressing NAT and a B_{max} of 55 fmol/mg in rat frontal cortex membrane preparations. Despite a high *in vitro* affinity, ¹²⁵I-INXT exhibited slow kinetics and high non-specific binding *in vivo* in rats. Consequently, it was concluded that further development of NAT radiotracers for SPECT imaging was required.

In 2008, Lakshmi *et al.* developed a new series of derivatives of idonisooxetine. The most promising radioligand, ¹²⁵I-PYINXT, displayed a high and saturable binding to the NAT in LLC-PK₁ cells overexpressing NAT with a K_D value of 0.53 ± 0.03 nM. Biodistribution studies in rats showed a moderate initial whole brain uptake of 0.54% injected dose at 2 minutes post radiotracer administration. The hypothalamus-to-striatum ratio was found to be 2.14 at 4 hours post-injection (40). Although better compared to ¹²⁵I-INXT, the *in vivo* kinetics of ¹²⁵I-PYINXT is still not ideal for SPECT imaging of NAT in brain, due to the persistent slow kinetics in rats, where a target to non-target ratio above 2 was only reached at the late time point of 4 hours post-injection. Recently, a novel reboxetine analogue ¹²³I-INER (also denoted (*S,S*)-IPBM) was radioiodinated (114-116). ¹²³I-INER has a high affinity and selectivity for the NAT in rat forebrain, with a K_i value of 0.84 ± 0.12 nM and a selectivity for NAT versus DAT of 270 and for NAT versus SERT of 51 (114). In rat biodistribution studies, ¹²³I-INER displayed good initial brain uptake with maximum accumulation in the rat brain at 30 minutes after injection (0.54% injected dose/g). The washout in rat brain was gradual and a high midbrain-to-striatum ratio was observed at 180 minutes post-injection (116). In baboons, the maximum brain uptake (1.0% injected dose) was observed 10 minutes post-injection. A slow washout in baboon brain, over more than 2 hours, was observed. Despite the longer physical half-life of ¹²³I being compatible with slower kinetics, the washout of ¹²³I-INER over 2 hours *in vivo* in baboons suggested improvement of NAT radiotracers for SPECT was needed (40, 114).

3.1.3 Design and synthesis of novel iodoreboxetine analogues for imaging of NAT in brain

Due to the important role that the NAT plays in the control of brain function (section 3.1.1) and the limitations of the previously developed SPECT radiotracers (section 3.1.2), the radiotracer development group in Glasgow set out to develop a novel NAT

radiotracer for SPECT brain imaging based on the antidepressant drug, reboxetine. The antidepressant compound 2-[α -(2-ethoxyphenoxy)benzyl]morpholine or reboxetine is a SNRI that acts by binding to the NAT and blocking reuptake of noradrenaline back to the terminals. Table 3.1 compares the different binding affinities of four antidepressant drugs: reboxetine, nisoxetine, desipramine and mazindol. These drugs have been or are currently being investigated as parent structures for the design and development of novel radiotracers for PET or SPECT. Examples of radiotracers developed, based on these drugs structures were outlined in section 3.1.2. Reboxetine has the highest affinity for the NAT compared to nisoxetine, desipramine and mazindol. In addition, reboxetine's low affinity for other brain receptors and transporters (Table 3.2) demonstrates its high selectivity for the NAT (104, 117-118). As a consequence of its high selectivity and high affinity for the NAT (117), reboxetine was chosen as a potential target for radiolabelling. Other favourable pharmacodynamic properties of reboxetine include: a half life in humans around 13 hours; full excretion after 96 hours; 10-15% excretion by faeces; 10% clearance by renal excretion; a primary route of elimination via hepatic metabolism, mostly by cytochrome P450 3A4 (118).

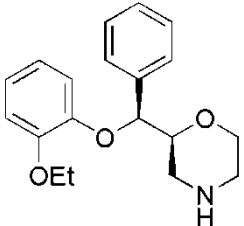
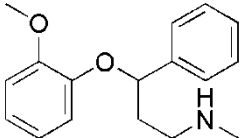
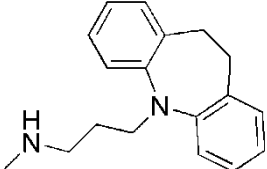
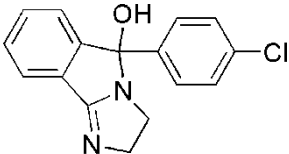
Compound	Chemical structure	NAT K_i (nM)
Reboxetine		1.1±0.2 (5)
Nisoxetine		1.5±0.1 (3)
Desipramine		1.6±0.2 (3)
Mazindol		1.4±0.1 (3)

Table 3.1 Binding affinity (K_i) of four antidepressant drugs for NAT reuptake sites in rat frontal cortical membranes.

Adapted from (117) and (119). Values are mean±SEM (number of separate determinations).

<i>Receptor</i>	<i>K_i (μM)</i>	<i>Receptor</i>	<i>K_i (μM)</i>	<i>Receptor</i>	<i>K_i (μM)</i>
α ₁ adrenergic	10±2	H ₁ histamine	1.4±0.2	m1	2.6±0.2
α ₂ adrenergic	43±3	Muscarinic	3.9±0.2	m2	2.8±0.5
β ₁ adrenergic	10300	5-HT _{1A}	18±3	m3	2.8±0.1
D ₂ dopamine	9±5	5-HT _{2A}	7.3±0.4	m4	4.2±0.8
D ₃ dopamine	20±2	5-HT _{2C}	1.5±0.5	m5	2.0±0.6
D ₄ dopamine	>49				

Table 3.2 Affinity (K_i) of reboxetine for other brain receptors and transporters in rat whole brain homogenates.

Adapted from (118). Values are mean±SEM of at least three separate determinations.

Reboxetine is marketed as an antidepressant drug in a racemic mixture of (2*R*,3*R*)- and (2*S*,3*S*)-enantiomers, but it is (2*S*,3*S*)-reboxetine (Figure 3.2) that has the highest affinity and selectivity for the NAT (45). However, little was known about the potency of the other stereoisomers of reboxetine. In 2006, the radiotracer development group in Glasgow set out to synthesise and evaluate all four stereoisomers of an iodinated analogue of reboxetine, in order to gain insight into the structure-activity relationship with the NAT (44-45). Competition binding assays using rat whole brain homogenates showed for the first time that the (2*R*,3*S*)-iodoreboxetine stereoisomer (Table 3.3 and Figure 3.2) was as potent as the (2*S*,3*S*)-stereoisomer. In 2007, Tamagnan and co-workers published data on a range of iodinated analogues of (2*S*,3*S*)-reboxetine, one of which was INER (Figure 3.2), with high affinity for the NAT but some limitations as a SPECT imaging agent (as outlined in section 3.1.2) (114, 116). Together these findings prompted the radiotracer development group in Glasgow to prepare NKJ64 (Figure 3.2), a (2*R*,3*S*)-isomer of INER. NKJ64 was found to have low nanomolar affinity for the NAT against ³H-nisoxetine in rat whole brain (Table 3.3) (43). NKJ64 was also shown to have good selectivity for the NAT; affinities for SERT or DAT binding sites were 5 and 50 times lower than for the NAT, respectively (Table 3.3)(43). Therefore, NKJ64 was chosen as lead candidate for future radiolabelling and biological evaluation and the results are presented in this thesis. It should be noted that the lead candidate, NKJ64, was selected prior to development of the HPLC tool previously described in chapter 2. Results from applying the HPLC developed tool to investigate NKJ64 physicochemical properties (Appendix 1) were obtained at later stages of NKJ64 biological evaluation and not during the radiotracer discovery stage, due to the chronological order that the experiments were performed (detail in thesis outline section 1.5).

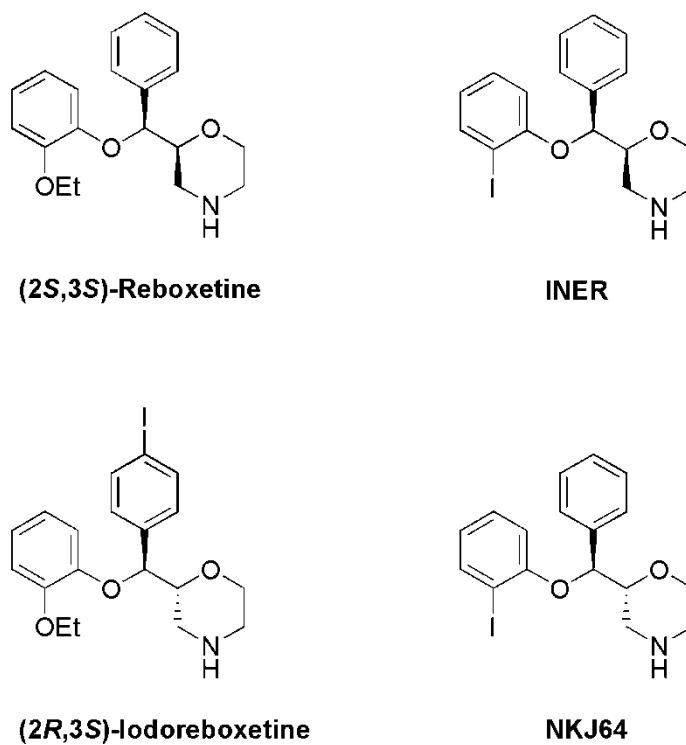


Figure 3.2 Chemical structures of reboxetine and iodinated analogues for *in vivo* imaging of NAT.

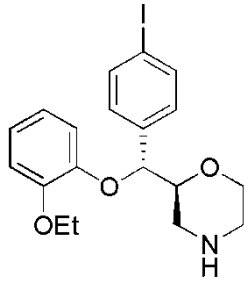
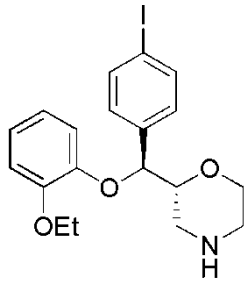
Compound	K_i for NAT (nM)	K_i for SERT (nM)	K_i for DAT (nM)
 (2S,3R)-Iodorexetine	320.8±9.0	---	---
 (2R,3S)-Iodorexetine	58.2±9.4	---	---

Table 3.3 Affinity (K_i) of iodorexetine analogues for NAT, SERT and DAT in rat whole brain homogenates.

Adapted from (44) and (43). Results reported as mean±SEM (n=3, except for NKJ64 where n=5).

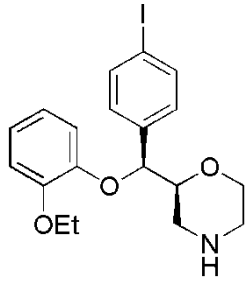
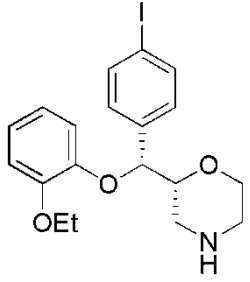
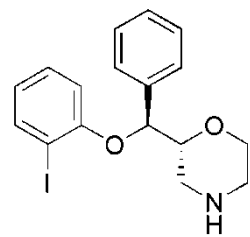
Compound	K_i for NAT (nM)	K_i for SERT (nM)	K_i for DAT (nM)
 (2S,3S)-Iodorexetine	53.8±2.7	2793±480	1457.8±150
 (2R,3R)-Iodorexetine	64.0±2.4	646±142	176±20
 NKJ64	8.4±1.7	51.5±8.4	525.9±125.5

Table 3.3 (cont).

3.1.4 Introduction to radiosynthesis of novel radiotracers

The radiosynthesis of novel radiotracers for SPECT imaging needs to result in the final radiolabelled product having a high specific activity, typically of the order of Ci/ μ mol or GBq/ μ mol. A high radiochemical yield and high radiochemical purity of the final product are also necessary (32, 120-121). High specific activity is an essential characteristic for a radiotracer to be used for *in vivo* imaging in humans and animals, as the presence of large amounts of cold ligand in low specific activity radiotracer formulations can potentially result in a pharmacological mass effect, contradicting the principle of radiotracer imaging (31-32, 121). Furthermore, the radiochemical yield from the radiosynthesis of a radiotracer should be as high as possible to minimise the cost associated with radioisotope production and to keep operator radiation exposure as low

as possible (32). Since both high specific activity and radiochemical yield are important characteristics in radiotracer production and use, Section 3.1.5 outlines different labelling strategies that could be used to obtain novel radioiodinated tracers with high specific activity and high radiochemical yield. High radiochemical purity is also desirable, in order to ensure that the image obtained *in vivo* reflects the interaction of the radiotracer with the target site, and not any impurities. In addition, high radiochemical purity is important in terms of dosimetry, as non-desirable radioactive species may bind to other structures, increasing unnecessarily the radiation exposure to non-target regions. For example, free radioiodine can bind to non-target tissues, such as the thyroid and stomach, increasing the radiation exposure of these organs. Different methodologies for the purification of novel radiotracers, in order to obtain the final radiolabelled product with high radiochemical purity, are outlined in section 3.1.6.

3.1.5 Nucleophilic and electrophilic radiolabelling techniques

The aliphatic carbon-iodine bond is relatively weak (222 kJ/mol), which results (especially *in vivo*), in a fast deiodination either by nucleophilic substitution (S_N2) or β -elimination. Thus, when a radioiodine atom has to be incorporated in a radiotracer, it is preferentially designed to be located on a sp^2 carbon atom in a vinylic or aromatic moiety, since the carbon-iodine bond strength is higher (268 and 297 kJ/mol, respectively) than the aliphatic carbon-iodine bond. The first decision to be made when designing the radiolabelling methodology for a radiotracer is whether a nucleophilic or electrophilic approach should be used (120).

In nucleophilic substitution reactions, the attacking reagent (an iodide anion) brings an electron pair to the substrate to form a new bond and the leaving group is eliminated with an electron pair. There are several mechanisms possible depending on the substrate (aliphatic or aromatic), the leaving group and the reaction conditions (for example, solvent and temperature) (32). The method of choice in nucleophilic radioiodination is typically the well-established Cu(I)-catalysed halogen-halogen exchange reaction in an acidic and aqueous medium. The versatility of this nucleophilic Cu(I) method is demonstrated by the possibility of non-isotopic exchange ($^*I/Br$), which enables the synthesis of radiotracers with the high specific activity essential for brain receptor imaging. In general, nucleophilic exchange can be successfully applied on activated (electron-deficient substituent, e.g. carbonyl group) or non-activated (e.g. alkyl group) aromatic compounds. During iododebromination, it is important that the compound structure does not contain any other moieties that are functionally susceptible to iodination or reaction with the added reducing agents, as this could

reduce the radiolabelling yield or inhibit the reaction completely. For example, the presence of a thiourea group, which complexes copper (I,II)-species, inhibits the radiolabelling with radioiodide completely (120). Some other relevant experimental parameters involved in the Cu(I)-catalysed halogen-halogen exchange reaction are the Cu^{1+} -concentration and the amount of substrate/precursor. Higher yields are obtained with higher amounts of precursor and the optimal precursor to Cu^{1+} ratio is at least 5-10, for precursor in μmol amounts. Frequently, the amount of precursor is determined or limited by the required specific activity of the radiotracer being synthesised. Carrier-free preparations necessitate non-isotopic exchange and the amount of precursor should be as small as possible in order to minimise the risk of breakthrough during the radiolabelling process. When using isotopic exchange reactions, a relatively high specific activity can be achieved by lowering the amount of precursor, although low radiolabelling yields are associated with lowering the amount of precursor (120).

Electrophilic radioiodination is a process in which positively charged iodine (I^+) attacks a system with high electron density such as an aromatic ring or an alkane. As a result a covalent carbon-iodine bond is formed with loss of a positively charged leaving group (32). Within electrophilic reactions, radioiododestannylation has increasingly become the method of choice. The weakness of the carbon-tin bond readily gives site-specific radioiodination, even at room temperature, while the precursor can be made from the bromo- or iodoaryl compound. Oxidising agents that are most commonly used include peracetic acid and the *N*-chloro-compounds, such as chloramine-T, iodogen and succinimides. Since the *N*-chloro compounds have relatively strong oxidising properties they often induce the formation of by-products and therefore it may be necessary to limit these oxidative side reactions. This can be achieved using various methods including immobilisation of chloramine-T on spherical polystyrene particles (iodobeads[®]) or by coating a thin layer of iodogen on the walls of a reaction vessel. Peracetic acid is often preferred for the radiolabelling of small organic molecules due to its mild oxidising properties (31, 120).

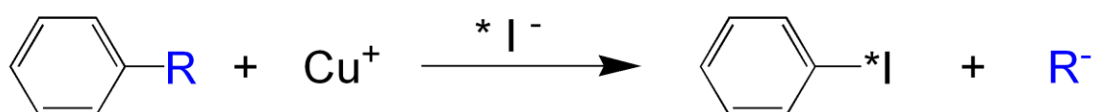
In summary, the R-group(s) present on the aromatic ring that is to be radiolabelled is key in determining the radiolabelling methodology used for production of a radiotracer. The R-group(s) can either activate towards nucleophilic or electrophilic substitution (Figure 3.3).

Electrophilic radioiodination



where R=H, SnMe₃, SiMe₃...

Nucleophilic radioiodination



where R=I, Br...

Figure 3.3 Schematic of electrophilic and nucleophilic radioiodination methods.

For both nucleophilic and electrophilic substitution the stability of the precursor needs to be verified. For example, nucleophilic substitution requires frequently higher reaction temperatures (100–180 °C) and longer reaction times (20–60 minutes), which may not be tolerated by a precursor. In contrast, electrophilic substitution exposes a precursor to an oxidising agent, but more favourably, requires short reaction times (5–20 minutes) often at room temperature. In addition, for highly lipophilic precursors, nucleophilic substitutions tend to require higher amounts of precursor to assure a good labelling yield and the separation step when using isotopic exchange can be problematic. Conversely, electrophilic substitution only requires small amounts of precursor (µg-scale) and offers more versatility in terms of solvent choice. A summary of the main radiolabelling routes discussed is provided in Table 3.4 (32, 120).

	<i>Electrophilic radioiodination</i>	<i>Nucleophilic isotopic exchange</i>	<i>Nucleophilic non-isotopic exchange</i>
Type of precursor (substitution on aromatic)	Electron-rich substituent, and/or modification of precursor: -SnMe ₃ , -SnBu ₄ , -SiMe ₃	Electron-deficient substituent, Cu ¹⁺ catalysis preferable	Electron-deficient substituent, mostly Cu ¹⁺ catalysis
Specific activity	Non-carrier added (NCA) or carrier-added	Low/moderate due to presence of carrier	High/NCA (traces of precursor might act as pseudo-carrier)
Reaction times	5–20 min	20–60 min	20–60 min
Reaction conditions	<ul style="list-style-type: none"> • Mostly room temperature • Presence of an oxidising agent <ul style="list-style-type: none"> • Amount of precursor: µg-scale • Labelling yield less proportional with amount of precursor 	<ul style="list-style-type: none"> • Elevated temperature (100–180 °C) • Presence of a reducing agent (Cu¹⁺-catalysis) <ul style="list-style-type: none"> • Amount of precursor: mg-scale • Labelling yield proportional with amount of precursor 	<ul style="list-style-type: none"> • Elevated temperature (100–180 °C) • Presence of a reducing agent (Cu¹⁺-catalysis) <ul style="list-style-type: none"> • Amount of precursor: mg-scale • Labelling yield proportional with amount of precursor
Purification step	Facile purification	Often little, or no purification required	Sometimes difficult to purify

Table 3.4 Summary of the main radioiodination methods.

3.1.6 Separation and purification of radiotracers

Purification of radiotracers is frequently successfully accomplished by HPLC (122-126). Alternatively, radiotracer purification can be achieved using solid phase extraction (SPE) (38, 40, 127). One advantage of preparative HPLC over SPE relates to the ability of HPLC purification to provide both radiodetection and UV analysis of all the constituents within the reaction. Furthermore, it is a robust and versatile technique, which is able to efficiently separate a wide range of compounds with high resolution.

Conversely, SPE is a more rapid and less expensive method, which can shorten the overall radiosynthesis and formulation time. This is of particular interest when working with short-life radionuclides, such as ^{11}C for PET imaging (128). Figure 3.4 presents a schematic representation of each purification method, HPLC and SPE.

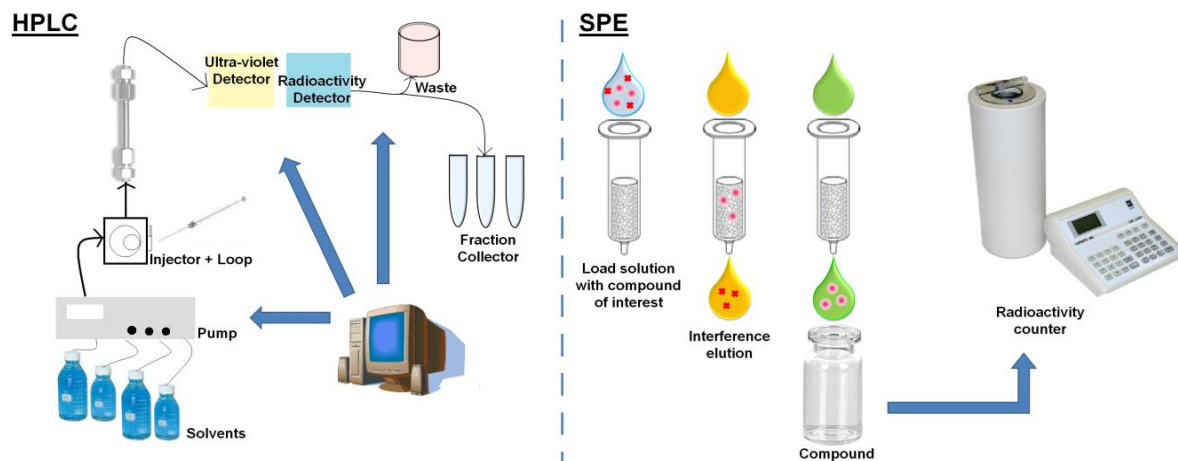


Figure 3.4 Schematic representations of HPLC and SPE purification methods.

3.1.7 Hypothesis and aims

It was hypothesised that NKJ64 could be radiolabelled by iododestannylation in order to produce $^{123/125}\text{I}$ -NKJ64. This chapter aims to develop the radiolabelling methodology for the production of high-specific activity $^{123/125}\text{I}$ -NKJ64 for subsequent biological evaluation in rats. Iododestannylation of the corresponding trimethylstannyl precursor was investigated, *via* a two-step reaction, using peracetic acid as an oxidising agent. Two different agents (HCl and TFA) were investigated for the deprotection step and purification was investigated using HPLC.

3.2 Material and Methods

3.2.1 General

All chemicals, unless otherwise stated, were obtained from Sigma Aldrich, UK. Sterile water and sodium chloride (0.9% NaCl) were obtained from Braun Medical, UK and Baxter, UK, respectively. Organic HPLC solvents were obtained from Rathburn Chemicals, UK and ethanol from Fisher Scientific, UK. Sodium hydroxide (NaOH) was purchased from VWR, UK. Na^{125}I was obtained from Perkin Elmer, USA and Na^{123}I from GE Healthcare, UK. The SnMe_3 -precursor of NKJ64, cold NKJ64 and cold BOC-intermediate,

used for testing the identity of the final product and for radiolabelling reactions, were produced by colleagues in the School of Chemistry at the University of Glasgow.

3.2.2 Analytical HPLC system

A Dionex Ultimate 3000 series HPLC (Dionex, UK) was used and data acquisition and processing was carried out using Chromeleon 6.8 chromatography software (Dionex, UK). All analytical HPLC was performed on a Phenomenex 4 μm Synergi Hydro RP80A (150 \times 4.6 mm + 10 mm guard cartridge) column eluted with a 0.1% trifluoroacetic acid (TFA) in methanol and 0.1% TFA in water gradient described in Figure 3.5. UV detection was carried out at 220 nm and radiodetection was carried out using a Berthold FlowStar LB513 series radiodetector. The identity of the radioiodinated I-NKJ64 ($t_r=6$ minutes) was confirmed by co-injection of the cold I-NKJ64.

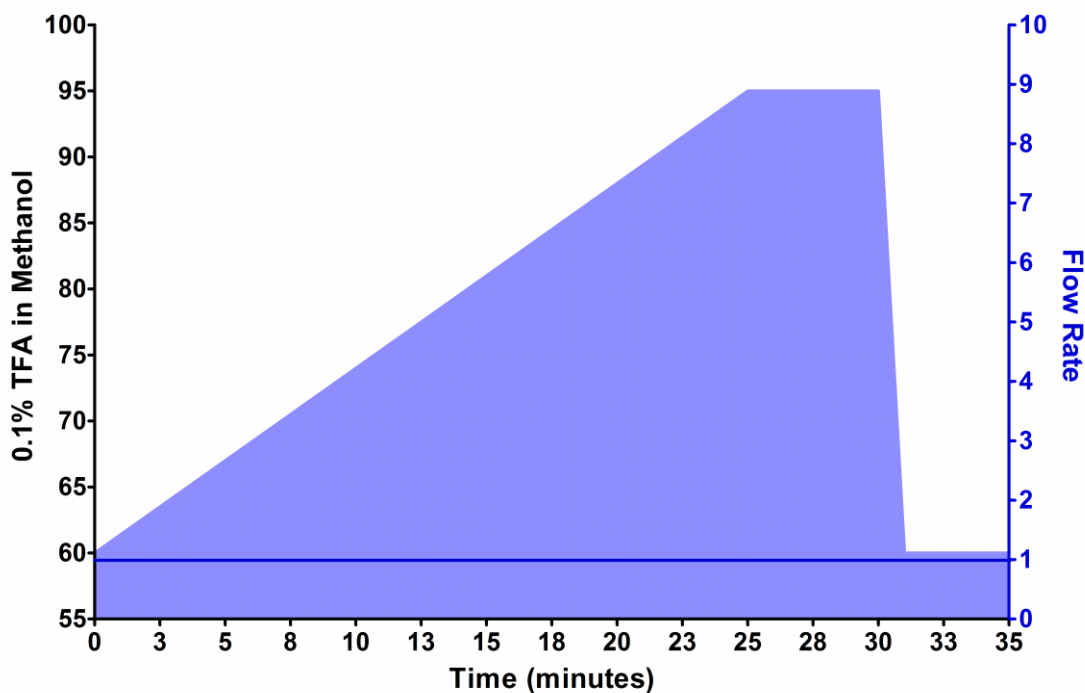


Figure 3.5 Analytical HPLC system used for radiosynthesis of NKJ64.

3.2.3 Radiolabelling

Radiolabelling of NKJ64 was investigated *via* electrophilic iododestannylation of the corresponding organotin precursor (SnMe_3 -precursor). To a vial containing 20-74 MBq of $\text{Na}^{123/125}\text{I}$ in 50 μl of 0.05 M NaOH was added 50 μl of 0.5 M phosphoric acid, 50 μg of SnMe_3 -precursor in 100 μl of ethanol and 10% v/v peracetic acid (PAA), (Figure 3.6 A). The reaction was mixed *via* vortex and incubated at room temperature for 5 minutes.

Removal of the BOC protecting group on the radiolabelled BOC-intermediate was investigated by adding either 50 μ l of 2 M HCl or TFA, (Figure 3.6 B), followed by incubation at either room temperature or heating at 60 °C for different time intervals. The reaction mixture was then analysed by using the analytical HPLC (outlined in section 3.2.2) and/or purified by semi-preparative HPLC (outlined in section 3.2.4) to determine the incorporation radiochemical yield and/or the isolated radiochemical yield and specific activity, respectively.

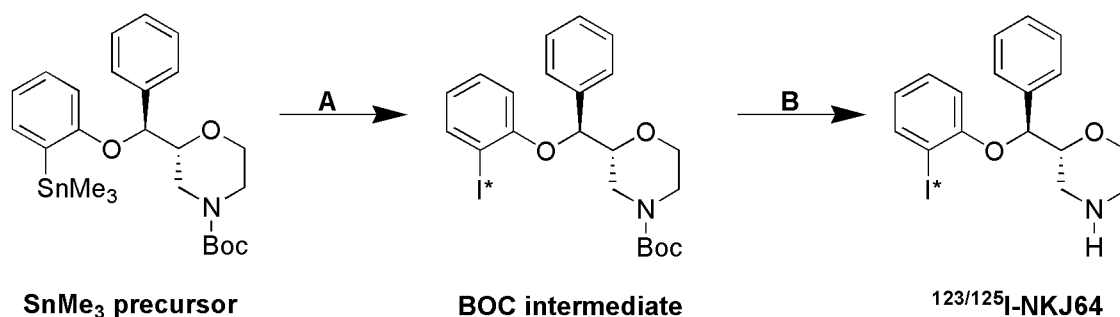


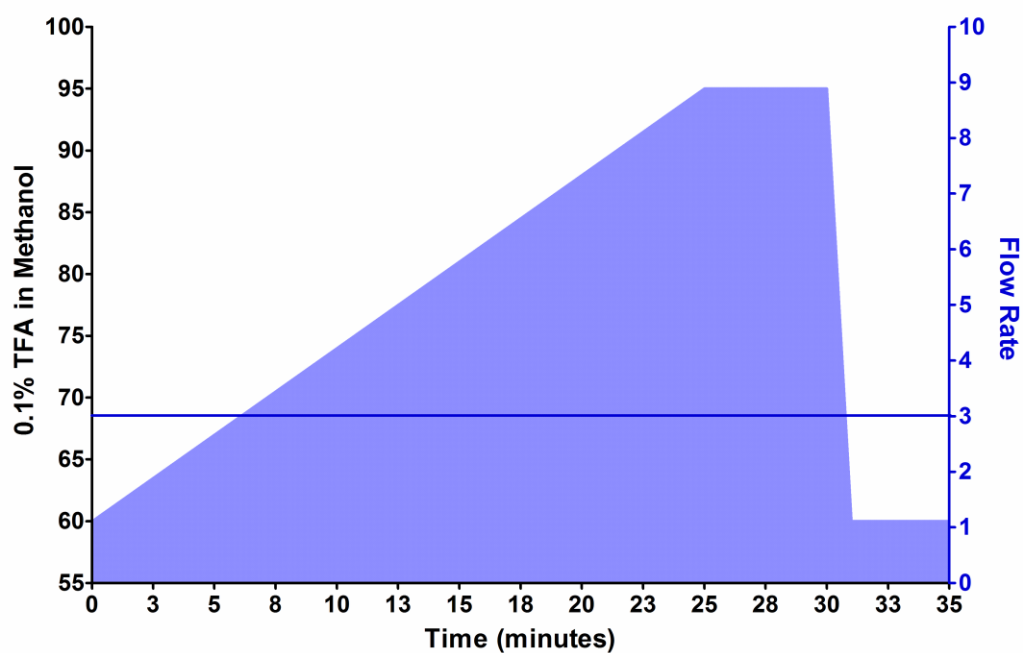
Figure 3.6 Radiolabelling of $^{123/125}\text{I}$ -NKJ64 from the corresponding organotin precursor via a two step reaction.

a. Na^{123}I or Na^{125}I , PAA, EtOH. b. 2 M HCl or TFA.

3.2.4 Purification and specific activity determination

A Dionex Ultimate 3000 series HPLC (Dionex, UK) was used and data acquisition and processing was carried out using Chromeleon 6.8 chromatography software (Dionex, UK). Radiolabelled $^{123/125}\text{I}$ -NKJ64 was purified by injection of the total reaction mixture onto a Phenomenex 4 μm Synergi Hydro-RP80A (150 \times 10 mm + 10 mm guard cartridge) column. Two HPLC semi-preparative methodologies were investigated using either 0.1% TFA in methanol and 0.1% TFA in water or 0.1% TFA in acetonitrile and 0.1% TFA in water as the mobile phase. Method A used a mobile phase of 0.1% TFA in methanol and 0.1% TFA in water and the gradient described in Figure 3.7A (NKJ64; $t_r=6$ minutes). Method B used a mobile phase of 0.1% TFA in acetonitrile and 0.1% TFA in water and gradient described in Figure 3.7B (NKJ64; $t_r=25$ minutes). UV detection was carried out at 220 nm and radiodetection was carried out using a BioScan Flow Count radiodetector. The fraction containing $^{123/125}\text{I}$ -NKJ64 was collected, and the solvent was removed by rotatory evaporation. Reconstitution of the purified $^{123/125}\text{I}$ -NKJ64 was performed using 0.9% saline solution. The radiochemical purity of the final product was measured using analytical HPLC (outlined in section 3.2.2).

(a)



(b)

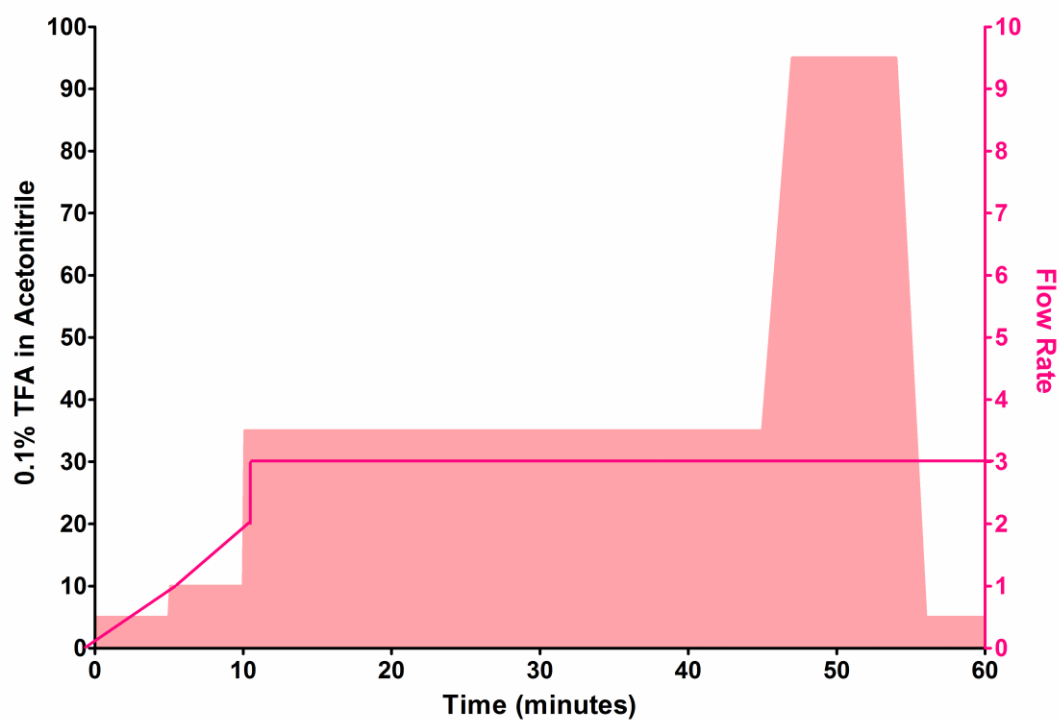


Figure 3.7 Semi-preparative HPLC systems used for radiosynthesis of $^{123/125}\text{I-NKJ64}$.
(a) Semi-preparative methodology A and (b) semi-preparative methodology B.

The specific activity of the final product was calculated using a concentration-response curve obtained from a range of concentrations of NKJ64. A concentration-response curve (Figure 3.8) was generated on both semi-preparative HPLC systems (methods A and B, outlined in section 3.2.4) and by injection of 10 μl of cold NKJ64 diluted in ethanol in different concentrations: 1 mg/mL, 0.5 mg/mL, 0.25 mg/mL, 0.1 mg/mL, 0.05 mg/mL, 0.01 mg/mL and 0.005 mg/mL. The UV response for each concentration was plotted against the amount of NKJ64 in moles. The equation of the concentration-response curve was used to convert the UV response co-eluting with $^{123/125}\text{I}$ -NKJ64 into moles. The amount of radioactivity corresponding to $^{123/125}\text{I}$ -NKJ64 was calculated using integration of the radioisotope trace peaks and the injected activity, assuming no loss of radioactivity on the HPLC semi-preparative system. The specific activity was determined as the amount of radioactivity per mol ($\text{Ci}/\mu\text{mol}$).

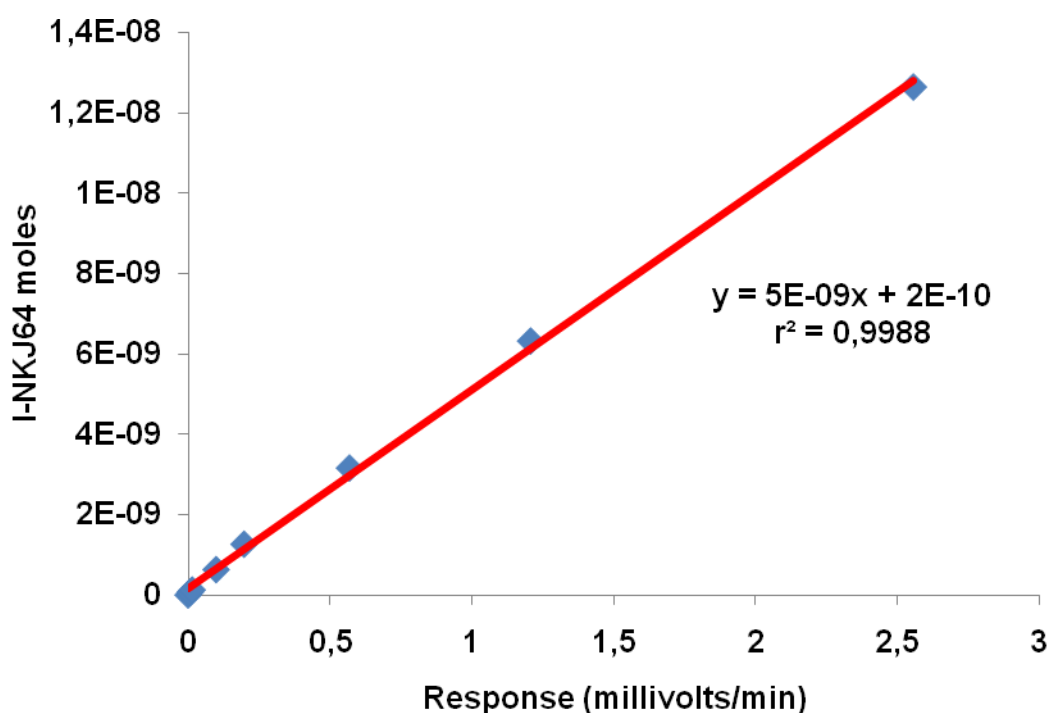


Figure 3.8 Representative amount /response curve for I-NKJ64 (method B).
X=UV response (millivolts/min) and Y=amount of I-NKJ64 in moles.

3.2.5 Labelling using Na^{127}I and mass spectrometry analysis

Analysis of the product obtained during the synthesis of NKJ64 using cold Na^{127}I was performed. The synthesis was performed using a slight modification of the protocols outlined above in section 3.2.3. Briefly, to a vial containing 1.26 ng of Na^{127}I in 50 μl 0.05 M NaOH was added 50 μl of 0.5 M phosphoric acid, 50 μg of SnMe_3 -precursor in 100 μl of ethanol and 10% v/v PAA. The reaction was mixed *via* vortex and incubated at

room temperature for 5 minutes. The Boc protecting group was then removed by adding 50 μl of 2 M HCl, followed by heating at 60 °C for 45 minutes. The reaction mixture was purified using semi-preparative HPLC (Method B). The peaks were collected, the solvent was removed by rotatory evaporation and reconstitution of the purified sample was performed using ethanol. The peak of interest was then analysed by chemical ionisation (CI) mass spectrometry (MS).

3.2.6 Stability testing

Samples of the purified and reconstituted ^{123}I -NKJ64 and ^{125}I -NKJ64 were stored at 4 °C and radiochemical purity was determined using analytical HPLC (outlined in section 3.2.2) over a 24 h and 8 days period, respectively.

3.3 Results

A typical HPLC trace obtained following co-injection of NKJ64 precursor, cold NKJ64 and Boc-intermediate onto the analytical HPLC is shown in Figure 3.9. The retention times of the cold compounds were used to identify the radiolabelled products after radiosynthesis steps a and b (Figure 3.6). Identity of the final radiolabelled product was confirmed by co-elution with cold NKJ64.

Radioiodination of the SnMe_3 -precursor to obtain the Boc-intermediate (step a, Figure 3.6) was achieved with an incorporation radiochemical yield of $91.2 \pm 6.0\%$ (mean \pm SD, $n=17$). The results from the deprotection reactions investigated using analytical HPLC are summarised in Table 3.5. No deprotection of the radiolabelled Boc-intermediate occurred at room temperature. Maximum radiochemical yields of ^{123}I -NKJ64 were obtained after 45 minutes incubation at 60 °C for both evaluated deprotecting agents (TFA and 2 M HCl). ^{123}I -NKJ64 was obtained with the highest radiochemical yield when 2 M HCl was used as deprotecting agent. However, semi-preparative HPLC (method A) revealed that the specific activity of $^{123/125}\text{I}$ -NKJ64 was lower when 2 M HCl was used as deprotecting agent (Table 3.6).

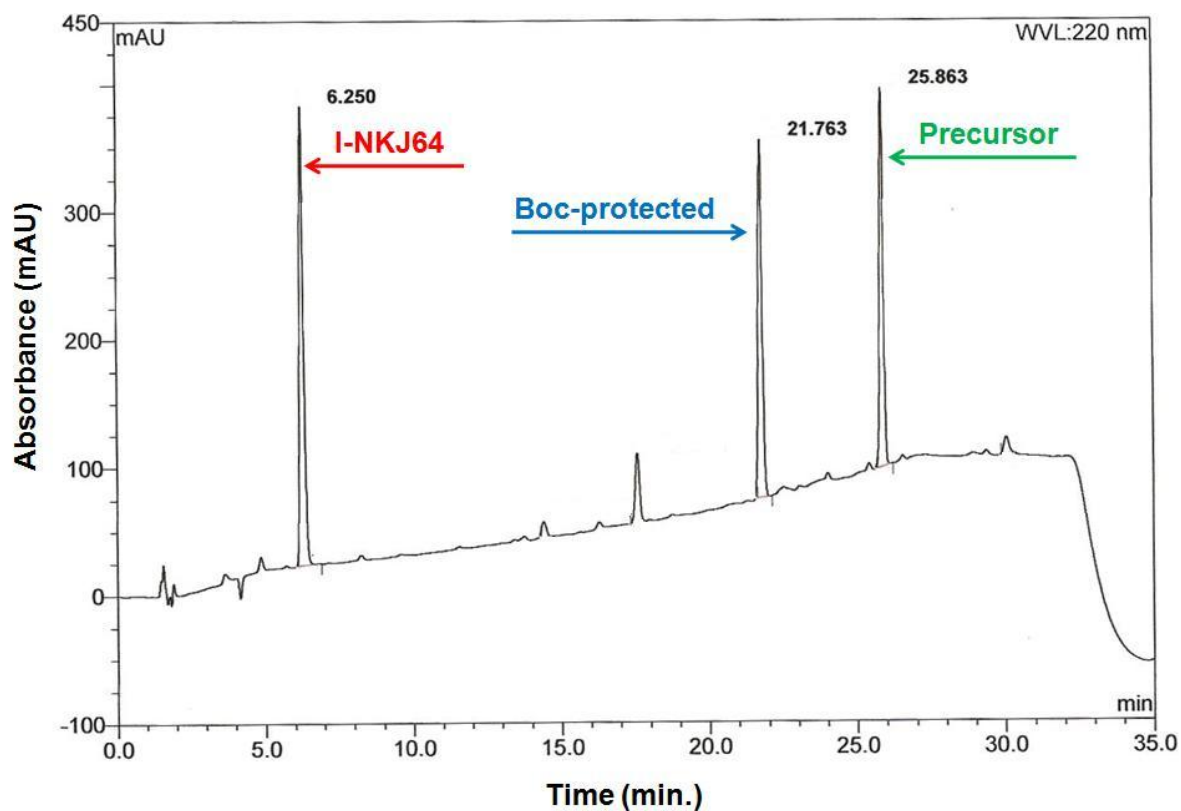


Figure 3.9 A typical analytical HPLC trace following co-injection of NKJ64 precursor, BOC-intermediate standard and I-NKJ64 standard.

I-NKJ64 t_r =6.250 minutes, Boc-protected standard t_r =21.763 minutes and SnMe_3 precursor t_r =25.863 minutes.

<i>Deprotecting Agent</i>	<i>Incubation Method</i>	<i>Radiochemical Yield (%)</i>
TFA	25 minutes at RT	0.00
	5 minutes at 60 °C	38.54
	15 minutes at 60 °C	71.80
	45 minutes at 60 °C	81.94
	60 minutes at 60 °C	80.05
2 M HCl	5 minutes at 60 °C	32.39
	15 minutes at 60 °C	58.47
	30 minutes at 60 °C	97.45
	45 minutes at 60 °C	99.01
	60 minutes at 60 °C	99.02

Table 3.5 Summary of analytical HPLC results showing the yield of ^{123}I -NKJ64 from the small scale reactions investigated.

Starting radioactivity 20-25 MBq, $n=1$.

<i>Method of deprotection</i>	<i>Radiochemical yield (%)</i>	<i>Isolated radiochemical yield (%)</i>	<i>Radiochemical purity (%)</i>	<i>Retention time (min)</i>	<i>Specific activity (Ci/μmol)</i>
¹²³I-NKJ64					
Using TFA	83.95±13.24 (n=8)	68.40±13.50 (n=8)	>99	25	1.76±0.60 (n=8)
Using 2 M HCl	98.05±1.63 (n=9)	80.52±13.74 (n=9)	>99	6	0.15±0.23 (n=9)
¹²⁵I-NKJ64					
Using TFA	93.92 (n=1)	75.00 (n=1)	>99	25	0.73 (n=1)
Using 2 M HCl	99.44±1.25 (n=5)	73.45±18.08 (n=5)	>99	6	0.15±0.04 (n=5)

Table 3.6 Summary of radiolabelling reactions for the preparation of ^{123/125}I-NKJ64.
Starting radioactivity 74 MBq, reaction temperature of 60 °C and reaction duration of 45 minutes, semi-preparative HPLC method A.

Further analysis of the semi-preparative UV trace, showed that when using 2 M HCl as the deprotecting agent and HPLC semi-preparative method A, a single absorbance peak co-eluted with the ^{123}I -NKJ64 radioactive peak (Figure 3.10a). However, the UV trace obtained after purification of a radiolabelling reaction using the same conditions (2 M HCl as a deprotecting agent) and HPLC semi-preparative method B showed two peaks (albeit not fully separated, t_r peak A = 24.93 minutes and t_r peak B = 25.34 minutes), both of which co-elute with the ^{123}I -NKJ64 radioactive peak, (Figure 3.10b). The comparison between semi-preparative HPLC traces (method B) obtained when using TFA and 2 M HCl as deprotecting agents is shown in Figure 3.10c. The traces show the absence of the larger by-product (peak A) when using TFA, where the minor peak B eluted at 25 minutes. In order to determine the identity of the co-eluting peak A, MS analysis of purified by-product (Peak A) obtained from a cold synthesis with Na^{127}I was performed. MS of the purified by-product (Peak A) revealed that the collected sample contained the deprotected protodestannylated precursor (Figure 3.11); m/z (CI) 270 (MH^+ , 6%), 256 (29), 228 (29), 191 (5), 149 (7), 113 (6), 71 (14).

The reconstituted ^{123}I -NKJ64 in 0.9% saline had a radiochemical purity of >99% after 24 h of storage at 4 °C. ^{125}I -NKJ64 in 0.9% saline was stable up to 8 days at 4 °C (radiochemical purity > 99%) (Figure 3.12).

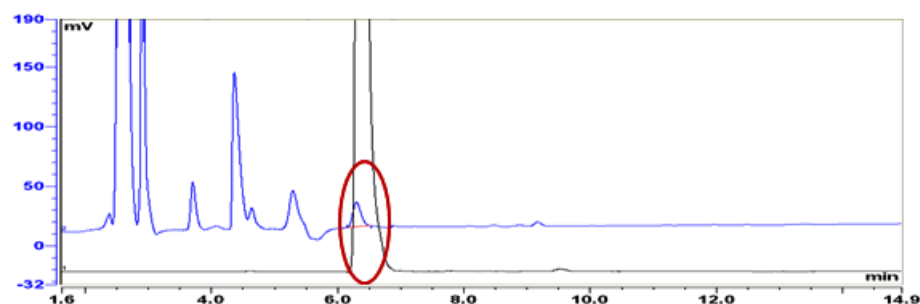
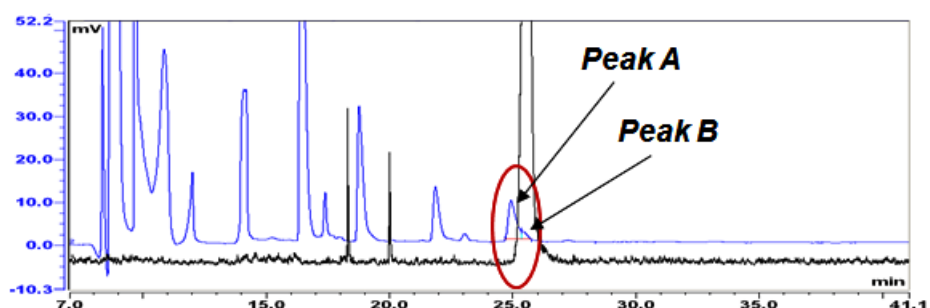
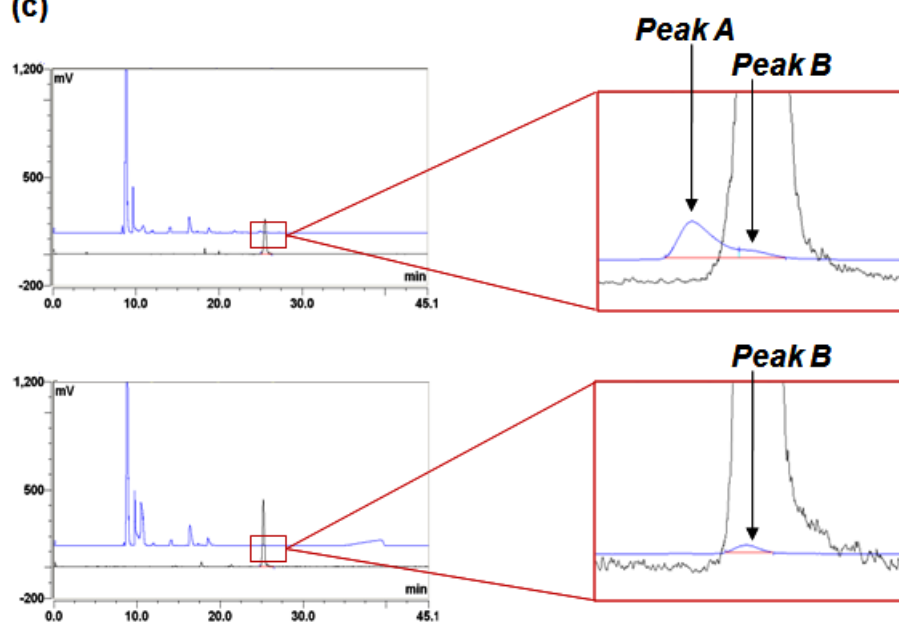
(a) 2 M HCl – Method A**(b) 2 M HCl – Method B****(c)**

Figure 3.10 Representative semi-preparative HPLC UV trace and radiotracer from a radiosynthesis of ^{123}I -NKJ64.

The final product elution is highlighted by red box. (a) deprotection with 2 M HCl and HPLC semi-preparative method A; (b) deprotection with 2 M HCl and HPLC semi-preparative method B; (c) comparison between deprotection with 2 M HCl and TFA, using HPLC semi-preparative method B. Blue line=UV trace and black line=radiotracer.

Note that by using semi-preparative HPLC method A, one single UV peak co-eluted with ^{123}I -NKJ64 ($t_r = 6.0$ minutes), when using 2 M HCl for the deprotection step (a). However, by using semi-preparative HPLC method B it was possible to dissect the single UV peak (HPLC method A (a)), into two peaks (peak A, $t_r = 24.93$ minutes and peak B, $t_r = 25.34$ minutes) which co-eluted with ^{123}I -NKJ64 (b and c). Note the absence of the larger peak A when TFA was used as the deprotecting agent (c).

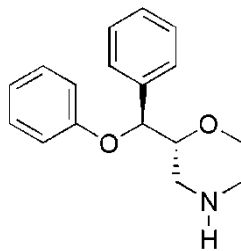


Figure 3.11 Deprotected protodestannylated precursor.

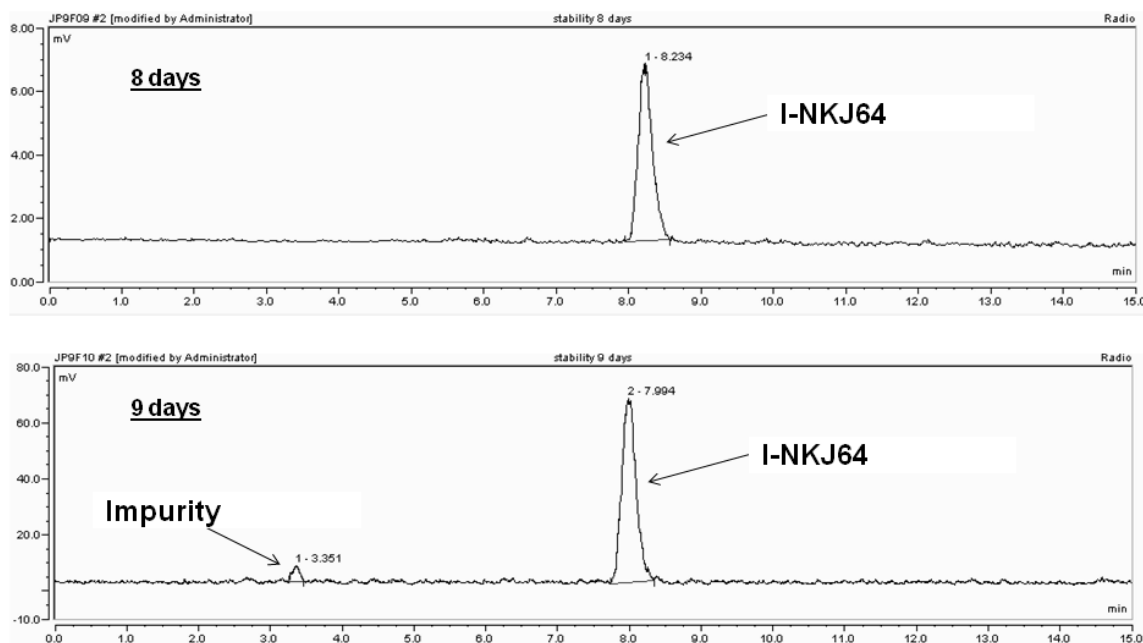


Figure 3.12 Representative analytical HPLC trace of ^{125}I -NKJ64 stability tests. Note stability of the formulation up to 8 days post radiosynthesis.

3.4 Discussion

The radiosynthesis of ^{123}I -NKJ64 was investigated *via* electrophilic iododestannylation of the corresponding organotin precursor. The radioiodination step (step a, Figure 3.6) was successfully accomplished using PAA as an oxidant (91.2±6.0% radiochemical incorporation yield). Two different agents, TFA and 2 M HCl were evaluated for the removal of the Boc-protecting group (step b, Figure 3.6).

Novel radiosynthesis methodologies are commonly evaluated by carrying out small-scale radiosynthesis and sampling the different reaction mixtures (122, 129-130). HPLC analysis can be used to determine the radiochemical yield, enabling the selection of the best reaction conditions. For the radiolabelling of NKJ64, multiple small-scale reaction mixtures samples were tested using analytical HPLC, in order to determine the best incubation duration and temperature for the deprotection step. The highest

radiochemical yield of ^{123}I -NKJ64 was obtained using 2 M HCl after 45 minutes incubation at 60 °C (Table 3.5), indicating that 2 M HCl was appropriate for the deprotection step.

Following purification using semi-preparative HPLC (method A), the 2 M HCl deprotection method revealed the measured specific activity of $^{123/125}\text{I}$ -NKJ64 to be low, compared with the higher specific activity measured when TFA was used as the deprotecting agent (Table 3.6). Moreover, the specific activity measured when using 2 M HCl as the deprotecting agent was similar when the radiosynthesis was performed using Na^{125}I or Na^{123}I (Table 3.6). It is known that the specific activity of non-carried added Na^{125}I is considerably lower than Na^{123}I (the specific activity of Na^{125}I and Na^{123}I was typically around 2.6 Ci/ μmol and 240 Ci/ μmol , respectively). Therefore, the absence of a difference in the specific activity measured when using Na^{125}I and Na^{123}I contradicts the expected theoretical outcome. Subsequent investigation using alternative HPLC methodology containing less organic solvent in the mobile phase over time (method B) showed that two UV peaks could be visualized (Figure 3.10). Both UV peaks co-eluted with the radio-peak identified as $^{123/125}\text{I}$ -NKJ64, indicating the presence of a by-product when 2 M HCl was used as the deprotecting agent. In an attempt to further improve separation of the peaks, multiple HPLC methodologies were investigated (Appendix 2), however, none of the evaluated methods allowed either of the peaks to be fully separated from the $^{123/125}\text{I}$ -NKJ64 radio-peak. In contrast, when deprotection was performed using TFA, subsequent semi-preparative HPLC (method B) revealed the presence of only one minor peak, indicating the by-product observed with 2 M HCl was not present. It was hypothesised that the by-product detected when using 2 M HCl as a deprotecting agent, was likely to be the deprotected protodestannylated precursor, formed due to the high acidity of 2 M HCl. In order to confirm the identity of the by-product, MS analysis (chemical ionisation) was performed on the purified by-product (Peak A) obtained from the synthesis of cold NKJ64 using Na^{127}I . This analysis confirmed the presence of the deprotected protodestannylated precursor (Figure 3.11). This is consistent with the breakdown of the precursor, which is present in large excess in the radiolabelling reaction, under strong acidic conditions. The pharmacology of the deprotected protodestannylated precursor is unknown. However its similar chemical structure to reboxetine suggests this compound may have some action at the NAT, thereby potentially interfering with the pharmacology of $^{123/125}\text{I}$ -NKJ64.

The specific activity of a ^{123}I -labelled radiotracer for SPECT imaging can range between 1 and 2 Ci/ μmol (131) to values as high as 5-20 Ci/ μmol (124, 126, 131-132). Few studies, on the other hand, have reported lower specific activity in the range of 0.1 to 0.2 Ci/ μmol (127). As discussed in section 3.1.4, specific activity is an important parameter for a radiotracer since the presence of large amounts of cold ligand in low

specific activity radiotracer formulations can potentially result in a pharmacological mass effect. A range of methodologies are commonly used to measure specific activity. For example, specific activity measurements have been made by testing an aliquot of the final product on the analytical HPLC (122-123, 125, 133) or by measuring its value during HPLC purification in a semi-preparative system (126, 132). In addition, some researchers assume that the specific activity of the final product will be comparable to the specific activity of non carrier Na^{123/125}I used (38). Often when using analytical HPLC sample testing, the specific activity of a radiotracer is stated to be greater than the known detection limits of the HPLC system, where no UV response could be detected (122-123, 125, 133). A more accurate method is to measure the specific activity during HPLC purification (following injection of the whole reaction mixture), by converting the UV response into mass of radiotracer using a concentration-response calibration curve (126, 132). Using this method our results showed an approximately tenfold difference in the calculated specific activity between the two deprotecting agents; the highest specific activity being obtained with TFA. The difference in the calculated specific activity values when using different deprotecting agents can be explained by the presence or absence of the by-product which co-eluted with the final product. These findings suggest that unless specific activity is accurately measured during HPLC purification (following injection of the whole reaction mixture), it may not be possible to identify potentially confounding impurities.

Purification of novel radiotracers can be accomplished by HPLC (122-126) or SPE (38, 40, 127) (for a review on the main characteristics of these two methods see section 3.1.6). One advantage of preparative HPLC over SPE relates to the ability of HPLC to provide both radiodetection and UV analysis of the total reaction constitutes, thus allowing direct measurement of the specific activity of the final product. This is especially important when establishing the radiosynthesis methodology for novel radiotracers. In the present study, the use of semi-preparative HPLC for purification of ^{123/125}I-NKJ64 highlighted the presence of a by-product in the final product that otherwise would not have been identified. Despite its advantages over SPE, particularly when establishing radiosynthesis methodologies of novel radiotracer, the repeated use of a HPLC system for radiopharmaceutical purification can be the source of bacterial growth. Consequently, validation of HPLC purification for the production of radiopharmaceuticals for human use may be more difficult, involving cleaning procedures, in comparison to SPE, which uses a single disposable unit for each radiopharmaceutical preparation. Therefore, there is an argument that SPE can be the method of choice for human formulations if adequate radiotracer separation and purification can be achieved using SPE.

Despite multiple attempts to maximise the specific activity of ^{123}I -NKJ64, its value was still below the theoretical specific activity of ^{123}I (240 Ci/ μmol) (31). The oxidant PAA was used to initiate the radiolabelling reaction due to its mild oxidant properties (31-32, 120), reducing the potential for by-product formation. The use of an organotin precursor reduces the risk of any intact precursor remaining co-eluting with the final radiotracer during the HPLC purification step. Furthermore, the purity of precursor was tested by colleagues in the School of Chemistry at the University of Glasgow and was found to be 100% with no presence of iodine impurities. This excludes the possibility of the precursor impurities being an explanation for the specific activity values being lower than possible theoretically. One potential explanation could relate to the high incubation temperature of 60 °C required in the deprotection step. As previously explained (section 3.1.5), electrophilic iododestannylation reactions, which are typically carried out at room temperature, require short incubation times and frequently provide the final radiotracer with high specific activities. Conversely, nucleophilic isotopic exchange reactions require higher incubation temperatures and typically provide lower specific activities (32, 120). Since higher temperatures have been associated with a degree of precursor instability and consequent low specific activities (32, 120), this could be a putative explanation for the specific activity obtained when preparing ^{123}I -NKJ64. Although the specific activity of ^{123}I -NKJ64 was below the calculated theoretical value, the radiolabelling using TFA as the deprotecting agent obtained ^{123}I -NKJ64 with a high-specific activity for *in vivo* imaging of NAT.

3.5 Conclusion

The radiosynthesis of $^{123/125}\text{I}$ -NKJ64, a novel radiotracer for imaging of NAT in brain, was successfully achieved. The radiochemical yield was higher when using 2 M HCl as the deprotecting agent, however a co-eluting by-product present in the final product means this radiosynthetic route would not be acceptable for production of $^{123/125}\text{I}$ -NKJ64 for *in vivo* imaging or *in vitro* studies. In contrast, radiosynthesis of $^{123/125}\text{I}$ -NKJ64 using TFA as the deprotecting agent produced the radiotracer without the co-eluting by-product, with a high specific activity and adequate radiochemical yield. The radiolabelling results highlighted that purification by HPLC and the accurate measurement of specific activity provides the opportunity to confirm the absence of impurities generated during radiolabelling.

For evaluation in rodents, NKJ64 was radiolabelled *via* the electrophilic iododestannylation reaction outlined above, deprotection using TFA and purification using semi-preparative HPLC method B. According to the results obtained from stability

testing, all studies using ^{123}I -NKJ64 and ^{125}I -NKJ64 reported in subsequent thesis chapter were performed within 24 hours and 8 days of radiotracer preparation, respectively.

4 Biological evaluation of $^{123/125}\text{I}$ -NKJ64 in rodents

Following the successful radiolabelling of high specific activity $^{123/125}\text{I}$ -NKJ64, reported previously in chapter 3, the next step was to evaluate the characteristics of $^{123/125}\text{I}$ -NKJ64 in rodents. This chapter reports the biological evaluation of $^{123/125}\text{I}$ -NKJ64 in rats.

4.1 Introduction

This section provides an overview of the central noradrenergic system in rodents, describing the distribution of NAT binding sites in rat brain. The purpose of the introduction section is to outline information that will aid the interpretation of the results in this chapter.

4.1.1 *Central noradrenergic system in rodent brain*

In rats, the locus coeruleus is a prominent nucleus located in the brainstem reticular formation at the level of the isthmus. A quantitative analysis of the locus coeruleus indicates that it includes 43% of all the noradrenaline producing neurons in the rat brain and comprises approximately 1400-1800 neurons on each side of the brainstem (106-107, 134).

Extensive and widespread collateralisation throughout the neuroaxis by the neurons arising from the locus coeruleus, especially extensive innervation of the telencephalic structures, has been reported since the early 70's (Figure 4.1). Autoradiography and histochemical techniques have been used to determine the major pathways that originate from the locus coeruleus. Terminal projections of locus coeruleus include: (1) all segments of the spinal cord, (2) brainstem, (3) cerebellum, (4) hypothalamus (the major hypothalamic innervation arises from the brainstem noradrenergic cell groups, except for the dorsomedial nucleus, the paraventricular nucleus and the supraoptic nucleus), (5) thalamus and telencephalon (the entire telencephalon appears to receive some input from locus coeruleus, except the basal ganglia, the olfactory tubercle and the nucleus accumbens), especially the anterior thalamic nuclei (particularly the anteroventral nucleus), the plexus of fibres in the stratum radiatum of CA3 and in the area dentata of the hippocampus; and (6) the entire neocortex, especially the cingulate and the frontal cortex (106, 134). Additionally, it was determined that: (1) at least 40% of all locus coeruleus neurons project to the olfactory bulb, which represents the sole source of noradrenergic innervation to the bulb; (2) the dorsal striatum is the only

major brain region essentially devoid of noradrenergic fibres (except the caudal medial shell of the nucleus accumbens, which showed considerable noradrenergic innervations) and (3) the amygdala receives topographically organised innervations by noradrenergic fibres throughout the various locus coeruleus subnuclei in addition to the locus coeruleus neurons (134).

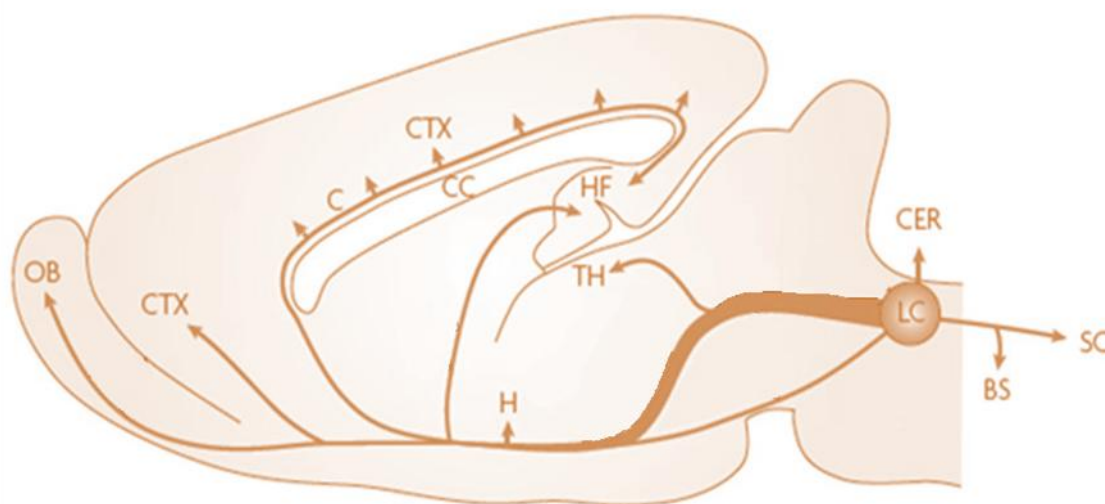


Figure 4.1 Anatomical distribution of the main noradrenergic projections in the rat brain.

Adapted from (107). Abbreviations: locus coeruleus (LC), brainstem nuclei (BS), cingulum (C), corpus callosum (CC), cerebellum (CER), cortex (CTX), hypothalamus (H), hippocampal formation (HF), olfactory bulb (OB), spinal cord (SC), thalamus (TH).

Tejani-Butt in 1992 used quantitative autoradiography and ^3H -nisoxetine for quantification of NATs in rat brain (Table 4.1). Results showed that specific binding was highest in the locus coeruleus and anteroventral thalamic nucleus, while the lowest density was measured in the caudate putamen (135).

Brain Region	^3H-nisoxetine Binding (fmol/mg)
Locus Coeruleus	1526±39
Anteroventral thalamic n., dorsomedial	1444±147
Bed n. of stria term., lat. div., ventral	1348±57
Dorsomedial hypothalamic n.	1062±37
Paraventricular hypothalamic n.	847±81
Paraventricular thalamic n.	845±46
Dentate gyrus	716±40
Medial zona incerta	672±50
Dorsal raphe	639±27
Mammillothalamic tract	544±86

Table 4.1 Distribution of specific binding of ^3H -nisoxetine to NATs in rat brain. Results shown as mean±S.E.M, adapted from (135).

Brain Region	³H-nisoxetine Binding (fmol/mg)
Bed n. of the stria term., lat. divl., dorsal	529±10
Median raphe	500±77
Basolateral amygdaloid n.	497±30
CA 2 and 3 of the hippocampus	375±32
Frontoparietal cortex	358±25
Ventral posterior thalamic n.	321±21
Central amygdaloid n.	309±42
Centromedial thalamic n.	307±10
Ventromedial hypothalamic n.	301±12
Lateral dorsal thalamic n.	297±26
Lateral amygdaloid n.	267±18
Centrolateral thalamic n.	205±7
CA 1 layer of hippocampus	204±15
Medial amygdaloid n.	180±10
Caudate Putamen	54±11

Table 4.1 (cont).

4.1.2 Hypothesis and aims

It was hypothesised that ^{123/125}I-NKJ64 distribution in rat brain was consistent with known NAT labelling. A secondary hypothesis was that ^{123/125}I-NKJ64 had high affinity for the NAT in rat brain and whole body kinetics suitable for *in vivo* imaging. This chapter aims to evaluate ^{123/125}I-NKJ64 as a novel NAT radiotracer for SPECT in rodents by performing studies to determine the affinity, biodistribution, kinetics and target:non-target ratio of ^{123/125}I-NKJ64 in rats using *in vitro*, *in vivo* and *ex vivo* imaging techniques.

4.2 Material and Methods

4.2.1 General

All chemicals, unless otherwise stated, were obtained from Sigma Aldrich, UK. Sodium chloride (0.9% NaCl) was obtained from Baxter, UK. Sodium hydroxide (NaOH), potassium chloride (KCl) and sodium chloride (NaCl) used for buffer preparation were purchased from VWR, UK. Reboxetine was obtained from Tocris Bioscience, USA.

4.2.2 Rats

All procedures were carried out at the University of Glasgow in accordance with the Animals (Scientific Procedures) Act, 1986 (United Kingdom). Male Sprague-Dawley rats (Harlan Olac Bicester, UK) weighing 250-300 g were housed in small groups ($n \leq 4$) under a 12 h light/dark cycle and allowed free access to laboratory diet and water.

4.2.3 General preparation and monitoring of rats

For *in vivo* studies rats were weighed and anaesthetised in a perspex chamber containing isoflurane (2.5-4.5% in a mixture of 40% O₂/60% NO₂), then maintained under isoflurane anaesthesia (1.5-3% in a mixture of 40% O₂/60% NO₂) using a face mask. Throughout the experiment period, respiration rate was monitored and rectal temperature was maintained at 37-38 °C by means of a heating lamp or heating blanket with feedback control.

4.2.4 Saturation binding assays using ¹²⁵I-NKJ64

Rats were killed by an overdose of anaesthetic and the brains rapidly removed and dissected on ice. Cerebral cortex was homogenised in ice-cold 50 mM Tris-Base, 300 mM NaCl and 5 mM KCl buffer pH 7.4 and centrifuged at 39100 g for 10 minutes at 4 °C. The resulting pellet was washed twice by resuspension and centrifugation in buffer, then stored at - 50 °C until use. For K_D and B_{max} determination, aliquots of membrane suspensions (0.35-0.75 mg of protein) were incubated for 240 minutes at 4 °C in 50 mM Tris-Base, 300 mM NaCl and 5 mM KCl buffer, pH 7.4, in the presence of 8 different concentrations of ¹²⁵I-NKJ64 (0.05-50 nM). Total incubation volume was 500 µL and non-specific binding was determined in the presence of 10 µM of reboxetine. Assays were performed in triplicate. The reaction was terminated by rapid filtration through Whatman GF/B glass filters, presoaked in 0.3% w/v polyethylenimine, using a Brandel cell harvester. Filters were washed three times rapidly in ice-cold buffer and radioactivity on the filters determined by liquid scintillation counting. K_D and B_{max} values were determined by nonlinear regression analysis using GraphPad Prism Version 4.0 (GraphPad Software, USA). The total protein content was determined by using the Bicinchoninic Acid (BCA)-based protein assay. Briefly, the Bio-Rad reagent was prepared using solutions A and B in a 50:1 ratio and 1 mL of the freshly prepared reagent was added to each test tube. The calibration curve was performed by adding 50 µL of bovine serum albumin (BSA) in the following pre-made concentrations 2000, 1500, 1000, 750, 500, 250, 125, 25 and 0 µg/mL to the test tubes containing the Bio-Rad reagent. In

addition, 20 μL of brain homogenate was added to test tubes containing the Bio-Rad reagent. All test tubes were then vortexed and incubated at 37°C for 30 minutes. Following incubation, the test tubes were kept at room temperature for 5 minutes and then the absorbance was read on a spectrophotometer using a wavelength of 562 nm. Results from the BSA standards absorbance readings were plotted against the protein content. The calibration curve was subsequently used to determine the protein content in rat brain homogenates.

4.2.5 *In vitro* rat brain autoradiography using ^{123}I -NKJ64

Coronal sections (20 μm thick) were cut in a cryostat at -20°C at 0.3 mm intervals from frozen rat brain and thaw-mounted onto poly-L-lysine-coated slides then dried at room temperature. All steps of the autoradiography procedure were performed in 50 mM Tris-HCl, 300 mM NaCl and 5 mM KCl buffer (pH 7.4) at 4°C . Sections were pre-incubated in buffer for 30 minutes. The sections were then incubated for 240 minutes with 5 nM ^{123}I -NKJ64. Non-specific binding to NAT was determined in adjacent sections in the presence of 10 μM reboxetine. At the end of the incubation period, sections were rinsed three times for 5 minutes in ice-cold buffer, and dipped for 10 seconds in ice-cold distilled water. Sections were then dried at room temperature in a stream of cool air overnight and exposed to Kodak Biomax MR film (Sigma and Aldrich, UK) for 1 h (Figure 4.2). Films were developed and then analysed using a MCID with MCID Basic 7.0 software (MCID, UK). Relative optical density measurements were obtained from brain regions defined with reference to the Paxinos and Watson rat brain atlas (136).

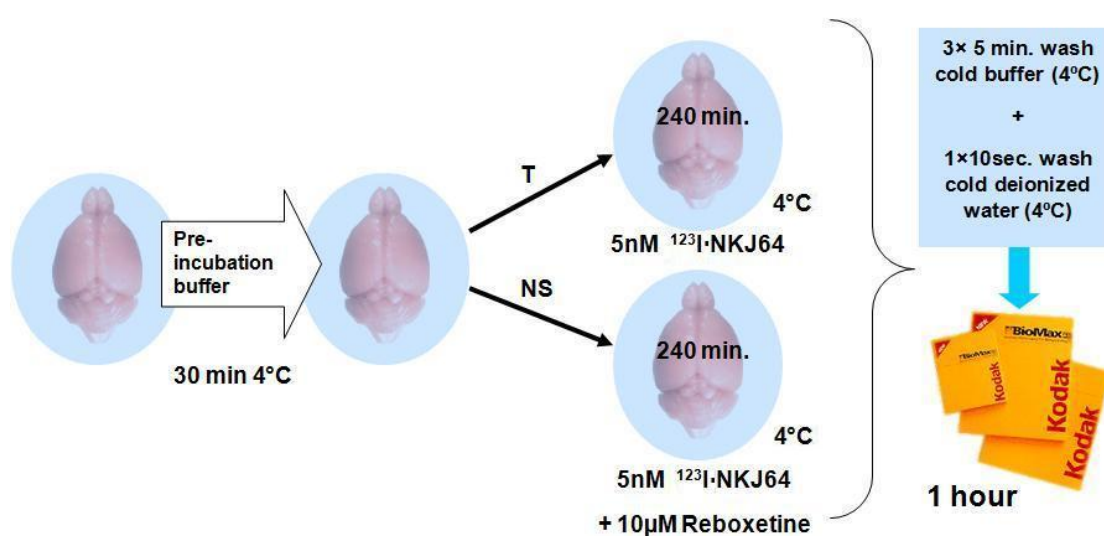


Figure 4.2 Schematic representation of *in vitro* rat brain autoradiography using ^{123}I -NKJ64. T=total binding; NS=non-specific binding.

4.2.6 Whole body dynamic planar imaging of rats following intravenous administration of $^{123}\text{I-NKJ64}$

In vivo whole-body imaging in rats was accomplished using dynamic imaging protocols after tail vein injection of 25-30 MBq of $^{123}\text{I-NKJ64}$ (volume 0.3 to 0.4 mL). Rats were anaesthetised and prepared as described above (section 4.2.3). Immediately after injection of $^{123}\text{I-NKJ64}$, dynamic imaging was acquired on a large field of view gamma camera (Medical Imaging Electronics (MIE), Germany) using SCINTRON software (MIE, Germany). Total scan time was 4 hours, with four dynamic phases: 1) sequential images every 2 seconds for first 60 seconds; followed by 2) sequential images every 15 seconds for next 15 minutes; followed by 3) sequential images every 60 seconds for next 45 minutes; and then 4) 120 seconds per frame at 75, 90, 105, 120, 150, 180, 210, 240 minutes post-injection (Figure 4.3). A low energy high resolution collimator and an energy window of 15% centre at 159 keV were used on all four phases. Acquisitions were obtained using a 256×256 matrix and a zoom of one. Using the SCINTRON software, regions of interest (ROI) were drawn on the brain, lungs, intestine and left ventricle chamber of the heart, as well as a background region outside the rat. The total counts for each ROI were decay corrected and background corrected. For each rat, images of the syringe used to administer $^{123}\text{I-NKJ64}$ (pre- and post- injection) were acquired over 1 minute (Figure 4.3). ROIs of the syringe pre- and post-injection were used to calculate the total counts associated with the total injected dose. The %ID for each time point was calculated by dividing the total counts in each ROI by the total counts associated with the total injected dose, multiplied by 100. The chamber of the left ventricle of the heart ROI, used as an indirect measurement of blood clearance, was also normalised for area. To calculate the %ID in blood, the total counts per pixel in the heart ROI were divided by the total counts per pixel in the syringe pre-injection minus the total counts per pixel in the syringe post-injection, multiplied by 100. The peak %ID, the time of peak %ID, effective and biological half-life (Eq. 4.1) were calculated from the time-activity curves generated. Elimination rate was determined using peak %ID minus %ID value of selected time points (5, 15, 30, 60 and 240 minutes) divided by peak %ID, multiplied by 100. Then the percentage of peak uptake was calculated by subtracting elimination rate value to 100.

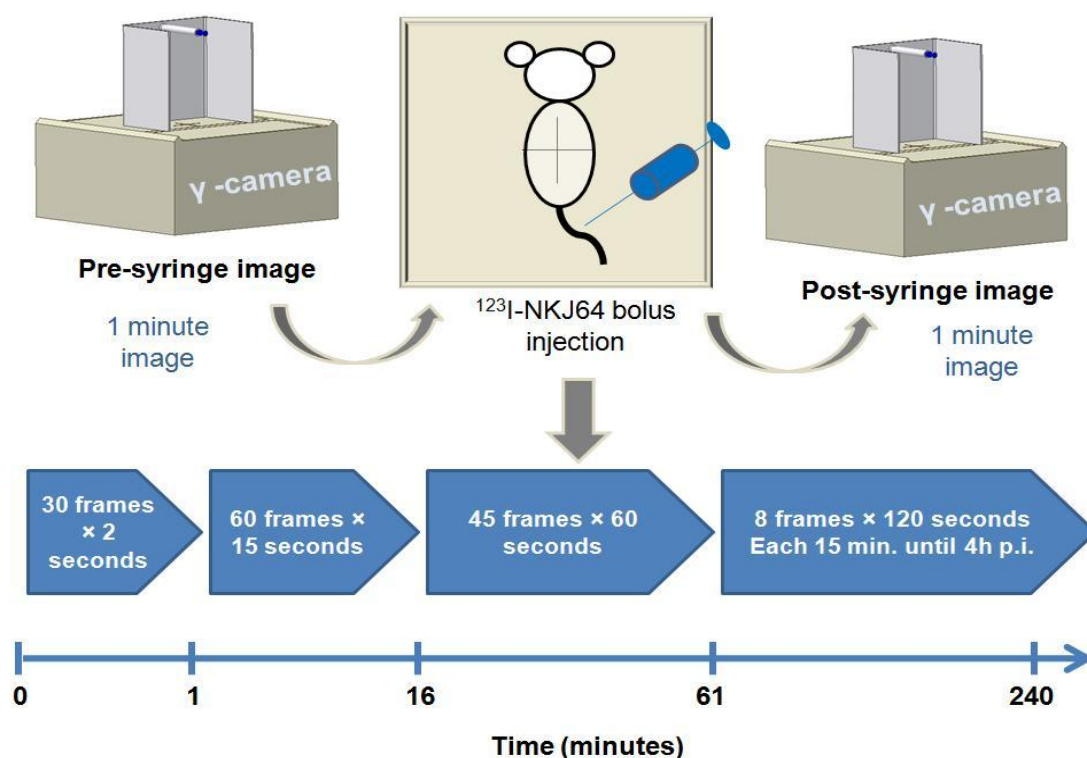


Figure 4.3 Schematic representation of whole body dynamic planar imaging acquisition using ^{123}I -NKJ64.

$$T_{1/2 \text{ eff}} = \frac{(T_{1/2 \text{ phys}}) \times (T_{1/2 \text{ bio}})}{(T_{1/2 \text{ phys}}) + (T_{1/2 \text{ bio}})} \quad \text{Eq. 4.1}$$

where $T_{1/2 \text{ eff}}$ is effective half life, $T_{1/2 \text{ bio}}$ is biological half-life and $T_{1/2 \text{ phys}}$ is physical half-life.

4.2.7 *In vivo/ex vivo* pharmacological blocking experiments using ^{123}I -NKJ64

For pharmacological blocking studies, rats were anaesthetised as previously described (section 4.2.3). Rats received an intravenous injection *via* tail vein of either reboxetine (2 mg/kg in saline; 1 mL/kg body weight) or saline (1 mL/kg body weight) 15 minutes prior to the injection of ^{123}I -NKJ64 (15-25 MBq in 0.4-0.5 mL saline). Thirty minutes following injection of ^{123}I -NKJ64, animals were killed by an overdose of anaesthesia and the brain rapidly removed and frozen in isopentane at $-50\text{ }^{\circ}\text{C}$ for subsequent autoradiography (Figure 4.4). Other organs were then excised, blotted and weighed and blood, urine and faeces collected. The amount of radioactivity in tissues and ^{123}I standards was measured using an automated Packard Cobra gamma counter. Counts were decay-corrected to time of injection and converted into %ID/g. Coronal sections (20 μm thick) were cut in a cryostat at $-20\text{ }^{\circ}\text{C}$ at 0.3 mm intervals from frozen rat

brains and thaw-mounted onto slides on the day following the *in vivo* experiment. Sections were dried quickly and exposed to Kodak Biomax MR film (Sigma Aldrich, UK) for 3 days. Films were developed and then analysed using a MCID with MCID Basic 7.0 software (MCID, UK). Relative optical density measurements were obtained from regions defined with reference to Paxinos and Watson rat brain atlas (136). Target-to-caudate putamen ratios were calculated for the corpus callosum, locus coeruleus, hippocampus, anterior thalamus, ventricles, raphe and motor cortex. The caudate putamen was selected as representing an area of non-specific uptake as this brain region is known to have the lowest density of NAT (135).

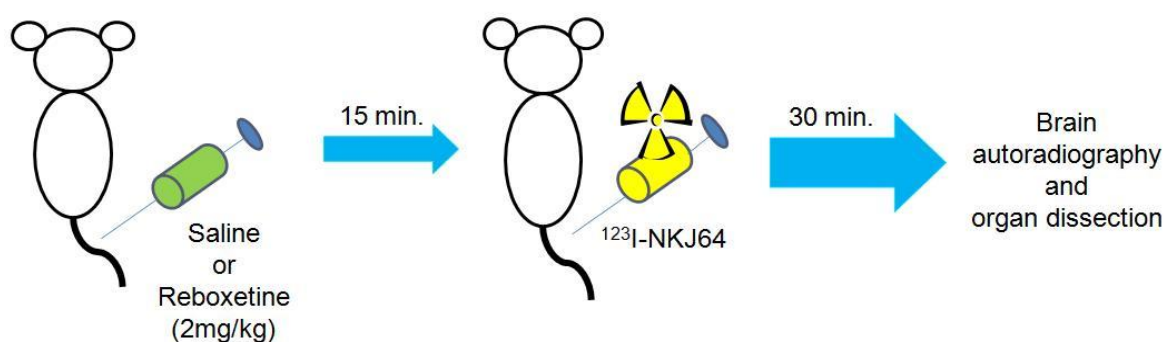


Figure 4.4 Schematic of *in vivo/ex vivo* pharmacological studies using ^{123}I -NKJ64.

4.3 Results

Specific binding of ^{125}I -NKJ64 to rat cortical homogenates at 4 °C was saturable (Figure 4.5 a, b). Nonlinear regression analysis of saturation binding curves from three independent determinations produced a mean \pm SEM K_D of 4.82 \pm 0.87 nM and a mean \pm SEM B_{max} of 548 \pm 99 fmol/mg. The percentage non-specific binding, determined in the presence of reboxetine, in cortical homogenates was 77% at 6.25 nM ^{125}I -NKJ64. The anatomical distribution of ^{123}I -NKJ64 binding to rat brain sections revealed by *in vitro* autoradiography was consistent with the known distribution of the NAT (Figure 4.6). The highest level of radioactivity was observed in the locus coeruleus and anteroventricular thalamic nucleus, which are known to be rich in NATs. Conversely, there was less radioactivity in the cerebral cortex and caudate putamen regions known to have the low densities of the NAT. In brain sections there was minimal blocking of ^{123}I -NKJ64 by reboxetine in majority of regions, although in the locus coeruleus ^{123}I -NKJ64 binding was displaced by reboxetine (Figure 4.6).

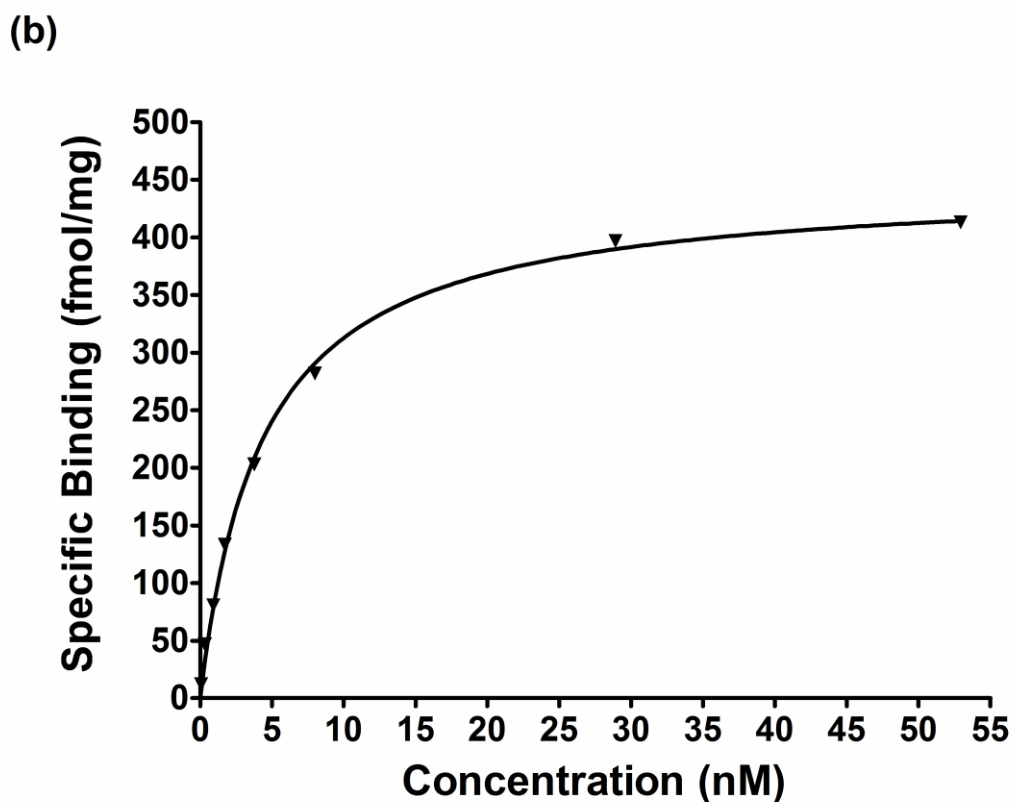
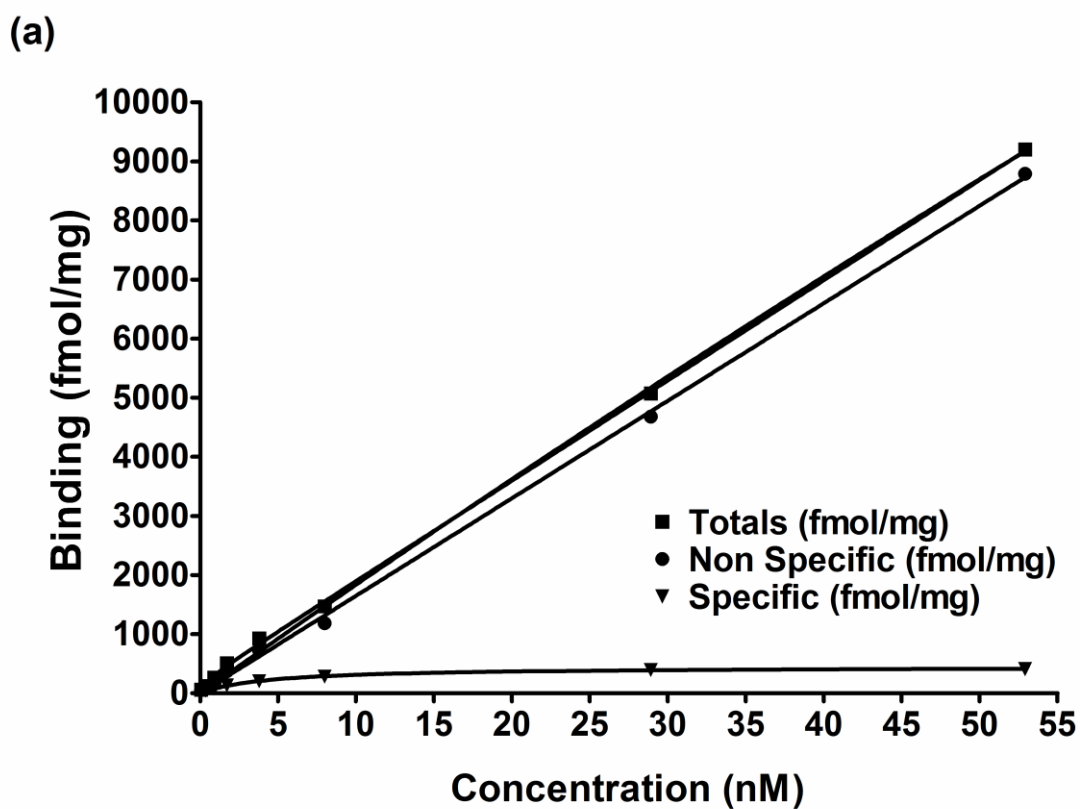


Figure 4.5 *In vitro* binding of ^{125}I -NKJ64 to rat cortex.

(a) a representative saturation binding plot of ^{125}I -NKJ64 binding to rat cortical homogenates; and (b) a representative specific binding curve for ^{125}I -NKJ64. Note the high levels of non-specific binding, determined in the presence of reboxetine, (a).

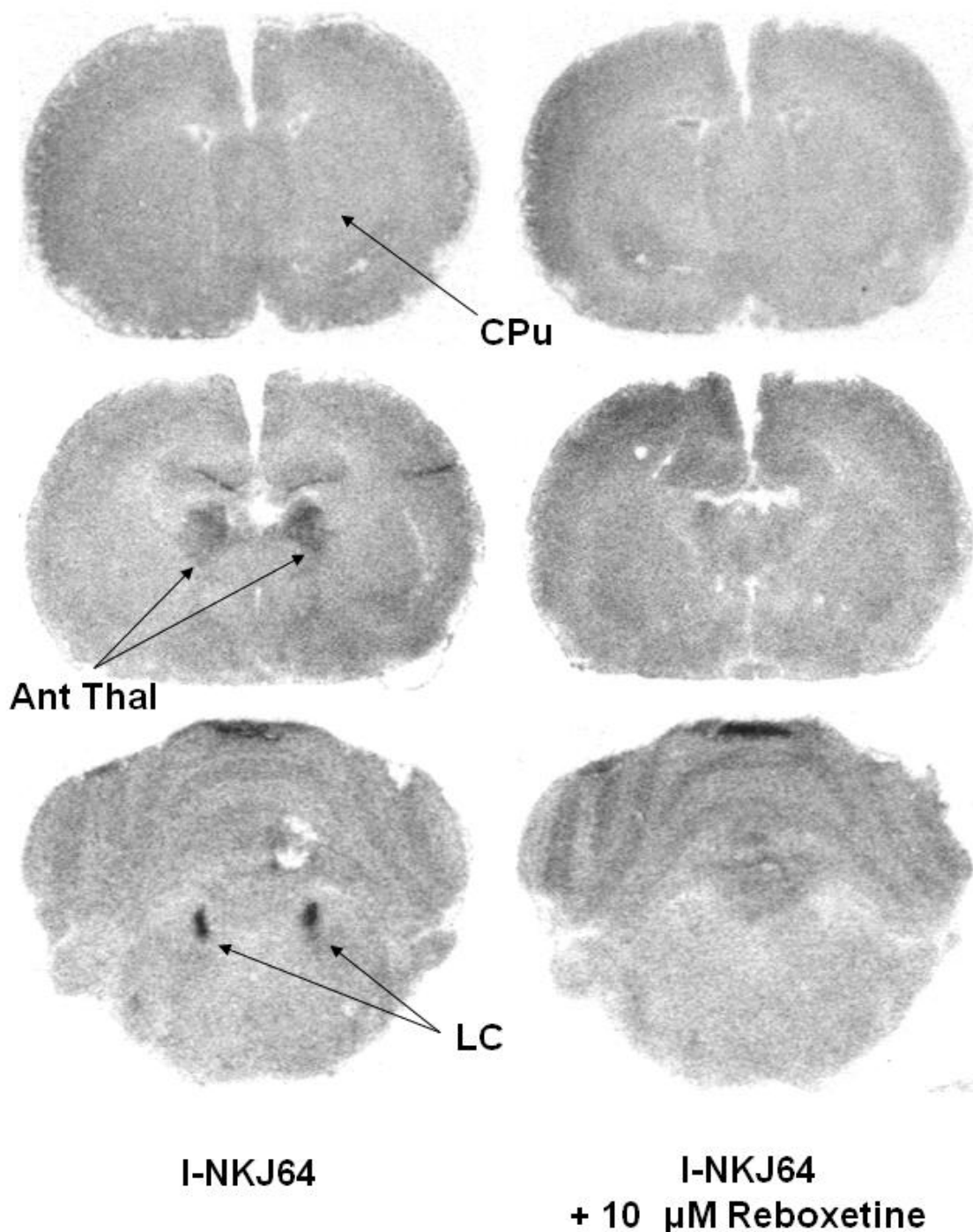


Figure 4.6 Representative autoradiogram of *in vitro* binding of ^{123}I -NKJ64 to rat coronal brain sections.

Note the reduced levels of binding specifically in the locus coeruleus (LC) in the presence of reboxetine. Legend: CPu=caudate putamen and Ant Thal=anterior thalamus.

The *in vivo* biodistribution of radioactivity after intravenous injection of ^{123}I -NKJ64 is shown in Figures 4.7 to 4.12. In Figure 4.7 it is possible to visualise a sum image (a) of the first two seconds, showing the injection site and the heart/blood, where rapid delivery of the radiotracer to the heart is shown. From the heart, ^{123}I -NKJ64 rapidly passes to the systemic circulation and consequently enters the remaining organs (Figure

4.7b). The effective half-life in blood was 0.32 minutes (Table 4.2), and the radioactivity in blood cleared rapidly, with less than 10% of injected dose remaining in the circulation at 240 minutes post-injection (Figure 4.8 to 4.10).

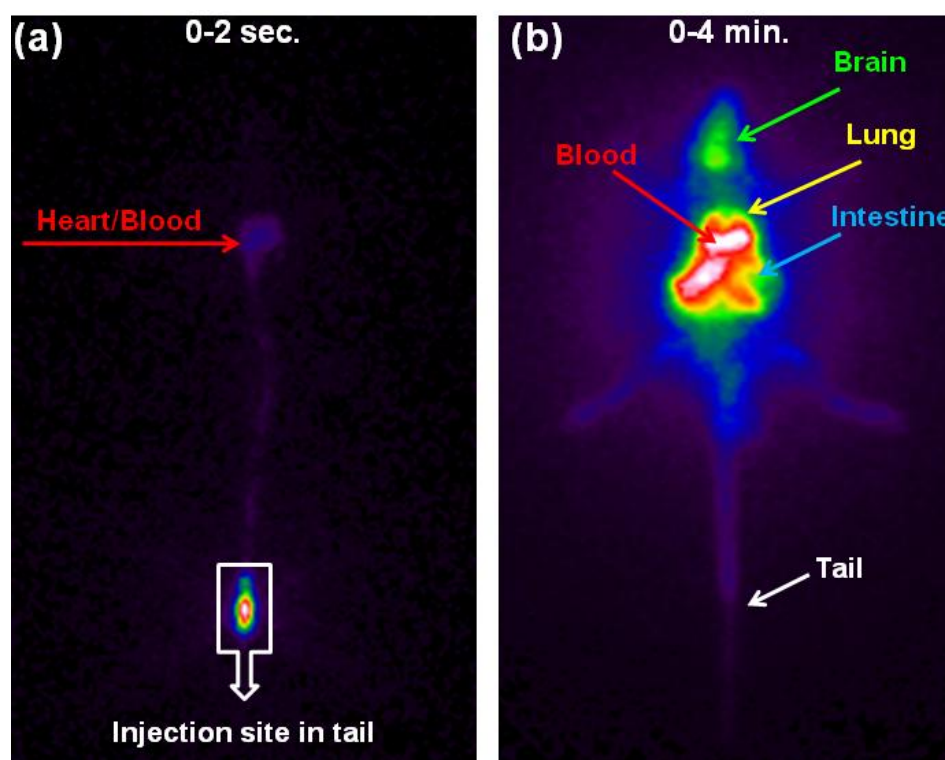


Figure 4.7 $^{123}\text{I-NKJ64}$ whole rat body sum images.

(a) sum image from 0-2 seconds; and (b) sum image from 0-4 minutes post radiotracer administration.

<i>Organ</i>	<i>T_½ effective (min.)</i>	<i>T_½ biologic (min.)</i>	<i>%ID max.</i>
Whole Brain	48.85±2.60	52.17±2.97	2.93±0.14
Brain Anterior	35.97±2.76	34.34±2.52	1.23±0.05
Brain Posterior	49.37±2.64	46.39±2.33	1.84±0.11
Lung	2.30±0.29	2.31±0.29	6.01±0.78
Blood	0.32±0.03	0.32±0.03	96.91±0.44

Table 4.2 Elimination half-life and peak %injected dose of total radioactivity in rats.

Values are derived from time-activity curves obtained by whole body dynamic planar imaging after intravenous injection of $^{123}\text{I-NKJ64}$. Data are expressed as mean±SEM, n=3 rats.

A longitudinal analysis of $^{123}\text{I-NKJ64}$ biodistribution over time is provided in Figures 4.8 and 4.9. Visual inspection of sum images, every 15 minutes (Figure 4.8) and every 3 minutes (Figure 4.9) provided information on the regional distribution and clearance of the $^{123}\text{I-NKJ64}$ over time. The brain time-activity curve showed that $^{123}\text{I-NKJ64}$ rapidly entered the brain and the level of radioactivity was highest at 0.49±0.04 minutes post-injection (mean±SEM, n=3) (Figure 4.10). The peak level of radioactivity in the brain was 2.93±0.14 %ID (Table 4.2).

In order to provide information on regional distribution of radioactivity in brain, dynamic planar whole brain images were divided into anterior and posterior brain regions. As previously mentioned (section 4.1.1), the locus coeruleus is located in the brainstem of the rodent brain, and so the posterior brain region was assumed to be the target region. Results from this regional analysis showed that there was higher uptake in the posterior region of the brain (peak %ID of $1.84 \pm 0.11\%$) in comparison with the anterior region of the brain (peak %ID of $1.23 \pm 0.05\%$) (Table 4.2 and Figure 4.11). Elimination from anterior brain was faster than in posterior brain (effective half life of 34.34 ± 2.52 minutes and 46.39 ± 2.33 minutes, respectively) (Table 4.2) and around 15% of peak uptake was present in the anterior brain, in comparison with approximately 30% peak uptake in the posterior brain at 240 minutes post-injection (Figure 4.12). Whole brain washout was rapid, but slower than the washout from blood and lungs (Table 4.2). High uptake of radioactivity was observed in the lungs (Table 4.2), followed by a rapid clearance (Figure 4.10). Negligible radioactivity accumulated in the thyroid and did not increase until 240 minutes post-injection (Figure 4.8 and 4.9). The intestine was the main elimination route (Figure 4.10).

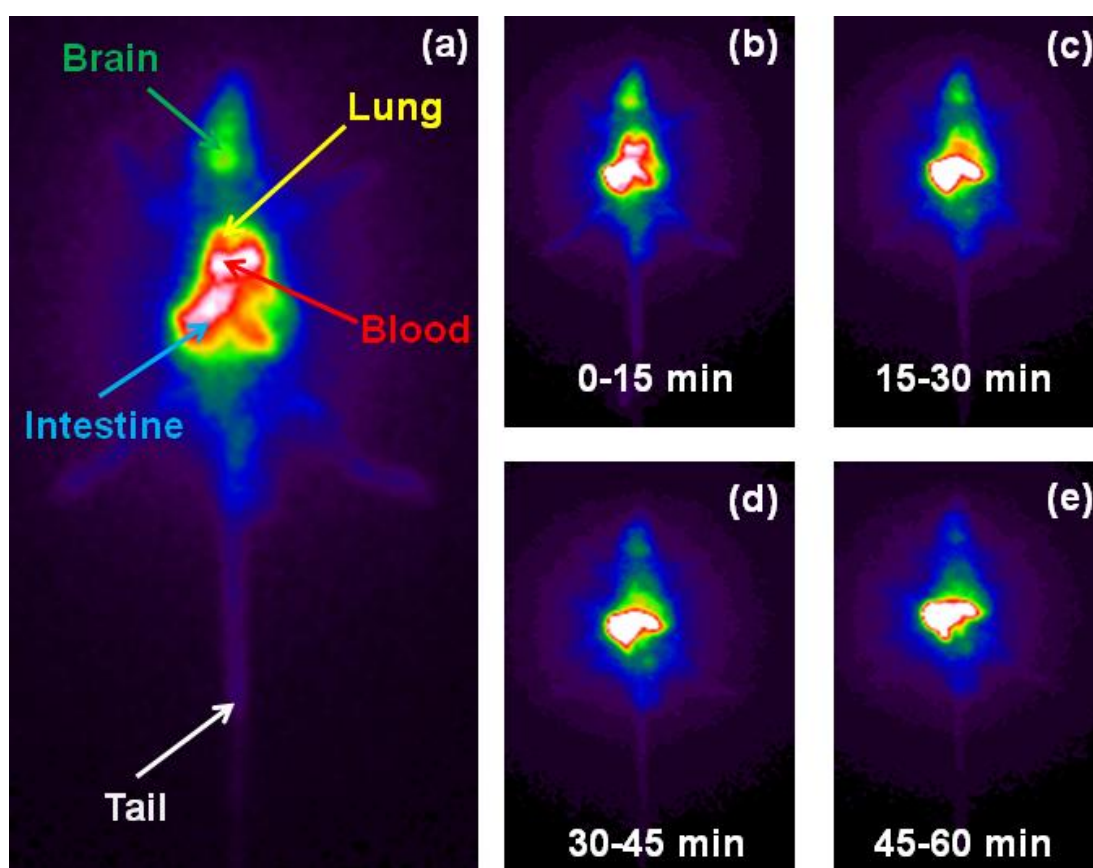


Figure 4.8 Whole rat body *in vivo* ^{123}I -NKJ64 images obtained by dynamic planar imaging. (a) A representative sum image obtained over the first 4 minutes after injection of ^{123}I -NKJ64; (b), (c), (d), (e) sequential sum images, each summed over a 15 minute period, from 0-60 minutes. Note the initial high brain uptake which is reduced over time and the absence of significant thyroid uptake.

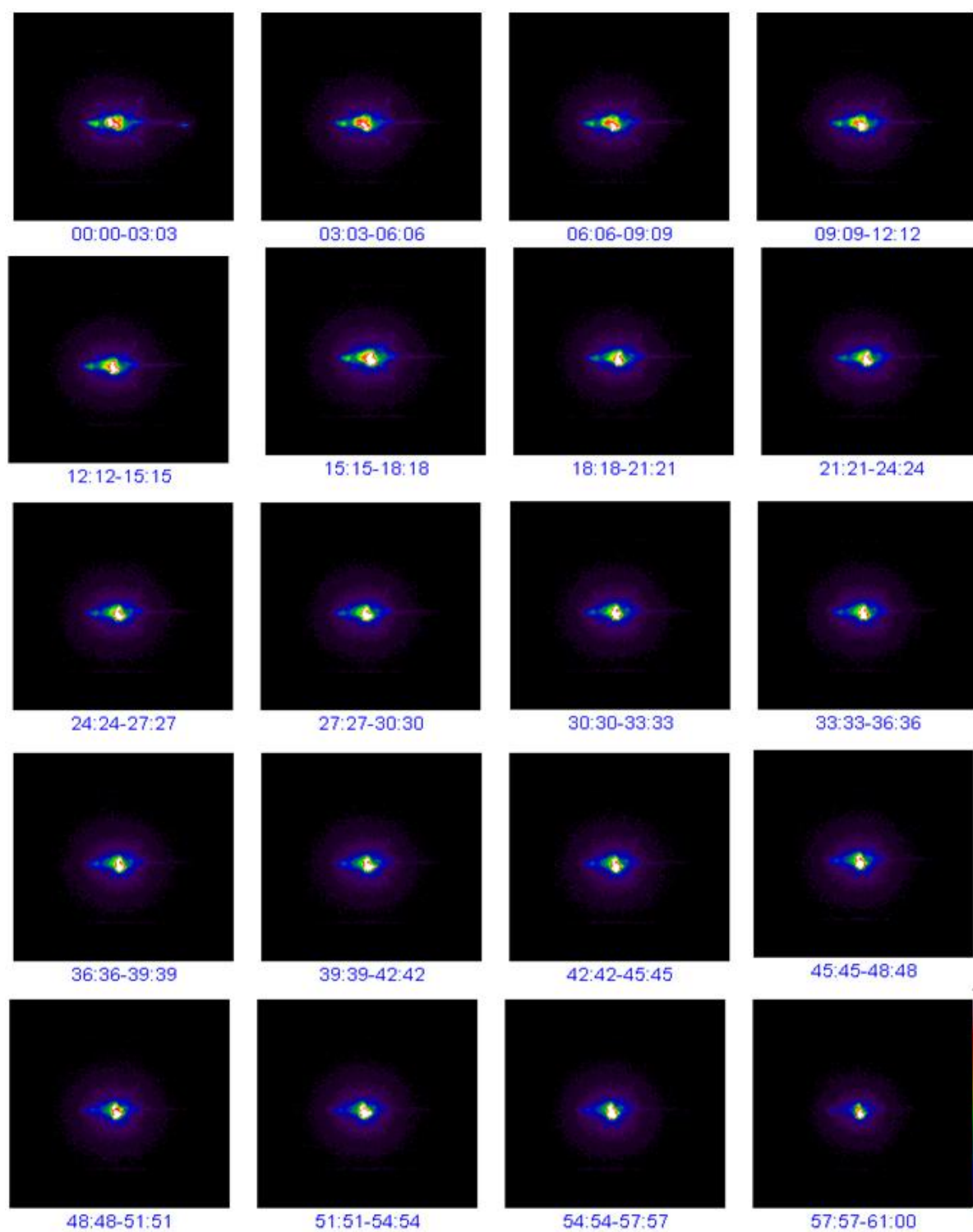


Figure 4.9 Whole rat body *in vivo* ^{123}I -NKJ64 sequential images, each summed over a 3 minute period, from 0-60 minutes.

Note the initial high brain uptake which is reduced over time and the absence of significant thyroid uptake.

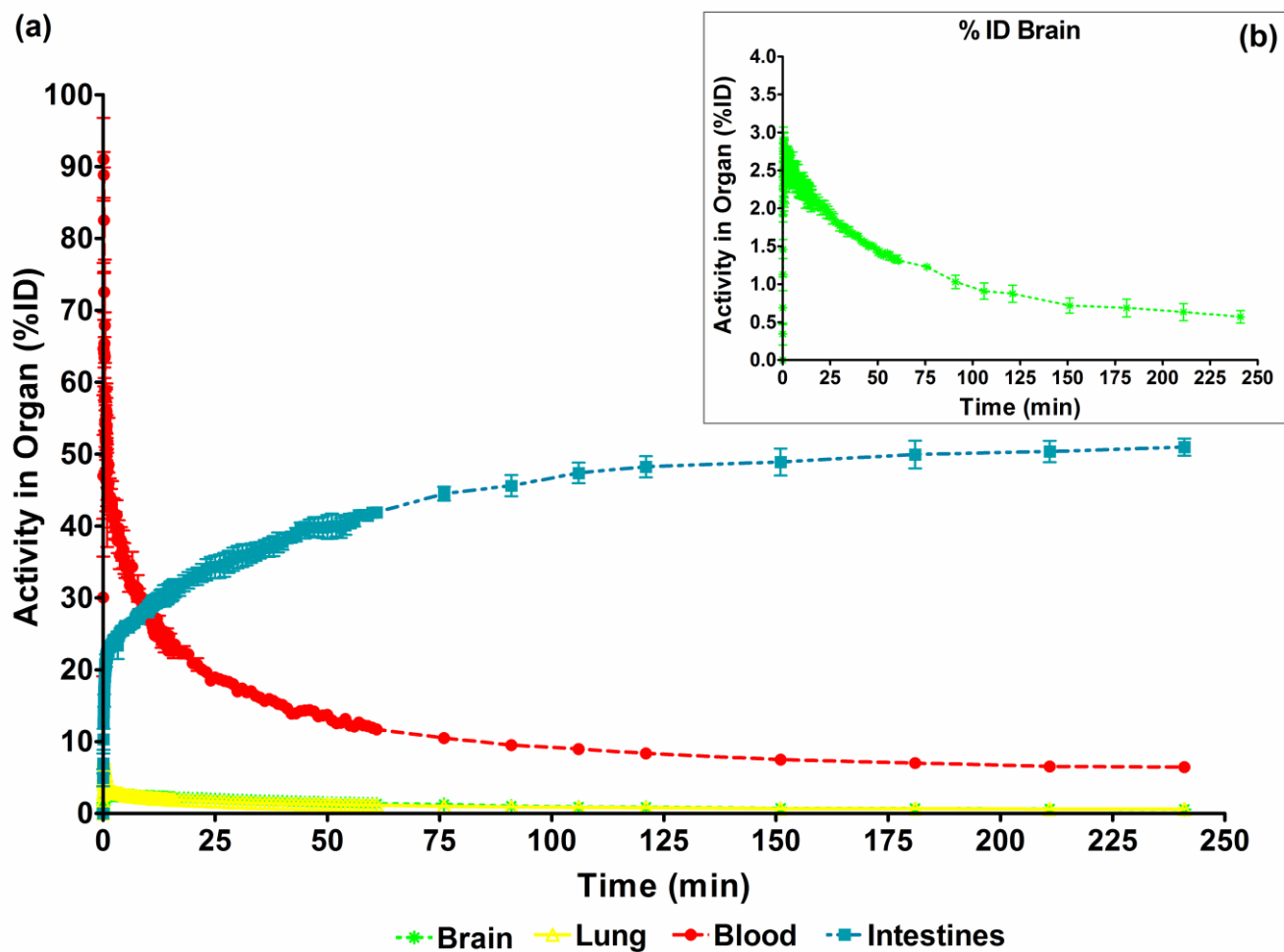


Figure 4.10 Time activity curves of ^{123}I -NKJ64 uptake in different organs.

(a) Time activity curves of ^{123}I -NKJ64 uptake in brain, lung, blood and intestine expressed as % ID and (b) time activity curve in brain. Data are presented as mean \pm SEM (n=3). Note the fast clearance from blood and lungs, the increasing levels of radioactivity in the intestine and the fast wash out from the whole brain.

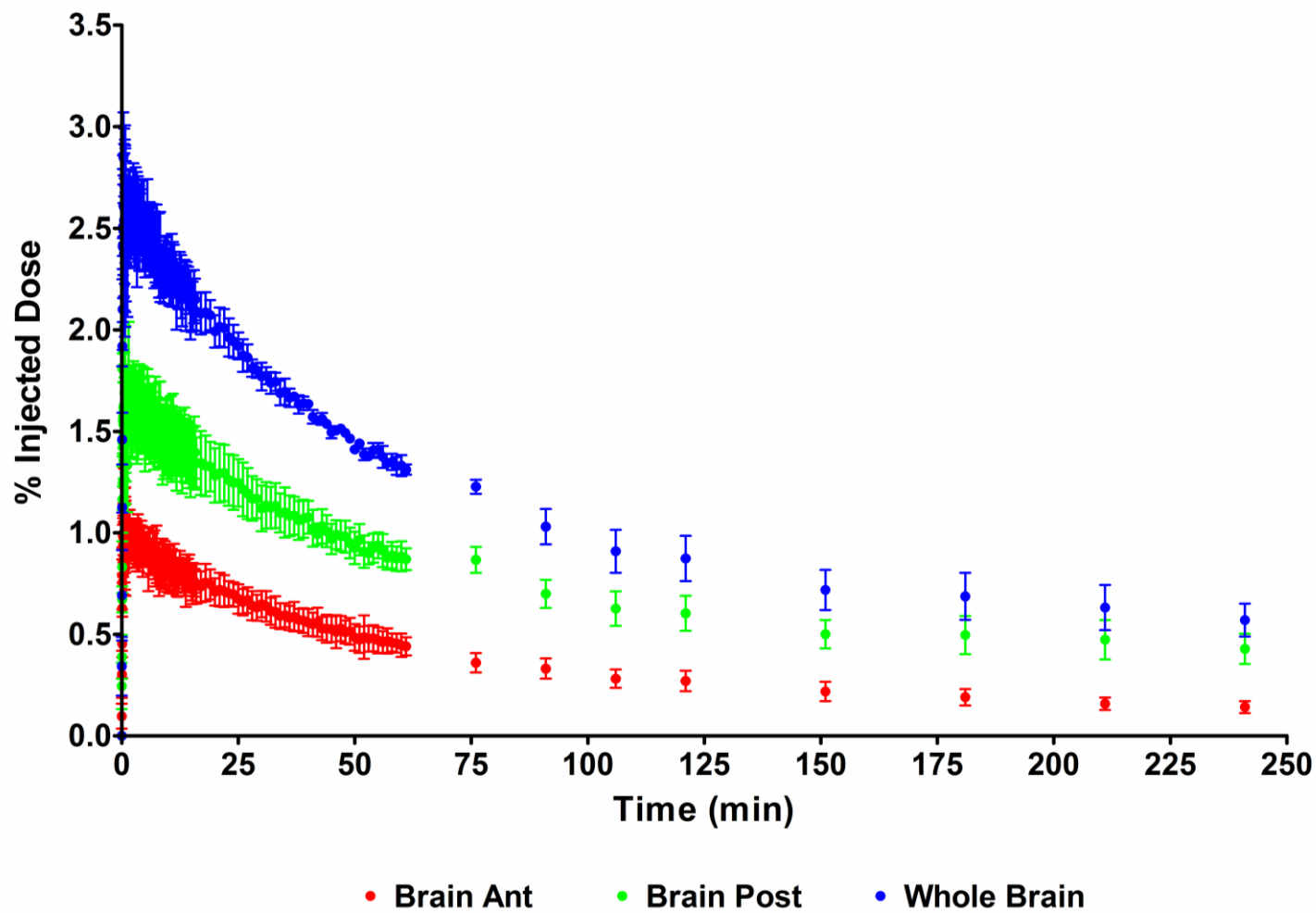


Figure 4.11 Time activity curves of ^{123}I -NKJ64 uptake in anterior brain, posterior brain and whole brain.

Data are presented as mean \pm SEM (n=3). Note the higher percentage injected dose in the posterior brain in comparison with the anterior brain over time.

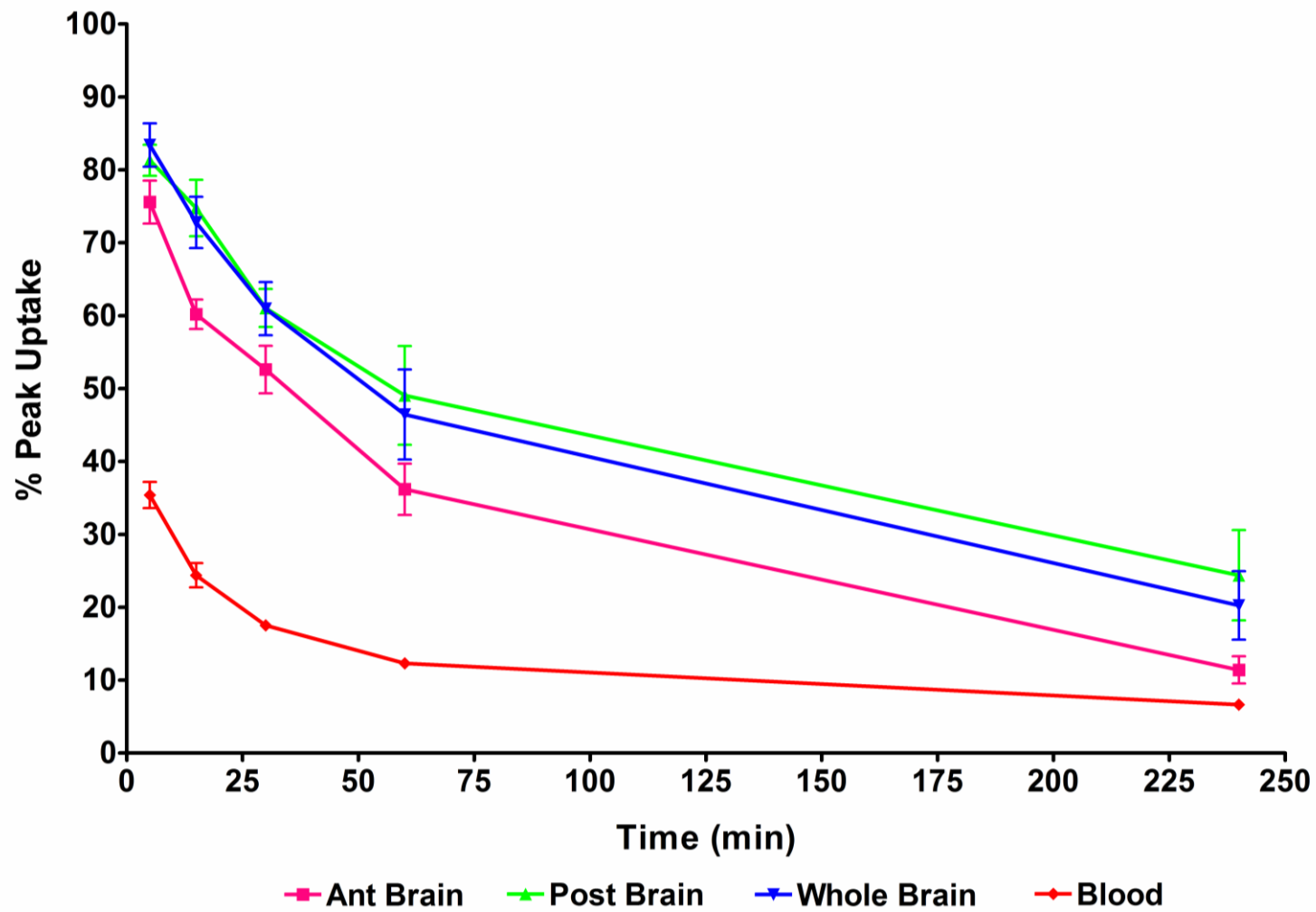


Figure 4.12 Percentage of peak uptake of ¹²³I-NKJ64 in anterior, posterior and whole brain and blood over time. Data presented as mean±SEM (n=3). Note the faster elimination of radioactivity from anterior brain in comparison with posterior brain.

To further determine the regional distribution of ^{123}I -NKJ64 in the brain following intravenous injection, *ex vivo* autoradiographic analysis was performed at 30 minutes post-injection (Figure 4.13a). The highest levels of radioactivity were in the locus coeruleus and anteroventral thalamus and there was relatively less radioactivity in the caudate putamen and cerebral cortex. The locus coeruleus to caudate putamen ratio was 2.84 ± 0.01 (mean \pm SEM, $n=3$). Administration of reboxetine prior to that of ^{123}I -NKJ64 significantly reduced the radioactive signal in the locus coeruleus (Figure 4.13a). The locus coeruleus to caudate putamen ratio was significantly reduced by more than 50% in reboxetine- compared to saline-treated rats (Figure 4.13b). A comparison of *in vivo/ex vivo* and *in vitro* autoradiograms is shown in Figure 4.14. Results from *in vitro* studies are consistent with *in vivo/ex vivo* pharmacological studies, where the highest level of radioactivity was seen in the NAT rich structures (locus coeruleus and anteroventral thalamus) and the lowest level was seen in the caudate putamen. Reboxetine displaced the locus coeruleus signal in both *in vitro* and *in vivo/ex vivo*, but did not reduce the amount of radioactivity in any of the extra-cranial organs or fluids collected (Table 4.3).

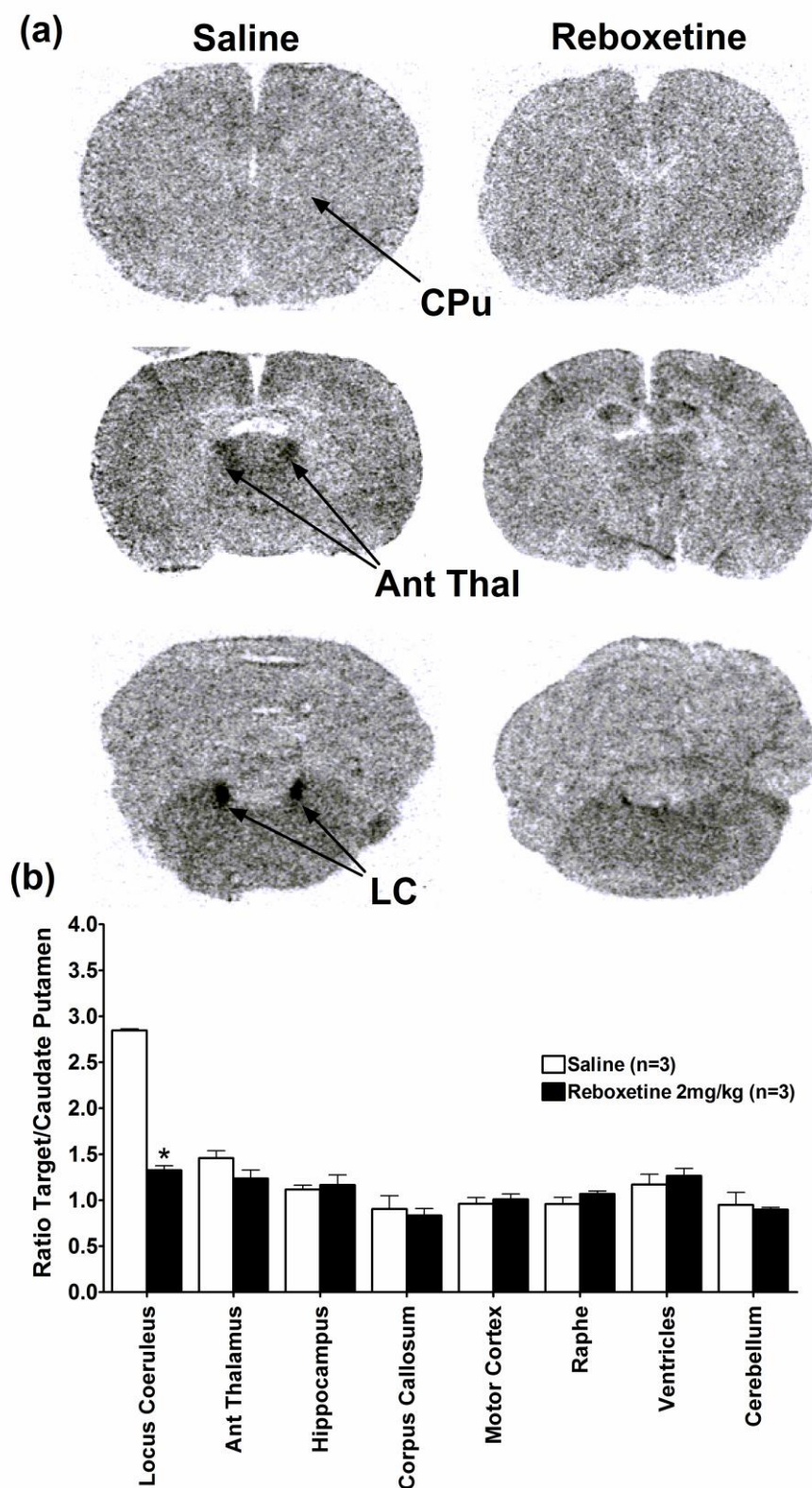


Figure 4.13 *In vivo/ex vivo* pharmacological studies results of $^{123}\text{I-NKJ64}$ in rat brain.

(a) *Ex vivo* autoradiograms of rat coronal brain sections 30 minutes post-injection of $^{123}\text{I-NKJ64}$. Rats were pre-treated with either saline or reboxetine (2.0 mg/kg; 15 minutes prior to $^{123}\text{I-NKJ64}$). The radioactive signal in the locus coeruleus of the reboxetine-treated rat is reduced compared to that in the saline-treated animal. (b) Target to non-target ratios in brain regions of rats pre-treated with either saline or reboxetine (data are presented as mean \pm SEM, n=3 per treatment group). The caudate putamen was selected as the non-target region due to the known low density of NAT binding sites. *p<0.05 (unpaired t-test).

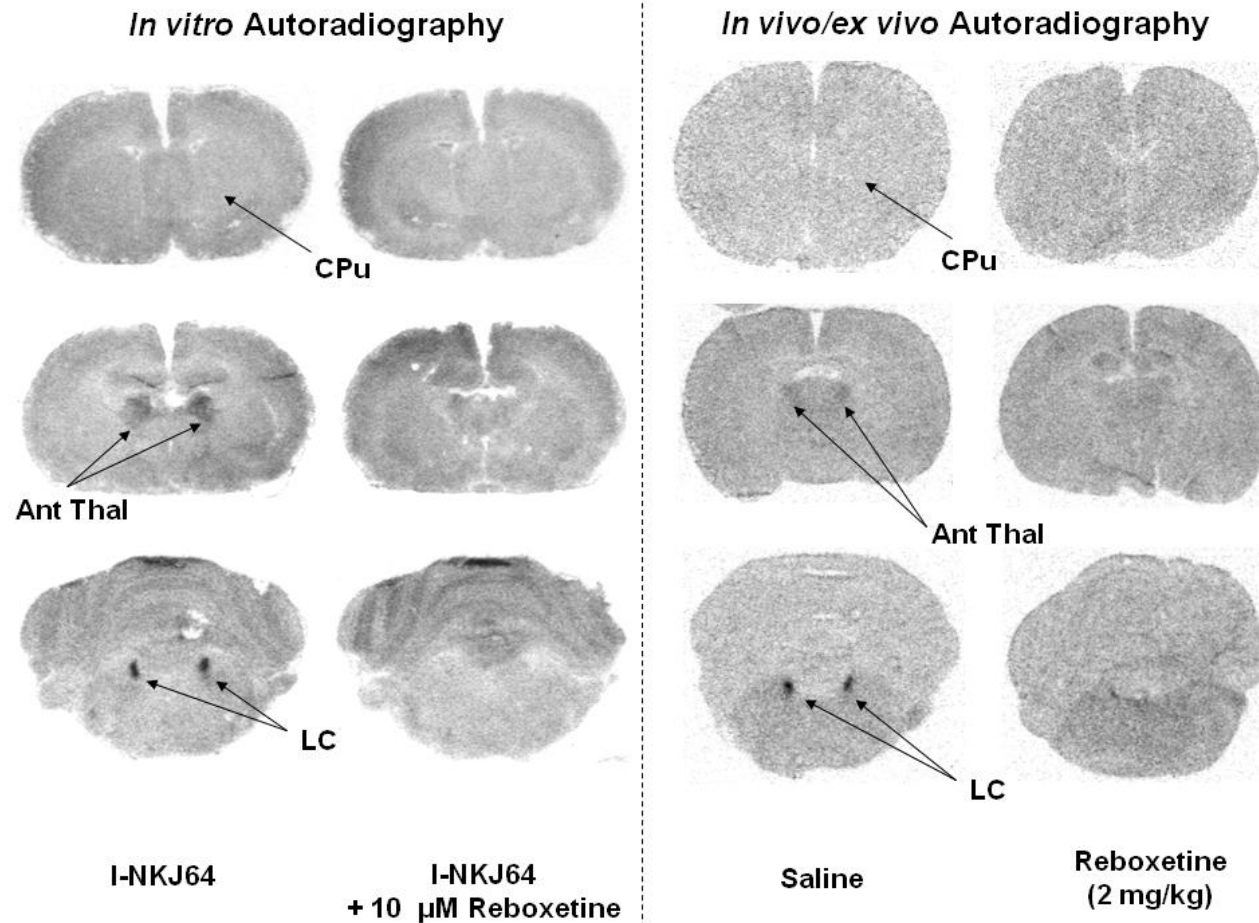


Figure 4.14 Comparative analysis of ¹²³I-NKJ64 rat brain autoradiograms.

In vitro and *in vivo/ex vivo* autoradiographic results. Note reduction of signal in locus coeruleus in reboxetine treated sections (left side figures) and animals (right side figures). Also note absence of differences in brain distribution *in vitro* and *in vivo* suggesting no brain-generated metabolites are produced *in vivo* follow intravenous injection of ¹²³I-NKJ64.

<i>Organ</i>	<i>Saline</i>	<i>Reboxetine (2.0 mg/kg)</i>
Urine	0.40±0.07	0.36±0.09
Blood	0.09±0.003	0.12±0.005
Faeces	0.06±0.01	0.08±0.02
Heart	0.39±0.04	0.44±0.03
Lung	3.82±0.35	4.85±0.05
Liver	0.95±0.02	1.20±0.12
Spleen	2.02±0.13	1.98±0.08
Stomach	1.04±0.10	1.87±0.17
Small Intestine	12.78±2.25	8.35±0.85
Large Intestine	0.47±0.04	0.49±0.03
Adrenal	1.42±0.12	1.85±0.19
Kidney	0.87±0.08	0.96±0.04
Bladder	0.51±0.05	0.52±0.07
Muscle	0.29±0.05	0.34±0.04
Bone (femur)	0.38±0.05	0.49±0.03
Testis	0.45±0.05	0.57±0.02
Fat Tissue	0.93±0.07	1.21±0.02
Cartilage	0.31±0.04	0.35±0.03
Thyroid	0.81±0.2	1.03±0.18

Table 4.3 Biodistribution of radioactivity in saline and reboxetine pre-treated rats at 30 minutes post-injection.

Data are expressed as %ID/g (mean±SEM, n=3). *p<0.05 (unpaired t-test).

4.4 Discussion

The biological evaluation of $^{123/125}\text{I}$ -NKJ64 in rodents showed that ^{125}I -NKJ64 has low nanomolar affinity (<5 nM) for the NAT in rat brain cortical homogenates. This is in accordance with previously obtained data showing that the K_i of NKJ64 against the specific NAT ligand, ^3H -nisoxetine, was less than 10 nM in rat whole brain homogenates (43). NKJ64 is the (2R,3S)-stereoisomer of the previously reported NAT SPECT radiotracer INER (or IPBM), which is the (2S,3S)-stereoisomer of reboxetine (further detail in section 3.1). INER has a K_i for NAT against ^3H -nisoxetine of less than 5 nM in rat whole brain homogenates and less than 1 nM in rat forebrain homogenates (114, 116). NKJ64 and INER are stereoisomers and therefore the determined K_D for ^{125}I -NKJ64 is consistent with the previous studies. However, this is the first report of the biological evaluation of the radiolabelled (2R,3S)-stereoisomer.

The rapid elimination of radioactivity from blood following intravenous injection of ^{123}I -NKJ64 supports the efficient delivery of the radiotracer to the tissues. The brain uptake of ^{123}I -NKJ64 measured by whole body dynamic planar imaging was 2.93% of injected

dose at 0.5 minutes post-injection, representing a rapid and marked accumulation of the radiotracer in the brain. This level of whole brain uptake compares favourably with other NAT radiotracers assessed in rats. For example, using ^{125}I -2-INXT, Kung *et al.* 2004, reported a maximum %ID/organ of 0.69 at 30 minutes post-injection (38) while Lakshmi *et al.* 2008, using ^{125}I -PYINXT, reported a maximum uptake of 0.54% ID/organ at 2 minutes post-injection (40). Other studies using (S,S)- ^{125}I -IPBM, (S,S)- ^{11}C -MeNER and (R)- ^{125}I -MIPP reported whole brain uptake of 0.89%, 0.53% and 0.45%, respectively, all at 5 minutes post-injection (37, 110, 116).

To obtain high resolution images of ^{123}I -NKJ64 distribution in rat brain, autoradiographic techniques were used. The locus coeruleus has the highest density of NAT in rat brain, followed by the anteroventricular thalamic nucleus; the cerebral cortex has low densities and the lowest density of NAT is in the caudate putamen (106, 135). The regional distribution of ^{123}I -NKJ64 binding sites as determined by *in vitro* autoradiography was similar to the known distribution of the NAT in the brain. The *ex vivo* distribution of ^{123}I -NKJ64 brain uptake 30 minutes post-injection was consistent with the *in vitro* distribution and the known regional densities of the NAT. The highest level of radioactivity revealed by both *in vitro* and *ex vivo* autoradiography was in the locus coeruleus. High levels of non-specific binding were detected when ^{125}I -NKJ64 was incubated with cortical homogenates *in vitro*, however, the labelling of the NAT by ^{123}I -NKJ64 in the locus coeruleus *in vivo* is supported by the finding that uptake of radiotracer was significantly reduced in this region following pre-treatment with the selective noradrenaline reuptake inhibitor, reboxetine. The present data are comparable to results reported by Wilson *et al.* 2003 using (S,S)- ^{11}C -MeNER showing that reboxetine pre-treatment significantly reduced the uptake of the radiotracer in rat brain (110). In baboons reboxetine pre-treatment resulted in up to 60% blocking displacement of ^{123}I -INER in NAT rich regions at 210 minutes post-injection (114). Similar levels of *in vivo* pharmacological blocking were achieved with ^{123}I -NKJ64 as have been reported previously with other NAT radiotracers.

One of the important properties an imaging agent should possess is a target:non-target ratio greater than 2 (40). Amongst all of the NAT radiotracers developed to date for PET or SPECT imaging, the highest target:non-target ratio reported is for (S,S)- ^{11}C -MeNER, a potent PET radiotracer. In rats at 60 minutes post-injection the hypothalamic:striatum ratio for (S,S)- ^{11}C -MeNER was 2.5 (110). Kung *et al.*, 2004 using ^{125}I -2-INXT and Lakshmi *et al.*, 2008 using ^{125}I -PYINXT (SPECT radiotracers) reported a hypothalamus:striatum ratio of 1.5 at 3 hours post-injection and 2.1 at 4 hours post-injection, respectively (38, 40). In the present study, using the NAT-rich locus coeruleus as the target region and the caudate putamen as the non-target region, the ratio for ^{123}I -NKJ64 at 30 minutes

post-injection was 2.8, as measured by *ex vivo* autoradiography. Although it is not possible to directly compare, the target:non-target ratio for ^{123}I -NKJ64 is greater than 2 and therefore is in line with other potent NAT radiotracers. Target:non-target ratio was measured at 30 minutes post-injection, based on the planar images obtained from whole body dynamic planar imaging which showed faster elimination from the anterior in comparison to the posterior brain regions (half-life of 35 minutes for anterior brain and 49 minutes for posterior brain, Table 4.2). Furthermore, at 30 minutes time-activity curves showed a difference in signal between the anterior brain region (where NAT density is low) and the posterior brain region (where the highest NAT density region, the locus coeruleus, is located) that was more pronounced than at earlier imaging time points. However, further *in vivo* high resolution dynamic imaging studies of the brain are desirable to confirm the regional specific binding distribution of ^{123}I -NKJ64 over time. Another important property of a radiotracer for brain imaging is the absence of substantial radiolabelled metabolites in the brain following intravenous injection. Comparison of ^{123}I -NKJ64 images from *in vitro* autoradiography (carried out at 4 °C) to those generated from *ex vivo* autoradiography, revealed a similar pattern of distribution. This observation suggests adequate *in vivo* stability of the radiotracer, at least in rats.

^{123}I -NKJ64 rapidly entered the lungs, reaching a maximum of 6% of injected dose consistent with previous reports of significant lung uptake for other NAT radiotracers (37-40, 116, 137). Both Kiyono *et al.* (2004) and Kanegawa *et al.* (2006), reported significant uptake in the lungs of ^{125}I -MIPP and ^{125}I -IPBM, respectively (37, 116). A putative explanation proposed by these authors for the observed lung uptake is the expression of neuronal NAT in the pulmonary endothelium (138). In contrast, Takano *et al.* (2008) suggested that a possible mechanism underlying accumulation of (S,S)-[^{18}F]FMeNER-D2 in the lungs is non-specific uptake by macrophages (137). Ding *et al.* (2003) also observed significant lung uptake of [^{11}C]MRB, however pre-treatment with desipramine failed to inhibit uptake into this organ (139). Similarly, the lung uptake of ^{123}I -NKJ64 was not reduced in reboxetine pre-treated compared to saline pre-treated rats. These findings demonstrate that radioactivity in the lungs following intravenous injection of ^{123}I -NKJ64 does not represent binding to the NAT. This conclusion is also supported by the short biological and effective half-lives of ^{123}I -NKJ64 in the lungs. Other peripheral organs such as the heart and the adrenals express NAT (38, 116, 139). However, uptake in these two organs was considerably lower than in the lungs, similar to previously developed NAT radiotracers that were also taken up minimally by the heart and adrenals (37-39, 116). Uptake in the heart and adrenals was not inhibited in reboxetine pre-treated compared to saline pre-treated rats suggesting that uptake in the heart and adrenals is predominantly non-specific and does not reflect binding to the

NAT. Low levels of radioactivity in the other organs examined, including testes and bone (with bone marrow) will result in low dosimetry for these radiosensitive tissues.

The main elimination route of radioactivity was intestinal as assessed by both whole body dynamic planar imaging and *ex vivo* dissection. Reboxetine is metabolised by cytochrome P450 3A4 in the liver (118) and since ^{123}I -NKJ64 is a reboxetine analogue it is possible it is metabolised by the same route. Therefore, the high levels of radioactivity in the small intestine could be due to rapid liver metabolism of ^{123}I -NKJ64. Neither kidneys nor bladder were detected during the 4 hours dynamic image acquisition and these organs, as well as urine, contained minimal amounts of radioactivity measured by *ex vivo* dissection. These results are consistent with minimal ^{123}I -NKJ64 elimination *via* renal filtration. Kung *et al.* 2004 and Lakshmi *et al.* 2008 also found a similar elimination pattern in their *ex vivo* dissection studies (38, 40). Other groups developing NAT SPECT radiotracers, however, have published results that suggest two elimination routes occurring simultaneously: the renal and the hepatointestinal route (37, 116). These observable differences in the elimination routes may be potentially explained by structural differences among the evaluated compounds.

In vivo stability is a desirable characteristic for any radiotracer (40). Free iodine is captured by the thyroid gland (140) and therefore free radioiodine concentrations due to breakdown of iodinated radiotracers must be kept as low as possible to minimise the dosimetry of this radiosensitive gland. Following administration of ^{123}I -NKJ64 the level of radioactivity in the thyroid was negligible which indicates minimal *in vivo* deiodination of the radiotracer. Further evidence supporting the *in vivo* stability of ^{123}I -NKJ64 is indicated by the low level of radioactivity present in the stomach.

Methodological considerations

Different methods have been used for determination of radiotracers K_i and K_D , including assays using cell lines overexpressing the brain transporter or receptor and assays using native tissues, namely rat and human brain tissue. Cell lines overexpressing NAT have been used to provide a convenient source of specific NAT protein for *in vitro* binding assays. For example, Lakshmi *et al.* 2008 used cells overexpressing NATs for determination of ^{125}I -PYINXT K_D (results outlined in section 3.1.2, Chapter 3)(40). However, homogenate binding assays in rat frontal cortex or striatum provides an *in vitro* assay for NAT affinity that is closer to the *in vivo* brain environment since other regulatory and structural proteins present on the cell membrane are included in the assay (38-41, 114). In fact, according to Kung *et al.* 2004, affinity results obtained with cell lines overexpressing NAT, SERT or DAT are conservative and do not account for the

potential for non-specific binding seen in brain (38). The variability of methods used to determine K_D and B_{max} by multiple groups makes comparisons between different radiotracers difficult. Even when the same assay methodology is used, inter-laboratory differences may influence the results. Therefore, care should be taken when comparing radiotracer affinity data. Based on the estimation of B_{max} , it has been suggested that the K_D of a useful NAT radiotracer should be approximately 40 times higher than the binding affinity of DAT radiotracers (38, 40). For example, if a successful DAT radiotracer has a binding affinity of 10 nM an equally successful NAT radiotracer would require a K_D value of 0.25 nM (38). This estimation is based on the difference in the B_{max}/K_D ratio for DAT versus NAT. Since the target density for a DAT radiotracer is significantly higher than for a NAT radiotracer, the target/non-target ratio should be higher for a DAT radiotracer compared to a NAT radiotracer at a given level of non-specific binding. However, some studies have shown a weak correlation between *in vitro* affinity and *in vivo* binding. For example, McConathy *et al.* 2004 observed a high *in vitro* affinity of ^{11}C -talopram and ^{11}C -talsupram for the NAT, however this high *in vitro* affinity did not translate to high specific binding *in vivo* (39). This highlights that radiotracer properties, other than affinity, including pharmacokinetics *in vivo*, metabolism and ability to penetrate the BBB, are also important for a radiotracer to be successful. Therefore, *in vivo* evaluation is essential for the characterisation of a novel radiotracer for use in human imaging.

In vivo whole body dynamic planar imaging was performed in order to determine whole body biodistribution and kinetics, brain uptake and elimination and excretion routes of ^{123}I -NKJ64. Since the advent of the gamma camera, multiple studies using animals and whole body dynamic planar imaging have been conducted (141-150). Most of them used rats or mice, but other animals such as rabbits, dogs, cats and non-human primates have also been imaged with the gamma camera. Examples of applications include radiotracer discovery, tumour imaging and drug delivery studies. This is, therefore, a well validated method for evaluation of *in vivo* biodistribution and kinetics of either novel or already established radiotracers. The evaluation of the biodistribution and kinetics of a radiotracer by *in vivo* dynamic planar imaging has multiple advantages over *ex vivo* dissection studies at selected time points (detailed in Section 1.2.2). Hence, whole body dynamic planar imaging was selected for the evaluation of ^{123}I -NKJ64 biodistribution and kinetics in rodents.

All *in vivo* and *ex vivo* experiments were carried out under anaesthesia. Although *in vivo* imaging is essential for evaluation of radiotracers in physiological and pathological systems, the use of anaesthesia, which is frequently necessary, creates some potential pitfalls in terms of data analysis, particularly when developing novel radiotracers (30, 33). The most common physiological effect of anaesthetic agents is induction of

hypothermia, but other more specific effects may arise. Barbiturates used for short-term anaesthesia have been shown to enter the brain rapidly and some negative effects have been linked to this particular type of anaesthetic, including respiratory depression, reduced stroke volume and hypotension. On the other hand, ketamine does not depress respiration or cardiac output, but has indirect sympathomimetic effects and increases noradrenaline plasma levels. These sympathomimetic effects may interfere with studies that involve sympathetic nervous system or experiments evaluating NAT. Using isoflurane, an inhalation anaesthetic agent, the cardiac function is better maintained than with injectable anaesthetics. Previous studies have shown an influence of anaesthesia on radiotracer uptake and other *in vivo* characteristics. For example, ketamine significantly increased binding of ^{11}C -labelled dopamine D1 receptor agonist, ^{11}C -SCH23390, in the striatum compared to conscious control animals. Conversely, pentobarbital significantly decreases the ^{11}C -SCH23390 binding in the striatum compared to conscious control animals. Animals anaesthetised with isoflurane showed significantly lower brain uptake of ^{11}C -SCH23390 than either awake animals or ketamine/xylazine anaesthetised animals (30). Urethane, on the other hand, produced a variety of endocrine effects and increase blood levels of glucose and adrenaline (151). Together, these studies demonstrated the importance of careful study design when considering the anaesthetic agent to be used. Ideally *in vivo* imaging in conscious animals would be preferable, particularly for imaging of brain receptors. Nevertheless, considerable technical challenges are still to be overcome prior to the general utility of *in vivo* imaging in the conscious state. For example, prior studies have shown that imaging while animals are awake may provoke acute stress, which has been implicated in the release of adrenaline and corticosteroids, leading to increase of heart rate and hyperthermia (30). All these previous studies show the complexity associated with the design of studies using living animals.

4.5 Conclusion

In summary, radiolabelled NKJ64 has a high affinity for NAT in rat brain. ^{123}I -NKJ64 has adequate stability *in vivo* in rats indicated by negligible thyroid and stomach uptake, and high target:non target ratio and brain uptake compared to previously developed NAT radiotracers. The distribution of ^{123}I -NKJ64 in the rodent brain after intravenous injection was consistent with that previously reported for NAT expression. Results showed that ^{123}I -NKJ64 binding to the locus coeruleus is displaceable *in vivo* by the selective noradrenaline reuptake inhibitor, reboxetine. Due to the size of the locus coeruleus, if ^{123}I -NKJ64 were to be used for SPECT, high resolution imaging would be required. In rats ^{123}I -NKJ64 has high non-specific binding and rapidly eliminates from the

brain, particularly the forebrain. The fast kinetics and high non-specific binding in rats are issues that need to be further addressed in higher species and using high resolution brain imaging, in order to establish the utility of ^{123}I -NKJ64 for SPECT imaging. Together, these findings suggest that ^{123}I -NKJ64 possesses most of characteristics required for a successful NAT imaging agent (8 out of 10, section 3.1.2, Chapter 3) and therefore further evaluation of ^{123}I -NKJ64 in non-human primates is warranted.

5 Biodistribution and pharmacokinetics of ^{123}I -NKJ64 in non-human primate brain

Results from the preliminary evaluation of $^{123/125}\text{I}$ -NKJ64 in rodents (Chapter 4) indicated that further evaluation in non-human primates was required in order to determine the utility of ^{123}I -NKJ64 as a SPECT imaging agent for the NAT. In this chapter studies using non-human primates and ^{123}I -NKJ64 were performed at Molecular NeuroImaging (MNI) LLC and Yale University, New Haven, Connecticut, USA.

5.1 Introduction

In this introductory section, the noradrenergic system in non-human primate brain is outlined, in order to facilitate the interpretation of the imaging results. In addition, a brief overview of the main principles of kinetic modelling is provided in this section, since modelling was used to quantify the biodistribution and pharmacokinetics of ^{123}I -NKJ64 in baboon brain.

5.1.1 Noradrenergic system in non-human primate brain

The normal topography of NAT in non-human primate brain was investigated by Smith *et al.* 2006 using autoradiography with ^3H -nisoxetine (Table 5.1). In rhesus monkey brain the locus coeruleus had the highest density of NAT, followed by the raphe complex, thalamus and hypothalamus, amygdala, cortex and cerebellum. The lowest NAT density was found in the striatum. Overall the regional distribution of NAT in non-human primate brain is similar to the distribution of NAT in rodent brain, with comparable relative binding densities in areas such as brainstem and hypothalamus. However, the maximum density of NAT measured by autoradiography with ^3H -nisoxetine is considerably lower in non-human primates (Table 5.1) than in rodents (Chapter 4, Table 4.1). Differences between non-human primate brain and rodent brain were found in the thalamus, hippocampus and amygdala. The highest NAT density in monkey thalamus was seen in the midline and intralaminar structures. Conversely, in rats the highest NAT density in the thalamus was found in the anteroventral thalamic nucleus. In rodents, there was moderate ^3H -nisoxetine binding in the dentate gyrus of the hippocampus. On the contrary, in the monkey brain, the dentate gyrus showed low NAT density, indicating that contributions of noradrenaline to learning functions in primates may be different from rodents (152).

<i>Brain Region</i>	<i>³H-nisoxetine Binding (fmol/mg)</i>
Cortex	
Anterior cingulate (area 24)	13.49 ± 0.8
Medial PFC (area 26)	21.20 ± 1.5
Medial PFC (area 32)	13.34 ± 2.3
Gyrus rectus (area 14)	12.80 ± 0.6
Orbital PFC (area 13)	11.03 ± 0.3
Dorsolateral PFC (area 46)	10.23 ± 0.1
Somatosensory (area 3a)	11.98 ± 1.1
Somatosensory (area 3b)	12.96 ± 0.9
Motor (area 4)	11.68 ± 1.3
Entorhinal	9.91 ± 1.0
Precommissural striatum	
Anterior caudate	5.80 ± 0.6
Anterior putamen	5.42 ± 0.7
Anterior nucleus accumbens	5.67 ± 1.2
Posterior caudate	4.91 ± 0.8
Posterior putamen	5.18 ± 0.3
Accumbens shell (ventral)	13.01 ± 1.8
Accumbens core	9.31 ± 0.7
Bed nucleus of the striatus terminalis	
Lateral dorsal	45.63 ± 5.5
Medial	25.88 ± 1.5
Lateral	23.24 ± 1.9
Ventral	35.00 ± 3.0
Hypothalamus	
Paraventricular	53.87 ± 1.2
Periventricular	50.39 ± 3.7
Medial preoptic	23.40 ± 2.5
Lateral preoptic	28.45 ± 2.3
Supraoptic	40.23 ± 1.9
Arcuate	36.86 ± 3.1
Ventromedial	30.06 ± 5.3
Dorsomedial	28.21 ± 1.8
Lateral	23.7 ± 2.8
Hippocampus	
CA1-4	9.19 ± 1.9
Dentate gyrus	12.77 ± 2.2
Subicular cortex	7.86 ± 1.7

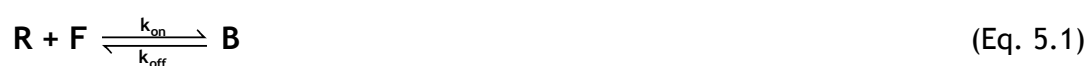
Table 5.1 Distribution of specific ³H-nisoxetine binding to NATs in rhesus monkey brain.
Data are mean±S.E.M, adapted from (152).

Brain Region	³H-nisoxetine Binding (fmol/mg)
Thalamus	
Paraventricular	71.62 ± 3.9
Intermediodorsal	32.14 ± 5.9
Mediodorsal, medial	27.88 ± 4.5
Centromedial	58.92 ± 7.2
Reuniens	47.48 ± 8.3
Paracentral/centrolateral	22.89 ± 1.1
Raphe complex	
Dorsal raphe	
Intrafascicular division	135.69±10.6
Ventral division	146.24±16.7
Ventrolateral division	61.64±16.6
Dorsal division	75.17±17.8
Caudal division	120.37±1.9
Caudalinear nucleus	77.41±5.1
Median raphe	70.44±4.7
Brainstem	
Locus coeruleus	219.63±9.6
Lateral parabrachial	137.75±22.6
Subcoeruleus nucleus	146.94±11.7
Dorsal tegmental area	47.75±8.1
A1 noradrenergic cell group	27.88±2.0
Cerebellum	10.41±1.7

Table 5.1 (cont).

5.1.2 Brain imaging and kinetic modelling - main concepts and considerations

Different quantification methods can be applied to describe the brain kinetics, biodistribution and binding properties of radiotracers *in vivo*. Quantification of the binding of a radiotracer to molecular targets, such as receptors, with PET or SPECT is based on an understanding gained from *in vitro* ligand binding assays obtained over several decades, where the equilibrium binding reaction occurs between receptors (R) and free ligand (F) to form the bound ligand-receptor complex (B), with rate constants k_{on} and k_{off} (Equation 5.1).



Similarly, the concept of binding potential (BP), which can be defined as the ratio of B_{\max} to K_D (Equation 5.2), was adopted as an outcome measure of *in vivo* imaging experiments.

$$BP = \frac{B_{\max}}{K_D} = B_{\max} \times \frac{1}{K_D} = B_{\max} \times \text{affinity} \quad (\text{Eq. 5.2})$$

Other measures have been adopted from clinical pharmacology. For example, volume of distribution (V_T), which in pharmacology refers to the volume of blood (or plasma) that would be required to account for the amount of drug in the entire body, has been adapted in two ways in the field of *in vivo* imaging. First, the target region is a particular organ, for example the brain, rather than the whole body; and second, instead of referring to the amount of drug in the entire organ, the V_T is expressed as the amount of radiotracer in a volume of tissue. For example, if the radiotracer concentration at equilibrium in the striatum is $100 \text{ kBq}\cdot\text{cm}^{-3}$ and in plasma is $5 \text{ kBq}\cdot\text{cm}^{-3}$, then its V_T will be $20 \text{ mL}\cdot\text{cm}^{-3}$. V_T *in vivo* is mathematically unitless, however it is important to assign $\text{mL}\cdot\text{cm}^{-3}$ to clarify that it is a ratio of millilitres of reference fluid to a volume of tissue. Thus, on the given example, a V_T of $20 \text{ mL}\cdot\text{cm}^{-3}$ means that 20 mL of plasma are necessary to account for the radiotracer in 1 cm^3 of the brain region.

Another important quantification method for analysis of brain radiotracer imaging is the measurement of receptor occupancy and displacement *in vivo* (153). Occupancy can be determined by imaging the brain at baseline conditions and then again following pre-administration of a non-radioactive drug that binds to the target receptor. The difference between radiotracer uptake and kinetics between the two measurements reflects the occupancy of the receptor by the drug (112-113). The measurement of radiotracer displacement by non-radioactive drugs can be determined in a single study. Following equilibrium, a non-radioactive drug is given as a bolus and the concentration in different brain regions before and after the drug administration is measured. The difference between radiotracer concentration before and after drug administration provides a measure of radiotracer displacement. Quantification of displacement can be used, for example, to investigate radiotracer affinity and selectivity for the target *in vivo*. In addition, displacement studies and occupancy measurements can be used to aid drug discovery, to investigate properties of currently available drugs and to determine best clinical dosing protocols.

Quantification of BP, V_T and occupancy *in vivo* can be achieved by applying mathematical models to correlate the time-activity curves obtained from *in vivo* measurements with the properties of the receptors and their interaction with the

radiotracer. The modelling approach that is widely used is compartmental analysis, in which a specified number of compartments communicate with each other *via* first-order kinetics (16). In order to apply kinetic models, some assumptions need to be made. The first is the “tracer principle”, which states that the physiological processes and molecular interactions are not influenced by the SPECT or PET measurement. This is considered to be an appropriate assumption since the injected mass of a high specific activity radiotracer is very low and therefore it is unlikely to have effects on physiology or molecular interactions (5). The second assumption states that physiological processes and molecular interactions are in a constant (or steady) state during the SPECT or PET measurement. This is an extension of the previous assumption and deals with the influence of the SPECT or PET measurement on the system. During the measurement period, the parameters of perfusion and metabolism should be constant. Finally, the compartmental model analysis relies on the assumption that the concentration in each compartment is homogenous (153).

Multiple models can be used to describe *in vivo* data, including for example, a one-tissue compartmental model (1T model) and a two-tissue compartmental model (2T model) (Figure 5.1). The 2T model is frequently used for modelling receptor binding of brain radiotracers. In this case, compartment 1 represents the vasculature, compartment 2 the exchangeable radiotracer pool and compartment 3 the trapped or bound radiotracer pool. The kinetics of the third compartment represent the exchange of the radiotracer on and off the receptor binding sites (16). Non-invasive alternatives to models that require arterial blood sampling, i.e. 1T and 2T models, are the reference tissue models (Figure 5.2). These models use a brain region devoid of specific binding as a reference tissue and calculate BP from V_T for both the target (specific) tissue and the reference tissue. These models take into account differences in delivery and free concentration between the target (specific) and reference tissues. The reference region tissue curve is used as an indirect input function and therefore avoids the need for arterial blood sampling.

One-tissue compartment model



Two-tissue compartment model



Figure 5.1 One tissue and two tissue compartmental model schematics.

Reference tissue model

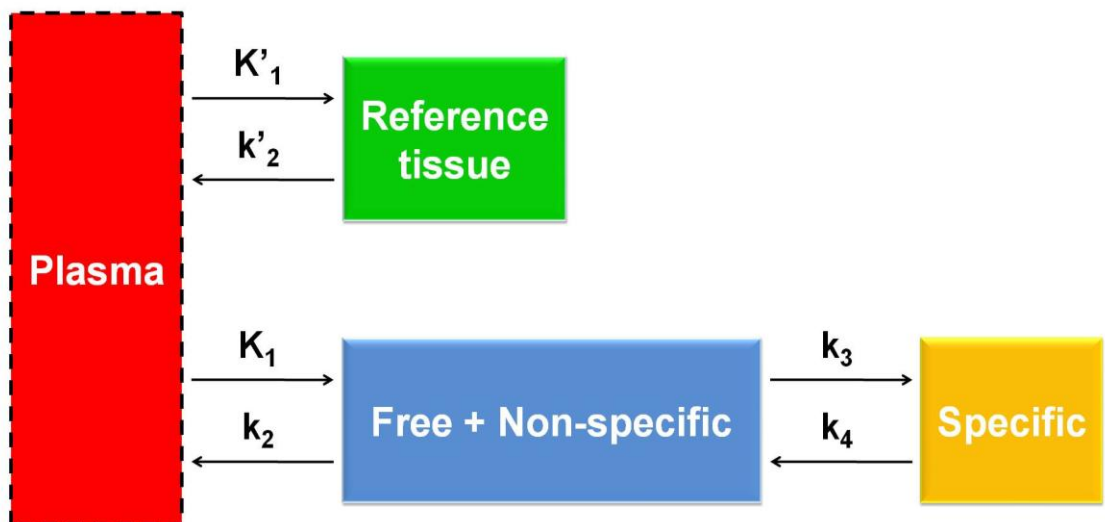


Figure 5.2 A reference tissue model schematic.

5.1.3 Hypothesis and aims

It was hypothesised that ^{123}I -NKJ64 distribution and kinetics in baboon brain could be investigated by applying compartmental analysis. It was also hypothesised that ^{123}I -NKJ64 distribution in baboon brain would be consistent with known NAT labelling in non-human primate. The main aim of this chapter was to investigate the distribution and kinetic properties of ^{123}I -NKJ64 in baboon brain as measured by SPECT, in order to determine its utility as a radiotracer for imaging of NAT in brain.

5.2 Material and Methods

Image acquisition and metabolite analysis were performed by colleagues at Yale University, USA and MNI LLC, New Haven, CT, USA, respectively. The radiosynthesis of ^{123}I -NKJ64 was performed by colleagues at MNI LLC, New Haven, CT, USA using previously described methodology for the production of ^{123}I -INER (114) and the stannyl precursor of NKJ64 provided by Nicola Jobson, University of Glasgow (details in Chapter 3).

5.2.1 Non-human primates

All procedures using non-human primates were conducted at Yale University, USA in accordance with institutional animal care protocols and in compliance with federal regulations. Two ovariectomised adult female baboons (*Papio anubis*, 14 and 18 kg) were used for *in vivo* evaluation of ^{123}I -NKJ64 reported in this chapter. Handling of the animals during the procedures was performed by colleagues at Yale University, USA.

5.2.2 Animal general preparation and monitoring

Baboons were fasted for 24 hours prior to imaging studies. On the imaging day, the baboon was first anaesthetised with intramuscular ketamine (10 mg/kg) and glycopyrrolate (0.1-0.2 mg/kg), transferred to the SPECT camera and immediately intubated with an endotracheal tube for continued anaesthesia with 2.5% isoflurane administered through a re-breathing circuit. A period of at least 2 hours between induction of anaesthesia and radiotracer injection was allowed, in order to stabilise the baboons under anaesthesia and minimise the effects of the initial administration of ketamine on ^{123}I -NKJ64 uptake, distribution and kinetics. An intravenous perfusion line was established in a femoral vein for injection of fluids for hydration and, if necessary, collection of blood samples for metabolite analysis. When arterial blood samples were required, a second line was established in a femoral artery. In the contralateral leg, an additional venous line was used for injection of the radiotracer. Body temperature was maintained using a heated water blanket and monitored by rectal thermometer. Vital signs, including heart rate, respiration rate, blood pressure and body temperature, were monitored every 15 minutes.

5.2.3 General SPECT acquisition protocol

SPECT studies were performed using a Neurofocus SPECT camera (Neurophysics Inc., USA), with a ring of 12 wide-aperture pinhole collimator detectors. Data acquisition started immediately after radiotracer injection using consecutive dynamic SPECT scans, where detectors moved side-to-side and in and out to completely sample each slice (154-155). The duration of each scan was approximately 20 minutes and a total of up to 18 slices were acquired. An energy window of 10% centred at 159 keV, 128×128×64 matrix, zoom of 1 and slice thickness of 5.0 mm were used for acquisitions starting at 0 minutes post-injection. Acquisition duration was 240 minutes for bolus baseline experiments and 420 minutes for bolus plus constant infusion studies with displacement drug. Raw SPECT data was reconstructed using Neurofocus proprietary software (Neurofocus Inc., USA) and the manufacturer's recommended iterative reconstruction algorithm, which was based on maximum a-posteriori (MAP) reconstruction methods, similar to algorithms used for scanning microscopes (154).

5.2.4 Administration of ¹²³I-NKJ64 and displacer

Two baboons were used for bolus baseline studies, in which arterial blood was collected, in order to perform kinetic modelling analysis (injected dose was 222 MBq for baboon 1 and 224.96 MBq for baboon 2). In addition, baboon 1 was also used for a displacement study (injected dose of 264.18 MBq) using reboxetine (Tocris Bioscience, USA), in which venous blood was collected (Figure 5.3). The displacement study was conducted using a bolus plus constant infusion protocol. The bolus/infusion (B/I) ratio (or K_{bol}) was calculated to be 2.5 hours using PMOD 3.203 software (PMOD Technologies, Switzerland) and results from bolus baseline studies. A Gemini PC 1 (IMED Inc., USA) infusion pump with 60 mL syringes was used for infusion of the radiotracer. Upon equilibrium, which was estimated to occur between 2.5 and 3 hours post radiotracer administration (based on estimations using PMOD 3.203 software), a single bolus of 2.0 mg/kg of reboxetine was injected intravenously.

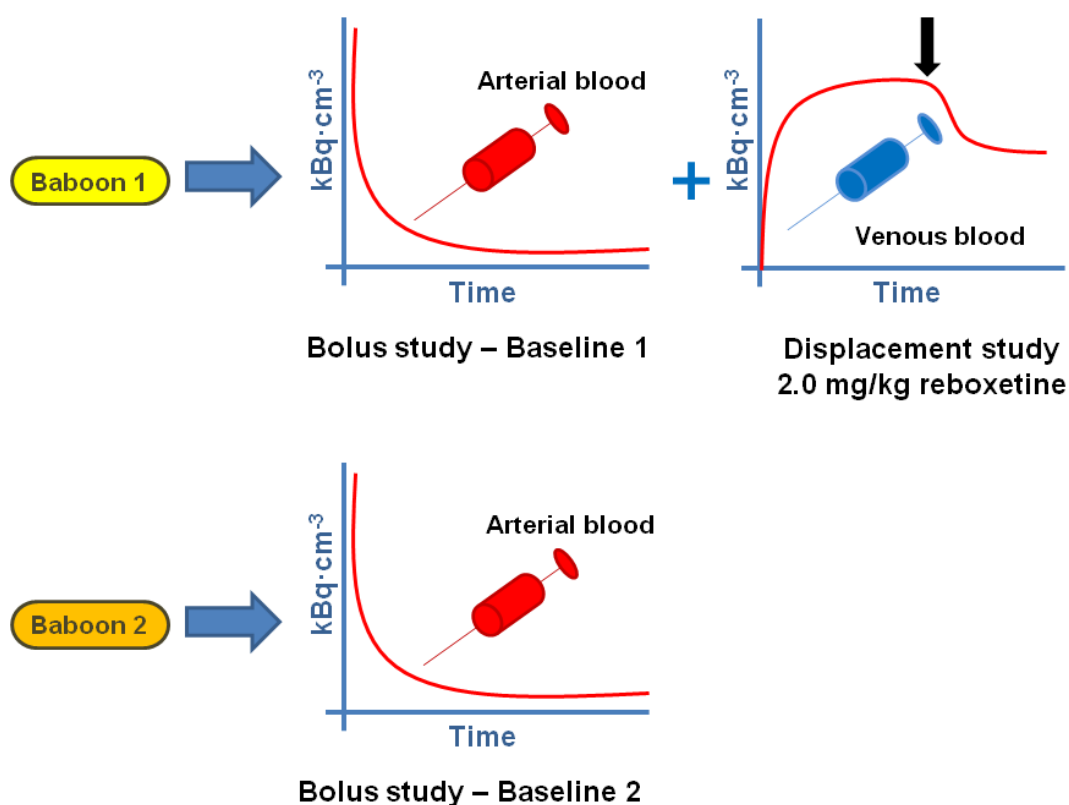


Figure 5.3 Schematic outline of the experimental procedure in baboons using $^{123}\text{I-NKJ64}$. Arterial blood was collected for baseline bolus experiments and venous blood was collected for displacement studies. Injection of reboxetine intravenously during the displacement study is represented by the black arrow (top right graph).

5.2.5 Analysis of plasma pharmacokinetics

For studies using the radiotracer bolus paradigm, i.e. baseline experiments, arterial blood samples (4-5 mL) were obtained from the femoral artery at baseline prior to start of the study (-5 minutes) and at 1, 3, 5, 10, 15, 30, 60, 120, 180 and 240 minutes post radiotracer injection. For displacement studies, where a bolus plus constant infusion paradigm was used, venous blood samples were collected at 15, 30 and 45 minutes prior to reboxetine injection and 15, 30, 45, 60 and 120 minutes following reboxetine administration. The samples were collected into ethylenediaminetetraacetic acid (EDTA)-coated tubes. Processing and analysis of blood was performed at the MNI LLC laboratories, using previously established methodology (156-159). Briefly, radioactive blood samples and blood samples incubated with radiotracer standards were centrifuged at 1800 g for 10 minutes. The concentration of radioactivity in plasma and in whole blood was counted in equal volume aliquots (50-200 μL) in an automatic well-type γ -counter. All radioactivity measurements were decay corrected to the time of radiotracer injection. Plasma protein extraction was performed three times with equal volumes of ethyl acetate. The percentage of extraction was calculated from the activity

in the aqueous phase counted before and after extraction at a constant geometry and corrected for decay. Beginning with samples of lowest activity, selected organic extracts were evaporated to dryness on a rotary evaporator under argon in a 37°C water bath. The residue was dissolved in 82.5 µL methanol, diluted with 67.5 µL water and injected onto analytical HPLC for metabolite quantification (157).

5.2.6 Image processing and co-registration with magnetic resonance images

Reconstructed scans were imported into PMOD 3.203 software and merged into a single file for image processing (Figure 5.4a). All image processing was performed using PMOD tools, starting with decay correction (Figure 5.4b). Motion correction was performed by creating an average image of consecutive scans with absence of motion, which was then used as a reference for rigid matching co-registration to all scans in the current study (Figure 5.4c). Attenuation correction was performed by applying the Chang algorithm (attenuation coefficient = 0.011 mm⁻¹) to a semi-automatically drawn volume of interest (VOI) of the object of study (Figure 5.4d) (160).

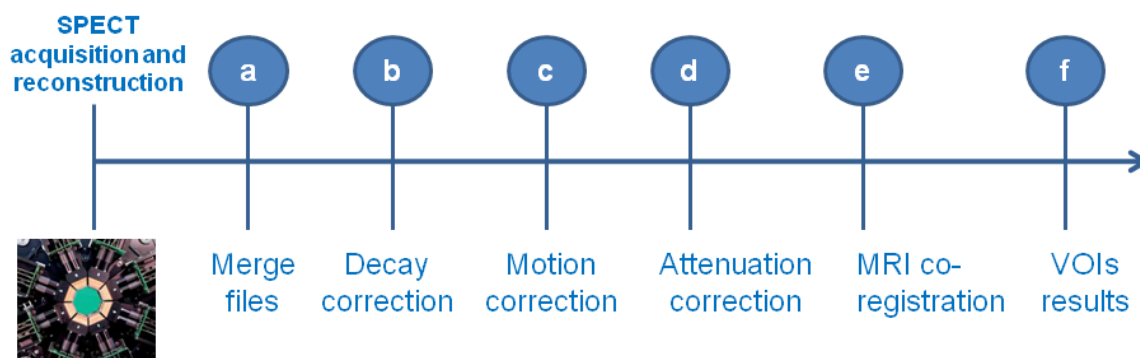


Figure 5.4 Summary of the main steps of SPECT image analysis and processing.

T1-weighted MR images were acquired with a GE Signa unit (General Electric, USA) at 1.5 T. The T1 sequence was a spoiled gradient recall protocol with the following settings: TR=25 ms, TE=5 ms, NEX=2, matrix=256×256, field of view = 16 cm. T1-weighted MR images were reduced from an initial matrix of 256×256 with 112 axial slices (axial slice thickness = 0.7 mm) to a 128×128 matrix, with 20 axial slices (axial slice thickness = 2.8 mm). Each animal used for the current study had a brain MR scan for purposes of image co-registration and placement of VOIs for SPECT quantification. All VOIs were drawn bilaterally; however due to the lack of considerable differences between VOIs in left and right hemispheres, the results for the average VOI are reported. For each animal, a standard VOI template included the following brain

regions: brainstem, midbrain, thalamus, caudate, putamen, frontal cortex, occipital cortex, cerebellum and subcortical white matter.

Average images of SPECT data were generated by averaging the scans presenting the highest radioactivity from cortical and subcortical brain structures. The average image generated was then co-registered to a MR template from the same animal using an automatic rigid matching tool or when necessary manual alignment of both imaging modalities, by adjusting translation and rotation of the images (Figure 5.4e). The transformation matrix was saved and consequently applied to all individual dynamic scans of the corresponding co-registered SPECT study. Finally, the MR-derived VOIs templates were apposed to the final co-registered SPECT images for generation of time-activity curves (Figure 5.4f). The data obtained was saved as an Excel spreadsheet or when kinetic modelling was performed (i.e. bolus studies) data was transferred to the PMOD kinetic modelling menu, to allow the application of different kinetic models to the data.

5.2.7 Data analysis

Time-activity curves were generated for each brain region and arterial plasma curves were corrected for metabolites. Standard uptake values (SUV) were calculated according to equation 5.3 and percentage injected dose (%ID) according to equation 5.4. The target:non-target ratio was expressed as SUVr, i.e. SUV value of target region divided by SUV of occipital cortex, which had been defined as the reference region. The percentage washout from the brain was determined using equation 5.5.

$$\text{SUV} = \frac{\text{Concentration VOI target}}{\frac{\text{Injected dose}}{\text{Animal weight}}} \quad (\text{Eq. 5.3})$$

$$\%ID = \frac{\text{Concentration VOI target}}{\text{Injected dose}} \times \text{calibration factor} \quad (\text{Eq. 5.4})$$

where the calibration factor = 1.35. The calibration factor was determined by colleagues at MNI LLC, CT, USA following cross calibration between the SPECT camera and a dose calibrator.

$$\% \text{ Washout} = \frac{\text{Initial conc. VOI target} - \text{Final conc. VOI target}}{\text{Initial conc. VOI target}} \times 100 \quad (\text{Eq. 5.5})$$

where conc. = concentration. The initial and final concentrations were the radioactive concentrations at beginning and end of acquisition.

The kinetic properties of ^{123}I -NKJ64 following bolus studies were calculated using PMOD and two different kinetic models: 1T and 2T compartmental models (153). The goodness of fit was assessed by evaluating the Akaike information criterion (AIC), the Schwartz criterion (SC, also denoted Bayesian information criterion) and the model selection criterion (MSC). The model presenting the lowest AIC and SC values and highest MSC value was defined as the preferred model. Arterial input functions were generated using the blood sampling results and were used to obtain kinetic parameters using 1T and 2T model. The displacement study data was plotted as $\text{kBq}\cdot\text{cm}^{-3}$ or SUVr against time, in order to identify and quantify the amount of displacement obtained post-administration of 2.0 mg/kg of reboxetine. GraphPad Prism 4.0 (GraphPad Software, USA) was used for curve fitting.

5.3 Results

The results from blood sampling following bolus injection of ^{123}I -NKJ64 are shown in Figures 5.5 and 5.6. The elimination and metabolism patterns of ^{123}I -NKJ64 in arterial blood were similar in both baboon 1 and 2. At 60 minutes post-injection the fraction of parent compound remaining in arterial plasma in baboon 1 was 31%, reaching a value of less than 14% at 240 minutes post-injection (Figure 5.5 and Table 5.2). In baboon 2 the fraction of parent compound remaining in arterial blood was 36% at 60 minutes post-injection and less than 26% at 240 minutes post-injection (Figure 5.6 and Table 5.2). Examples of HPLC chromatograms obtained from analysis of arterial blood samples taken at multiple time points following bolus injection of ^{123}I -NKJ64 are shown in Figure 5.7. SPECT images demonstrating the distribution of ^{123}I -NKJ64 in the brains of baboon 1 and baboon 2 are shown in Figures 5.8 and 5.9, respectively. A homogeneous distribution of the radioactivity was observed, such that the uptake in the brainstem, the region of baboon brain richest in NAT, was similar to that in other brain regions. Following intravenous bolus injection of ^{123}I -NKJ64, whole brain uptake peaked at 20 minutes with a brain percentage injected dose of 2.86% and 3.47% for baboon 1 and baboon 2 respectively. A rapid washout from the brain was observed (Figure 5.10) and at 240 minutes post ^{123}I -NKJ64 injection, 73% of whole brain initial uptake was eliminated (Table 5.3). The lowest uptake was found in the occipital cortex and

cerebellum, while the highest uptake was observed in the thalamus, caudate and putamen. The uptake in different brain regions was as follows: thalamus, caudate and putamen > midbrain, brainstem and subcortical white matter > frontal cortex, cerebellum and occipital cortex (Figure 5.10). The high level of radioactivity in the caudate and putamen compromised the quantification of ^{123}I -NKJ64 binding ratios and therefore these regions were not used as a reference regions. Consequently, for calculation of target:non-target ratios, the occipital cortex was used as the non-target region, as it was the brain region with the lowest radioactive concentration. Target:non-target ratios, expressed as target SUV relative to occipital SUV, were highest in the thalamus, caudate and putamen and lowest in the frontal cortex and cerebellum (Figure 5.11).

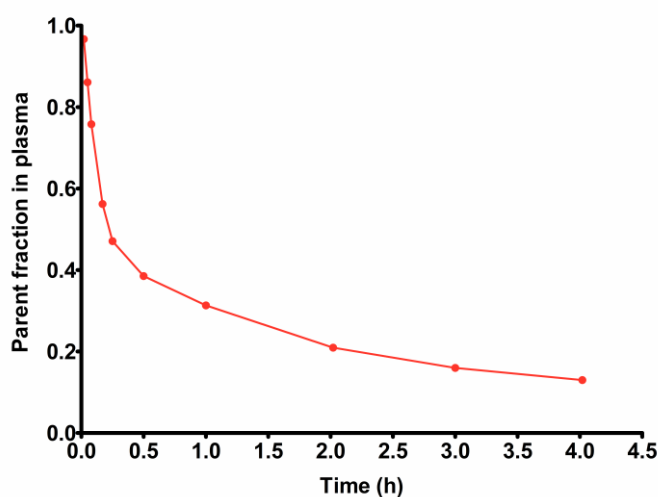


Figure 5.5 Parent radiotracer fraction present in arterial plasma following bolus injection of ^{123}I -NKJ64 in baboon 1.

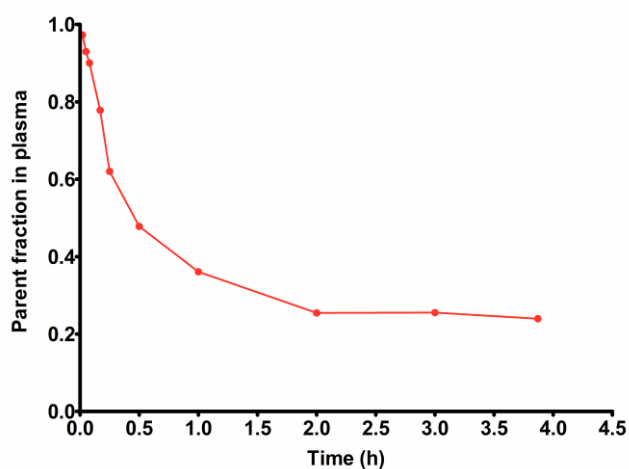


Figure 5.6 Parent radiotracer fraction present in arterial plasma following bolus injection of ^{123}I -NKJ64 in baboon 2.

Time (min.)	Percentage of parent in arterial blood (%)	
	Baboon 1	Baboon 2
30	47.11	62.04
60	31.32	36.10
240	13.00	23.96

Table 5.2 Percentage of ^{123}I -NKJ64 present in arterial blood over 4 hours.

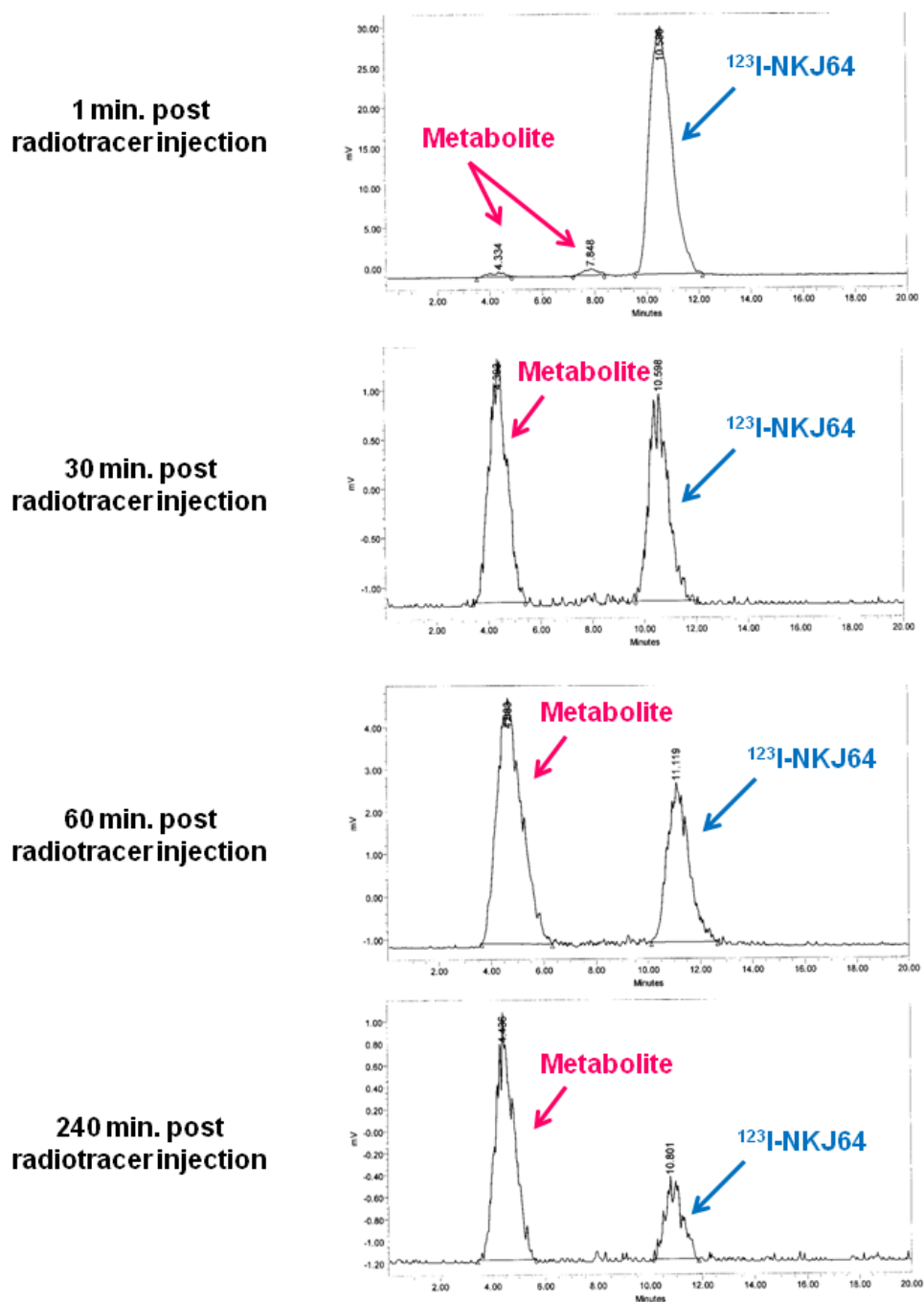


Figure 5.7 Examples of HPLC chromatograms obtained from analysis of arterial blood taken following bolus injection of ^{123}I -NKJ64.

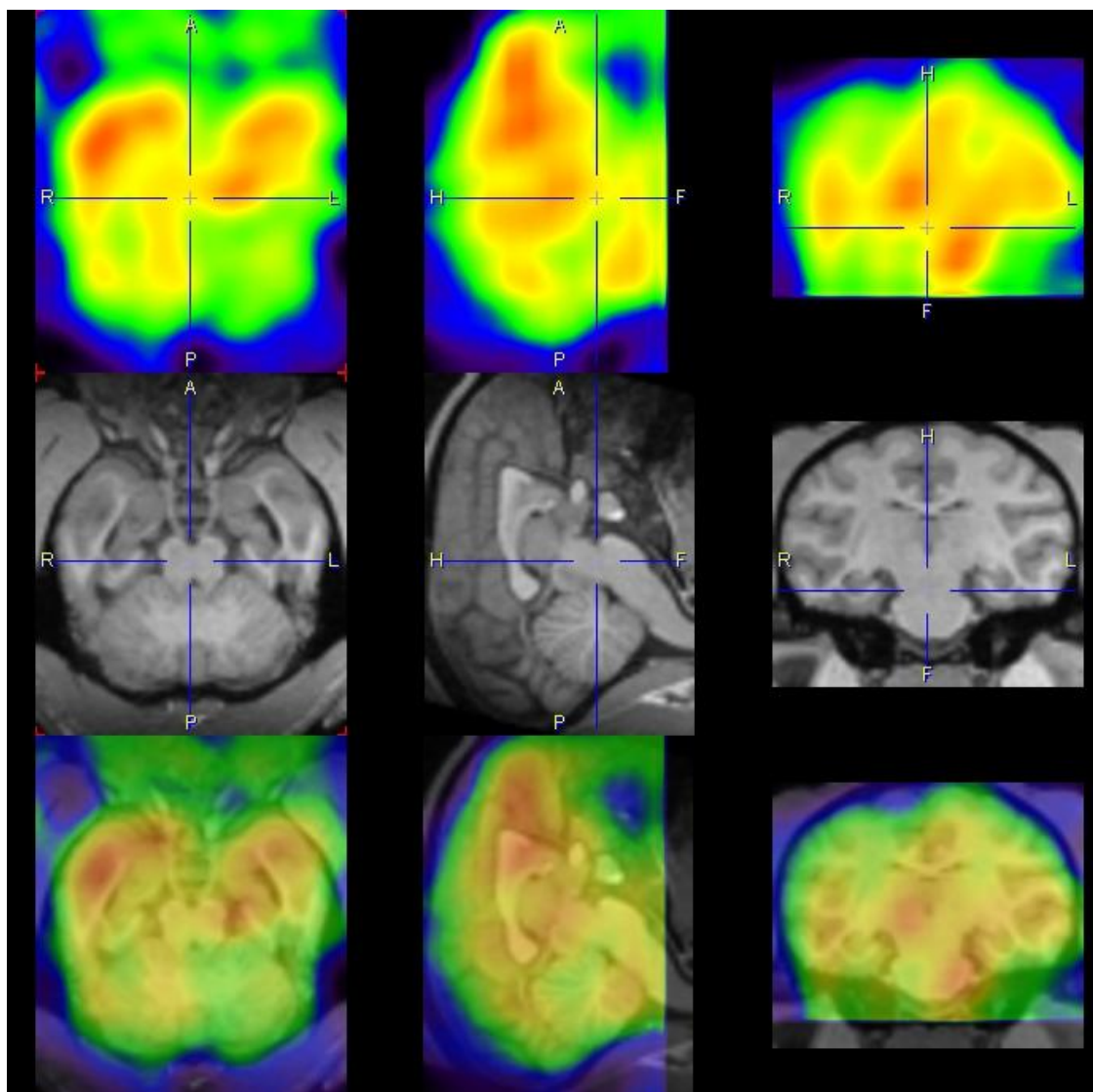


Figure 5.8 Brain SPECT images showing the distribution of $^{123}\text{I-NKJ64}$ in baboon 1.

Top row: transverse, sagittal and coronal planes (left to right) of the acquired SPECT image. Middle row: MR images for corresponding SPECT brain levels in the same animal. Bottom row: co-registration of SPECT and MR images. In SPECT images, the highest radioactive accumulation is showed in red and lowest in green.

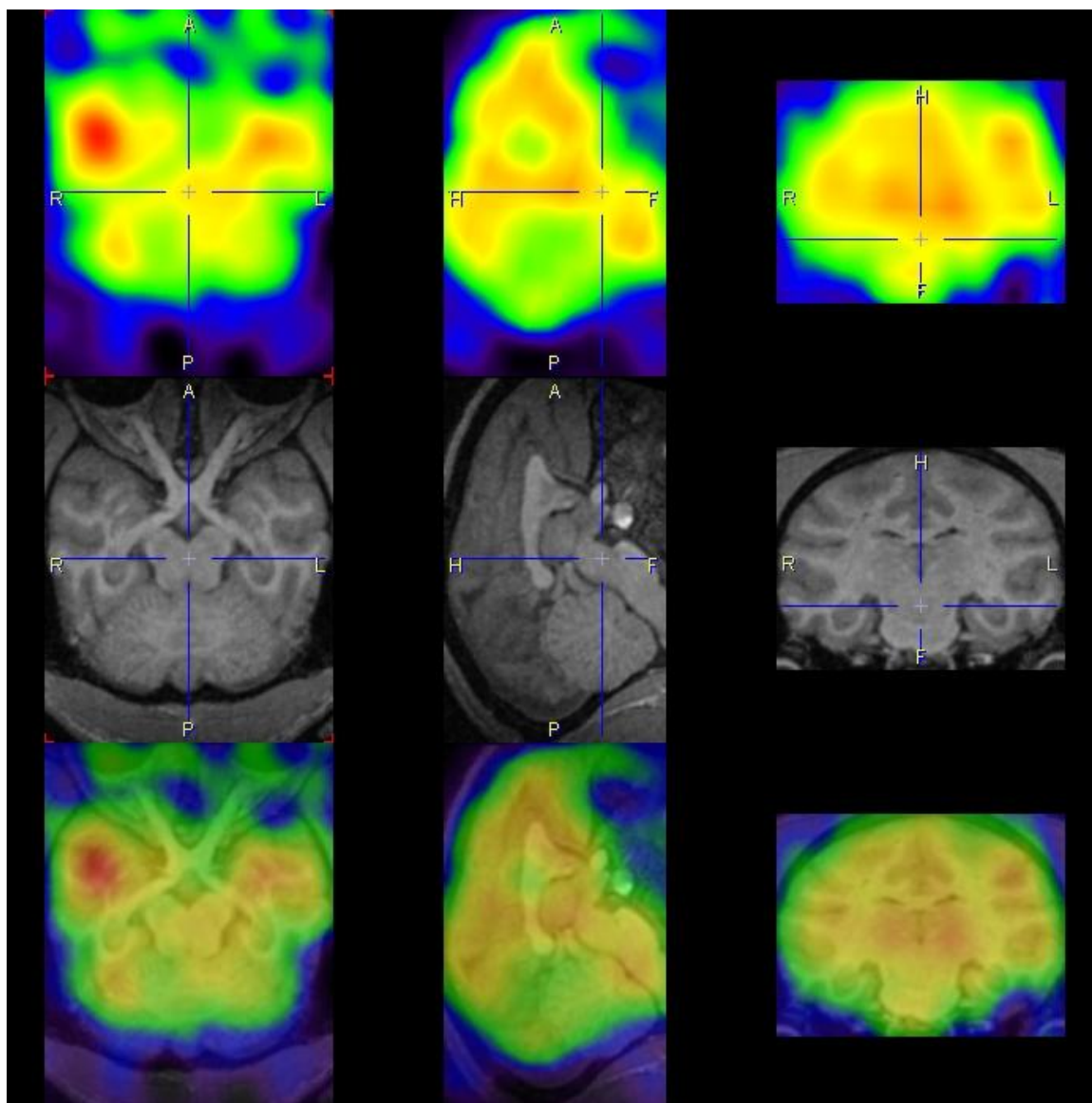


Figure 5.9 Brain SPECT images showing the distribution of $^{123}\text{I-NKJ64}$ in baboon 2.

Top row: transverse, sagittal and coronal planes (left to right) of the acquired SPECT image. Middle row: MR images for corresponding SPECT brain levels in the same animal. Bottom row: co-registration of SPECT and MR images. In SPECT images, the highest radioactive accumulation is showed in red and lowest in green.

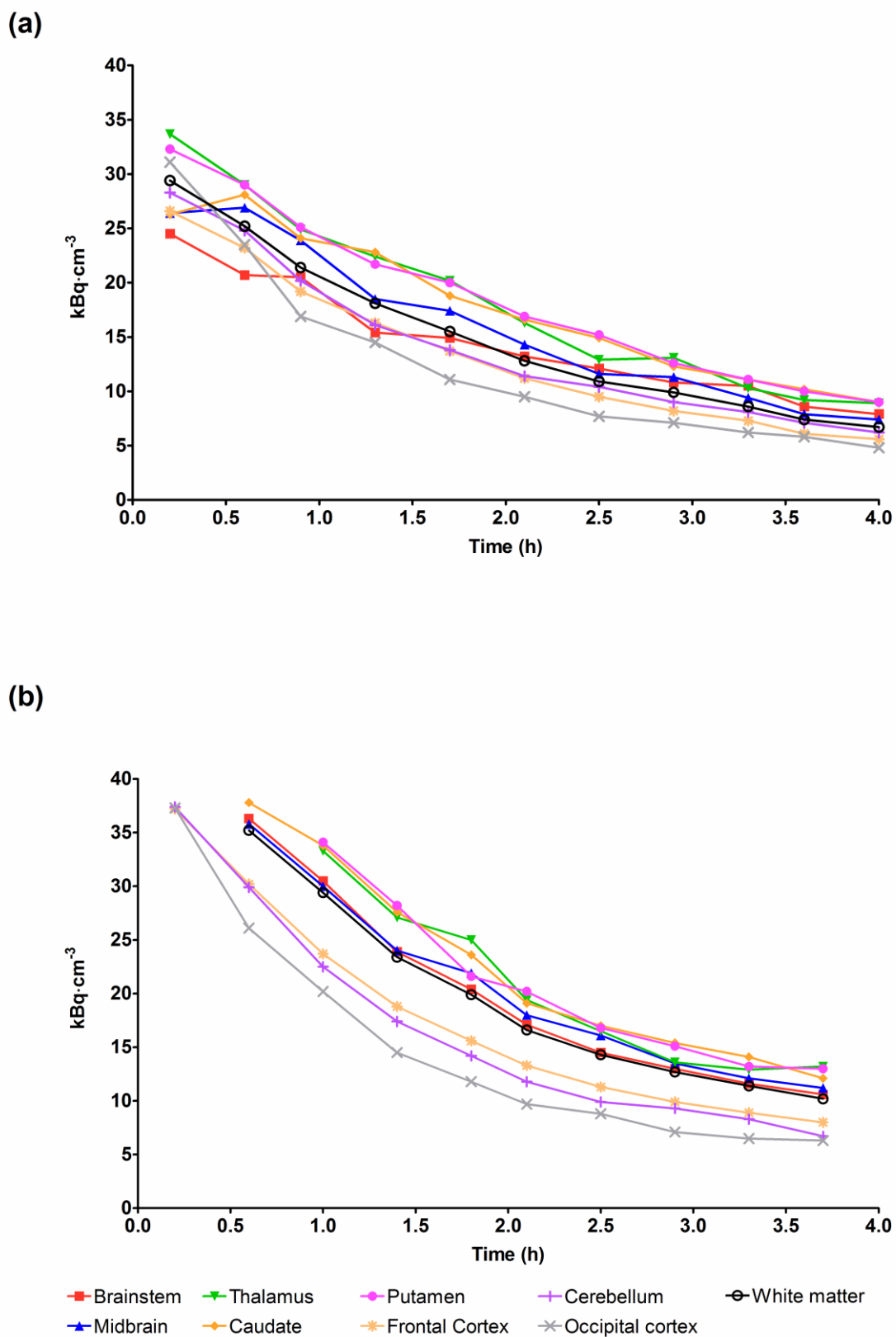


Figure 5.10 Time-activity curves for $^{123}\text{I-NKJ64}$ in multiple brain regions.
 (a) results from baboon 1 and (b) results from baboon 2.

Brain region	% Washout	
	Baboon 1	Baboon 2
Whole brain	73.0	73.0
Brainstem	63.5	72.1
Midbrain	71.2	69.6
Thalamus	71.2	67.9
Caudate	64.7	67.4
Putamen	69.0	70.2
Frontal cortex	76.5	75.0
Cerebellum	75.0	77.7
Occipital cortex	80.6	79.8
White matter	74.2	71.9

Table 5.3 Percentage washout of ^{123}I -NKJ64 from the whole brain and selected brain regions following radiotracer bolus intravenous injection.

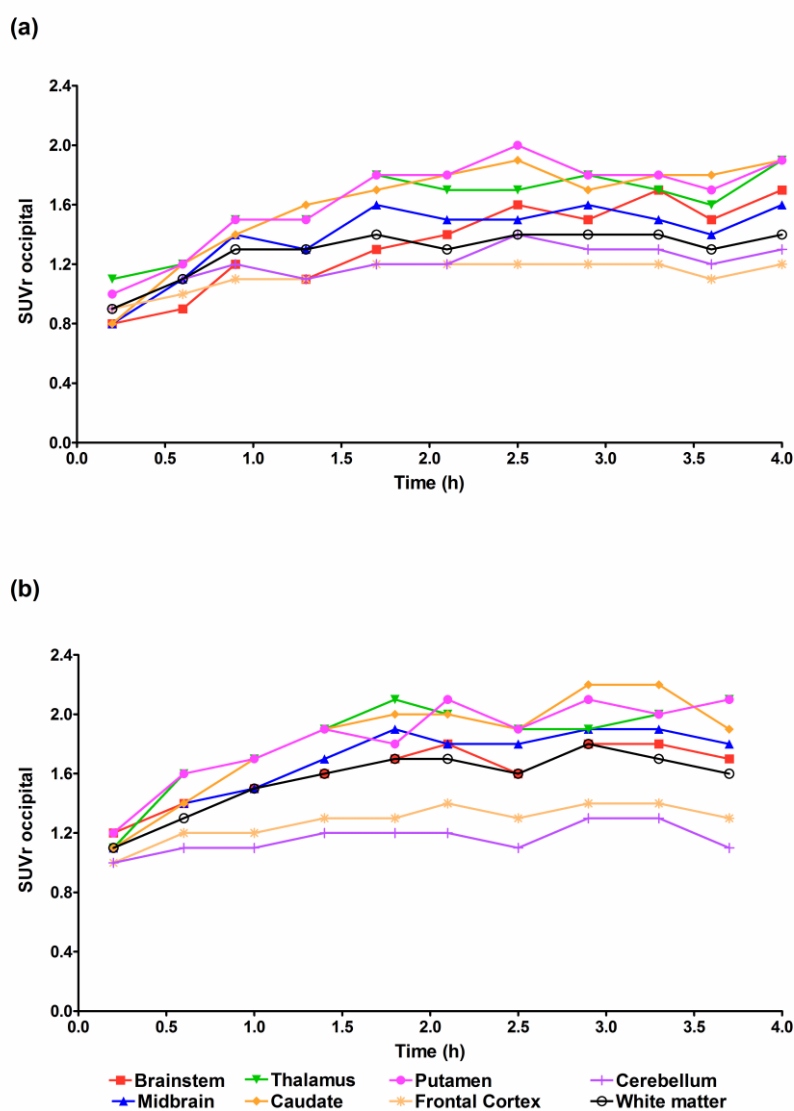


Figure 5.11 Binding ratios in brain regions over time following bolus injection of ^{123}I -NKJ64. Binding ratios are expressed as SUV of target region relative to SUV in occipital cortex (SUVR occipital). (a) results from baboon 1 and (b) results from baboon 2.

Results from kinetic modelling showed that the 2T compartmental model was the preferred model to evaluate and quantify the pharmacokinetic properties of ^{123}I -NKJ64 in baboon brain (lowest AIC and SC values and highest MSC value were obtained with the 2T model). The 2T compartmental analyses using arterial input function at baseline conditions for baboon 1 and baboon 2 are presented in Tables 5.4 and 5.5, respectively. The V_T and BP_{ND} ($BP_{ND}=k_3/k_4$) values did not agree with known NAT distribution in non-human primate, where V_T and BP_{ND} values were highest for the putamen, caudate and thalamus (Figure 5.12, Tables 5.4 and 5.5).

<i>Brain region</i>	<i>Parameters</i>													
	K_1 $\text{mL}\cdot\text{cm}^{-3}\cdot\text{min}^{-1}$	%COV	k_2 min^{-1}	%COV	k_3 min^{-1}	%COV	k_4 min^{-1}	%COV	V_T $\text{mL}\cdot\text{cm}^{-3}$	%COV	K_1/k_2	%COV	BP_{ND}^*	%COV
Brainstem	0.174	26.91	0.098	45.52	0.023	40.86	0.013	15.83	4.794	3.11	1.765	19.45	1.716	30.71
Midbrain	0.189	3.70	0.053	5.83	0.017	29.07	0.023	17.34	6.288	1.73	3.593	7.32	0.750	15.15
Thalamus	0.393	57.03	0.176	40.66	0.039	49.87	0.018	27.91	7.112	3.82	2.231	18.94	2.189	23.27
Caudate	0.199	4.18	0.070	11.93	0.032	8.94	0.021	16.84	7.192	2.39	2.856	8.05	1.518	10.09
Putamen	0.288	8.74	0.092	19.93	0.024	19.63	0.016	4.60	7.568	1.36	3.113	11.34	1.431	17.50
Frontal Ctx.	0.275	8.21	0.123	16.35	0.033	15.63	0.024	3.02	5.417	0.50	2.241	8.292	1.417	14.03
Cerebellum	0.225	9.77	0.073	10.94	0.013	18.60	0.017	11.01	5.403	1.93	3.062	5.07	0.764	10.74
Occipital Ctx.	0.250	5.24	0.093	11.39	0.009	34.10	0.016	20.39	4.110	2.27	2.689	6.97	0.528	17.52
White matter	0.284	1.97	0.113	8.25	0.027	16.15	0.020	6.21	5.911	0.77	2.522	6.46	1.343	10.88

Table 5.4 Summary of the kinetic parameters obtained from data following bolus injection of ^{123}I -NJK64 in baboon 1.
2T compartmental model and arterial input function. * BP_{ND} defined as k_3/k_4 . Ctx=cortex.

<i>Brain region</i>	<i>Parameters</i>													
	K_1 $\text{mL}\cdot\text{cm}^{-3}\cdot\text{min}^{-1}$	%COV	k_2 min^{-1}	%COV	k_3 min^{-1}	%COV	k_4 min^{-1}	%COV	V_T $\text{mL}\cdot\text{cm}^{-3}$	%COV	K_1/k_2	%COV	BP_{ND}^*	%COV
Brainstem	0.226	2.35	0.056	9.13	0.014	26.27	0.017	14.15	7.498	1.78	4.070	7.42	0.842	14.45
Midbrain	0.234	3.53	0.059	12.01	0.016	23.69	0.016	10.38	7.921	1.93	3.947	9.04	1.007	15.41
Thalamus	0.201	4.83	0.035	14.21	0.008	56.34	0.015	36.02	8.719	3.22	5.690	10.29	0.532	25.44
Caudate	0.233	3.74	0.054	18.40	0.018	37.25	0.018	14.04	8.663	2.71	4.282	15.36	1.023	26.21
Putamen	0.231	4.65	0.040	11.53	0.006	42.86	0.011	33.90	9.109	4.36	5.777	7.75	0.577	16.17
Frontal Ctx.	0.197	0.95	0.053	2.90	0.009	11.8	0.015	8.17	5.856	0.92	3.698	2.26	0.584	5.26
Cerebellum	0.209	3.21	0.054	6.47	0.007	22.38	0.014	15.02	5.679	1.34	3.897	3.56	0.457	9.97
Occipital Ctx.	0.228	13.47	0.067	22.55	0.007	51.94	0.016	27.88	4.975	2.22	3.413	9.45	0.458	27.69
White matter	0.227	3.88	0.053	9.59	0.012	23.56	0.016	12.81	7.479	1.47	4.313	6.07	0.734	12.92

Table 5.5 Summary of the kinetic parameters obtained from data following bolus injection of ^{123}I -NJK64 in baboon 2.
2T compartmental model and arterial input function. BP_{ND}^* defined as k_3/k_4 . Ctx=cortex.

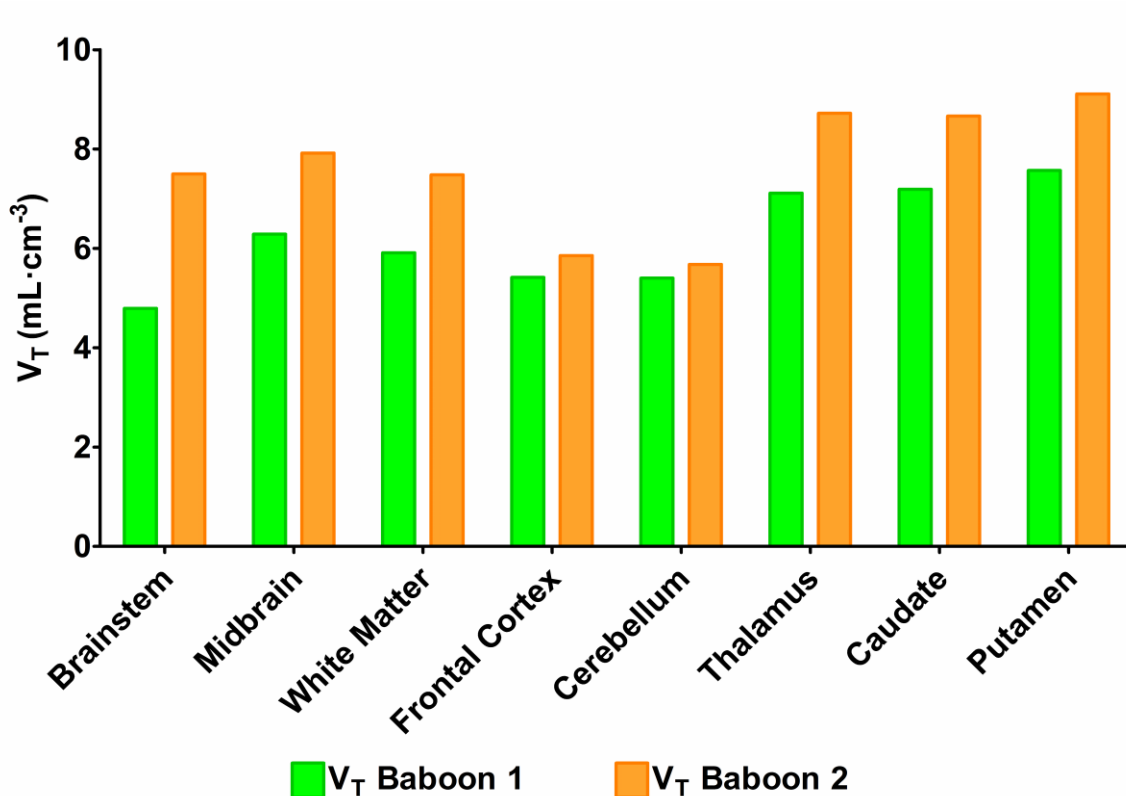


Figure 5.12 V_T values obtained using 2T compartmental model and arterial input function. Green bars are results for baboon 1 and orange bars for baboon 2.

SPECT images of ¹²³I-NKJ64 brain distribution pre- and post-administration of reboxetine are shown in Figure 5.13. Time-activity curves obtained from the displacement study are shown in Figure 5.14. Bolus injection of reboxetine did not reduce the levels of either radioactive concentration (Figure 5.14) or the target-non target ratio (Figure 5.15) in any of the evaluated brain regions. Analysis of HPLC chromatograms from venous blood samples collected pre- and post- administration of reboxetine showed a similar metabolic pattern, such that no increase in the parent compound fraction was observed.

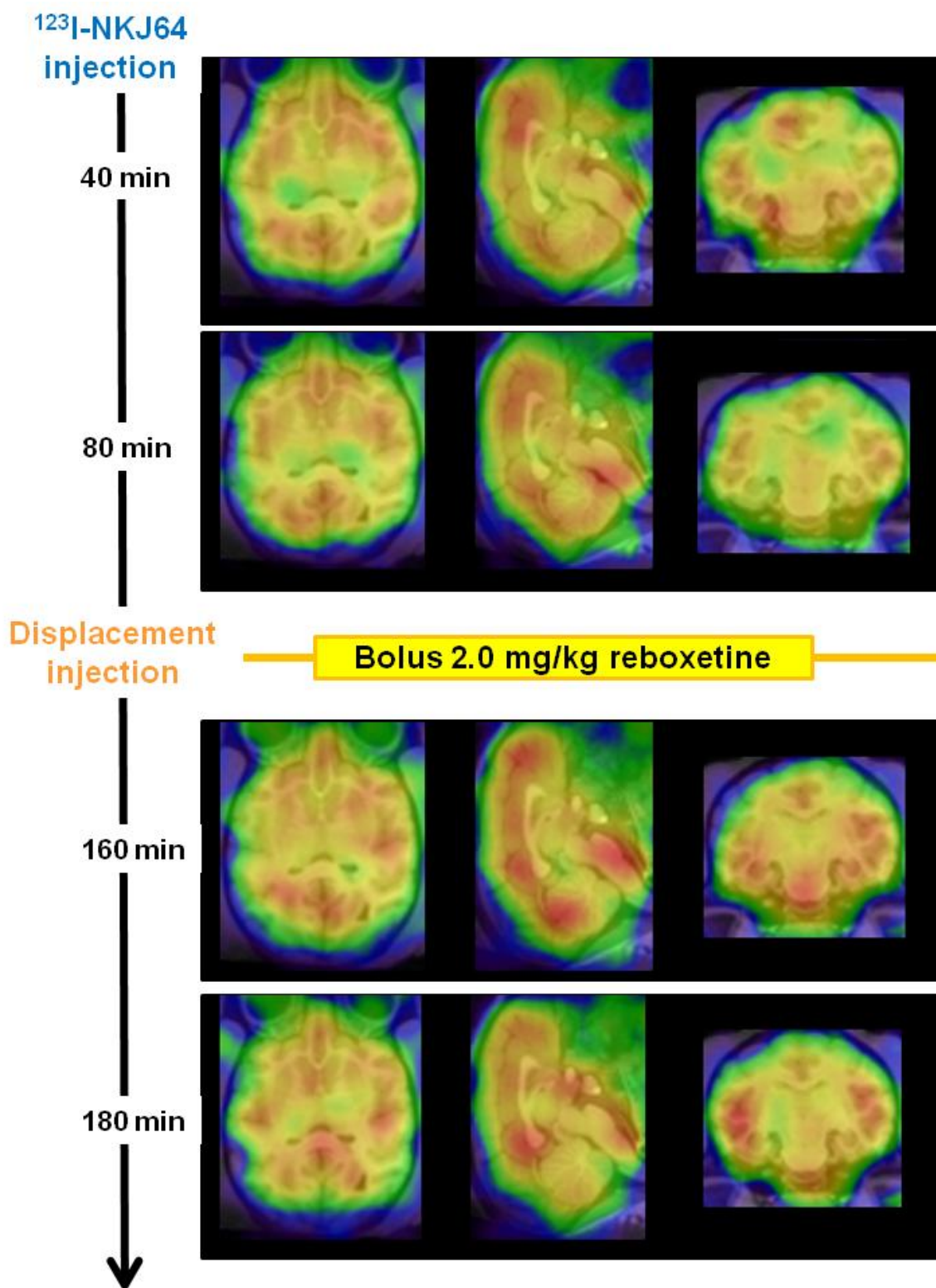


Figure 5.13 Brain ^{123}I -NKJ64 SPECT images pre- and post-administration of reboxetine in baboon 1.

Transversal, sagittal and coronal planes (left to right). Note the absence of reduction in radioactive accumulation in images post-administration compared with images pre-administration for any of the evaluated regions. The highest radioactive accumulation is showed in red and lowest in green.

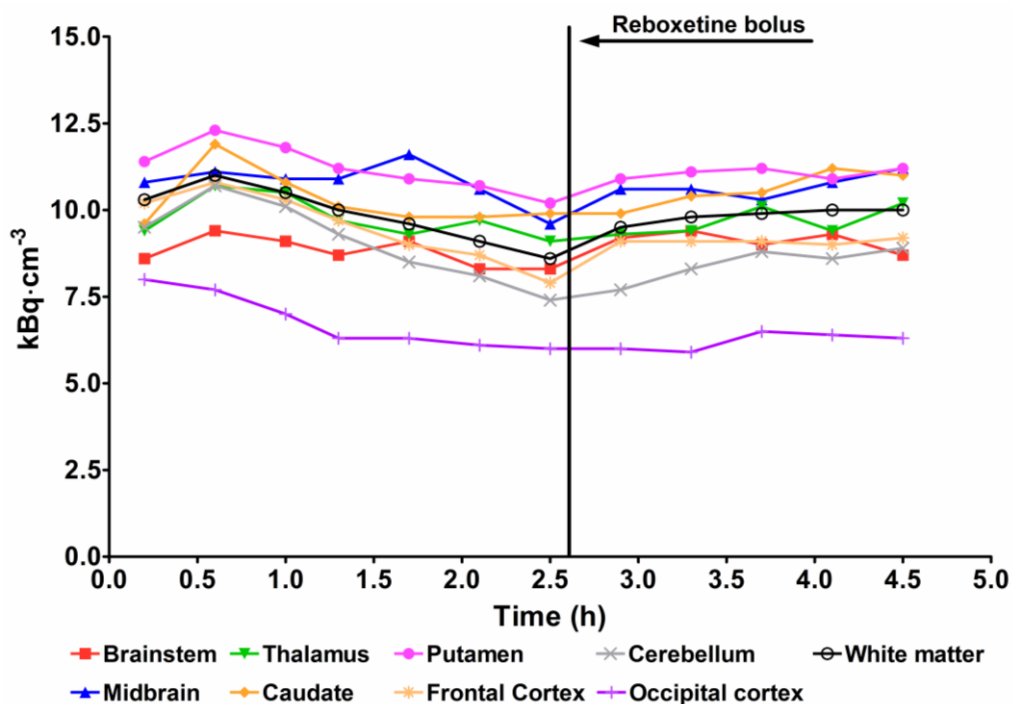


Figure 5.14 Uptake of $^{123}\text{I-NKJ64}$ in baboon 1 brain pre- and post-administration of reboxetine.

Time-activity curve obtained following bolus plus constant infusion of $^{123}\text{I-NKJ64}$. Reboxetine bolus given at 2.75 hours post radiotracer injection (shown in graph by black line and arrow). Note the absence of change in radioactive concentration post-administration of reboxetine in any of the evaluated brain regions.

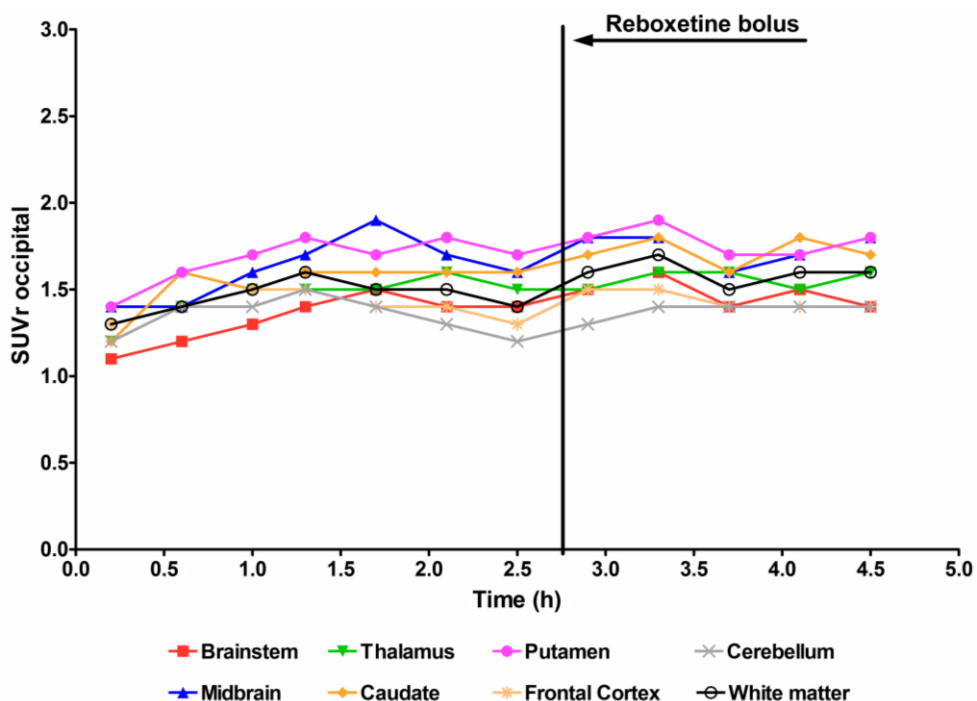


Figure 5.15 Target:non-target ratio of $^{123}\text{I-NKJ64}$ pre- and post-administration of reboxetine in baboon 1 brain.

Note the absence of change in target:non-target ratio following administration of reboxetine (shown in graph by black line and arrow) in any of the evaluated brain regions.

5.4 Discussion

The pharmacokinetics and brain distribution of ^{123}I -NKJ64 in non-human primates were investigated in this chapter. ^{123}I -NKJ64 rapidly and avidly entered the baboon brain, reaching a peak %ID in whole brain of around 3.0% of the injected dose. The whole brain uptake of ^{123}I -NKJ64 in baboons is either higher than or similar to the whole brain uptake seen for other SPECT and PET radiotracers for imaging the NAT in brain. In 2004, McConathy *et al.* showed that ^{11}C -talopram and ^{11}C -talsupram did not enter the rhesus monkey brain in adequate amounts to be used in PET imaging studies (%ID was determined to be 0.4 % in whole brain) (39). Intravenous injection of (*R*)- ^{11}C -OHDMI into cynomolgus monkeys showed that accumulation of radioactivity in brain was slow and reached only 1.1% of the injected radioactivity at 80 minutes (108). Tamagnan *et al.* reported that ^{123}I -INER, a stereoisomer of NKJ64, had a peak %ID in baboon whole brain of around 1.0% of injected dose (114). The whole brain %ID of ^{123}I -NKJ64 in baboons is similar to (*S,S*)- ^{18}F FMENR-D₂, where the measured %ID in whole brain was around 3.4% of injected dose in cynomolgus monkeys (112). In 2007, Schou *et al.* reported that intravenous injection of ^{11}C -DMI resulted in about 2.7% of radioactivity in cynomolgus monkey brain after 24 minutes (108). Intravenous injection of (*S,S*)- ^{11}C -MeNER resulted in 3.0% of the injected dose in cynomolgus monkey brain at 18 minutes post radiotracer administration (161).

The brain distribution of ^{123}I -NKJ64 in baboons was found to be inconsistent with the known distribution of NAT in non-human primate brain (152). Quantification of the ^{123}I -NKJ64 SPECT images obtained in baboons by generation of time-activity curves and kinetic modelling showed that ^{123}I -NKJ64 displayed high uptake in the caudate and putamen, regions that are known to have low NAT density (152). The uptake in the caudate and putamen was not due to specific binding to the NAT, since no displacement was observed in the caudate and putamen following intravenous administration of reboxetine. The mechanism underlying this relatively high uptake in the caudate and putamen remains unknown. However, some groups have hypothesised the existence of low-affinity binding sites in the striatum as an explanation of the high striatal uptake frequently observed with NAT radiotracers (139). The brainstem, where the NAT-rich locus coeruleus is located, had lower V_T values than non-target regions, such as caudate and putamen. Analysis of binding ratios showed a similar trend where the highest values were seen in non-target regions as opposed to the target region, i.e. the brainstem. *In vivo* administration of a high dose of reboxetine resulted in no displacement of ^{123}I -NKJ64 uptake in the brainstem or any of the other evaluated brain regions. This suggests that the *in vivo* uptake of ^{123}I -NKJ64 in baboons is not due to specific binding of

the radiotracer to the NAT. These findings, combined with the observations of a fast washout from the brain, kinetic rate constants similar in all brain regions and low k_3 and BP_{ND} values, suggest ^{123}I -NKJ64 has a low affinity for the NAT *in vivo* in baboon brain. In contrast, ^{123}I -INER, a stereoisomer of NKJ64, showed a distribution pattern in baboon brain consistent with known NAT densities in non-human primate brain and a 60% displacement following intravenous bolus injection of 2.0 mg/kg of reboxetine (114). The lower *in vitro* affinity of ^{123}I -NKJ64 in comparison with ^{123}I -INER (K_D in rat frontal cortex of 4.8 nM and 1.3 nM, respectively) (116, 162) may explain the differences in distribution and kinetics seen between ^{123}I -NKJ64 and ^{123}I -INER. The selectivity of ^{123}I -INER for NAT *in vitro* was also determined to be higher than ^{123}I -NKJ64 (43, 114). This may explain the higher ^{123}I -NKJ64 uptake measured in non-target regions *in vivo* in non-human primate brain in comparison to ^{123}I -INER.

A study evaluating the distribution and kinetics of ^{11}C -labelled (*S,S*)- and (*R,R*)-MRB, two reboxetine stereoisomers, also reported differences in distribution between stereoisomers. Of these, (*S,S*)- ^{11}C -MRB exhibited favourable characteristics for imaging of NAT *in vivo*. Conversely, no regional specificity or blocking effect by nisoxetine were observed for (*R,R*)- ^{11}C -MRB, suggesting the *in vivo* binding of MRB is enantioselective (139). In 2009, Zeng *et al.* also observed differences in the brain distribution and kinetics between different reboxetine analogues labelled with ^{11}C or ^{18}F . They postulated that although a high *in vitro* affinity does not guarantee the success of a radiotracer *in vivo*, it is desirable, particularly when imaging low density molecular targets such as NAT. Zeng and co-workers also suggested that radiotracers with low affinity for NAT will not allow the visualisation of a specific binding signal in NAT-rich regions using PET due to a low signal-to-noise ratio (41).

In rodents, the brain distribution of ^{123}I -NKJ64 was consistent with known NAT density and ^{123}I -NKJ64 had a good target:non-target ratio (Chapter 4). The differences between rodent and non-human primate data may be explained by numerous factors, including the known differences in NAT density in rat brain in comparison to non-human primate brain (Table 4.1 - Chapter 4 and Table 5.1). In non-human primate brain, the locus coeruleus has a NAT binding site density of around 220 fmol/mg, while the rodent locus coeruleus has a density of around 1500 fmol/mg. This represents a seven-fold decrease in NAT binding site density in non-human primate brain compared to rodent brain. It is also known that the density of NATs in human cortex is about nine times lower than in rodents (109). Consequently, the results in baboons and the known differences in NAT densities across species preclude the translation of ^{123}I -NKJ64 for use in humans.

In rodent studies, high non-specific binding and fast kinetics, particularly in the anterior brain, were observed following intravenous injection of ^{123}I -NKJ64 (Chapter 4). The implications of these findings were, at that time, unclear and therefore non-human primate imaging studies were suggested in order to study further the potential of ^{123}I -NKJ64 as a NAT imaging agent. The results in baboons also showed ^{123}I -NKJ64 to have high non-specific binding throughout the brain, since no displacement was observed following administration of reboxetine and a low BP_{ND} was determined. The inability of ^{123}I -NKJ64 to measure specific binding to the NAT could therefore be due to a combination of both high non-specific binding and low NAT density.

Results from blood sampling demonstrated that a single metabolite was present in plasma that was less lipophilic than the parent radiotracer. Since the metabolite is less lipophilic than the parent radiotracer it is unlikely to pass the BBB and contribute to brain radioactivity. Consequently, it is likely that the quantification of ^{123}I -NKJ64 kinetics and distribution in baboon brain was not affected by radiolabelled metabolites generated in blood. In addition, the time-activity curves obtained for all brain regions had a single initial peak followed by continuous elimination over the duration of the study, supporting the hypothesis that there were no metabolites present in the brain over time. Both these observations provide support for the interpretation that the uptake in baboon brain was not due to metabolites generated either in tissue or in blood. Analysis of blood collected during displacement experiments showed no difference in the parent compound fraction in plasma taken post-administration of reboxetine compared to plasma taken pre-administration of reboxetine. This suggests that there was no displacement of ^{123}I -NKJ64 binding in other non-target organs indicating that there is no specific binding of ^{123}I -NKJ64 to peripheral organs. A similar observation was found in rats where administration of reboxetine did not reduce ^{123}I -NKJ64 binding in any of the investigated organs (Chapter 4).

5.5 Conclusion

Investigation of the distribution and pharmacokinetics of ^{123}I -NKJ64 in baboons showed a high non-specific binding throughout the brain and a binding pattern inconsistent with the known NAT distribution in non-human primate brain. The data suggests that ^{123}I -NKJ64 may lack affinity and selectivity for NAT in baboon brain, and the high levels of non-specific binding may be obscuring any ^{123}I -NKJ64 specific binding that might be present *in vivo*. Species differences in NAT density in the brain may explain the differences observed between the results obtained from baboons and rats. The data obtained in this chapter from baboons showing high non-specific binding and a binding

pattern inconsistent with the known NAT distribution thus prevents the translation of ^{123}I -NKJ64 for use in human imaging studies.

6 Kinetic modelling and occupancy measures of NAT in baboons using SPECT with ^{123}I -INER

6.1 Introduction

^{123}I -INER was developed by Tamagnan *et al.* in 2007 as a SPECT radiotracer for imaging NATs in brain (for review refer to sections 3.1.2 and 3.1.3). The binding distribution of ^{123}I -INER in non-human primate brain was reported in 2007 and it was found to be consistent with the known distribution of NAT in baboon brain. Despite the reported slow kinetics in baboon brain (over a period of 2 hours) and a relatively low brain uptake of 1.0% injected dose (114), ^{123}I -INER was considered, at that time, to be the most promising SPECT radiotracer developed for imaging the NAT in brain. In an attempt to obtain a radiotracer for SPECT imaging of the NAT with brain kinetics superior to those of ^{123}I -INER, the Glasgow radiotracer group developed ^{123}I -NKJ64. However in chapter 5, ^{123}I -NKJ64 was found to have high non-specific binding and a binding pattern inconsistent with the known NAT distribution in non-human primate brain, preventing the translation of ^{123}I -NKJ64 for use in human imaging studies. As a result no further evaluation of ^{123}I -NKJ64 was warranted. Consequently, ^{123}I -INER is still considered to be the most promising SPECT radiotracer for imaging of NAT in brain developed to date.

Although the biodistribution of ^{123}I -INER in baboon brain was reported in 2007, quantification of the brain pharmacokinetics of this radiotracer by compartmental modelling has not been reported. Studies investigating the occupancy of NATs using SPECT with ^{123}I -INER and NAT selective drugs have also not been reported to date. Occupancy studies and full kinetic analysis are the next steps in the radiotracer development process after a radiotracer has shown promising results in preliminary non-human primate studies, and may be seen as the final steps prior to translation into human studies. Studies investigating the full kinetic analysis and occupancy of ^{123}I -INER in baboon were therefore conducted at MNI LLC and Yale University, New Haven, Connecticut, USA. In this chapter the analysis and processing of this data is reported.

6.1.1 Hypothesis and aims

It was hypothesised that the full kinetic analysis of ^{123}I -INER in baboons could be performed using compartmental models. In addition, it was also hypothesised that

occupancy of the NAT by NAT-selective drugs could be imaged and quantified using ^{123}I -INER SPECT imaging.

The present chapter aims to characterise the *in vivo* pharmacokinetic properties of ^{123}I -INER in non-human primate brain, including determination of the V_T and BP_{ND} in different brain regions. This chapter also aims to quantify the occupancy of the NAT by two selective NAT inhibitors, atomoxetine and reboxetine, in baboon brain.

6.2 Material and Methods

Image acquisition and metabolite analysis studies with ^{123}I -INER in non-human primates were performed by colleagues at Yale University, New Haven, CT, USA and MNI LLC, New Haven, CT, USA respectively. The radiolabelling and preparation of ^{123}I -INER for use in non-human primate experiments was performed by colleagues at MNI LLC, New Haven, CT, USA using previously described methodology (114).

6.2.1 Non-human primates

All procedures using non-human primates were conducted at Yale University, USA in accordance with institutional animal care protocols and in compliance with US federal regulations. Seven ovariectomised adult female baboons (*Papio anubis*, 10 – 17 kg) were used in the ^{123}I -INER SPECT imaging studies described below.

6.2.2 Animal general preparation and monitoring

Baboon preparation and monitoring was performed as previously described in chapter 5, section 5.2.2.

6.2.3 General SPECT acquisition protocol

The SPECT acquisition protocol for studies using ^{123}I -INER in baboons was as described in the previous chapter 5, section 5.2.3.

6.2.4 ^{123}I -INER baseline and pre-blocking experiments in non-human primates

Baseline and pre-blocking experiments were performed using a single baboon and two SPECT measurements: one at baseline and a second following pre-blocking with atomoxetine (Tocris Bioscience, USA). ^{123}I -INER was administered *via* a single bolus intravenous injection with an injected activity of 433.27 MBq and 472.49 MBq for baseline and pre-blocking SPECT scans, respectively. Arterial blood was collected during baseline measurements and venous blood was collected in both SPECT measurements in order to perform kinetic modelling analysis (Figure 6.1). Atomoxetine was given *via* intravenous injection using a prolonged infusion method that was designed to mimic the human oral absorption profile of the drug, based on previously described methodology (112). Briefly, intravenous administration of atomoxetine consisted of two successive infusions: a loading infusion over 10 minutes (0.25 mg/kg) followed by a maintenance infusion (0.15 mg/kg/h) until the end of the SPECT image acquisitions. The radiotracer was administered as a bolus 30 minutes after the start of atomoxetine infusion and images were acquired over 240 minutes. The infusion pump used was a Gemini PC1 (IMED Inc., USA) with 60 mL syringes.

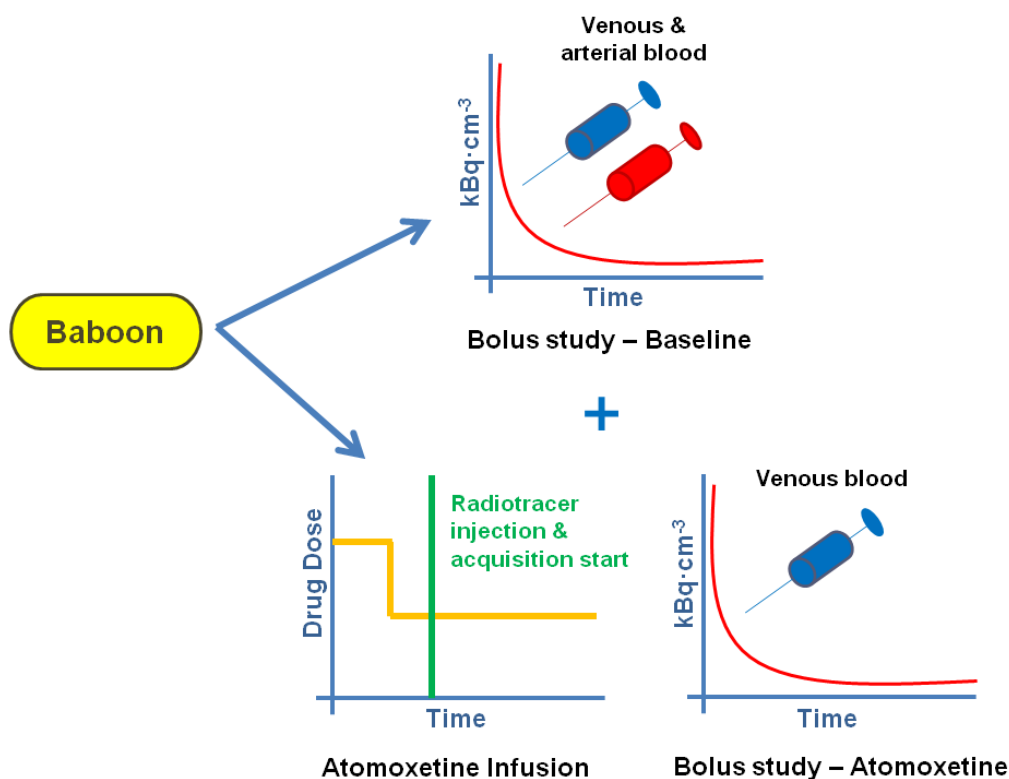


Figure 6.1 Experimental procedure for the baseline and pre-blocking experiments performed in a single baboon using ^{123}I -INER and atomoxetine.

6.2.5 ^{123}I -INER displacement studies in non-human primates

Six baboons were used for displacement studies. The aim was to obtain a dose-response curve for two NAT selective drugs: atomoxetine and reboxetine (Tocris Bioscience, USA). Six different doses of atomoxetine (0.03, 0.06, 0.15, 0.67, 0.69 and 0.85 mg/kg) and four different doses of reboxetine (0.5, 1.0, 1.5 and 3 mg/kg) were investigated (Table 6.1). Displacement studies were conducted using a bolus plus constant infusion protocol, where the K_{bol} (B/I ratio) was 1.30. The mean injected radioactivity of ^{123}I -INER was 392 ± 132 MBq (range 206-549 MBq, $n=10$, 6 atomoxetine displacement studies plus 4 reboxetine displacement studies). A Gemini PC 1 (IMED Inc., USA) infusion pump with 60 mL syringes was used for infusion of the radiotracer. Upon equilibrium, which was estimated to occur between 3 and 4 hours post radiotracer administration, a single bolus of atomoxetine or reboxetine was injected intravenously (Figure 6.2). The displacement drug was administered at 212 ± 48 minutes (mean \pm SD, $n=10$) post radiotracer injection.

Baboon	Atomoxetine dose (mg/kg)	Reboxetine dose (mg/kg)
1	N/A	1.0 and 1.5*
2	N/A	0.5 and 3.0*
3	0.67 and 0.15*	N/A
4	0.03 and 0.85*	N/A
5	0.06	N/A
6	0.69	N/A

Table 6.1 Summary of atomoxetine and reboxetine doses investigated using six baboons.

N/A = not applicable. *Animal used for two studies with 2 different doses of the drug, where each study was separated by at least 2 weeks.

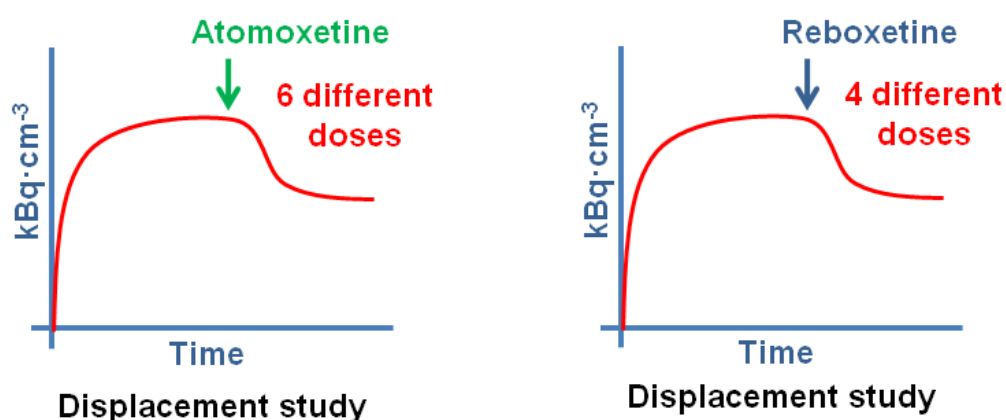


Figure 6.2 Experimental procedure for *in vivo* ^{123}I -INER displacement studies in baboons using atomoxetine and reboxetine.

6.2.6 Analysis of plasma pharmacokinetics

For studies using a single bolus injection of ^{123}I -INER i.e. the baseline and pre-blocking experiments, venous and arterial (for the baseline scan only) blood samples (4-5 mL) were obtained from the femoral vein and femoral artery, respectively prior to the start of the study (- 5 minutes) and at 1-2, 3, 5, 10, 15, 30, 60, 120, 180 and 240 minutes post radiotracer injection. Processing and analysis of blood samples was performed by colleagues at the MNI LLC laboratories, using previously established methodology (156-159). A brief description of the protocol used is provided in the previous chapter (Chapter 5) section 5.2.5.

6.2.7 Image processing and co-registration with magnetic resonance imaging (MRI)

Details of the image processing and co-registration with MRI methodology are outlined in section 5.2.6 (Chapter 5).

6.2.8 Data analysis

Time-activity curves were generated for each brain region in each study. Metabolite-corrected arterial and venous plasma curves were also generated for each study. The kinetic properties of ^{123}I -INER following bolus injection in the baseline and blocking study were calculated using PMOD and the 1T model and 2T model. The goodness of fit was assessed by evaluating the AIC, the SC and the MSC selection criteria. The model presenting the lowest AIC and SC values and highest MSC value was defined as the preferred model. In addition, the simplified reference tissue model (SRTM) and multilinear reference tissue model 2 (MRTM2) with k_2' fix at 0.02 were investigated (153, 163-164). For the 2T compartmental model, the V_T defined as the specific volume of distribution (V_s) plus the non-displaceable volume of distribution (V_{ND}) was calculated using Equation 6.1, with the definition of V_s and V_{ND} given in Equation 6.2 and 6.3, respectively.

$$V_T = V_s + V_{ND} = \frac{K_1}{k_2} \left(1 + \frac{k_3}{k_4} \right) \quad (\text{Eq. 6.1})$$

$$V_s = V_T - V_{ND} = \frac{K_1 k_3}{k_2 k_4} \quad (\text{Eq. 6.2})$$

$$V_{ND} = V_T - V_S = \frac{K_1}{k_2} \quad (\text{Eq. 6.3})$$

The BP_{ND} was calculated by an invasive (2T) direct method and invasive (2T) indirect method, where BP_{ND} was defined as k_3/k_4 and as $(V_T - V_{ND})/V_{ND}$, where V_{ND} was the V_T of the reference region, respectively. When non-invasive (SRTM and MRTM2) and invasive (2T) indirect methods were applied for quantification of BP_{ND} , the occipital cortex was used as reference region as this was the brain region with the lowest radioactive concentration.

For the baseline study, the V_T derived using an arterial input function was compared to the one derived using a venous input function. The aim of this comparison was to determine whether the venous blood sampling protocol would be suitable for kinetic modelling of ^{123}I -INER. The tissue to venous plasma activity concentration ratio (C_t/C_p) was calculated and plotted against time to determine whether transient equilibrium was reached during the late scans when the rate of clearance of ^{123}I -INER in tissue and in plasma is the same. The apparent volume of distribution ($V_{T\text{ app}}$) was calculated as an average over 3 time points of C_t/C_p at transient equilibrium. Subsequently, the correlation between the $V_{T\text{ app}}$ and the V_T from 2T compartmental model using a venous plasma input function was investigated.

The NAT occupancy induced by the atomoxetine infusion in the ^{123}I -INER pre-blocking study was calculated using two methods: percent change of BP_{ND} between baseline and atomoxetine pre-blocking experiments (Equation 6.4) and the Lassen plot method (Equation 6.5) (165).

$$\text{Occupancy (\%)} = \frac{BP_{ND\text{ baseline}} - BP_{ND\text{ blocking}}}{BP_{ND\text{ baseline}}} \times 100 \quad (\text{Eq. 6.4})$$

$$\text{Occupancy (\%)} = \frac{V_T\text{ baseline} - V_T\text{ blocking}}{V_T\text{ baseline} - V_{ND}} \times 100 \quad (\text{Eq. 6.5})$$

which when represented graphically for several regions ($x=V_T$ baseline, $y=V_T$ baseline - V_T pre-blocking) produces a linear relationship, where the x intercept equals V_{ND} and gradient equal to global target occupancy. A global occupancy was determined graphically as the slope of the line. Occupancy measurements in individual brain regions were also determined by deriving the V_{ND} from the Lassen plot and subsequently applying Equation 6.5 for occupancy determination.

For the displacement studies with bolus plus constant infusion of ^{123}I -INER, the specific binding in different brain regions was obtained by subtracting the mean occipital cortex uptake. The percentage specific binding displacement was calculated as the specific binding prior to displacement minus the lowest specific binding post displacement, divided by the specific binding prior displacement, multiplied by 100 (Equation 6.6).

$$\% \text{ Displaced} = \frac{\text{SB prior displacement} - \text{SB post displacement}}{\text{SB prior displacement}} \times 100 \quad (\text{Eq. 6.6})$$

where SB is specific binding.

The percentage specific binding displacement was then plotted against reboxetine or atomoxetine doses and the dose-occupancy curve was fitted in GraphPad Prism (GraphPad Software, version 4.0, USA) with a single specific binding site model according to the following equation:

$$\text{Occupancy (\%)} = \frac{O_{\max} \times D}{D + ED_{50}} \quad (\text{Eq. 6.7})$$

where O_{\max} is the maximum occupancy, ED_{50} is the drug dose for 50% occupancy and D is the dose of the drug.

6.3 Results

6.3.1 ^{123}I -INER baseline and pre-blocking experiments

Following intravenous bolus injection of ^{123}I -INER at baseline conditions, a high accumulation of radioactivity was found at the level of the brainstem (where the locus coeruleus is located) and the midbrain (where the raphe complex is located), regions that are known to contain high densities of NATs (Figure 6.3 and Figure 6.4). A low accumulation of radioactivity in the rest of the brain was found as follows: cerebellum > caudate > occipital cortex. A relatively slow washout of radioactivity from the whole brain over 4 hours was observed, where 64% of the whole brain uptake was eliminated at 4 hours post-injection. The specific binding of ^{123}I -INER peaked at around 3 hours post radiotracer injection. Sixty minutes post-injection, the parent fraction of ^{123}I -INER in venous and arterial plasma was 30% and 26%, respectively, reaching less than 15% at 240 minutes post-injection (Figure 6.5).

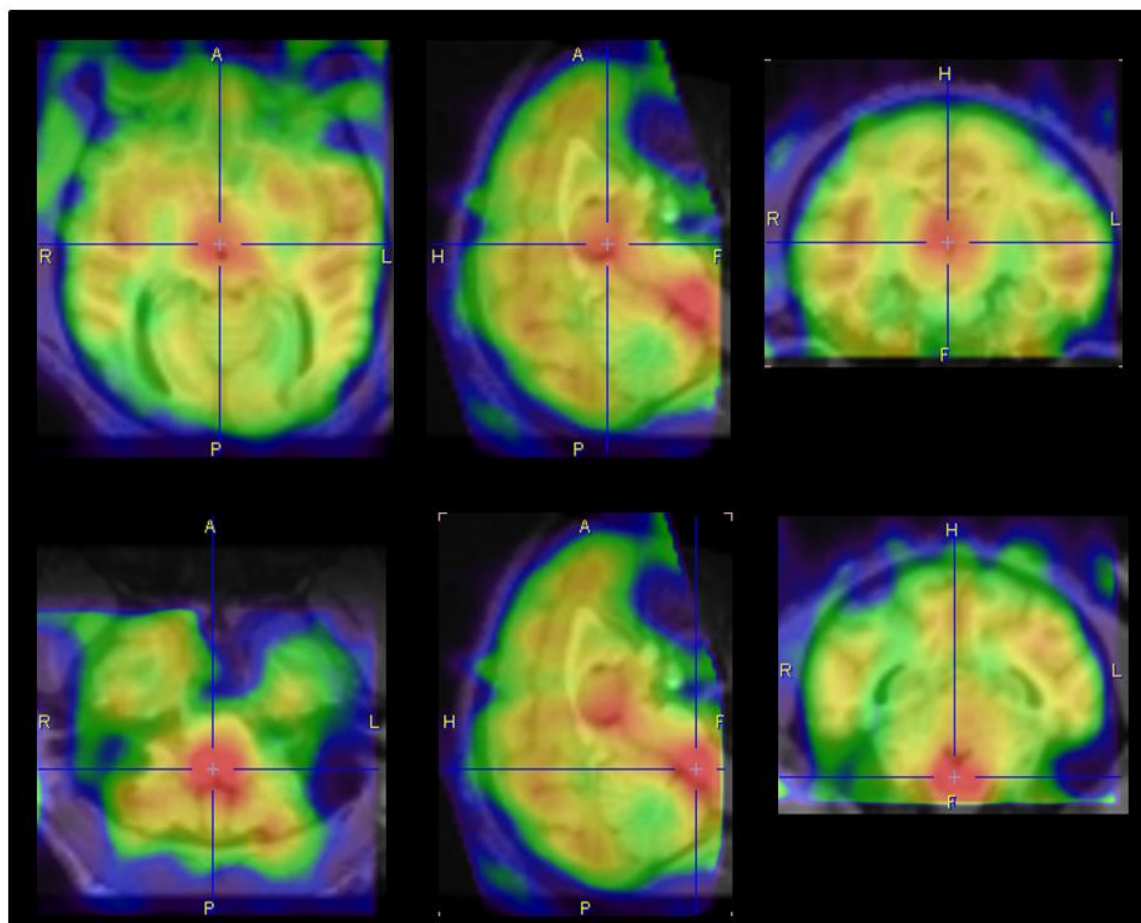


Figure 6.3 MRI co-registered SPECT images of ^{123}I -INER distribution in baboon brain at baseline.

Transverse, sagittal and coronal planes from left to right. Highest radioactivity accumulation is showed in red and lowest in green.

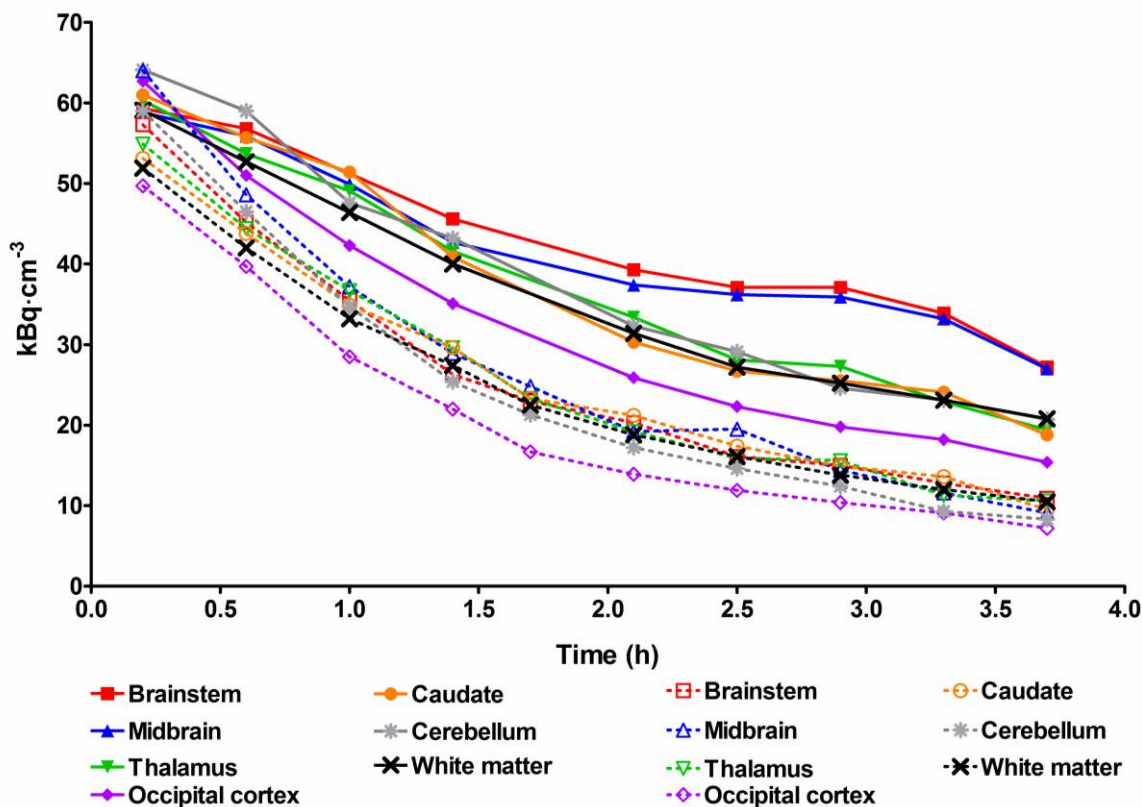


Figure 6.4 Time activity curves of ^{123}I -INER uptake in multiple baboon brain regions. Solid lines and closed symbols represent the uptake of ^{123}I -INER during the baseline scan. Dashed lines and open symbols represent the uptake of ^{123}I -INER following pre-blocking with atomoxetine.

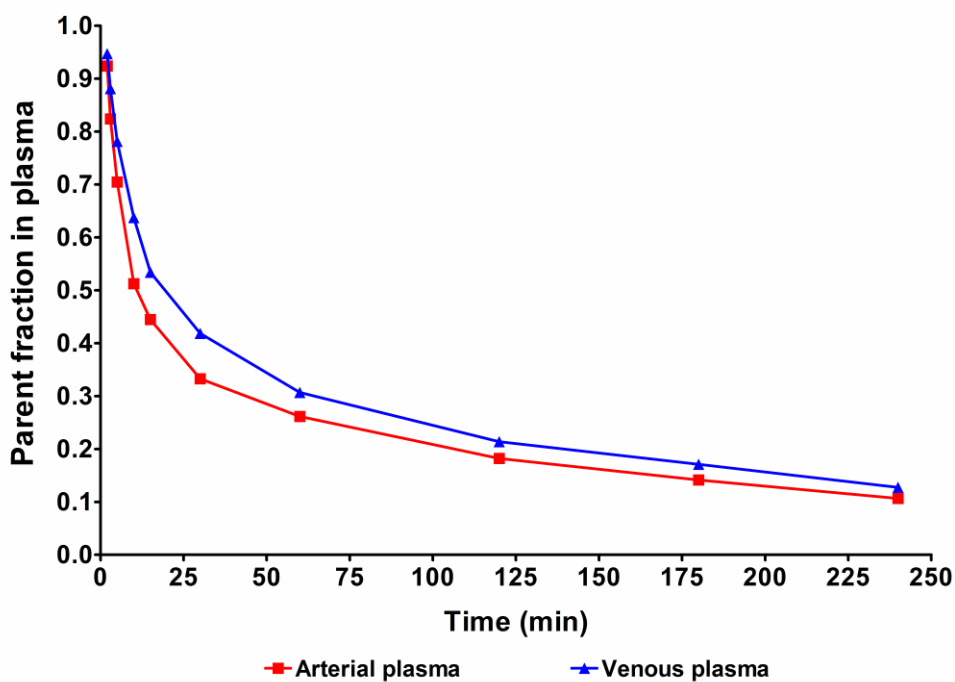


Figure 6.5 Time-activity curves of the parent fraction present in both venous and arterial plasma after intravenous injection of ^{123}I -INER in the baseline study.

Kinetic modelling showed that the 2T compartmental model was the preferred model to evaluate and quantify ^{123}I -INER pharmacokinetic properties in baboon brain in comparison with the 1T model (lowest AIC and SC values and highest MSC value were obtained with the 2T model). Kinetic modelling using the 2T compartmental analysis of the baseline study using either arterial or venous input functions showed that the highest V_T values were found in the NAT rich regions, the brainstem and midbrain, with lower V_T values in the caudate, white matter, cerebellum and occipital cortex. Similarly, the BP_{ND} and the V_s values were higher in the brainstem, midbrain and thalamus and lower in the other brain regions. V_T values determined from the baseline study using the venous input function correlated well with V_T values determined from the baseline study using the arterial input function (Figure 6.6). As a result, only venous samples were collected in the subsequent pre-blocking study. The results from kinetic modelling of the ^{123}I -INER time-activity curves using 2T compartmental analysis at baseline and after pre-blocking with atomoxetine are presented in Table 6.2. Pre-treatment with atomoxetine reduced the uptake, V_T , V_s and BP_{ND} values in NAT rich regions to the levels seen in non-target regions (Figure 6.4, Figure 6.7 and Table 6.2). SRTM and MRTM2 analysis also showed a reduction of brainstem and midbrain BP_{ND} following pre-treatment with atomoxetine (Table 6.3). BP_{ND} values determined by SRTM correlated with BP_{ND} values calculated with MRTM2 with a r^2 value of 0.98 (Figure 6.8a) and for both methods at baseline conditions the highest BP_{ND} values were seen in the brainstem and midbrain (Table 6.3). The BP_{ND} values obtained using the SRTM and MRTM2 models correlated with the BP_{ND} values determined using the invasive (2T) direct compartmental model with r^2 values of 0.50 and 0.45, respectively. However, when the BP_{ND} values determined by the invasive 2T indirect compartmental model were plotted against BP_{ND} values determined by SRTM and MRTM2 models, r^2 values of 0.92 and 0.86 were determined, respectively (Figure 6.8b and 6.8c).

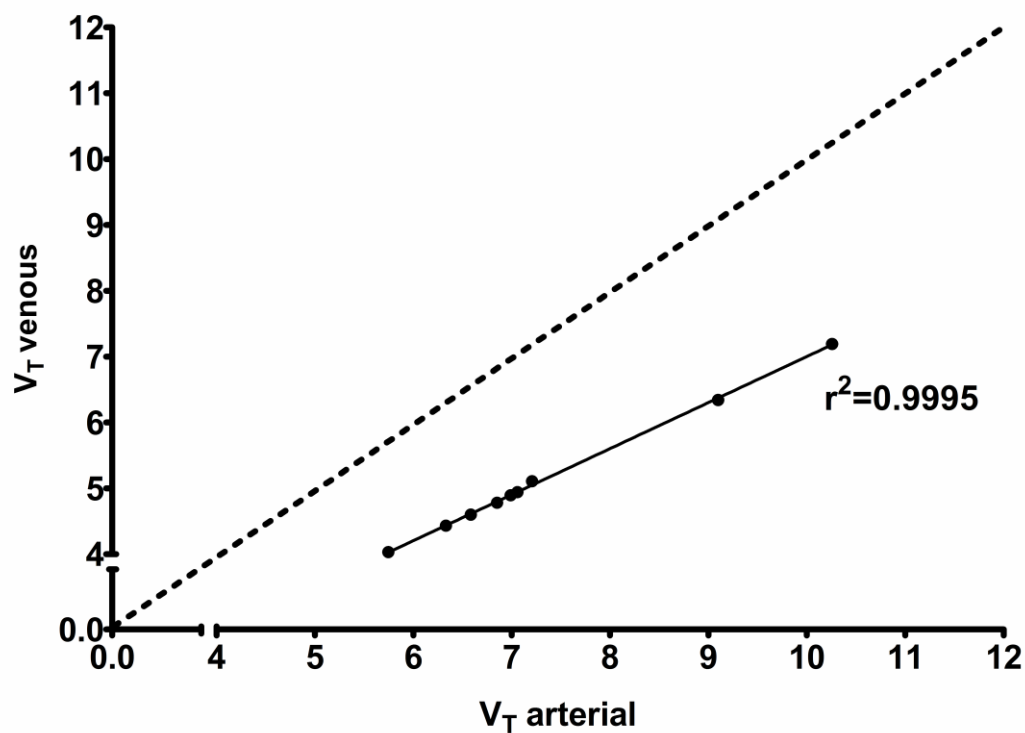


Figure 6.6 V_T values in baboon brain determined during the baseline study using the 2T compartmental model.

V_T values obtained using 2T compartmental model and arterial input function (x axis) compared with V_T values obtained by using 2T compartmental model and venous input function (y axis). Dashed line represents the line of identity. Note that the V_T calculated using the venous input function is lower in comparison with the V_T calculated using arterial input function.

Brain Regions	Parameters														
	K_1 mL·cm ⁻³ ·min ⁻¹	% COV	k_2 min ⁻¹	% COV	k_3 min ⁻¹	% COV	k_4 min ⁻¹	% COV	V_T mL·cm ⁻³	% COV	V_S mL·cm ⁻³	% COV	BP _{ND} ^a	% COV	BP _{ND} ^b
Brainstem															
Baseline	0.082	11.14	0.048	32.22	0.026	37.08	0.008	18.86	7.192	5.86	5.504	7.25	3.260	25.93	0.914
Atomoxetine	0.231	5.48	0.083	9.96	0.009	22.82	0.012	16.53	4.781	2.49	2.007	6.25	0.723	10.21	0.160
Midbrain															
Baseline	0.072	7.34	0.038	24.46	0.018	33.12	0.007	19.03	6.341	6.57	4.469	6.63	2.387	19.95	0.688
Atomoxetine	0.284	23.27	0.101	27.93	0.013	26.79	0.017	13.42	4.988	2.64	2.190	10.83	0.783	17.00	0.210
Thalamus															
Baseline	0.082	28.86	0.064	38.43	0.040	30.40	0.014	39.09	4.943	3.23	3.652	4.43	2.831	14.42	0.315
Atomoxetine	0.235	4.95	0.101	8.58	0.016	11.39	0.142	5.83	4.928	1.00	2.595	3.27	1.112	6.94	0.196
Caudate															
Baseline	0.073	11.93	0.030	37.50	0.012	78.16	0.011	45.63	5.106	8.00	2.703	17.73	1.124	41.93	0.359
Atomoxetine	0.210	5.58	0.096	11.33	0.018	16.34	0.016	7.38	4.813	1.21	2.545	4.81	1.122	10.66	0.167
Occipital cortex															
Baseline	0.073	5.87	0.045	16.54	0.015	24.54	0.012	10.68	3.757	2.43	2.131	5.93	1.310	16.46	---
Atomoxetine	0.206	3.16	0.073	5.69	0.006	20.29	0.012	16.48	4.122	1.87	1.310	5.78	0.466	7.81	---
Cerebellum															
Baseline	0.077	1.85	0.038	7.04	0.018	19.10	0.014	10.69	4.599	1.71	2.580	4.41	1.277	10.71	0.224
Atomoxetine	0.250	4.72	0.085	8.87	0.008	26.07	0.016	17.00	4.437	1.77	1.485	8.14	0.503	12.27	0.076
White matter															
Baseline	0.074	3.28	0.047	10.21	0.020	15.04	0.010	7.70	4.781	1.96	3.206	3.05	2.035	9.58	0.272
Atomoxetine	0.221	4.66	0.091	9.01	0.014	15.62	0.015	8.41	4.606	1.26	2.181	4.59	0.899	8.97	0.117

Table 6.2 Kinetic analysis of the results obtained from the baseline and pre-blocking experiments following bolus injection of ¹²³I-INER.

The data presented were obtained from the 2T compartmental model analysis using the venous plasma input function. Note the reduction in the V_T , V_S and BP_{ND} values of NAT rich regions when atomoxetine pre-treatment was given in comparison with the baseline measurements. ^aBP_{ND} determined using direct method (BP_{ND}= k_3/k_4). ^bBP_{ND} determined by indirect method (BP_{ND}=(V_T-V_{ND})/ V_{ND}). Data derived using a single animal.

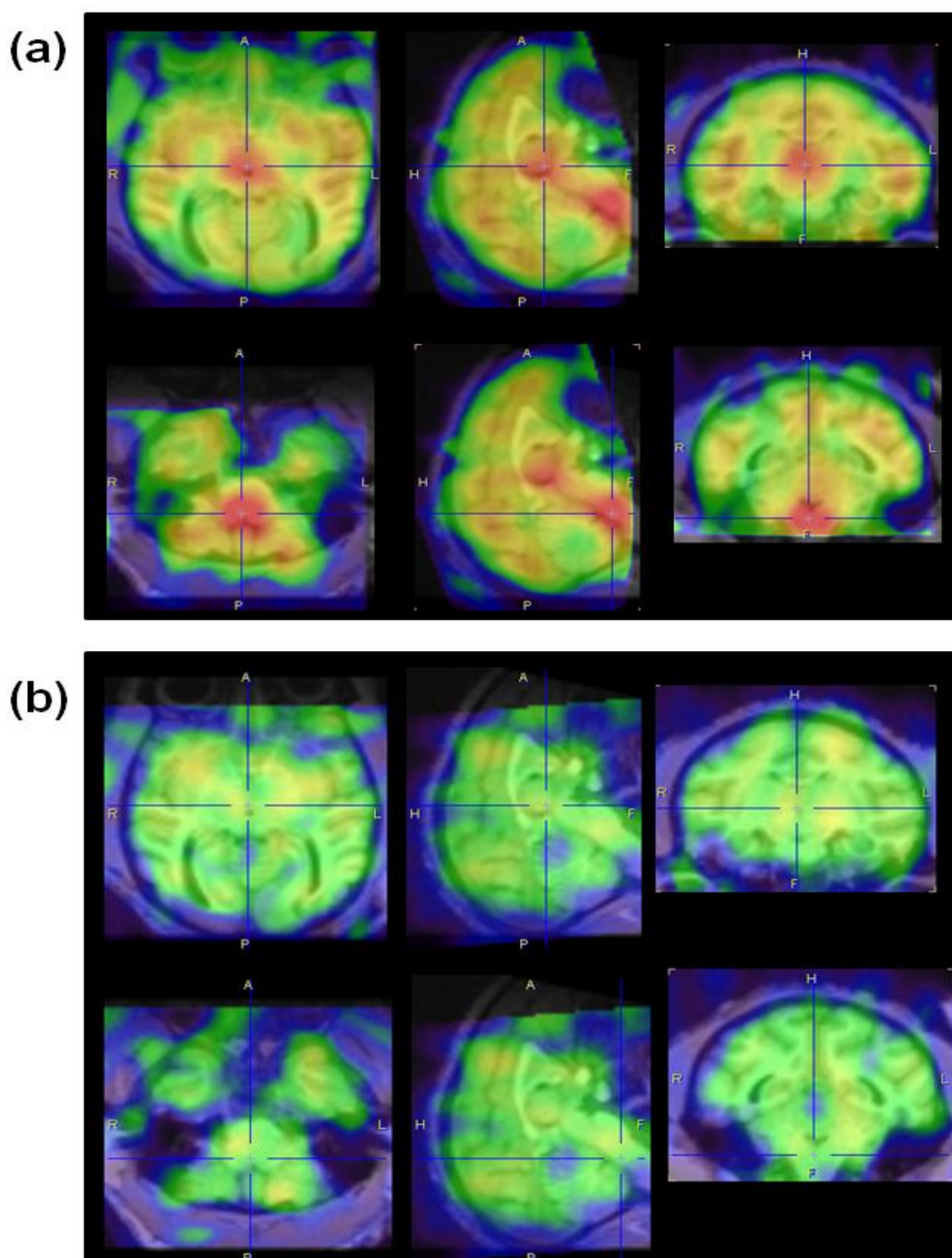


Figure 6.7 ^{123}I -INER brain SPECT images co-registered with MRI (transverse, sagittal and coronal planes from left to right), showing the distribution at baseline (a) and following pre-blocking with atomoxetine (b).

The highest radioactive accumulation is shown in red and the lowest in green.

Brain Regions	BP_{ND} SRTM	%COV	BP_{ND} MRTM2	%COV
Brainstem				
Baseline	0.731	14.98	0.670	3.59
Atomoxetine	0.184	45.47	0.142	5.54
Midbrain				
Baseline	0.537	14.06	0.469	3.24
Atomoxetine	0.237	38.96	0.234	3.36
Thalamus				
Baseline	0.325	7.04	0.330	3.22
Atomoxetine	0.231	15.49	0.201	4.92
Caudate				
Baseline	0.342	12.33	0.338	2.84
Atomoxetine	0.202	10.42	0.191	5.30
Cerebellum				
Baseline	0.248	8.82	0.248	3.10
Atomoxetine	0.105	---	0.096	6.42
White matter				
Baseline	0.215	18.34	0.151	6.11
Atomoxetine	0.147	12.75	0.130	6.48

Table 6.3 BP_{ND} values for ^{123}I -INER in baboon brain determined using analysis with SRTM and MRTM2 models.

Note that the SRTM model did not fit the cerebellum data from the blocking study.

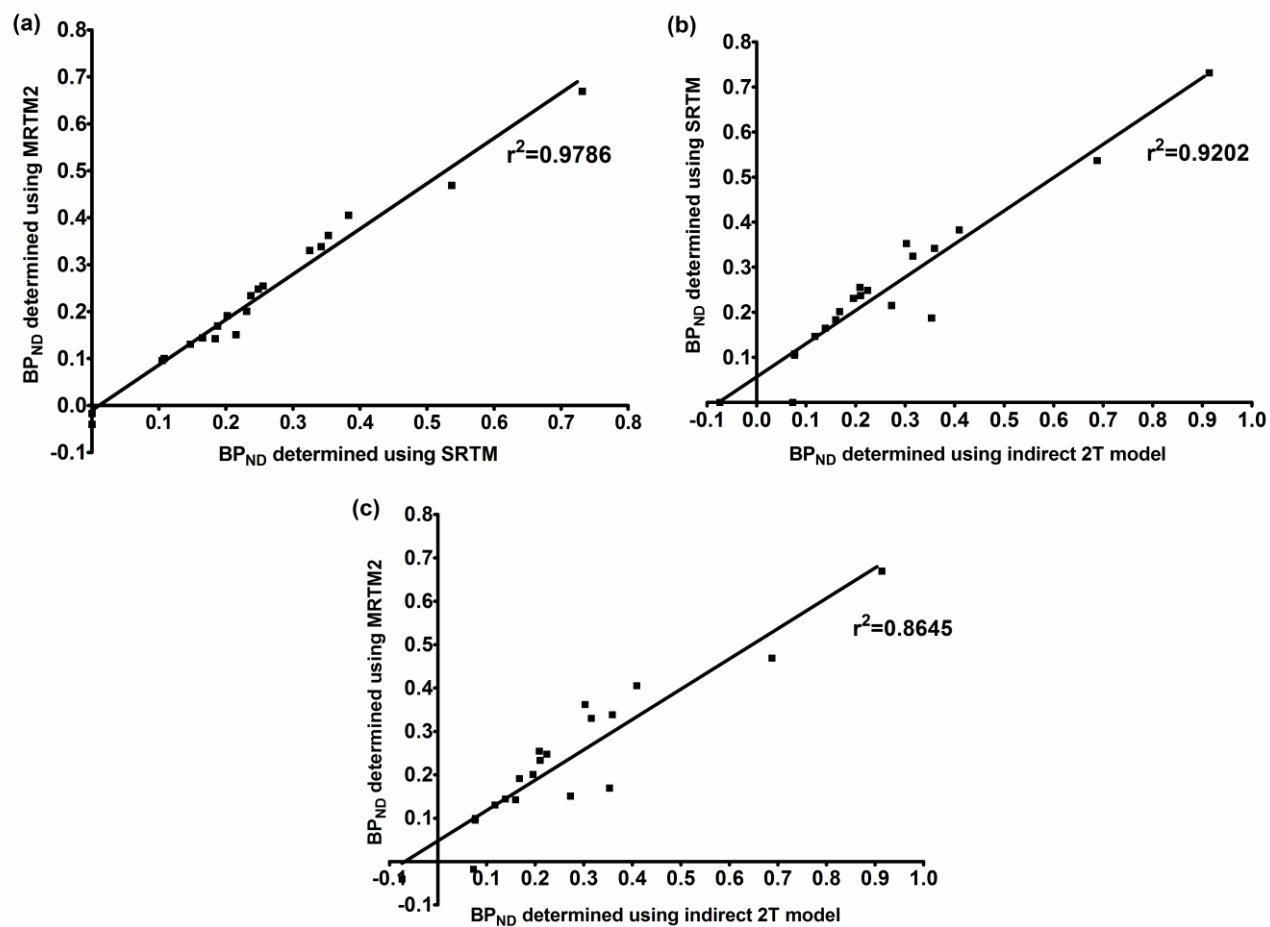


Figure 6.8 Comparison of the BP_{ND} values for ¹²³I-INER in baboon brain calculated using different methods.

Correlation between (a) SRTM and MRTM2, (b) SRTM and 2T compartmental model, where BP_{ND} was calculated using the indirect method and (c) MRTM2 and 2T compartmental model, where BP_{ND} was calculated using indirect method. A total of 20 values are plotted (2 SPECT measurements × 10 regions).

The C_t/C_p values were plotted against time for the baseline (Figure 6.9a) and blocking studies (Figure 6.9b) and transient equilibrium was found to occur around 3 hours post-injection. The $V_{T\text{ app}}$ was calculated at equilibrium, and the correlation between the V_T determined by the 2T compartmental model analysis and the $V_{T\text{ app}}$ was calculated and found to have $r^2=0.94$ for the baseline study and $r^2=0.81$ for the atomoxetine pre-blocking study (Figure 6.10a and 6.10b).

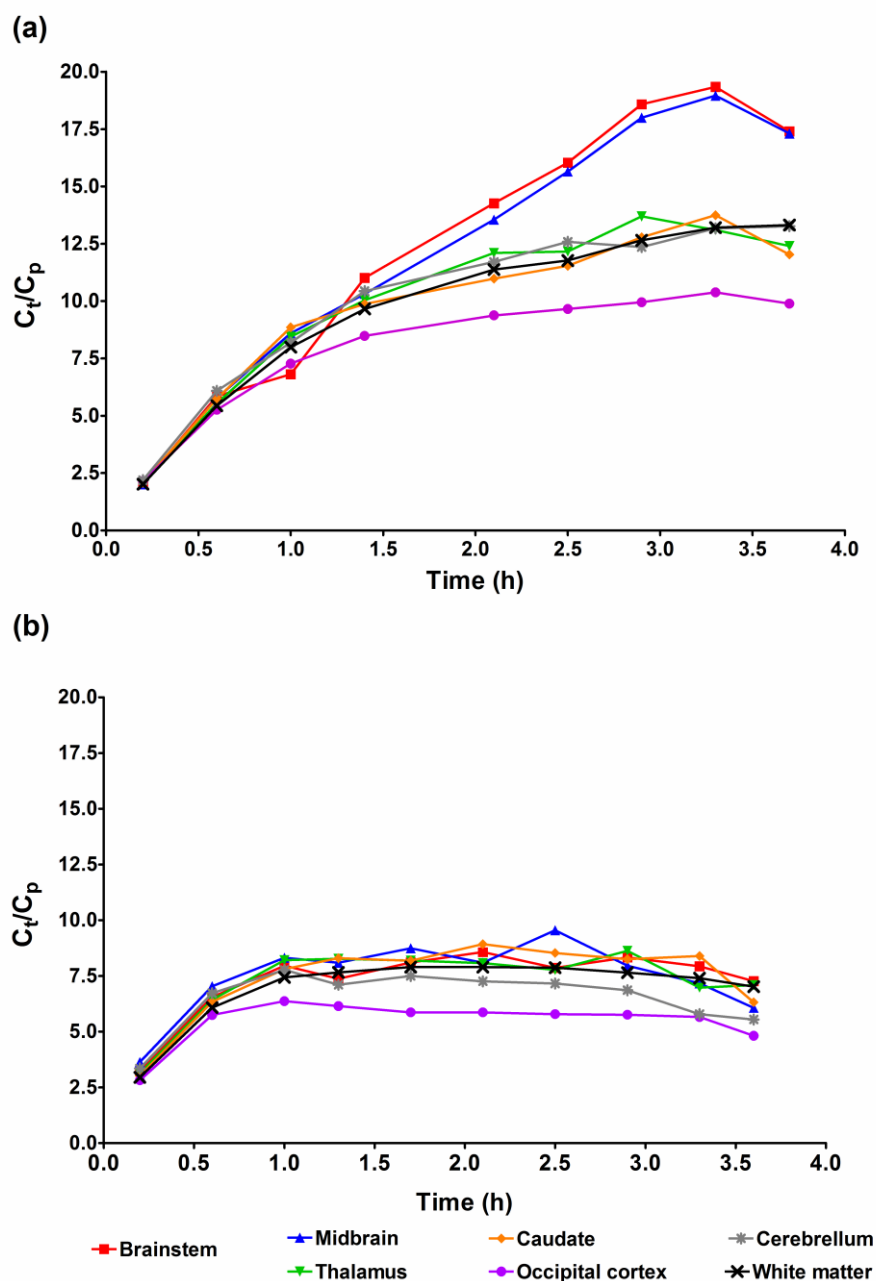


Figure 6.9 C_t/C_p values calculated for ^{123}I -INER in baboon brain over time. C_t/C_p values at baseline (a) and following pre-treatment with atomoxetine (b). Note a reduction of C_t/C_p in brainstem and midbrain following pre-blocking with atomoxetine. C_t/C_p was determined using the venous blood samples values.

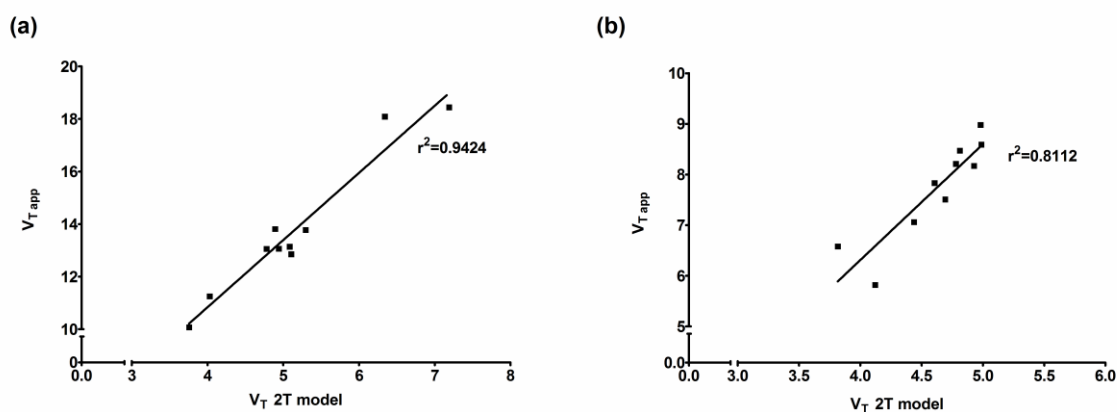


Figure 6.10 The relationship between $V_{T\text{ app}}$ and V_T values calculated for ^{123}I -INER in baboon brain.

Relationship between V_T values obtained by 2T compartmental model (x axis) and $V_{T\text{ app}}$ values at equilibrium (y axis) at baseline (a) and following pre-blocking with atomoxetine (b).

The occupancy of NATs by atomoxetine (0.85 mg/kg), determined from the baseline and pre-blocking experiments using the 2T compartmental model analysis and the change in BP_{ND} ($\Delta\text{BP}_{\text{ND}}$) calculated *via* the direct method, was 77% and 67% in brainstem and midbrain, respectively (Table 6.4). Similar occupancy values were obtained when using the BP_{ND} values calculated *via* the indirect method, where the occupancy was 83% and 69% in the brainstem and midbrain respectively. When the Lassen plot method was used to measure occupancy using the V_T values calculated from the 2T compartmental model analysis, the global occupancy of NATs by atomoxetine was 76%. Applying the Lassen plot equation to derive V_{ND} for subsequent calculation of occupancy in individual brain regions showed that 89% and 72% of brainstem and midbrain transporters were occupied by atomoxetine respectively. By using the Lassen plot and $V_{T\text{ app}}$ values, a global occupancy of 78% was determined, while the brainstem and midbrain occupancy was found to be 82% and 78% respectively (Table 6.4).

<i>Brain regions</i>	<i>% Occupancy</i>			
	ΔBP_{ND} direct method ^a	ΔBP_{ND} indirect method ^b	Lassen Plot – V_T from 2T model	Lassen Plot – $V_{T app}$
Brainstem	77.8	82.5	88.5	82.0
Midbrain	67.2	69.4	72.3	78.4
Thalamus	60.7	38.0	3.0	69.0
Caudate	0.2	53.3	46.0	63.7
Occipital	64.4	---	51.3	103.6
Cerebellum	60.6	66.0	124.6	82.4
White matter	55.8	56.9	56.1	73.7
Global occupancy	---	---	76.44	77.97

Table 6.4 The percentage NAT occupancy by atomoxetine in baboon brain determined by SPECT imaging with ¹²³I-INER and different calculation methods.
 ΔBP_{ND} : occupancy calculated according to Eq. 6.4. Lassen plot: regional occupancy calculated according to Eq. 6.5 following determination of V_{ND} using the Lassen plot; and global occupancy determined graphically as the slope of the line. ^a $BP_{ND}=k_3/k_4$. ^b $BP_{ND}=(V_T-V_{ND})/V_{ND}$ where $V_{ND}=V_T$ in occipital cortex (used as reference region for indirect method calculations).

6.3.2 ^{123}I -INER displacement studies

The displacement of ^{123}I -INER by atomoxetine varied in a dose-dependent fashion (Figure 6.11). The estimated ED_{50} values for atomoxetine were 0.15 mg/kg in the brainstem ($r^2=0.61$), 0.09 mg/kg in the midbrain ($r^2=0.71$) and 0.10 mg/kg when using a mean of both regions ($r^2=0.75$) (Figure 6.11). The maximum occupancy was estimated to be 22% and 37% for the brainstem and midbrain respectively (Figure 6.11), while the average occupancy was estimated to be 29%. When the maximum occupancy is normalised to 100%, an occupancy value of 81%, 88% and 87% in the brainstem, midbrain and combined brainstem and midbrain, respectively, was obtained for the highest dose of atomoxetine tested (0.85 mg/kg).

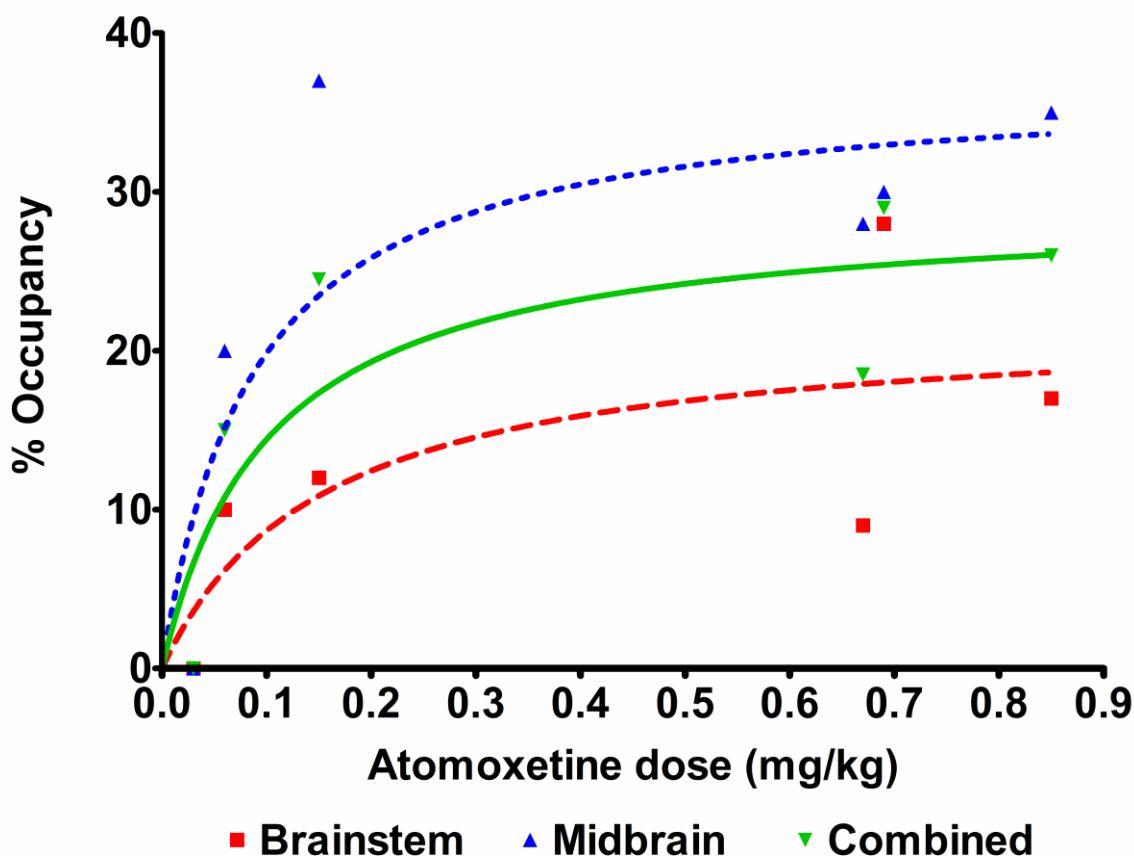


Figure 6.11 NAT occupancy by atomoxetine in baboon brain measured by SPECT with ^{123}I -INER.

Note that a one site hyperbola function fits well the experimental values ($r^2=0.61$, 0.71 and 0.74 for brainstem, midbrain and combined, respectively).

For reboxetine, the measured occupancy was also found to be dose-dependent with an ED_{50} of 2.33 mg/kg ($r^2=0.95$) in the brainstem, of 0.44 mg/kg ($r^2=0.57$) in the midbrain and of 1.07 mg/kg using a mean of both regions ($r^2=0.94$) (Figure 6.12). The maximum occupancy determined from the curve fitting was 104% and 56% for the brainstem and

midbrain, respectively (Figure 6.12), while the average maximum occupancy for both NAT rich regions was estimated to be 74%.

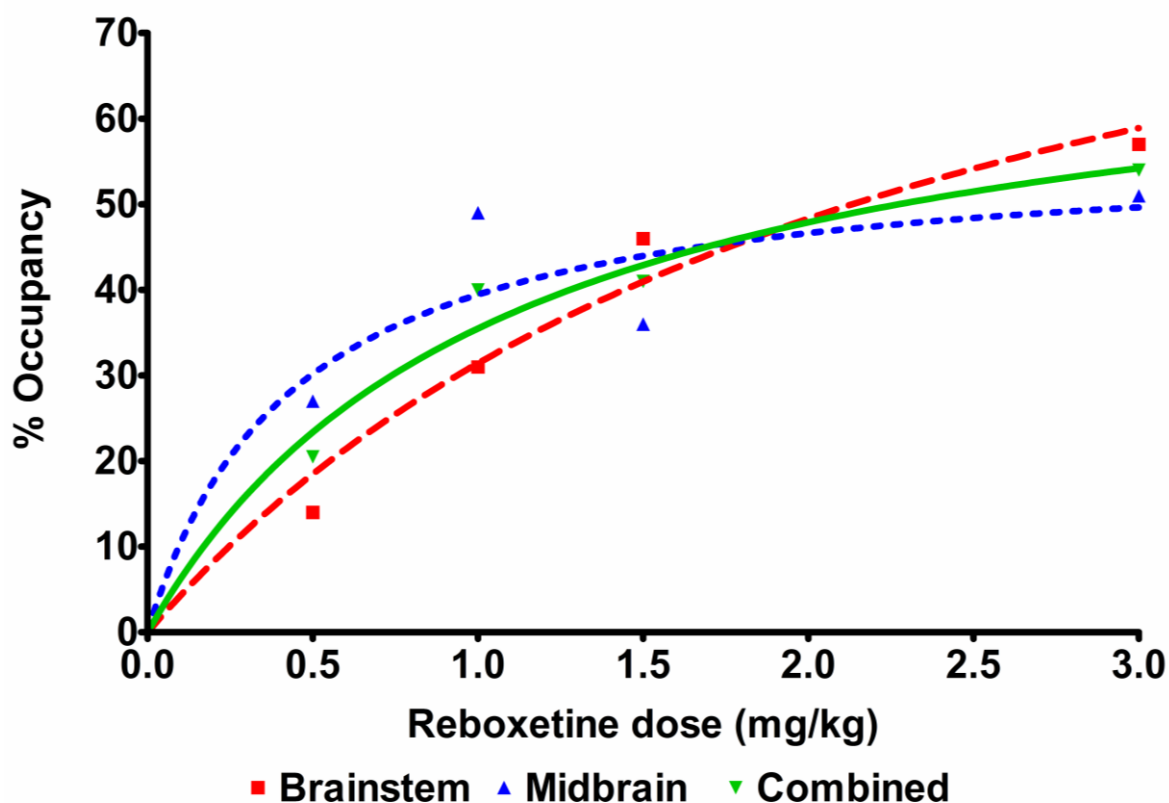


Figure 6.12 NAT occupancy by reboxetine in baboon brain measured by SPECT with ^{123}I -INER.

Note that a one site hyperbola function fits well the experimental values ($r^2=0.95$, 0.57 and 0.94 for brainstem, midbrain and combined, respectively).

6.4 Discussion

In this chapter, studies investigating the pharmacokinetic properties of ^{123}I -INER in non-human primate brain using SPECT were described. The uptake of ^{123}I -INER *in vivo* at baseline conditions was found to be consistent with the known distribution of NAT in baboon brain, in agreement with findings previously published (114). Furthermore, following pre-blocking or displacement with NAT selective drugs a reduction in ^{123}I -INER uptake confirmed the selectivity of ^{123}I -INER for the NAT *in vivo*, supporting its use as tool for imaging of the NAT in brain.

The occipital cortex had the lowest ^{123}I -INER uptake and the lowest V_T and was therefore a more reliable reference region than the caudate. Furthermore, the V_T of the occipital cortex was not reduced following pre-blocking with atomoxetine, providing further assurance that this region is suitable as a reference region for indirect

estimations and reference tissue models quantification. The choice of reference region for imaging studies of the NAT in brain has been controversial. Some authors have argued that there is no suitable reference region since the mapping of NAT in human brain is far from complete (139). The caudate and putamen have previously been considered as reference regions, due to the low density of NATs present (152). The occipital cortex has also been used as a reference region for the quantification of NAT radiotracer binding in non-human primates. Despite the controversy, both the striatum (caudate and putamen) and the occipital cortex have proven to be successful as reference regions for quantification of NAT radiotracer binding *in vivo* both in humans and non-human primates (41).

In an attempt to assess the suitability of the reference tissue models for the analysis of ^{123}I -INER data, a correlation analysis was performed between the BP_{ND} determined using the SRTM and MRTM2 and the BP_{ND} determined using the invasive 2T compartmental model analysis. The correlation between the BP_{ND} determined using each reference tissue model and the BP_{ND} determined using the invasive indirect 2T compartmental model was stronger than the correlation with BP_{ND} determined using the invasive direct 2T compartmental model. This can be explained by the error associated with estimation of k_3 and k_4 parameters by the 2T compartmental model, which will consequently affect the BP_{ND} results. The %COV determined for k_3 and k_4 was higher than the %COV measured for V_T (Table 6.1). Consequently, the smaller error associated with the calculation of V_T in comparison with the error associated with the determination of k_3 and k_4 by the 2T compartmental model shows that the indirect method for estimation of BP_{ND} is preferred over direct estimations based on k_3 and k_4 . Taking this into account, the strong correlation between the BP_{ND} determined *via* the SRTM and MRTM2 methods and BP_{ND} determined *via* the indirect 2T compartmental model ($r^2=0.92$ and $r^2=0.86$, respectively) suggests that non-invasive reference tissue methods can be used to estimate the binding potential of ^{123}I -INER, eliminating the need for arterial blood sampling. To date, ^{123}I -INER is the only NAT SPECT radiotracer for which quantification using reference tissue models has been shown to be useful. Using SRTM and MRTM2 models, the BP_{ND} for ^{123}I -INER in the baseline study was calculated to be around 0.7 and 0.5 in the brainstem and midbrain, respectively. This is in line with previously reported values measured using other NAT radiotracers currently used for human brain imaging using PET (113). The use of anaesthetics has been reported to increase the levels of noradrenaline in rat brain resulting in a reduction of the number of available receptors for binding (B_{avail}) (30, 113). It is therefore possible that the BP_{ND} was underestimated due to the effect of using anaesthesia in these imaging studies, and that in conscious animals BP_{ND} values may be higher.

Analysis of blood samples showed that the metabolic profile of ^{123}I -INER was similar in arterial and venous blood. The V_T calculated using an arterial plasma input function showed a correlation of 0.99 with the V_T calculated using a venous plasma input function. This suggests that quantification using the 2T compartmental model may be successfully achieved using data from venous blood sampling, rather than more invasive arterial blood sampling. The use of the venous plasma input function resulted in a lower V_T compared to that calculated using the arterial input function. However, when the aim is to compare baseline scans with disease state or drug treatment scans, the use of venous sampling may provide a reliable quantification of ^{123}I -INER pharmacokinetic parameters, reducing the risk of complications associated with arterial sampling. Also, results showed that a transient equilibrium was reached at around 3 hours post-injection, and the $V_{T\text{ app}}$ correlated well with the V_T from 2T kinetic modelling ($r^2=0.94$ for the baseline study and $r^2=0.81$ for the atomoxetine pre-blocking study), suggesting that an estimation of the V_T can be made using a simple ratio between the activity concentration in tissue and in venous plasma at 3 hours post-injection, without the use of kinetic modelling. This simple approach may be valuable for use in clinical studies conducted in hospitals or research institutions that do not have access to kinetic modelling software needed for non-invasive reference tissue methods.

Using the displacement study data, the occupancy plateau for atomoxetine was estimated to be around 30%, corresponding to atomoxetine doses of around 0.85 mg/kg. In contrast, using the pre-blocking protocol, 0.85 mg/kg of atomoxetine was able to block 80% of NATs in baboon brain. This considerable difference in the occupancy determined from the displacement studies compared to the blocking study may be due to technical difficulties in reaching equilibrium in the displacement study, resulting in an underestimation of occupancy. Inaccuracies in the occupancy determined using the displacement data may also result from inadequate sampling following displacement. Another factor that may contribute to the underestimation of occupancy using displacement data is the small difference between radioactive concentrations in regions of interest compared to the reference region, resulting in an error in the calculation of specific binding. Normalisation of occupancy data from displacement studies to 100% resulted in occupancy values in the brainstem and midbrain for 0.85 mg/kg of around 80%, which is in line with pre-blocking data.

Atomoxetine has been used for the treatment of ADHD in both adults and children (166-168). The half life of atomoxetine in plasma was determined to be around 3 hours, although studies have also reported longer elimination times, as a function of the degree of metabolism (166-167). The results from the displacement studies using multiple doses of atomoxetine showed that NAT occupancy by atomoxetine was dose

dependent with an estimated ED₅₀ of 0.15 and 0.09 mg/kg for brainstem and midbrain, respectively. This suggests that for doses of 0.10 mg/kg, around half of the transporters are occupied by atomoxetine. In addition, around 80% occupancy of NATs in the brain by atomoxetine (0.85 mg/kg) was determined using both the pre-blocking study and the displacement study (when normalised to 100%). In contrast however, previous clinical trials with atomoxetine have found that doses of 1.2 mg/kg were required for clinical efficacy and the effect of 0.5 mg/kg was not significantly different from that of a placebo (168). This discrepancy may be explained by differences in the modelled situation in this present study compared to the clinical situation. The present study only evaluated NAT occupancy at peak atomoxetine levels, whereas in the clinical situation drug levels peak and trough over the course of a day. Takano and co-workers in 2009, reported similar levels of NAT occupancy by atomoxetine when using (S,S)-[¹⁸F]FMeNER-D₂ and PET imaging. The implications of these observations need further investigation, but it was suggested by Takano *et al.* 2009 that a sustained high NAT occupancy by atomoxetine at trough levels could lead to different clinical outcomes (113).

Reboxetine has been used for the treatment of depression and therapeutic doses typically range between 4.0 and 10.0 mg per day (117-118). Reboxetine has been shown to be rapidly absorbed, with peak plasma concentrations being reached within 2 hours and an elimination half-life of approximately 13 hours (118). Studies investigating the therapeutic efficacy of reboxetine are contradictory and controversial. Recently published reviews showed reboxetine to have similar clinical effects to placebo using doses ranging between 4.0 and 10.0 mg per day (169-170). Conversely, others have found significant improvements in reboxetine-treated patients compared to placebo using doses between 4.0 and 10.0 mg per day (171-172). In this study reboxetine was shown to occupy the NAT in a dose-dependent manner, where an estimated ED₅₀ of 2.33 and 0.44 mg/kg was found for the brainstem and midbrain, respectively. Maximum occupancy of NATs by reboxetine was found to be 104% and 57% for the brainstem and midbrain, respectively. This difference between high NAT density sites is likely to be due to the occupancy at 3.0 mg/kg driving the curve fit. When combining the brainstem and midbrain, the measured occupancy at 3.0 mg/kg of reboxetine was 54%, allowing a more reliable estimation of the maximum occupancy of 74%. It is unknown whether high NAT occupancy is required for clinically-effective treatment of depression; however this study shows that high doses of reboxetine are required to reach maximum occupancy of NAT in the baboon brain. Further *in vivo* evaluation of NAT occupancy by reboxetine using ¹²³I-INER may provide insight into the pharmacokinetic profile of reboxetine and hence, potentially improve the current understanding of the contradictory observations seen clinically with reboxetine.

The estimated ED_{50} values of reboxetine were higher than the estimated ED_{50} values of atomoxetine. Using membranes from MDCK cell lines transfected with human NATs, the K_i of reboxetine was determined to be 11 nM, while the K_i of atomoxetine was determined to be 5 nM (173). The atomoxetine and reboxetine ED_{50} values determined *in vivo* using SPECT with ^{123}I -INER are in agreement with *in vitro* observations, showing atomoxetine to have a higher affinity for the NAT than reboxetine.

In this thesis the Lassen plot was applied to obtain the global occupancy in brain following pre-blocking with atomoxetine, as previously described in the literature (165). The Lassen plot is a method typically used for quantification of global occupancy when no suitable reference region is available. In addition, the Lassen plot was also used to obtain the V_{ND} , which was then applied to the Lassen plot equation for determination of NAT occupancy in individual brain regions. For regions with high density of NATs, such as brainstem and midbrain, the occupancies determined using the Lassen plot were similar to the occupancies determined using the change in BP_{ND} indirect method (2T), further supporting the use of the occipital cortex as a suitable reference region for SPECT imaging using ^{123}I -INER. There was, however, higher variability in occupancy measurement in the other brain regions investigated, depending on the method used. The lower NAT density in these regions may explain this high variability, suggesting a limited use of ^{123}I -INER for the successful quantification of NAT occupancy in regions with low densities of the transporter. In regions such as the thalamus and caudate, which are relatively small size and are in close proximity, the high variability may also be due to the partial volume effects.

The small sample size of the current study is a particular limitation and therefore data should be interpreted with caution and additional studies with more animals may be required to allow further interpretation of the results. In addition, the study design for the dose-occupancy experiments could be improved. As highlighted above, bolus plus constant infusion experiments in different animals may incur errors in the estimation of specific binding. Baseline and blocking experiments in the same animal may provide more reliable results than bolus plus constant infusion experiments in different animals, as these are technically difficult to perform without incurring errors in reaching steady-state equilibrium.

6.5 Conclusions

In conclusion, the results from this study showed that non-invasive reference tissue models can be used to quantify the binding potential of ^{123}I -INER *in vivo* using SPECT and

the occipital cortex can be used as a reference region. In addition, an estimation of the V_T may be obtained by dividing the concentration in tissue by the concentration in plasma from venous samples at transient equilibrium to give the $V_{T \text{ app}}$. Both these methods simplify the data acquisition and image analysis for ^{123}I -INER, providing a feasible and easy protocol for future studies in non-human primates. Furthermore, this study showed that SPECT imaging with ^{123}I -INER could be used to measure the dose-dependent occupancy of the NAT by atomoxetine and reboxetine in the non-human primate brain. Therefore SPECT imaging with ^{123}I -INER could be used to aid the development of novel drugs targeting the NAT and also improve current knowledge on existing drugs for treatment of ADHD, depression and other disorders associated with dysregulation of the NAT system.

7 Final conclusions and future work

This thesis focused on the process of developing novel radiotracers as tools for imaging the human brain. The radiotracer discovery and development pipeline was discussed and each step prior to clinical trials was investigated.

Brain radiotracer discovery and development is a rapidly expanding area but limited success has been achieved over the years. This thesis investigated some of the reasons for the high failure rate in brain radiotracer discovery and concluded that careful characterisation of the lead candidate prior to radiolabelling can reduce attrition in the early stages of radiotracer discovery. In the past, a radiotracer candidate progressed to the radiolabelling stage based only on simplistic measures such as affinity and lipophilicity. In addition, there was limited knowledge of the relationships between the physicochemical properties of a radiotracer and the *in vivo* characteristics ultimately observed. In order to address this issue a novel tool for aiding lead candidate identification was developed.

The HPLC tool developed for aiding lead molecule selection was applied to a library of compounds and the lead candidate was successfully identified. Compound LS 1 was shown to be the most likely to succeed within the library investigated, but the high PPB observed for LS 1 advised against taking this compound forward to further evaluation studies *in vivo*. Based on this finding, the Glasgow radiotracer development group went on to synthesise a novel library of PK11195 analogues with the aim of obtaining a candidate with improved characteristics for *in vivo* imaging of TSPO using SPECT. Future work will include testing of the new library using the HPLC tool developed here and competition binding assays.

Future work is required to confirm the utility of the developed HPLC tool in aiding the selection of compounds to be taken forward as radiotracers. This can be achieved by using the tool to select compounds as potential radiotracers and then comparing the HPLC predicted values with the measured *in vivo* imaging outcomes. This type of comparison was performed using the data obtained with NKJ64, the novel radiotracer for NAT developed as part of the present thesis. NKJ64 was selected prior to development of the HPLC tool and the affinity was used as the only selection criteria. When NKJ64 was analysed using the HPLC tool and guidelines outlined in Chapter 2, a %ID in human brain between 2 and 4% was predicted (Appendix 1). In baboons the %ID of NKJ64 in brain was determined to be around 3%, in agreement with the predicted %ID using the HPLC tool. Furthermore, the analysis of NKJ64 using the HPLC methodology

and guidelines resulted in a predicted $BP_{ND} \leq 2$ (Appendix 1), suggesting that high non-specific binding may be an issue with this radiotracer. *In vivo* data in baboons revealed high non-specific binding and a BP_{ND} between 1 and 2, in agreement with the predicted values using the HPLC tool. Although the *in vivo* data on NKJ64 is from baboon studies and not human studies, this provides some confidence that the new HPLC tool can predict *in vivo* characteristics and therefore aid lead molecule selection. However, further investigation is required with more radiotracers for this HPLC technique to be fully validated. Future work may also include establishing collaborations with other research centres in order to extend this analysis to include more radiotracers that are both successful and unsuccessful in humans.

The second part of this thesis focused on the development of a novel radiotracer for imaging of the NAT in brain. Radiolabelling of NKJ64 was successfully accomplished by iododestannylation and preliminary biological evaluation in rodents showed promising results. However, imaging in baboons showed a distribution that was inconsistent with the known NAT distribution and therefore studies using NKJ64 were halted and translation into humans was not recommended. As discussed in many parts of this thesis, radiotracer discovery and development is lengthy process, where multiple steps need to be taken prior to human studies. These steps typically involve the use of animals and frequently differences between species significantly affect whether the radiotracers can be translated into humans. NKJ64 is a good example of the influence of species differences on radiotracer performance *in vivo*. In fact, once the radiotracer enters the pre-clinical stage the failure rate is difficult to control as success is highly dependent on the species used and the behaviour of the radiotracer in the *in vivo* environment. At this stage, type I errors (going too far) and type II errors (not going far enough) are usually difficult to minimise, as species differences can hamper the successful separation of useful radiotracers from useless radiotracers.

The NAT radiotracer INER, developed by Tamagnan and colleagues at Yale University and the Institute for Degenerative Disorders, New Haven, USA, was also investigated as part of this thesis. Unlike NKJ64, initial studies with INER in baboons had been promising (114). This thesis presented the kinetic modelling analysis of INER, as well as data from further occupancy studies in baboons. The results supported the translation of INER into humans studies, despite the slow kinetics determined over the imaging period. Future studies in humans would represent the final step in determining the utility of INER as a SPECT radiotracer for imaging of NAT.

The studies evaluating NKJ64 and INER suggest that further work may be required to develop an ideal radiotracer for imaging of NAT in brain using SPECT. High affinity and

selectivity are required of a radiotracer for brain imaging, particularly when imaging low density sites, such as the NAT. A radiotracer with lower non-specific binding than NKJ64 and faster kinetics than INER is desirable. Testing of future libraries using the HPLC tool developed could enable the predicted non-specific binding to be compared to NKJ64, aiding the identification of a lead candidate to be taken forward to radiolabelling studies.

During the process of developing NKJ64, a *para*-iodophenoxy analogue of NKJ64 that was part of the original library of NAT candidates showed a moderate affinity for SERT ($K_i=34.5\pm 1.7$ nM, $n=3$) (43). As a result of this finding, the Chemistry group at the University of Glasgow set out to design a library of compounds based on this analogue with the aim of obtaining a high affinity SERT radiotracer. The resulting library of compounds will be tested for SERT affinity and the HPLC tool developed will be utilised as part of the lead candidate selection process.

Appendix 1

Using the HPLC tool developed as part of this thesis (Chapter 2), the physicochemical properties of NKJ64 were measured, including P_m , %PPB and K_m (Table A1.1). The relationships between *in vitro* HPLC measures and *in vivo* %ID and BP_{ND} in combination with proposed guidelines for lead molecule selection (Chapter 2, section 2.4.1) were used to estimate *in vivo* properties for NKJ64 (Table A1.2).

Compound name	P_m	%PPB	K_m
NKJ64	0.66	91.00	260.34

Table A1.1 NKJ64 physicochemical properties determined by HPLC.

HPLC measures	Predicted <i>in vivo</i> measures	NKJ64
$P_m < 1.5$	%ID > 2.0%	✓
$P_m < 0.5$	%ID > 4.0%	✗
PPB < 95%	%ID > 2.0%	✓
45% < PPB < 85%	%ID > 4.0%	✗
$K_m < 250$	$BP_{ND} > 2.0$	✗
$K_m < 150$	$BP_{ND} > 3.0$	✗
Summary	Predicted $BP_{ND} < 2.0$	
	Predicted %ID between 2.0% and 4.0%	

Table A1.2 Proposed guideline for lead molecule selection applied to NKJ64.

Appendix 2

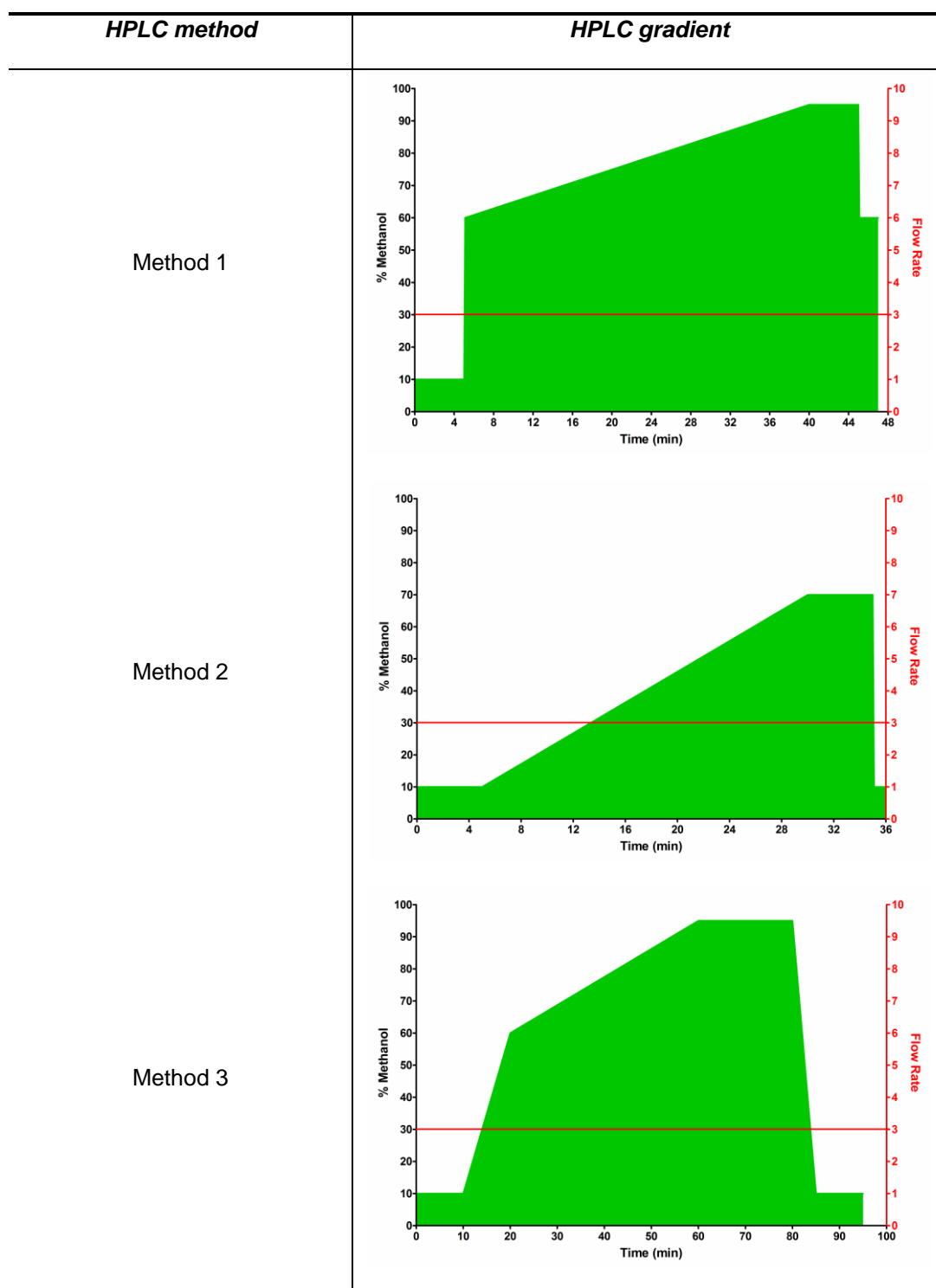


Table A2.1 Different HPLC methods investigated for separation of by-product peaks obtained during $^{123/125}\text{I-NKJ64}$ radiosynthesis using 2M HCl as deprotecting agent.

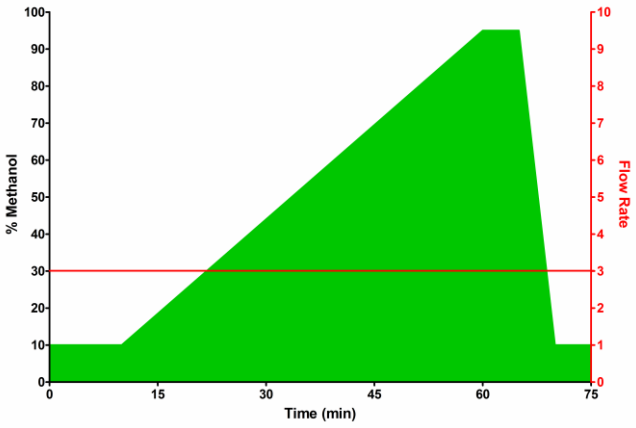
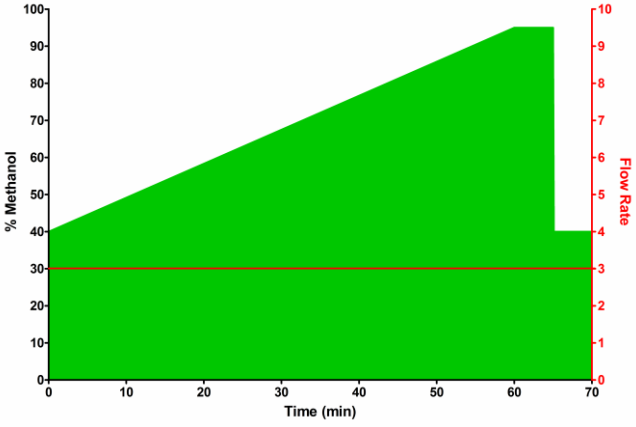
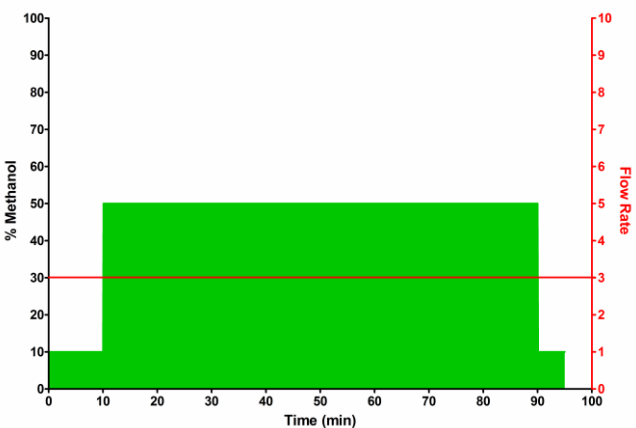
<i>HPLC method</i>	<i>HPLC gradient</i>																														
Method 4	 <p>The HPLC gradient plot for Method 4 shows the percentage of methanol (left y-axis, 0-100%) and flow rate (right y-axis, 0-10) over time (x-axis, 0-75 min). The methanol concentration starts at 10% at 0 min, remains constant until 15 min, then increases linearly to 95% at 60 min. It remains at 95% until 70 min, then drops sharply to 10% at 75 min. The flow rate is constant at 3.0 throughout the run.</p> <table border="1"><thead><tr><th>Time (min)</th><th>% Methanol</th><th>Flow Rate</th></tr></thead><tbody><tr><td>0</td><td>10</td><td>3.0</td></tr><tr><td>15</td><td>10</td><td>3.0</td></tr><tr><td>30</td><td>40</td><td>3.0</td></tr><tr><td>45</td><td>70</td><td>3.0</td></tr><tr><td>60</td><td>95</td><td>3.0</td></tr><tr><td>70</td><td>95</td><td>3.0</td></tr><tr><td>75</td><td>10</td><td>3.0</td></tr></tbody></table>	Time (min)	% Methanol	Flow Rate	0	10	3.0	15	10	3.0	30	40	3.0	45	70	3.0	60	95	3.0	70	95	3.0	75	10	3.0						
Time (min)	% Methanol	Flow Rate																													
0	10	3.0																													
15	10	3.0																													
30	40	3.0																													
45	70	3.0																													
60	95	3.0																													
70	95	3.0																													
75	10	3.0																													
Method 5	 <p>The HPLC gradient plot for Method 5 shows the percentage of methanol (left y-axis, 0-100%) and flow rate (right y-axis, 0-10) over time (x-axis, 0-70 min). The methanol concentration starts at 40% at 0 min and increases linearly to 95% at 60 min. It remains at 95% until 65 min, then drops to 40% at 70 min. The flow rate is constant at 3.0 throughout the run.</p> <table border="1"><thead><tr><th>Time (min)</th><th>% Methanol</th><th>Flow Rate</th></tr></thead><tbody><tr><td>0</td><td>40</td><td>3.0</td></tr><tr><td>10</td><td>45</td><td>3.0</td></tr><tr><td>20</td><td>55</td><td>3.0</td></tr><tr><td>30</td><td>65</td><td>3.0</td></tr><tr><td>40</td><td>75</td><td>3.0</td></tr><tr><td>50</td><td>85</td><td>3.0</td></tr><tr><td>60</td><td>95</td><td>3.0</td></tr><tr><td>65</td><td>95</td><td>3.0</td></tr><tr><td>70</td><td>40</td><td>3.0</td></tr></tbody></table>	Time (min)	% Methanol	Flow Rate	0	40	3.0	10	45	3.0	20	55	3.0	30	65	3.0	40	75	3.0	50	85	3.0	60	95	3.0	65	95	3.0	70	40	3.0
Time (min)	% Methanol	Flow Rate																													
0	40	3.0																													
10	45	3.0																													
20	55	3.0																													
30	65	3.0																													
40	75	3.0																													
50	85	3.0																													
60	95	3.0																													
65	95	3.0																													
70	40	3.0																													
Method 6	 <p>The HPLC gradient plot for Method 6 shows the percentage of methanol (left y-axis, 0-100%) and flow rate (right y-axis, 0-10) over time (x-axis, 0-100 min). The methanol concentration starts at 10% at 0 min, remains constant until 10 min, then increases to 50% at 15 min. It remains at 50% until 90 min, then drops to 10% at 95 min. The flow rate is constant at 3.0 throughout the run.</p> <table border="1"><thead><tr><th>Time (min)</th><th>% Methanol</th><th>Flow Rate</th></tr></thead><tbody><tr><td>0</td><td>10</td><td>3.0</td></tr><tr><td>10</td><td>10</td><td>3.0</td></tr><tr><td>15</td><td>50</td><td>3.0</td></tr><tr><td>30</td><td>50</td><td>3.0</td></tr><tr><td>45</td><td>50</td><td>3.0</td></tr><tr><td>60</td><td>50</td><td>3.0</td></tr><tr><td>75</td><td>50</td><td>3.0</td></tr><tr><td>90</td><td>50</td><td>3.0</td></tr><tr><td>95</td><td>10</td><td>3.0</td></tr></tbody></table>	Time (min)	% Methanol	Flow Rate	0	10	3.0	10	10	3.0	15	50	3.0	30	50	3.0	45	50	3.0	60	50	3.0	75	50	3.0	90	50	3.0	95	10	3.0
Time (min)	% Methanol	Flow Rate																													
0	10	3.0																													
10	10	3.0																													
15	50	3.0																													
30	50	3.0																													
45	50	3.0																													
60	50	3.0																													
75	50	3.0																													
90	50	3.0																													
95	10	3.0																													

Table A2.1 (cont).

HPLC method	HPLC gradient
Method 7	
Method 8	
Method 9	

Table A2.1 (cont).

HPLC method	HPLC gradient
Method 10	
Method 11	
Method 12	

Table A2.1 (cont).

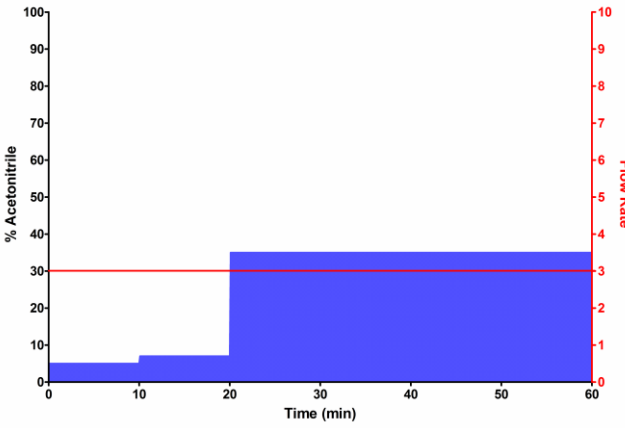
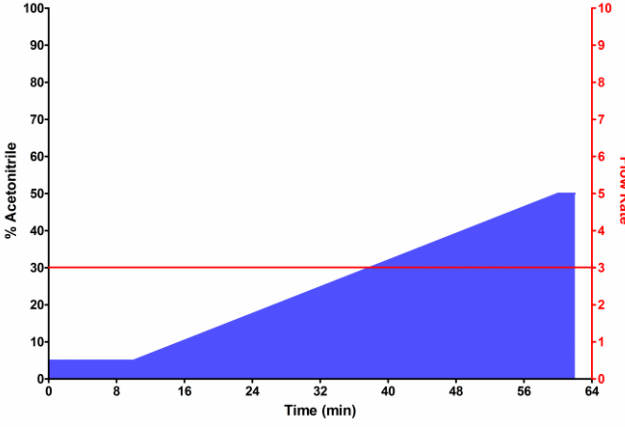
<i>HPLC method</i>	<i>HPLC gradient</i>															
Method 13	 <p>The graph for Method 13 shows the HPLC gradient. The x-axis is Time (min) from 0 to 60. The left y-axis is % Acetonitrile from 0 to 100. The right y-axis is Flow Rate from 0 to 10. The blue area represents the acetonitrile concentration, which is constant at approximately 5% until 10 minutes, then increases to approximately 8% at 20 minutes, and finally to approximately 35% at 60 minutes. The red line represents the flow rate, which is constant at approximately 3 until 20 minutes, then increases to approximately 3.5 at 60 minutes.</p> <table border="1"><thead><tr><th>Time (min)</th><th>% Acetonitrile</th><th>Flow Rate</th></tr></thead><tbody><tr><td>0</td><td>5</td><td>3</td></tr><tr><td>10</td><td>5</td><td>3</td></tr><tr><td>20</td><td>8</td><td>3.5</td></tr><tr><td>60</td><td>35</td><td>3.5</td></tr></tbody></table>	Time (min)	% Acetonitrile	Flow Rate	0	5	3	10	5	3	20	8	3.5	60	35	3.5
Time (min)	% Acetonitrile	Flow Rate														
0	5	3														
10	5	3														
20	8	3.5														
60	35	3.5														
Method 14	 <p>The graph for Method 14 shows the HPLC gradient. The x-axis is Time (min) from 0 to 64. The left y-axis is % Acetonitrile from 0 to 100. The right y-axis is Flow Rate from 0 to 10. The blue area represents the acetonitrile concentration, which is constant at approximately 5% until 8 minutes, then increases linearly to approximately 50% at 64 minutes. The red line represents the flow rate, which is constant at approximately 3 until 8 minutes, then increases linearly to approximately 5 at 64 minutes.</p> <table border="1"><thead><tr><th>Time (min)</th><th>% Acetonitrile</th><th>Flow Rate</th></tr></thead><tbody><tr><td>0</td><td>5</td><td>3</td></tr><tr><td>8</td><td>5</td><td>3</td></tr><tr><td>64</td><td>50</td><td>5</td></tr></tbody></table>	Time (min)	% Acetonitrile	Flow Rate	0	5	3	8	5	3	64	50	5			
Time (min)	% Acetonitrile	Flow Rate														
0	5	3														
8	5	3														
64	50	5														

Table A2.1 (cont).

List of references

1. Ottobriani L, Ciana P, Biserni A, Lucignani G, Maggi A. Molecular imaging: A new way to study molecular processes in vivo. *Mol. Cell. Endocrinol.* 2006;246:69-75.
2. Guo Q, Brady M, Gunn R. A Biomathematical Modeling Approach to Central Nervous System Radioligand Discovery and Development. *J. Nucl. Med.* 2009;50:1715-1723.
3. Laruelle M, Slifstein M, Huang Y. Relationships between Radiotracer Properties and Image Quality in Molecular Imaging of the Brain with Position Emission Tomography. *Mol. Imag. Biol.* 2003;5(6):363-375.
4. Cherry S. Multimodality In Vivo Imaging Systems: Twice the Power or Double the Trouble? *Annu. Rev. Biomed. Eng.* 2006;8:35-62.
5. Ruth T. The uses of radiotracers in the life sciences. *Rep. Prog. Phys.* 2009;72:1-23.
6. Haberkorn U, Eisenhuth M. Molecular imaging and therapy - a programme based on the development of new biomolecules. *Eur. J. Nuc. Med. Mol. Imag.* 2005;32:1354-1359.
7. Salvadori P. Radiopharmaceuticals, Drugs Development and Pharmaceutical Regulations in Europe. *Curr. Radiopharm.* 2008;1(1):7-11.
8. Kemp R, Epstein F, Catana C, Tsui B, Ritman E. Small-Animal Molecular Imaging Methods. *J. Nucl. Med.* 2010;51:18S-32S.
9. Frank R, Langstrom B, Antoni G, et al. The imaging continuum: bench to biomarkers to diagnostics. *J. Label. Compd. Radiopharm.* 2007;50:746-769.
10. Weng X, Ding Y, Volkow N. Imaging the functioning human brain. *PNAS.* 1999;96:11073-11074.
11. Kherlopian A, Song T, Duan Q, et al. A review of imaging techniques for systems biology. *BMC Syst. Biol.* 2008;2(74):1-18.
12. Alavi A, Basu S. Planar and SPECT imaging in the era of PET and PET-CT: can it survive the test of time? *Eur. J. Nuc. Med. Mol. Imag.* 2008.

13. Mariani G, Bruselli L, Duatti A. Is PET always an advantage versus planar and SPECT imaging? *Eur. J. Nuc. Med. Mol. Imag.* 2008;35:1560-1565.
14. von Schulthess G, Cyrill B. Integrating imaging modalities: what makes sense from a workflow perspective? *Eur. J. Nuc. Med. Mol. Imag.* 2010;37:980-990.
15. Nunn A. Molecular Imaging and Personalized Medicine: An Uncertain Future. *Cancer Biother. Radio.* 2007;22(6):722-739.
16. Kegeles L, Mann J. In vivo Imaging of Neurotransmitter Systems Using Radiolabeled Receptor Ligands. *Neuropsychopharmacology.* 1997;17(5):293-307.
17. Dischino D, Welch M, Kilbourn M, Raichle M. Relationship Between Lipophilicity and Brain Extraction of C-11-Labeled Radiopharmaceuticals. *J. Nucl. Med.* 1983;24:1030-1038.
18. Pike V. PET radiotracers: crossing the bloo-brain barrier and surviving the metabolism. *Trends Pharmacol. Sci.* 2009;30(8):431-440.
19. Waterhouse RN. Determination of Lipophilicity and Its Use as a Predictor of Blood-Brain Barrier Penetration of Molecular Imaging Agents. *Mol. Imag. Biol.* 2003;5(6):376-389.
20. Wong D, Pomper M. Predicting the Success of a Radiopharmaceutical for In Vivo Imaging of Central Nervous System Neuroreceptor Systems. *Mol. Imag. Biol.* 2003;5(6):350-362.
21. Hudson A, Lione L. Characterization of Imidazoline Receptors by Radioligand Binding. In: Keen M, ed. *Receptor Binding Techniques*. Vol 106. New Jersey: Humana Press; 1999.
22. Lazareno S. Quantification of Receptor Interactions Using Binding Methods. *J. Recept. Signal Transduct. Res.* 2001;21(2&3):139-165.
23. Qume M. Overview of Ligand-Receptor Binding Techniques. In: Keen M, ed. *Receptor Binding Techniques*. Vol 106. New Jersey: Humana Press; 1999.

24. Sen S, Jaakola V, Heimo H, et al. Development of scintiplate assay for recombinant human α_{2B} -adrenergic receptor. *Anal. Biochem.* 2002;307:280-286.
25. Carrick T, Kowal D, Nawoschik S, Zhang G, Chan K, Dunlop J. Development of a scintillation proximity assay binding method for the human 5-hydroxytryptamine 6 receptor using intact cells. *Anal. Biochem.* 2008;381:27-32.
26. Udenfriend S, Gerber L, Nelson N. Scintillation Proximity Assay: A Sensitive and Continuous Isotopic Method for Monitoring Ligand/Receptor and Antigen/Antibody Interactions. *Anal. Biochem.* 1987;161:494-500.
27. Cook N. Scintillation proximity assay: a versatile high-throughput screening technology. *Drug Discov. Today.* 1996;1(7):287-294.
28. Schuck P. Reliable determination of binding affinity and kinetics using surface plasmon resonance biosensors. *Curr. Opin. Biotechnol.* 1997;8:498-502.
29. Davis M. Bioimaging of Laboratory Animals: The Visual Translation of Molecular Insights. *ILAR J.* 2008;49(1):1-3.
30. Hildebrandt I, Su H, Weber W. Anesthesia and Other Considerations for in Vivo Imaging of Small Animals. *ILAR J.* 2008;49(1):17-26.
31. Kung M, Kung H. Peracetic Acid as a Superior Oxidant for Preparation of [123 I]IBZM: A Potential Dopamine D-2 Receptor Imaging Agent. *J. Label. Compd. Radiopharm.* 1989;27(6):691-700.
32. Coenen HH, Mertens J, Mazière B. *Radioiodination Reactions for Pharmaceuticals - Compendium for Effective Synthesis Strategies.* Netherlands: Springer; 2006.
33. Giron M. Radiopharmaceutical pharmacokinetics in animals: critical considerations. *Q. J. Nucl. Med. Mol. Imaging.* 2009;53(4):359-364.
34. Clark D. In silico prediction of blood-brain barrier permeation. *Drug Discov. Today.* 2003;8(20):927-933.

35. Stevenson L, Tavares A, Brunet A, et al. New iodinated quinoline-2-carboxamides for SPECT imaging of the translocator protein. *Bioorg. Med. Chem. Lett.* 2010;20:954-957.
36. Grandoso L, Pineda J, Ugedo L. Comparative study of effects of desipramine and reboxetine on locus coeruleus neurons in rat brain slices. *Neuropharmacology.* 2004;46:815-823.
37. Kiyono Y, Kanegawa N, Kawashima H, Kitamura Y, Iida Y, Saji H. Evaluation of radioiodinated (*R*)-*N*-methyl-3-(2-iodophenoxy)-3-phenylpropanamine as a ligand for brain norepinephrine transporter imaging. *Nucl. Med. Biol.* 2004;31:147-153.
38. Kung M, Choi S, Hou C, Zhuang Z, Foulon C, Kung HF. Selective binding of 2-[¹²⁵I]iodo-nisoxetine to norepinephrine transporters in the brain. *Nucl. Med. Biol.* 2004;31:533-541.
39. McConathy J, Owens MJ, Kilts CD, et al. Synthesis and biological evaluation of [¹¹C]talopran and [¹¹C]talsupran: candidate PET ligands for the norepinephrine transporter. *Nucl. Med. Biol.* 2004;31:705-718.
40. Lakshmi B, Kung M, Lieberman B, Zhao J, Waterhouse R, Kung HF. (*R*)-*N*-Methyl-3-(3-¹²⁵I-pyridin-2-yloxy)-3-phenylpropan-1-amine: a novel probe for norepinephrine transporters. *Nucl. Med. Biol.* 2008;35:43-52.
41. Zeng F, Mun J, Jarkas N, et al. Synthesis, Radiosynthesis, and Biological Evaluation of Carbon-11 and Fluorine-18 Labeled Raboxetine Analogues: Potential Positron Emission Tomography Radioligands for in Vivo Imaging of the Norepinephrine Transporter. *J. Med. Chem.* 2009;52:62-73.
42. Brunello N, Mendlewicz J, Kasper S, et al. The role of noradrenaline and selective noradrenaline reuptake inhibition in depression. *Eur. Neuropsychopharmacol.* 2002;12:461-475.
43. Jobson NK, Crawford AR, Dewar D, Pimlott SL, Sutherland A. Design and synthesis of (2*R*,3*S*)-iodreboxetine analogues for SPECT imaging of the noradrenaline transporter. *Bioorg. Med. Chem. Lett.* 2009;19:4996-4998.

44. Jobson NK, Crawford AR, Dewar D, Pimlott SL, Sutherland A. New iodoreboxetine analogues for SPECT imaging of the noradrenaline transporter. *Bioorg. Med. Chem. Lett.* 2008;18:4940-4943.
45. Jobson NK, Spike R, Crawford AR, Dewar D, Pimlott SL, Sutherland A. Stereoselective synthesis of (2*S*,3*R*)- and (2*R*,3*S*)-iodoreboxetine; potential SPECT imaging agents for the noradrenaline transporter. *Org. Biomol. Chem.* 2008;6:2369-2376.
46. Scherrmann J-M. Drug delivery to brain via the blood-brain barrier. *Vascul. Pharmacol.* 2002;38:349-354.
47. Reichel A, Begley D. Potential of Immobilized Artificial Membranes for Predicting Drug Penetration Across the Blood-Brain Barrier. *Pharmaceut. Res.* 1998;15(8):1270-1274.
48. Goodwin J, Clark D. In Silico Predictions of Blood-Brain Barrier Penetration: Considerations to "Keep in Mind". *J. Pharmacol. Exp. Ther.* 2005;315(2):477-483.
49. Yoon C, Kim S, Shin B, Lee K, Yoo S. Rapid Screening of Blood-Brain Barrier Penetration of Drugs Using the Immobilized Artificial Membrane Phosphatidylcholine Column Chromatography. *J. Biomol. Screen.* 2006;11:13-20.
50. Pardridge W. The Blood-Brain Barrier: Bottleneck in Brain Drug Development. *NeuroRx.* 2005;2:3-14.
51. Abbott N. Prediction of blood-brain barrier permeation in drug discovery from *in vivo*, *in vitro* and *in silico* models. *Drug Discover. Today Technol.* 2004;1(4):407-416.
52. Yang C, Cai S, Lui H, Pidgeon C. Immobilized Artificial Membranes - screens for drug membrane interaction. *Adv. Drug Deliv. Rev.* 1996;23:229-256.
53. Eckelman WC, Kilbourn MR, Mathis CA. Specific to nonspecific binding in radiopharmaceutical studies: it's not so simple as it seems! *Nucl. Med. Biol.* 2009;36(3):235-237.
54. Eckelman WC, Mathis CA. Discussion of targeting proteins *in vivo*: *in vitro* guidelines. *Nucl. Med. Biol.* 2006;33(2):161-164.

55. Alavijeh M, Chishty M, Qaiser M, Palmer A. Drug Metabolism and Pharmacokinetics, the Blood-Brain Barrier, and Central Nervous System Drug Discovery. *NeuroRx*. 2005;2:554-571.
56. Giaginis C, Tsantili-Kakoulidou A. Alternative Measures of Lipophilicity: From Octanol-Water Partitioning to IAM Retention. *J. Pharm. Sci.* 2008;97:2984-3004.
57. Ong S, Lui H, Pidgeon C. Immobilized-artificial-membrane chromatography: measurements of membrane partition coefficient and predicting drug membrane permeability. *J. Chromatogr. A.* 1996;728:113-128.
58. Giaginis C, Tsantili-Kakoulidou A. Current State of Art in HPLC Methodology for Lipophilicity Assessment of Basic Drugs: A Review. *J. Liq. Chromatogr. Related Technol.* 2008;31:79-96.
59. My Du C, Valko K, Bevan C, Reynolds D, Abraham M. Rapid Gradient RP-HPLC Method for Lipophilicity Determination: A Solvation Equation Based Comparison with Isocratic Methods. *Anal. Chem.* 1998;70:4228-4234.
60. Valko K. Application of high-performance liquid chromatography based measurements of lipophilicity to model biological distribution. *J. Chromatogr. A.* 2004;1037:299-310.
61. Valko K. HPLC-Based Measurements of Various Lipophilicity Parameters to Aid Drug Design. *LCGC North America.* 2007;25(3):284-291.
62. Valko K, Bevan C, Reynolds D. Chromatographic Hydrophobicity Index by Fast-Gradient RP-HPLC: A High-Throughput Alternative to logP/logD. *Anal. Chem.* 1997;69:2022-2029.
63. Pidgeon C, Ong S, Lui H, et al. IAM Chromatography: An in Vitro Screen for Predicting Drug Membrane Permeability. *J. Med. Chem.* 1995;38:590-594.
64. Lázaro E, Ràfols C, Abraham M, Rosés M. Chromatographic Estimation of Drug Disposition Properties by Means of Immobilized Artificial Membranes (IAM) and C18 Columns. *J. Med. Chem.* 2006;49(16):4861-4870.

65. Cheng Y, Ho E, Subramanyam B, Tseng J. Measurements of drug-protein binding by using immobilized human serum albumin liquid chromatography - mass spectrometry. *J. Chromatogr. B.* 2004;809:67-73.
66. Valko K, Nunhuck S, Bevan C, Abraham M, Reynolds D. Fast Gradient HPLC Method to Determine Compounds Binding to Human Serum Albumin. Relationships with Octanol/Water and Immobilized Artificial Membrane Lipophilicity. *J. Pharm. Sci.* 2003;92(11):2236-2248.
67. Singh S, Mehta J. Measurement of drug-protein binding by immobilized human serum albumin-HPLC and comparison with ultrafiltration. *J. Chromatogr. B.* 2006;834:108-116.
68. Valko K, My Du C, Bevan C, Reynolds D, Abraham M. Rapid-Gradient HPLC method for measuring drug interactions with immobilized artificial membrane: comparison with other lipophilicity measures. *J. Pharm. Sci.* 2000;89(8):1085-1096.
69. Taillardat-Bertschinger A, Galland A, Carrupt P-A, Testa B. Immobilized artificial membrane liquid chromatography: proposed guidelines for technical optimization of retention measurements. *J. Chromatogr. A.* 2002;953:39-53.
70. Oya S, Choi S-R, Hou C, et al. 2-((2-((Dimethylamino)methyl)phenyl)thio)-5-iodophenylamine (ADAM): An Improved Serotonin Transporter Ligand. *Nucl. Med. Biol.* 2000;27:249-254.
71. Kawai K, Fujibayashi Y, Saji H, et al. A Strategy for the Study of Cerebral Amino Acid Transport Using Iodine-123-Labeled Amino Acid Radiopharmaceutical: 3-Iodo-alpha-methyl-L-tyrosine. *J. Nucl. Med.* 1991;32:819-824.
72. Huang Y, Hwang D-R, Narendran R, et al. Comparative Evaluation in Nonhuman Primates of Five PET Radiotracers for Imaging the Serotonin Transporters: [¹¹C]McN5652, [¹¹C]ADAM, [¹¹C]DASB, [¹¹C]DAPA, and [¹¹C]AFM. *J. Cereb. Blood Flow Metab.* 2002;22:1377-1398.
73. Wester HJ, Herz M, Weber W, et al. Synthesis and Radiopharmacology of O-(2-[¹⁸F]fluoroethyl)-L-Tyrosine for Tumor Imaging. *J. Nucl. Med.* 1999;40:205-212.

74. Li H, Gildehaus FJ, Dresel S, et al. Comparison of in vivo dopamine D2 receptor binding of [¹²³I]AIBZM and [¹²³I]IBZM in rat brain. *Nucl. Med. Biol.* 2001;28:383-389.
75. Beer H-F, Bläuenstein PA, Hasler PH, et al. In Vitro and In Vivo Evaluation of Iodine-123-Ro 16-0154: A New Imaging Agent for SPECT Investigations of Benzodiazepine Receptors. *J. Nucl. Med.* 1990;31:1007-1014.
76. Kudo Y, Okamura N, Furumoto S, et al. 2-(2-[2-Dimethylaminothiazol-5-yl]Ethenyl)-6-(2-[Fluoro]Ethoxy)Benzoxazole: A Novel PET Agent for In Vivo Detection of Dense Amyloid Plaques in Alzheimer's Disease Patients. *J. Nucl. Med.* 2007;48:553-561.
77. Roivainen A, Någren K, Hirvonen J, et al. Whole-body distribution and metabolism of [N-methyl-¹¹C](R)-1-(2-chlorophenyl)-N-(1-methylpropyl)-3-isoquinolinecarboxamide in humans; an imaging agent for in vivo assessment of peripheral benzodiazepine receptor activity with positron emission tomography. *Eur. J. Nuc. Med. Mol. Imag.* 2009;36:671-682.
78. Blasberg R, Patlak C, Hiraga S, et al. Kinetic Analysis of IQNB and the Muscarinic ACh-Receptor System in Brain. *J. Nucl. Med.* 1985;26(7):827.
79. Saji H, Ogawa M, Ueda M, et al. Evaluation of radioiodinated 5-iodo-3-(2(S)-azetidinylmethoxy)pyridine as a ligand for SPECT investigations of brain nicotinic acetylcholine receptors. *Ann. Nucl. Med.* 2002;16(3):189-200.
80. Dey HM, Seibyl JP, Stubbs JB, et al. Human Biodistribution and Dosimetry of the SPECT Benzodiazepine Receptor Radioligand Iodine-123-lomazenil. *J. Nucl. Med.* 1994;35:399-404.
81. Abi-Dargham A, Laruelle M, Seibyl J, et al. SPECT Measurement of Benzodiazepine Receptors in Human Brain with Iodine-123-lomazenil: Kinetic and Equilibrium Paradigms. *J. Nucl. Med.* 1994;35:228-238.
82. Abi-Dargham A, Innis RB, Wisniewski G, Baldwin RM, Neumeyer JL, Seibyl JP. Human biodistribution and dosimetry of iodine-123-fluoroalkyl analogs of B-CIT. *Eur. J. Nucl. Med.* 1997;24:1422-1425.

83. Laruelle M, Wallace E, Seibyl J, et al. Graphical, kinetic, and equilibrium analyses of in vivo [^{123}I] beta-CIT binding to dopamine transporters in healthy human subjects. *J. Cereb. Blood Flow Metab.* 1994;14(6):982-994.
84. Fujita M, Seibyl JP, Vaupel DB, et al. Whole-body biodistribution, radiation absorbed dose, and brain SPET imaging with [^{123}I]5-I-A-85380 in healthy human subjects. *Eur. J. Nucl. Med.* 2002;29:183-190.
85. Fujita M, Ichise M, Dyck CH, et al. Quantification of nicotinic acetylcholine receptors in human brain using [^{123}I]5-I-A-85380 SPET. *Eur. J. Nuc. Med. Mol. Imag.* 2003;30:1620-1629.
86. Saha GB, MacIntyre WJ, Go RT. Radiopharmaceuticals for Brain Imaging. *Semin. Nucl. Med.* 1994;24(4):324-349.
87. Norbury R, Travis MJ, Erlandsson K, et al. SPET imaging of central muscarinic receptors with (R,R)[^{123}I]-I-QNB: Methodological considerations. *Nucl. Med. Biol.* 2004;31:583-590.
88. Lu J-Q, Ichise M, Liow J-S, Ghose S, Vines D, Innis RB. Biodistribution and Radiation Dosimetry of the Serotonin Transporter Ligand ^{11}C -DASB Determined from Human Whole-Body PET. *J. Nucl. Med.* 2004;45:1555-1559.
89. Ginovart N, Wilson AA, Meyer JH, Hussey D, Houle S. Positron Emission Tomography Quantification of [^{11}C]-DASB Binding to the Human Serotonin Transporter: Modeling Strategies. *J. Cereb. Blood Flow Metab.* 2001;21:1342-1353.
90. Kung H, Alavi A, Chang W, et al. In Vivo SPECT Imaging of CNS D-2 Dopamine Receptors: Initial Studies with Iodine-123-IBZM in Humans. *J. Nucl. Med.* 1990;31:573-579.
91. Meyer PT, Sattler B, Winz OH, et al. Kinetic analyses of [^{123}I]IBZM SPECT for quantification of striatal dopamine D2 receptor binding: A critical evaluation of the single-scan approach. *Neuroimage.* 2008;42:548-558.
92. Kauppinen TA, Bergström KA, Heikman P, Hiltunen J, Ahonen AK. Biodistribution and radiation dosimetry of [^{123}I]ADAM in healthy human subjects: preliminary results. *Eur. J. Nucl. Med.* 2003;30:132-136.

93. Yang B-H, Wang S-J, Chou Y-H, et al. Evaluation of reference tissue model and tissue ratio method for 5-HTT using [¹²³I] ADAM tracer. *Comput. Methods Programs Biomed.* 2008;92:294-298.
94. Hirvonen J, Roivainen A, Virta J, Helin S, Någren K, Rinne JO. Human biodistribution and radiation dosimetry of ¹¹C-(R)-PK11195, the prototypic PET ligand to image inflammation. *Eur. J. Nuc. Med. Mol. Imag.* 2010;37:606-612.
95. Kropholler MA, Boellaard R, Schuitemaker A, et al. Development of a tracer kinetic plasma input model for (R)-[¹¹C]PK11195 brain studies. *J. Cereb. Blood Flow Metab.* 2005;25:842-851.
96. Versijpt J, Dumont F, Thierens H, et al. Biodistribution and dosimetry of [¹²³I]iodo-PK 11195: a potential agent for SPET imaging of the peripheral benzodiazepine receptor. *Eur. J. Nucl. Med.* 2000;27:1326-1333.
97. Tolboom N, Yaqub M, Flier WMvd, et al. Detection of Alzheimer Pathology In Vivo Using Both ¹¹C-PIB and ¹⁸F-FDDNP PET. *J. Nucl. Med.* 2009;50:191-197.
98. Ohtsuki S, Terasaki T. Contribution of Carrier-Mediated Transport System to the Blood-Brain Barrier as a Supporting and Protective Interface for the Brain; Importance for CNS Drug Discovery and Development. *Pharm. Res.* 2007;24(9):1745-1758.
99. Pardridge W. CNS Drug Design Based on Principles of Blood-Brain Barrier Transport. *J. Neurochem.* 1998;70:1781-1792.
100. Liu X, Chen C, Smith B. Progress in Brain Penetration Evaluation in Drug Discovery and Development. *J. Pharmacol. Exp. Ther.* 2008;325(2):349-356.
101. Jeffrey P, Summerfield S. Assessment of the blood-brain barrier in CNS drug discovery. *Neurobiol. Dis.* 2010;37:33-37.
102. Jeffrey P, Summerfield S. Challenges for blood-brain barrier (BBB) screening. *Xenobiotica.* 2007;37(10-11):1135-1151.

103. Chauveau F, Boutin H, van Camp N, Dollé F, Tavitian B. Nuclear imaging of neuroinflammation: a comprehensive review of [¹¹C]PK11195 challengers. *Eur. J. Nuc. Med. Mol. Imag.* 2008;35:2304-2319.
104. Ressler KJ, Nemeroff CB. Role of Norepinephrine in the Pathophysiology and Treatment of Mood Disorders. *Biol. Psychiatry.* 1999;46:1219-1233.
105. Ding Y, Singhal T, Planeta-Wilson B, et al. PET Imaging of the Effects of Age and Cocaine on the Norepinephrine Transporter in the Human Brain Using (S,S)-[¹¹C]O-Methylreboxetine and HRRT. *Synapse.* 2010;64:30-38.
106. Moore RY, Bloom FE. Central Catecholamine Neuron Systems: Anatomy and Physiology of the Norepinephrine and Epinephrine Systems. *Annu. Rev. Neurosci.* 1979;2:113-168.
107. Sara S. The locus coeruleus and noradrenergic modulation of cognition. *Nature Reviews: Neuroscience.* 2009;10:211-223.
108. Schou M, Pike VW, Sóvágó J, et al. Synthesis of ¹¹C-labelled (R)-OHDMI and CFMME and their evaluation as candidate radioligands for imaging central norepinephrine transporters with PET. *Bioorg. Med. Chem.* 2007;15:616-625.
109. Schou M, Pike VW, Varrone A, Gulyás B, Farde L, Halldin C. Synthesis and PET evaluation of (R)-[S-methyl-¹¹C]thionisoxetine, a candidate radioligand for imaging brain norepinephrine transporters. *J. Label. Compd. Radiopharm.* 2006;49:1007-1019.
110. Wilson AA, Johnson DP, Mozley D, et al. Synthesis and in vivo evaluation of novel radiotracers for the in vivo imaging of the norepinephrine transporter. *Nucl. Med. Biol.* 2003;30:85-92.
111. Takano A, Varrone A, Gulyás B, Karlsson P, Tauscher J, Halldin C. Mapping of the norepinephrine transporter in the human brain using PET with (S,S)-[¹⁸F]FMeNER-D₂. *Neuroimage.* 2008;42:474-482.
112. Seneca N, Gulyás B, Varrone A, et al. Atomoxetine occupies the norepinephrine transporter in dose-dependent fashion: a PET study in nonhuman primate brain using (S,S)-[¹⁸F]FMeNER-D₂. *Psychopharmacology (Berl).* 2006;188:119-127.

113. Takano A, Gulyás B, Varrone A, Maguire R, Halldin C. Saturated norepinephrine transporter occupancy by atomoxetine relevant to clinical doses: a rhesus monkey study with (S,S)-[¹⁸F]FMeNER-D₂. *Eur. J. Nuc. Med. Mol. Imag.* 2009;36:1308-1314.
114. Tamagnan GD, Brenner E, Alagille D, et al. Development of SPECT imaging agents for the norepinephrine transporters: [¹²³I]INER. *Bioorg. Med. Chem. Lett.* 2007;17:533-537.
115. Brenner E, Baldwin RM, Tamagnan GD. Asymmetric Synthesis of (+)-(S,S)-Reboxetine via a New (S)-2-(Hydroxymethyl)morpholine Preparation. *Org. Lett.* 2005;7(5):937-939.
116. Kanegawa N, Kiyono Y, Kimura H, et al. Synthesis and evaluation of radioiodinated (S,S)-2-(α -(2-iodophenoxy)benzyl)morpholine for imaging brain norepinephrine transporter. *Eur. J. Nucl. Med. Mol. Imag.* 2006;33:639-647.
117. Wong EHF, Sonders MS, Amara SG, et al. Reboxetine: A Pharmacologically Potent, Selective and Specific Norepinephrine Reuptake Inhibitor. *Biol. Psychiatry.* 2000;47:818-829.
118. Page ME. The Promises and Pitfalls of Reboxetine. *CNS Drug Rev.* 2003;9(4):327-342.
119. Cheetham SC, Viggers JA, Butler SA, Prow MR, Heal DJ. [³H]Nisoxetine - A Radioligand for Noradrenaline Reuptake Sites: Correlation with Inhibition of [³H]Noradrenaline Uptake and Effects of DSP-4 Lesioning and Antidepressant Treatments. *Neuropharmacology.* 1996;35(1):63-70.
120. Eersels JLH, Travi MJ, Herscheid JDM. Manufacturing ¹²³I-labelled radiopharmaceuticals. Pitfalls and solutions. *J. Label. Compd. Radiopharm.* 2005;48:241-257.
121. Hutchins G, Miller M, Soon V, Receveur T. Small Animal PET Imaging. *ILAR J.* 2008;49(1):54-65.
122. Collier TL, Schiller PW, Waterhouse RN. Radiosynthesis and in vivo evaluation of the pseudopeptide δ -opioid antagonist [¹²⁵I]-ITIPP (ψ). *Nucl. Med. Biol.* 2001;28:375-381.

123. Horti AG, Koren AO, Lee KS, et al. Radiosynthesis and Preliminary Evaluation of 5- $^{123/125}$ Iodo-3-(2(S)-azetidinylmethoxy)pyridine: A Radioligand for Nicotinic Acetylcholine Receptors. *Nucl. Med. Biol.* 1999;26:175-182.
124. Bois F, Baldwin RM, Amici L, et al. Synthesis, radiolabeling and baboon SPECT imaging of 2B-carbomethoxy-3B-(3'- 123 I)iodophenyl)tropane (123 I]YP256) as a serotonin transporter radiotracer. *Nucl. Med. Biol.* 2008;35:53-59.
125. De Bruyne S, Boos TL, Wyffels L, Goeman JL, Rice KC, Vos F. Synthesis, radiosynthesis and in vivo evaluation of 123 I]-4-(2-(bis(4-fluorophenyl)methoxy)ethyl)-1-(4-iodobenzyl)piperidine as a selective tracer for imaging the dopamine transporters. *J. Label. Compd. Radiopharm.* 2009;53:304-311.
126. Pimlott S, Stevenson L, Wyper D, Sutherland A. Rapid and efficient radiosynthesis of 123 I]-PK11195, a single photon emission computed tomography tracer for peripheral benzodiazepine receptors. *Nucl. Med. Biol.* 2008;35:537-542.
127. Gildersleeve DL, Van Dort ME, Johnson JW, Sherman PS, Wieland DM. Synthesis and Evaluation of 123 I]-Iodo-PK11195 for Mapping Peripheral-Type Benzodiazepine Receptors (ω_3) in Heart. *Nucl. Med. Biol.* 1996;23:23-28.
128. Zeng Q, Mock B. Purification of carbon-11 PET radiotracers from unlabeled precursors by preparative HPLC and SPE. *Biomed. Chromatogr.* 2005;19:671-676.
129. Mathis CA, Enas JD, Hanrahan SM, Akgün E. Synthesis of 123 I]- and 125 I]-labelled 5-Iodo-6-Nitroquipazine. *J. Label. Compd. Radiopharm.* 1994;34(10):905-913.
130. Carpinelli A, Matarrese M, Moresco RM, et al. Radiosynthesis of 123 I]BCIT, a selective ligand for the study of the dopaminergic and serotonergic systems in human brain. *Appl. Radiat. Isot.* 2001;54:93-95.
131. Bolton R. Radiohalogen incorporation into organic systems. *J. Label. Compd. Radiopharm.* 2002;45:485-528.
132. Musachio JL, Villemagne VL, Scheffel UA, et al. Synthesis of an I-123 Analogue of A-85380 and Preliminary SPECT Imaging of Nicotinic Receptors in Baboon. *Nucl. Med. Biol.* 1999;26:201-207.

133. Papazian V, Jackson T, Pham T, et al. The preparation of 123I/125I-clioquinol for the study of A β protein in Alzheimer's disease. *J. Label. Compd. Radiopharm.* 2005;48:473-484.
134. Aston-Jones G. Locus Coeruleus, A5 and A7 Noradrenergic Cell Groups. In: Paxinos G, ed. *The Rat Nervous System*. 3rd ed. San Diego: Elsevier; 2004.
135. Tejani-Butt SM. [^3H]Nisoxetine: A Radioligand for Quantitation of Norepinephrine Uptake Sites by Autoradiography or by Homogenate Binding. *J. Pharmacol. Exp. Ther.* 1992;260(1):427-436.
136. Paxinos G, Watson C. *The Rat Brain in Stereotaxic Coordinates*. 4th ed. San Diego: Academic Press; 1998.
137. Takano A, Halldin C, Varrone A, et al. Biodistribution and radiation dosimetry of the norepinephrine transporter radioligand (S,S)-[^{18}F]FMeNER-D $_2$: a human whole body PET study. *Eur. J. Nucl. Med. Mol. Imag.* 2008;35:630-636.
138. Tseng Y-T, Padbury JF. Expression of a pulmonary endothelial norepinephrine transporter. *J. Neural Transm.* 1998;105:1187-1191.
139. Ding Y, Lin K, Garza V, et al. Evaluation of a New Norepinephrine Transporter PET Ligand in Baboons, Both in Brain and Peripheral Organs. *Synapse*. 2003;50:345-352.
140. Van De Graaff K. *Human Anatomy*. 3rd ed: McGrawHill; 2003.
141. Miroslavov AE, Gorshkov NI, Lumpov AL, et al. Evaluation of $^{99\text{m}}\text{Tc}(\text{CO})_5\text{I}$ as a potential lung perfusion agent. *Nucl. Med. Biol.* 2009;36:73-79.
142. Al-Saeedi FJ. Perfusion scanning using $^{99\text{m}}\text{Tc}$ -HMPAO detects early cerebrovascular changes in the diabetic rat. *BMC Med. Phys.* 2008;8:1-4.
143. Bauwens M, Lahoutte T, Kersemans K, Caveliers V, Bossuyt A, Mertens J. D- and L-[^{123}I]-2-l-phenylalanine show a long tumour retention compared with D- and L-[^{123}I]-2-l-tyrosine in R1M rhabdomyosarcoma tumour-bearing Wag/Rij rats. *Contrast Media Mol. I.* 2007;2:172-177.

144. Roberts J, Chen B, Curtis L, Agarwal A, Sanders P, Zinn K. Detection of early changes in renal function using ^{99m}Tc -MAG3 imaging in a murine model of ischemia-reperfusion injury. *Am. J. Physiol. Renal Physiol.* 2007;293:1408-1412.
145. Fu C, Wang Y, Guo Y, Lin T, Chiu J. *In Vivo* Bio-Distribution of Intravenously Injected Tc-99m Labelled Ferrite Nanoparticles Bounded With Biocompatible Medicals. *IEEE T. Magn.* 2005;41(10):4120-4122.
146. Núñez E, Faintuch B, Teodoro R, et al. Influence of colloid particle profile on sentinel lymph node uptake. *Nucl. Med. Biol.* 2009;36:741-747.
147. Samnick S, Romeike B, Kusbuschok B, et al. *p*-[^{123}I]iodo-L-phenylalanine for detection of pancreatic cancer: basic investigations of the uptake characteristics in primary human pancreatic tumour cells and evaluation in *in vivo* models of human pancreatic adenocarcinoma. *Eur. J. Nucl. Med. Mol. Imag.* 2004;31(4):532-541.
148. Visser M, Bernard H, Erion J, et al. Novel ^{111}In -labelled bombesin analogues for molecular imaging of prostate tumours. *Eur. J. Nucl. Med. Mol. Imag.* 2007;34:1228-1238.
149. Yoon J, Park B, Shim W, Shin J, Lee G, Ahn Y. *In vivo* tracking of ^{111}In labeled bone marrow mesenchymal stem cells in acute brain trauma model. *Nucl. Med. Biol.* 2010;37:381-388.
150. Chandra S, De K, Ganguly S, Sarkar B, Mirsa M. Synthesis, radiolabeling and biological evaluation of a neutral tripeptide and its derivatives for potential nuclear medicine applications. *Peptides.* 2009;30:2399-2408.
151. Koblin D. Urethane: Help or Hindrance? *Anesth. Analg.* 2002;94:241-242.
152. Smith HR, Beveridge TJR, Porrino LJ. Distribution of Norepinephrine Transporters in the Non-Human Primate Brain. *Neuroscience.* 2006;138:703-714.
153. Innis R, Cunningham V, Delforge J, et al. Consensus nomenclature for *in vivo* imaging of reversibly binding radioligands. *J. Cereb. Blood Flow Metab.* 2007;27:1533-1539.

154. Seibyl JP, Stobbert HA, Martin D, Smith E, Wisniewsk G, Stoddart HF. Evaluation of high resolution NeuroFocus SPECT device for small animal imaging. *J. Nucl. Med.* 2002;43(UNSP 202375|936).
155. Stoddart HAS, Stoddart HF. New multidimensional reconstructions for the 12-detector, scanned focal point, single photon tomograph. *Phys. Med. Biol.* 1992;37(3):579-586.
156. Gandelman M, Baldwin R, Zoghbi SS, Zea-Ponce Y, Innis R. Evaluation of Ultrafiltration for the Free-Fraction Determination of Single Photon Emission Computed Tomography (SPECT) Radiotracers: β -CIT, IBF and Iomazenil. *J. Pharm. Sci.* 1994;83(7):1014-1019.
157. Zoghbi SS, Baldwin R, Seibyl J, et al. Pharmacokinetics of the SPECT Benzodiazepine Receptor Radioligand [^{123}I]Iomazenil in Human and Non-human Primates. *Nucl. Med. Biol.* 1992;19(8):881-888.
158. Baldwin R, Zea-Ponce Y, Zoghbi SS, et al. Evaluation of the Monoamine Uptake Site Ligand [^{123}I]Methyl 3 β -(4-Iodophenyl)-tropane-2 β -carboxylate ([^{123}I] β -CIT) in Non-human Primates: Pharmacokinetics, Biodistribution and SPECT Brain Imaging Coregistered with MRI. *Nucl. Med. Biol.* 1993;20(5):597-606.
159. Baldwin R, Zea-Ponce Y, Al-Tikriti M, et al. Regional Brain Uptake and Pharmacokinetics of [^{123}I]N- ω -Fluoroalkyl-2 β -carboxy-3 β -(4-iodophenyl)nortropane Esters in Baboons. *Nucl. Med. Biol.* 1995;22(2):211-219.
160. Chang L-T. A Method for Attenuation Correction in Radionuclide Computed Tomography. *IEEE T. Nucl. Med.* 1978;25(1):638-643.
161. Schou M, Halldin C, S ov ag o J, et al. Specific *in vivo* binding to the norepinephrine transporter demonstrated with the PET radioligand, (S,S)-[^{11}C]MeNER. *Nucl. Med. Biol.* 2003;30:707-714.
162. Tavares A, Jobson NK, Dewar D, Sutherland A, Pimlott S. ^{123}I -NKJ64: A Novel Single Photon Emission Computed Tomography Radiotracer for Imaging the Noradrenaline Transporter in Brain *Synapse*. 2011;65:658-667.

163. Ichise M, Liow J-S, Lu J-Q, et al. Linearized Reference Tissue Parametric Imaging Methods: Application to [¹¹C]DASB Positron Emission Tomography Studies of the Serotonin Transporter in Human Brain. *J. Cereb. Blood Flow Metab.* 2003;23:1096-1112.
164. Lammerstma A, Hume S. Simplified reference tissue model for PET receptor studies. *Neuroimage.* 1996;4:153-158.
165. Cunningham VJ, Rabiner EA, Slifstein M, Laruelle M, Gunn R. Measuring drug occupancy in the absence of a reference region: the Lassen plot re-visited. *J. Cereb. Blood Flow Metab.* 2010;30(1):46-50.
166. Witcher J, Long A, Smith B, et al. Atomoxetine pharmacokinetics in children and adolescents with attention deficit hyperactivity disorder. *J. Child Adolesc. Psychopharmacol.* 2003;13(1):53-63.
167. Simpson D, Plosker GL. Atomoxetine: A Review of its Use in Adults with Attention Deficit Hyperactivity Disorder. *Drugs.* 2004;64(2):205-222.
168. Michelson D, Faries D, Wernicke J, et al. Atomoxetine in the Treatment of Children and Adolescents With Attention-Deficit/Hyperactivity Disorder: A Randomized, Placebo-Controlled, Dose-Response Study. *Pediatrics.* 2001;108(5):e83.
169. Eyding D, Lelgemann M, Grouven U, et al. Reboxetine for acute treatment of major depression: systematic review and meta-analysis of published and unpublished placebo and selective serotonin reuptake inhibitor controlled trials. *Br. Med. J.* 2010;341:c4737.
170. Cipriani A, Furukawa TA, Salanti G, et al. Comparative efficacy and acceptability of 12 new-generation antidepressants: a multiple-treatments meta-analysis. *Lancet.* 2009;373:746-758.
171. Ferguson J, Mendels J, Schwartz G. Effects of reboxetine on Hamilton Depression Rating Scale factors from randomized, placebo-controlled trials in major depression. *Int. Clin. Psychopharmacol.* 2002;17(2):45-51.
172. Montgomery S, Ferguson J, Schwartz G. The antidepressant efficacy of reboxetine in patients with severe depression. *J. Clin. Psychopharmacol.* 2003;23(1):45-50.

173. Bymaster F, Katner J, Nelson D, et al. Atomoxetine increases extracellular levels of norepinephrine and dopamine in prefrontal cortex of rat: a potential mechanism for efficacy in attention deficit/hyperactivity disorder. *Neuropsychopharmacology*. 2002;27(5):699-711.